



THE HONG KONG
POLYTECHNIC UNIVERSITY

香港理工大學

Pao Yue-kong Library

包玉剛圖書館

Copyright Undertaking

This thesis is protected by copyright, with all rights reserved.

By reading and using the thesis, the reader understands and agrees to the following terms:

1. The reader will abide by the rules and legal ordinances governing copyright regarding the use of the thesis.
2. The reader will use the thesis for the purpose of research or private study only and not for distribution or further reproduction or any other purpose.
3. The reader agrees to indemnify and hold the University harmless from and against any loss, damage, cost, liability or expenses arising from copyright infringement or unauthorized usage.

IMPORTANT

If you have reasons to believe that any materials in this thesis are deemed not suitable to be distributed in this form, or a copyright owner having difficulty with the material being included in our database, please contact lbsys@polyu.edu.hk providing details. The Library will look into your claim and consider taking remedial action upon receipt of the written requests.

Pao Yue-kong Library, The Hong Kong Polytechnic University, Hung Hom, Kowloon, Hong Kong

<http://www.lib.polyu.edu.hk>

**ENGINEERING PEROVSKITE
CRYSTALLIZATION KINETICS FOR HIGH-
EFFICIENCY AND STABILITY
PEROVSKITE SOLAR CELLS**

QIONG LIANG

PhD

The Hong Kong Polytechnic University

2024

The Hong Kong Polytechnic University

**Department of Electrical and Electronic
Engineering**

**Engineering Perovskite Crystalization Kinetics
For High-Efficiency and Stability Perovskite
Solar Cells**

Qiong LIANG

**A thesis submitted in partial fulfillment of the
requirements for the degree of Doctor of Philosophy**

May 2024

CERTIFICATE OF ORIGINALITY

I hereby declare that the thesis is my work and that, to the best of my knowledge and belief, it reproduces no material previously published or written, nor material that has been accepted for the award of any other degree or diploma, except where due acknowledgment has been made in the text.

_____ (Signed)

Qiong Liang (Name of student)

Abstract

Researchers have recently paid close attention to the perovskite thin film technology because of its rapid growth in power conversion efficiency (PCE) over a relatively short time. A highly advanced photovoltaic material called perovskite, used in solar cells, can absorb sunlight and instantly transform it into electricity. This method is ideal for producing energy using ubiquitous solar power since it is environmentally friendly and renewable. Perovskite solar cells (PSCs) must have excellent stability, exceptional photovoltaic performance, and affordable large-area devices to be industrialized.

Many studies have been conducted on the film-coating process for PSC production. In the mainstream one-step method, researchers have realized the formation of the intermediate phase of the perovskite complex in conjunction with antisolvent drop-casting, often followed by annealing to convert it into high-quality perovskite film. Due to its restrictions on substrate size, the lab spin-coating process only successfully covers limited, flat surfaces, making it unsuitable for large-scale manufacturing. Even though additive engineering in perovskite precursors has a solid track record in spin-coated PSCs, more thorough research into coating-friendly multifunctional additives that are specially designed for scalable deposition of perovskite films to improve PSC performance is still lacking. The stability issue is the main obstacle in the commercialization of PSCs due to the delicate and ionic nature of halide perovskite materials. Intrinsic defects at the perovskite surface and grain boundaries, which can negatively impact device performance, can hasten perovskite breakdown.

In my PhD research, I have conducted the following research projects on addressing some of the important challenges in the PSC field. I first integrated a multifunctional zwitterionic surfactant into perovskite ink to facilitate room-temperature meniscus coating of superior perovskite films. The inclusion of the surfactant into the ink provides many benefits for film development, including

enhanced crystallization kinetics, defect passivation, and protection against moisture barrier weakness. Then, we created a quick and efficient green solvent engineering (GSE) approach to use green ethyl alcohol (EtOH) instead of the conventional harmful solvent. With the aid of this technology, it is possible to create high-performance room-temperature blade-coated PSCs and modules while minimizing risks to the environment and health. In the third project, my research focuses on addressing the PSC stability issue with a new cross-linking strategy. Specifically, a novel cross-linking initiator divinyl sulfone (DVS), is incorporated into the perovskite precursor solution and achieves high-quality perovskite films with low defect density and high stability. This DVS successfully replaces benchmark DMSO, and furthermore, made it possible for a controlled co-polymerization to occur both at the perovskite surface and in the GBs, ensuring a balanced kinetics for the formation of perovskite crystals by modifying the intermediate-dominated perovskite crystallization and passivating the intrinsic defects at the near-surface region.

Publications

1. K Liu, **Q Liang**, et al. Zwitterionic-surfactant-assisted room-temperature coating of efficient perovskite solar cells, *Joule* 4 (11), 2404-2425, 119, 2020. (Chapter 3)
2. **Q Liang**, et al. Manipulating Crystallization Kinetics in High-Performance Blade-Coated Perovskite Solar Cells via Cosolvent-Assisted Phase Transition, *Advanced Materials*, 34 (16), 2200276, 43, 2022. (Chapter 4)
3. **Q Liang**, et al. Highly stable perovskite solar cells with 0.30 voltage deficit enabled by a multi-functional asynchronous cross-linking. (Under submission) (Chapter 5)
4. X Qin, Y He, CK Tao, A Sergeev, KS Wong, Z Ren, **Q Liang**, et al. Effect of Passivating Molecules and Antisolvents on Lifetime of Green Dion–Jacobson Perovskite Light-Emitting Diodes. *ACS Applied Materials & Interfaces*, 15 (25), 30083-30092, 2023
5. D Li, Y Huang, R Ma, H Liu, **Q Liang**, et al. Surface Regulation with Polymerized Small Molecular Acceptor Towards Efficient Inverted Perovskite Solar Cells. *Advanced Energy Materials*. 13 (18), 2204247, 4, 2023.
6. J Huang, Z Lu, J He, H Hu, **Q Liang**, et al. Intrinsically stretchable, semi-transparent organic photovoltaics with high efficiency and mechanical robustness via a full-solution process. *Energy & Environmental Science*, 16 (3), 1251-1263, 10, 2023.
7. H Zhang, W Yu, J Guo, C Xu, Z Ren, K Liu, G Yang, M Qin, J Huang, Z Chen, **Q Liang**, et al. Excess PbI₂ Management via Multimode Supramolecular Complex

- Engineering Enables High-Performance Perovskite Solar Cells. *Advanced Energy Materials*, 12 (35), 2201663, 12, 2022.
8. J Huang, Z Ren, Y Zhang, PWK Fong, HT Chandran, **Q Liang**, et al. Tandem self-powered flexible electrochromic energy supplier for sustainable all-day operations. *Advanced Energy Materials*, 12 (30), 2201042, 10, 2022.
 9. Y Wang, J Lin, Y He, Y Zhang, **Q Liang**, et al. Improvement in the performance of inverted 3D/2D perovskite solar cells by ambient exposure. *Solar RRL*, 6 (7), 2200224, 7, 2022.
 10. N Li, S Apergi, CCS Chan, Y Jia, F Xie, **Q Liang**, et al. Diammonium-Mediated Perovskite Film Formation for High-Luminescence Red Perovskite Light-Emitting Diodes. *Advanced Materials*, 34 (30), 2202042, 16, 2022.
 11. J Yu, X Liu, Z Zhong, C Yan, H Liu, PWK Fong, **Q Liang**, et al. Copper phosphotungstate as low cost, solution-processed, stable inorganic anode interfacial material enables organic photovoltaics with over 18% efficiency. *Nano Energy*, 94, 106923, 17, 2022.
 12. Z Ren, K Liu, H Hu, X Guo, Y Gao, PWK Fong, **Q Liang**, et al. Room-temperature multiple ligands-tailored SnO₂ quantum dots endow in situ dual-interface binding for upscaling efficient perovskite photovoltaics with high V_{OC}. *Light: Science & Applications*, 10 (1), 239, 32, 2021.
 13. K Liu, PWK Fong, **Q Liang**, et al. Upscaling perovskite solar cells via the ambient deposition of perovskite thin films. *Trends in Chemistry*, 3 (9), 747-764, 10, 2021.

14. G Yang, Z Ren, K Liu, M Qin, W Deng, H Zhang, H Wang, J Liang, F Ye, **Q Liang**, et al. Stable and low-photovoltage-loss perovskite solar cells by multifunctional passivation. *Nature Photonics* 15 (9), 681-689, 217, 2021.
15. H Zhang, M Qin, Z Chen, W Yu, Z Ren, K Liu, J Huang, Y Zhang, **Q Liang**, et al. Bottom-Up Quasi-Epitaxial Growth of Hybrid Perovskite from Solution Process—Achieving High-Efficiency Solar Cells via Template-Guided Crystallization. *Advanced Materials*, 33 (22), 2100009, 42, 2021.
16. PWK Fong, H Hu, Z Ren, K Liu, L Cui, T Bi, **Q Liang**, et al. Printing high-efficiency perovskite solar cells in high-humidity ambient environment—an in situ guided investigation. *Advanced Science* 8 (6), 2003359, 34, 2021.
17. H Hu, W Deng, M Qin, H Yin, TK Lau, PWK Fong, Z Ren, **Q Liang**, et al. Charge carrier transport and nanomorphology control for efficient non-fullerene organic solar cells. *Materials Today Energy*, 12, 398-407, 25, 2019.

Acknowledgments

It is a wonderful pleasure to receive my PhD from the Hong Kong Polytechnic University. Over the past five years, it has been a fantastic, unforgettable, and valuable experience for my career. I would like to express my deepest gratitude to my supervisor, Professor Gang Li, who is an erudite, patient, and enthusiastic mentor, encouraging me to investigate scientific research, develop my potential, and find my research direction.

Table of Contents

Abstract.....	4
Publications.....	6
Acknowledgments.....	9
Table of Contents	10
List of Figures	13
List of Tables.....	27
Chapter 1 Introduction	29
1.1 Characteristics of Solar Cells.....	31
1.1.1 Solar Irradiance	31
1.1.2 Solar Energy Conversion Methods	33
1.1.3 The Working Principle	34
1.1.4 Prerequisites for Ideal Solar Cells.....	35
Band Gap	35
Absorption	36
Carriers Separation	37
Carriers Transport	37
Load Resistance	38
1.2 Solar Cell Equivalent Circuit	38
1.2.1 Ideal P-N junction	38
1.2.2 Non-Ideal P-N Junction and Parasitic Resistances	40
1.3 Solar Cell Critical Parameters.....	40
1.3.1 Current	41
Photocurrent.....	41
Dark Current	41
1.3.2 Open Circuit Voltage.....	43
1.3.3 Efficiencies.....	46
Power Conversion Efficiency	46
Chapter 2 Perovskite Solar Cells	48
2.1 Device Structure and Components of Perovskite Solar Cells.....	50

2.1.1 ITO/FTO glasses	51
2.1.2 The hole transport layer (HTL).....	51
2.1.3 The active layer.....	52
2.1.4 The electron transport layer (ETL)	53
2.2 Photovoltaic Materials of The Perovskite Active Layer	54
2.3 Perovskite Nucleation and Crystal Growth Mechanisms	56
2.3.1 Perovskite Nucleation	56
2.3.2 Perovskite Growth Mechanisms	58
2.4 Basics of Perovskite Solvent Engineering	58
2.5 Perovskite Solar Cell Deposition Techniques	60
2.5.1 Spin Coating.....	61
2.5.2 Doctor Blading.....	61
2.5.3 Slot-die coating	63
2.5.4 Bar coating	63
2.6 Material characterization and application.....	64
2.6.1 Chemical Composition Analysis.....	64
Fourier-Transform Infrared Spectroscopy (FTIR)	65
2.6.2 Structure determination.....	67
X-Ray Diffraction (XRD).....	67
2.6.3 Morphology observation.....	71
Scanning Electron Microscopy (SEM)	71
2.7 Research motivation and objectives.....	73
2.7.1 Primary Challenges and Research Motivation.....	73
2.7.2 Research objectives.....	74
2.7.3 Thesis outline	74
Chapter 3 Zwitterionic-Surfactant-Assisted Room Temperature Coating of Efficient Perovskite Solar Cells	76
3.1 Introduction.....	76
3.2 Results and Discussion	79
3.2.1 Perovskite Film Deposition and Morphology.....	79
3.2.2 Perovskite Crystallization and Orientation	85

3.2.3	Charged Defects Passivation.....	92
3.2.4	Photovoltaic Device Performance.....	99
3.2.5	Water-Resistant Perovskite Films and Device Stability.....	112
3.3	Conclusion	115
3.4	Experimental Procedures	116
Chapter 4 Manipulating Crystallization Kinetics in High-Performance Blade-Coated Perovskite Solar Cells via Cosolvent-Assisted Phase Transition		120
4.1	Introduction.....	120
4.2	Results and Discussion	122
4.3	Conclusion	147
4.4	Experimental Section	149
Chapter 5 Highly stable perovskite solar cells with 0.30 voltage deficit enabled by a multi-functional asynchronous cross-linking.....		153
5.1	Introduction.....	153
5.2	Result and discussion.....	156
5.3	Conclusion	180
5.4	Experimental Section	180
Chapter 6 Summary and Outlook		184
6.1	Summary	184
6.2	Outlook	186
References.....		189

List of Figures

Figure 1. 1 Global primary energy consumption by source. Source: Our World in Data based on Vaclav Smil (2017) and BP Statistical Review of World Energy.	30
Figure 1. 2 Annual change in solar energy generation.....	30
Figure 1. 3 The electromagnetic spectrum Extra-terrestrial (Air Mass 0) solar spectrum (black line) compared with the 5760 K black body spectrum reduced by the factor of 4.6×10^4 (thick grey line) and with the standard terrestrial (Air Mass 1.5) spectrum (thin grey line). ⁵	32
Figure 1. 4 The angle of elevation from Earth to the sun in air mass. ⁵	32
Figure 1. 5 The three fundamental optical processes between two energy levels. The dark spot reveals the state of the electron. ⁶	34
Figure 1. 6 Power spectrum of a black body sun at 5760 K and power available to the optimum band gap cell. ⁵	35
Figure 1. 7 Thermodynamic theoretical limiting efficiency for a single band gap solar cell in AM 1.5. ⁵	36
Figure 1. 8 The solar cell equivalent circuit with series and parallel resistance. ⁵	38
Figure 1. 9 Intrinsic and Quasi Fermi levels and intrinsic potential in the P-N junction under depletion approximation. ⁵	39
Figure 1. 10 Solar cell characteristics for current and voltage under light and in the dark. ⁵	42
Figure 1. 11 The current density - voltage characteristic curve (black) and the power density - voltage typical curve (grey) of an ideal cell. ⁵	47
Figure 2. 1 perovskite structure.source: https://www.x-mol.com/news/13131 . ..	48
Figure 2. 2 Best research-cell efficiencies between 1975 and 2023. ¹⁸	50
Figure 2. 3 The structure of perovskite solar cells.	51

Figure 2. 4 Diagram of HOMO and LUMO molecular orbitals.	53
Figure 2. 5 The materials of each functional layer of perovskite solar cells.	54
Figure 2. 6 Exploring the Relationship between Tolerance Factor and Crystal Structure in Perovskite Materials. ²⁰	55
Figure 2. 7 The diagram illustrates the dynamics of nucleation and growth. 51.74	57
Figure 2. 8 The process of the deposition using the spin coating method. ²²	61
Figure 2. 9 The process of the deposition using the doctor blading method.	62
Figure 2. 10 Deposition methods of perovskite solar cells	64
Figure 2. 11 Bragg Diffraction.....	69
Figure 3. 1 The molecular structure of TAH.	79
Figure 3. 2 Perovskite Film Deposition and Morphology. (A) Schematic illustration of the zwitterionic surfactant-assisted meniscus coating at room temperature. (B) Schematic illustration of the coordinate interaction between TAH and charged defects at the perovskite surface and GBs and spontaneous formation of moisture barrier. (C) Photographs of the blade-coated perovskite films with different amount of TAH on PTAA-coated ITO substrates. (D) Contact angles of the corresponding perovskite ink droplets on PTAA-coated ITO substrates. (E) ToF-SIMS depth-profile analysis in the TAH-incorporated perovskite film.	81
Figure 3. 3 Photographs of the as-cast perovskite films with different amounts of TAH before thermal annealing.....	81
Figure 3. 4 SEM images of the blade-coated perovskite films with different amount of TAH on PTAA/ITO substrate. Scale bar: 500 nm.	82
Figure 3. 5 Cross-sectional SEM images of the pristine and TAH-based perovskite films blade-coated on PTAA/ITO substrate and corresponding EDX mapping. Scale bar: 500 nm.....	83
Figure 3. 6 AFM height images of the blade-coated perovskite films with different amount of TAH. Scale bar: 500 nm.	84

- Figure 3. 7 (A) UV-vis absorption spectra of the perovskite films with different amounts of TAH. (B) Tauc plots as a function of $(\alpha h\nu)^2$ vs energy for the respective perovskite films. The band gap can be determined via linear extrapolation of the leading edges of the $(\alpha h\nu)^2$ curve to the baseline.....84
- Figure 3. 8 XRD patterns of the as-cast pristine and TAH incorporated perovskite films before annealing.....85
- Figure 3. 9 Crystallization Dynamics of the Intermediate Complex and Perovskite. (A) In-situ GIWAXS intensity profiles measured within 100 frames during the drying process of the perovskite inks without (left) and with 0.1 wt% TAH (right). (B) In-situ GIWAXS false-color intensity maps versus q and frame numbers during the drying process of the corresponding perovskite inks. (C) In-situ UV-vis absorption spectra as a function of annealing time for the perovskite without and with 0.1 wt% TAH annealed at 100 °C. (D) Time-resolved UV-vis absorption intensity at the wavelength of 550 nm for the corresponding perovskite films annealed at 100 °C.....87
- Figure 3. 10 2D GIWAXS patterns of the respective perovskite inks at different crystallization stages versus drying time.88
- Figure 3. 11 (A) In-situ GIWAXS intensity profile and (B) the corresponding false-color intensity map versus q and frame numbers during the drying process of the 0.05 wt% TAH incorporated perovskite ink.....88
- Figure 3. 12 Perovskite Crystallization and Orientation. (A) XRD patterns of the annealed perovskite films incorporated with different amounts of TAH. (B) 2D GIWAXS patterns of the pristine (left) and TAH-incorporated perovskites (right) at the upper surface ($\alpha=0.2^\circ$) and in the bulk ($\alpha=1^\circ$). (C) The polar intensity profiles along the (110) ring in the range of $q = 0.95-1.05 \text{ \AA}^{-1}$ from 2D GIWAXS patterns of the pristine and TAH-incorporated perovskites in the bulk ($\alpha=1^\circ$)......91

Figure 3. 13 Full width at half maximum (FWHM) of (110) peaks in the perovskite films with different amounts of TAH.....	92
Figure 3. 14 GIWAXS intensity profiles of (A) the pristine and (B) TAH-incorporated perovskites at the upper surface (black curve, $\alpha_i = 0.2^\circ$) and in the bulk (red curve, $\alpha_i = 1^\circ$), respectively.....	92
Figure 3. 15 Charged Defects Passivation. (A) Steady-state PL spectra of the perovskite films with different amounts of TAH. All the samples were prepared on quartz substrates excited with a 636.2 nm laser. (B)TRPL decays of the respective perovskite films. All the samples were prepared on quartz substrates excited with a 636.2 nm laser. (C)Excitation intensity dependence of the PL lifetime in the TAH incorporated perovskite film. (D)XPS Pb 4f spectra of the pristine and 0.1 wt% TAH incorporated perovskites. (E).FITR spectra of the pure TAH, pristine perovskite, and TAH-based perovskite films. (F)SCLC analysis of the pristine and TAH-incorporated perovskite films (fitting the slope in the trap-free regime). Inset: structure of electron-only device.	94
Figure 3. 16 (A) Excitation fluence dependence of the initial PL intensity just after the excitation in the TAH-incorporated perovskite film. (B) TRPL decay in the TAH incorporated perovskite with the excitation of 636.2 and 375.2 nm, respectively.	95
Fluence-dependent TRPL decay for the sample of TAH-incorporated perovskite was performed in order to reveal the PL lifetime and initial PL intensity right after the excitation of a 636.2 nm pulsed laser as a function of its fluence (Figure 3. 15C and Figure 3. 16A). The initial PL intensity exhibited a linear dependence on the excitation fluence, and the PL lifetime remained almost constant (Table 3.2), which confirmed low excitation fluence ($\leq 5 \text{ nJ/cm}^2$) in TRPL mainly triggered the trapping and nonradiative recombination behaviors of photogenerated carriers.	96

Figure 3. 17 XPS survey for (A) the pristine and (B) 0.1 wt% TAH incorporated perovskites.98

Figure 3. 18 Perovskite Solar Cells Performance. (A) Schematic device architecture of the inverted p-i-n PSCs. (B) Energy-level diagrams of corresponding components in the inverted p-i-n PSCs. (C) J-V curves of the best-performance control and TAH-based devices with p-i-n structure. (D) EQE spectra and integrated JSC values for the control and TAH-based devices. (E) EL spectra for the TAH-based device under voltage bias from 1.2 to 1.8 V. Inset: a photograph showing a TAH-based PSC operating as an LED (active area: 0.04 cm²) with visible red emission. (F) EQEEL as a function of the applied voltage bias for the control and TAH-based PSCs operating as LEDs. (G) Mott-Schottky plots in the control and TAH-based devices. (H) Nt distribution as a function of defect energy level E_u for the control and TAH-based devices, as measured in the TAS method. (I) J-V curves of the best-performance TAH-based PSCs with 0.04 and 0.8 cm² active area in the conventional n-i-p structure. Inset: a photograph showing a 0.8 cm² device. 101

Figure 3. 19 UPS spectra of PTAA, pristine MAPbI₃, TAH based MAPbI₃ and PC₆₁BM respectively..... 102

Figure 3. 20 Energy band structure of a complete p-i-n structured PSCs under short-circuit condition and vacuum level offset due to the interfacial dipole. 102

Figure 3. 21 (A) J-V curves of the best-performance TAH-based devices under different concentrations. (B) Transmittance of ITO/glass substrates with and without AR film. 103

Figure 3. 22 Hysteresis effect in J-V curves under different scanning directions for the representative (A) control and (B) TAH based device. (C) Steady-state photocurrent outputs and stabilized PCEs under MPP for the control and TAH based devices. (D) PCEs histogram of 20 control and TAH based devices. 103

- Figure 3. 23 (A) EQ_{EEL} as a function of the driving current density for the control and TAH-based PSCs when operating as LEDs. (B) Capacitance spectra as a function of AC frequency for the control and TAH-based devices..... 107
- Figure 3. 24 (A) Capacitance spectra as a function of AC frequency for the control and TAH-based devices. (B) Mott–Schottky plots for the corresponding devices..... 108
- Figure 3. 25 (A) $J-V$ curves of the best-performance control and TAH-based devices in conventional n-i-p architecture (0.04 cm^2 active area). (B) Steady-state photocurrent output and stabilized PCE under MPP at 0.98 V bias for the TAH-based n-i-p device (0.8 cm^2 active area). Inset: photograph of a blade-coated perovskite film on an FTO substrate with a $3\text{ cm} \times 2\text{ cm}$ dimension..... 109
- Figure 3. 26 State-of-the-art PCEs of the upscaling coated PSCs under different deposition temperatures summarized from previous works. 110
- Figure 3. 27 (A) Contact angles of the water droplet on the surface of pristine and TAH-based perovskite films. (B) Evolution of the perovskite phase for the pristine and TAH-incorporated perovskite films exposed under $25 \pm 5\text{ }^\circ\text{C}$ and $60 \pm 10\%$ RH for over 14 days..... 113
- Figure 3. 28 Water-Resistant Perovskite Films and Device Stability. (A) Dynamic dissolving process of a water droplet on the surface of pristine and TAH-incorporated perovskite films. (B) Ambient stability of the unencapsulated devices shelved under $25^\circ\text{C} \pm 5^\circ\text{C}$ and $20\% \pm 5\%$ RH. Data were represented as the mean value and the standard deviation from 10 samples in each condition. (C) Thermal stability of the unencapsulated devices at $80^\circ\text{C} \pm 5^\circ\text{C}$ in a nitrogen atmosphere. Data were represented as the mean value and the standard deviation from 5 samples in each condition. (D) Light stability of the encapsulated devices exposed under continuous 0.7 sun illumination at

- 40°C ± 5°C and 50% ± 5% RH. Data were represented as the mean value and the standard deviation from 5 samples in each condition. 114
- Figure 4. 1 Perovskite precursor ink in the mixed solvent system with different volume of DMF and EtOH (e.g., 8:2 means volume ratio of DMF/EtOH is 9:1).. 123
- Figure 4. 2 (A) Schematic illustration of the nitrogen-quenching-assisted room-temperature blade coating technique (step I), trace-solvent-assisted phase transition (step II), and thermal annealing (step III). Crystal structure of the involved intermediate phases. (B) In situ UV–vis absorption spectra as a function of gas-quenching time for the perovskite wet films fabricated by the ink with different volume ratios of DMF/EtOH. (C) UV–vis absorption intensity evolution at the wavelength of 500 nm during the gas quenching. (D) Corresponding nucleation rates are calculated by their first derivative..... 125
- Figure 4. 3 (A) XRD patterns for the as-prepared perovskite/intermediate films after gas quenching. (B) Evolution for the perovskite (100) peak at $2\theta = 14.06^\circ$ during the SAPT process..... 127
- Figure 4. 4 (A) In situ XRD false-color intensity maps during the TSAT process for the perovskite/intermediate films fabricated by the 10:0 and 9:1 ink, respectively, where * represents cubic perovskite phase; # represents MA₂Pb₃I₈·2DMSO; @ represents FA₂PbBr₄·DMSO. (B) XRD intensity evolution for the FA-based adduct (FA₂PbBr₄·DMSO) at $2\theta = 15.20^\circ$ during the TSAT process. C, D) 3D contour plot of electronic distributions of FA₂PbBr₄·DMSO. (C) and FA₂PbBr₄·DMSO incorporated with EtOH. (D), in which dark gray balls = Pb, brown balls = Br, blue balls = N, red balls = O, yellow balls = S, light gray balls = C, and white balls = H; the blue isosurfaces

- represent bonding orbitals, and the green isosurfaces represent antibonding orbitals. E)..... 130
- Figure 4. 5 (A) Projected partial density of states (PDOS) for the $\text{PbBr}_2 \cdot 2\text{DMSO}$. (B) The formation energy of $\text{FA}_2\text{PbBr}_4 \cdot \text{DMSO}$ as a function of the volume ratio between DMSO and EtOH. 131
- Figure 4. 6 In situ XRD false-color intensity maps versus 2θ and annealing time for the perovskite films fabricated by the ink with 10:0 (A) and 9:1 (B) volume ratios of DMF/EtOH, in which * represents cubic perovskite phase; # represents $\text{MA}_2\text{Pb}_3\text{I}_8 \cdot 2\text{DMSO}$; @ represents $\text{FA}_2\text{PbBr}_4 \cdot \text{DMSO}$. (C) XRD intensity evolution for the intermediate phases at $2\theta = 6.58^\circ, 7.26^\circ, 9.26^\circ,$ and 15.20° , respectively, during the annealing process. (D) XRD intensity evolution for the perovskite main peak at $2\theta = 14.06^\circ$ and corresponding crystal growth rates. (E) XRD patterns of the annealed perovskite films fabricated by the inks with different volume ratios between DMF and EtOH. (F) FWHM of (100) peak for the corresponding perovskite films. 133
- Figure 4. 7 (A) In-situ XRD false-color intensity map versus 2θ and annealing time for the 9:1 based perovskite films without trace solvent assisted transition process (TSAT), in which * represents cubic perovskite phase; # represents $\text{MA}_2\text{Pb}_3\text{I}_8 \cdot 2\text{DMSO}$; @ represents $\text{FA}_2\text{PbBr}_4 \cdot \text{DMSO}$. (B) XRD intensity evolution of the intermediate phases at $2\theta = 6.58^\circ, 7.26^\circ, 9.26^\circ$ and 15.20° , and the perovskite main peak at $2\theta = 14.06^\circ$, respectively. The crystal growth rate is calculated from the first derivative of the corresponding intensity. 133
- Figure 4. 8 2D GIWAXS patterns of the corresponding perovskite films fabricated by the inks with (A) 10:0 and (B) 9:1 volume ratio of DMF and EtOH. (C)

The polar intensity profiles along the (100) ring in the range of $q = 0.95-1.05 \text{ \AA}^{-1}$ from 2D GIWAXS patterns.....	134
Figure 4. 9 (A) Steady-state PL spectra of the perovskite films fabricated by the ink with different volume ratios between DMF and EtOH. All samples were prepared on quartz substrates with the excitation at 636.2 nm. (B) TRPL decays of the corresponding perovskite films. (C) $J-V$ curves of the champion blade-coated PSCs in a 1.60 eV perovskite system (0.04 cm^2 device area) from the ink with different volume ratios between DMF and EtOH. (D) Plot of the light intensity-dependent V_{OC} for the control and ECS-based devices. (E) Fill factor limitation is composed of nonradiative loss (pink area) and transport loss (orange area). (F) Energetic trap density distribution for the control and ECS-based devices measured by admittance spectroscopy. ...	136
Figure 4. 10 (A) Cross-sectional SEM images of the conventional n-i-p PSCs assembled with the structure of ITO/SnO ₂ /perovskite/spiro-OMeTAD/Au; scale bar: 1 μm . (B) Tauc plots as a function of $(\alpha h\nu)^2$ vs. energy for the CsFAMA-based perovskite films fabricated by the ink with different volume ratios between DMF and EtOH. The band gap can be determined via linear extrapolation of the leading edges of the $(\alpha h\nu)^2$ curve to the baseline. (C) Top-view SEM images of the corresponding perovskite films by the 10:0, 9:1, and 8:2 inks, respectively; scale bar:1 μm	137
Figure 4. 11 UPS spectra of the control and ECS-based perovskite films.....	138
Figure 4. 12 (A) PCE distribution of the blade-coated PSCs from the ink with different volume ratios of DMF/EtOH. (B) $J-V$ curves of the best-performance ECS-based devices with device areas of 0.04 and 0.98 cm^2 , respectively. (C) EQE spectra of the control and ECS-based devices. (D) Steady-state photocurrent output and stabilized PCEs for the control and ECS-based devices.....	138
Figure 4. 13 $J-V$ curves of the representative control and ECS-based devices without TSAT.	139

Figure 4. 14 Calculation of the bandgap for the control (A) and ECS-based perovskite films through EQE spectra. The maximum differential value of EQE can determine E_g^{IP} 139

Figure 4. 15 J - V curves under forward and reverse scanning for the representative control and ECS-based devices..... 139

Figure 4. 16 EQE_{EL} as a function of the injection current density (A) and applied voltage bias (B) for the control and ECS-based PSCs when operating as LEDs. (C) EL spectra for the representative ECS-based device under voltage bias from 1.2 to 2.5 V; inset is a photograph showing an ECS-based PSC operating as an LED (device area: 0.04 cm²) with visible red emission. (D) V_{OC} deficit from band-to-band radiative and non-radiative recombination loss for the control and ECS-based devices, respectively..... 143

Figure 4. 17 SCLC analysis for the electron-only devices based on the pristine and ECS-based perovskite films. 144

Figure 4. 18 Nyquist plots of the control (A) and ECS-based devices (B) in the dark under 0.7 to 1.0 V bias voltage, respectively. Inset: equivalent circuit for the simulation of charge transfer and recombination process. The relationship between bias voltage and (C) R_S and (D) R_{rec} 145

Figure 4. 19 (A) J - V curves of the champion control and ECS-based PSCs in a 1.54 eV perovskite system from forward and reverse scan directions. (B) EQE spectrum of the ECS-based devices with an integrated J_{SC} of 23.55 mA cm⁻². (C) J - V curves of the champion ECS-based device (0.98 cm² device area) and minimodule (2.7 cm², 3-subcells). (D) Comparison of the state-of-the-art PCEs from the previous relevant works as a function of device area.¹⁴⁶ (E) EQE_{EL} as a function of the injection current density for the control and ECS-based PSCs when operating as LEDs. (F) Long-term stability for the control and ECS-based devices under different aging conditions..... 148

Figure 4. 20 V_{OC} (left) and PCE (right) distribution for ten representative ECS-based devices in a 1.54 eV perovskite system. 148

- Figure 5. 1 (A) Schematic illustration of intermediate-dominated perovskite crystallization by pre-embedded DVS and all-around co-polymerization protection through the post-treatment of gly. (B) Linear fitting of ^{23}Na NMR chemical shift and DN of the selected organic solvents to calculate the DN of DVS. (C) ^1H NMR spectra of FAI, DVS, and FAI/DVS into DMSO- d_6 solution, respectively. (D) Two-dimensional pseudo-color absorption intensity mapping as a function of spin-coating time during the in-situ measurement. 158
- Figure 5. 2 ^{23}Na nuclear magnetic resonance (NMR) spectra for common organic solvents and DVS..... 159
- Figure 5. 3 Photo images of PbI_2 power in DVS (left), FAI powder in DVS (middle), and DVS solvent (right) 159
- Figure 5. 4 XRD patterns of FAI powder and quasi-wet films by FAI/DMSO and FAI/DVS solutions; inset: the diffraction peaks of FAI-DVS solvate. 159
- Figure 5. 5 UV-vis absorption intensity evolution at the wavelength of 450 nm during anti-solvent assisted spin coating of the control and DVS-based perovskite inks. 160
- Figure 5. 6 (A) Pseudo-colour mapping of the UV-vis absorption spectra as a function of annealing time. (B) In-situ XRD measurement of the control and DVS-gly based perovskite films during thermal annealing (intermediate phases presented by # and * symbol can be ascribed to FAI-DVS solvate). (C) Corresponding XRD spectra as a function of annealing time. (D) XRD intensity evolution of the perovskite prominent peak at $2\theta=14.01^\circ$ 161
- Figure 5. 7 UV-vis absorption intensity evolution at the wavelength of 450 nm and t for the control and DVS-gly based perovskite films during thermal annealing and their corresponding crystal growth rate. 162
- Figure 5. 8 (A) XRD patterns of the as-cast control and DVS-based perovskite films (intermediate phases presented by # and * symbol can be ascribed to FAI-DVS solvate); inset: intermediate phase presented by @ is assigned to

MAI-PbI ₂ -DMSO based solvate. (B) XRD patterns as a function of annealing time for the DVS-based sample in intervals of 4 minutes each (▲ is corresponding to the perovskite central peak).	162
Figure 5. 9. The JV curves at different glycerol concentrations.	163
Figure 5. 10 (a) After annealing, FITR spectra in selected regions for the DVS solvent, as-cast DVS-based perovskite film, and DVS-gly-based perovskite final film. (b) MALDI-TOF-MS measurement for the DVS/gly mixture solution. (c-d) GI-XRD spectra in 2θ - $\sin^2\psi$ mode for (c) control and (d) DVS-gly based perovskite films at near-surface region (50 nm depth), respectively. (e) In-depth XPS spectra for the DVS-gly-based perovskite film. (f) TRPL decay for the control, DVS, and DVS-gly-based perovskite films.	165
Figure 5. 11 FITR spectra for the DVS solvent, as-cast DVS-based perovskite film, and DVS-gly-based perovskite final film after annealing.	165
Figure 5. 12 Nucleophile-mediated oxa-Michael addition reactions between DVS and gly.	166
Figure 5. 13 (A) After thermal annealing, XRD patterns of the final control, DVS-based, and DVS-gly-based perovskite films. (B) FWHM of the perovskite prominent peak at $2\theta=14.01^\circ$ for the corresponding samples.....	168
Figure 5. 14 SEM top view images of the control, DVS-based, and DVS-gly-based perovskite films; scale bar: 1 μm	168
Figure 5. 15 GI-XRD spectra in 2θ - $\sin^2\psi$ mode for the DVS-gly based perovskite films at near-surface region (50 nm depth, left) and in bulk (200 nm depth, right), respectively.....	169
Figure 5. 16. Steady-state PL spectra for the control and DVS-gly-based perovskite films.	171
Figure 5. 17. UPS results at the cut-off region for the control, DVS-based, and DVS-gly-based perovskite films.....	171

- Figure 5. 18 (A) J - V curves for the PSCs based on the ink with different volume ratio of DVS. (B) Representative J - V curves of the DVS-gly-based devices under forward and reverse scanning, respectively. 172
- Figure 5. 19 (A) J - V curves of the best-performance control and DVS-gly-based devices. (B) EQE spectrum of the DVS-gly based PSCs. (C) EQE_{EL} as a function of the injection current density to calculate the nonradiative recombination loss. (D) Energetic distribution of trap density for the control and DVS-gly based PSCs measured by admittance spectroscopy. 172
- Figure 5. 20. Certified results from an Taiwan Accreditation Foundation (TAF) accredited photovoltaic certification laboratory (Enli Tech. Optoelectronic Calibration Lab., Taiwan). The certified PCE is 24.63% - certified aperture with the area of 0.067 cm². 173
- Figure 5. 21 Calculation of the bandgap for the DVS-gly-based perovskite films through EQE spectra. The maximum differential value of EQE can determine E_{g}^{IP} 173
- Figure 5. 22 (A) EQE_{EL} as a function of the applied voltage bias for the DVS-gly based PSCs when operating as LEDs. (B) EL spectra for the representative DVS-gly based device under voltage bias from 1 to 1.5 V. 174
- Figure 5. 23. J - V curve for the DVS-gly based minimodule (3-subcells, 3.6*3.6 cm² substrate, active area: 5.85 cm²). 175
- Figure 5. 24 (A-B) Nyquist plots of the control (A) and DVS-gly based PSC (B) in the dark under 0.7 to 1.0 V bias voltage, respectively; Inset: equivalent circuit for the simulation of charge transfer and recombination process. (C-D) The relationship between bias voltage and (C) R_{s} and (D) R_{rec} for the corresponding PSCs, respectively. 177
- Figure 5. 25 (A) Images of a DVS-gly-based perovskite film directly immersed in water. (b-d) Long-term stability test under (B) MPP tracking (encapsulated devices: 1-sun, 30 ± 5 °C, 60 ± 10% RH), (C) thermal stress (unencapsulated

device: dark, 80 ± 5 °C, N₂), (D) shelf storage (unencapsulated device: dark,
25 ± 5 °C, 20 ± 5% RH)..... 179

List of Tables

Table 3. 1 Fitting parameters of the bi-exponential decay function in TRPL spectra of the perovskites with different amount of TAH.	95
Table 3. 2 Fitting parameters of the bi-exponential decay function in fluence-dependent TRPL spectra of the TAH incorporated perovskite excited at 636.2 nm (0.1 to 4 nJ/cm ²).	95
Table 3. 3 Fitting parameters of the bi-exponential decay function in TRPL spectra of the TAH incorporated perovskite excited at 375.2 and 636.2 nm (4 nJ/cm ²), respectively.	97
Table 3. 4 Band structure of PTAA, pristine MAPbI ₃ , TAH-based MAPbI ₃ , and PC ₆₁ BM.	103
Table 3. 5 Photovoltaic parameters of the blade-coated inverted p-i-n PSCs incorporated with different amounts of TAH.	104
Table 3. 6 Photovoltaic parameters of the blade-coated PSCs in conventional n-i-p structure.	110
Table 3. 7 State-of-the-art PCEs of the upscaling coated PSCs under different deposition temperatures summarized from previous works.	111
Table 4. 1 Summary of the related solvent properties.	124
Table 4. 2 Calculation of the vapor pressure of the mixed solvent systems.	126
Table 4. 3 Fitting parameters of the bi-exponential decay function in TRPL spectra for the perovskite films fabricated by the ink with different volume ratios between DMF and EtOH.	137
Table 4. 4 Band structure of the control and ECS-based perovskite films.	140
Table 4. 5 Photovoltaic parameters of the control and ECS-based devices with different volume ratios between DMF and EtOH.	140
Table 4. 6 Photovoltaic parameters of the representative control and ECS-based devices without TAST.	141

Table 4. 7 Photovoltaic parameters for the representative control and ECS-based PSCs ($E_g=1.60$ eV) under forward and reverse scanning.	141
Table 4. 8 Photovoltaic parameters for the representative control and ECS-based PSCs ($E_g=1.54$ eV) under forward and reverse scanning.	149
Table 4. 9 Summary of the state-of-the-art values of V_{OC} deficit and non-radiative recombination loss ($\Delta V_{OC,nr}$) reported in other relevant works.....	149
Table 5. 1 ^{23}Na NMR shift for a series of common organic solvents to calculate the DN for DVS.	160
The resulting cross-link scaffold provided superior water resistance, released residual tensile strain near the perovskite surface, and suppressed deep-level defects. Compared with the control device, our strategy significantly improved the overall device performance, especially in open-circuit voltage (V_{oc}) and fill factor (FF). We also demonstrated the device performance dependence on the molar ratio of gly versus DVS, as shown in Figure 5. 9 and Table 5. 2. From 0 to 1.5 mol%, there is a slight improvement in V_{oc} , whereas, further increasing to 3 mol% shows a downtrend in FF values..	163
Table 5. 2 Photovoltaic parameters at different glycerol concentrations under optimized conditions.	164
Table 5. 3 Fitting parameters of the bi-exponential decay function in TRPL spectra for the corresponding perovskite films.	174
Table 5. 4 Photovoltaic parameters of the DVS based devices with different volume ratios of DVS into DMF host solvent.	174
Table 5. 5 Summary of the state-of-the-art values of V_{OC} deficit and non-radiative recombination loss ($\Delta V_{OC,nr}$) reported in other relevant works.....	175
Table 5. 6 Photovoltaic parameters of unencapsulated devices immersed in water as a function of time.....	179

Chapter 1 Introduction

The evolution of human lifestyles fuels the rise in global energy demand, and the world's primary energy consumption has dramatically increased over time. However, as shown in Figure 1. 1, between 1800 and 2021, the majority of the world's energy is from non-renewable resources such as coal and crude oil, which are known to be environmentally destructive. Unfortunately, only a tiny fraction of energy is produced using renewable sources, which are ecologically beneficial and safe. It is widely recognized that fossil fuels are a finite resource, and their burning releases harmful pollutants, including large amounts of carbon dioxide, which contribute to global warming. Air pollution caused by burning fossil fuels is also causing severe health problems worldwide. For example, many cities are experiencing severe air pollution problems, such as severe haze, due to the rapid increase in cars on the road and coal burning. These challenges have led to a critical question: How can we meet the increasing energy demand without harming the environment and replacing the existing fossil fuel energy supply? Renewable energy solutions such as hydroelectric, wind, nuclear, bioenergy, and solar have developed quickly and displaced some environmentally harmful non-renewable sources, while still not significant. Among these alternative green solutions, solar power is the most abundant and clean energy source on Earth. Unlike fossil fuels, solar power emits no greenhouse gases while operating, making it a sustainable and environmentally friendly alternative. The annual change in solar energy generation has significantly increased in various countries, particularly China, as shown in Figure 1. 2 for from 2010 to 2021. The most common form of solar energy harvesting is solar photovoltaic (PV) technology, which converts solar energy directly into electricity, fitting modern lifestyle well. Therefore, there is growing interest in studying and developing high-efficiency, reliable, and cost-effective solar PV technology as a sustainable solution to global energy demand while contributing to environmental protection.

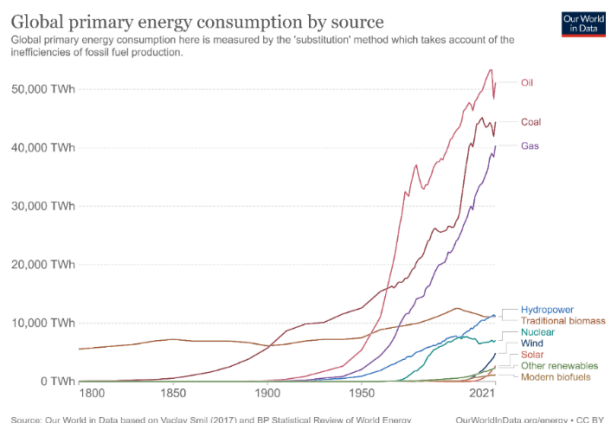


Figure 1. 1 Global primary energy consumption by source. Source: Our World in Data based on Vaclav Smil (2017) and BP Statistical Review of World Energy.

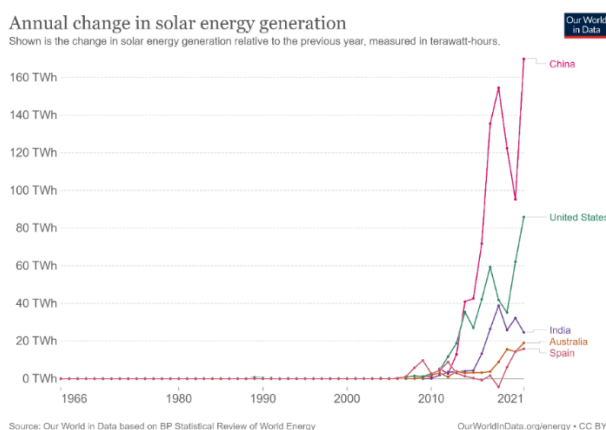


Figure 1. 2 Annual change in solar energy generation.

Source: Our World in Data based on BP Statistical Review of World Energy(2022).

The history of photovoltaic (PV) technology dates back to 1839 when Alexandre-Edmond Becquerel presented the first report on the photovoltaic effect. His research discovered that when incident light passed through a silver-covered platinum cathode in the electrolyte, it generated an electric current. Interestingly, in the same year, Gustav Rose discovered a CaTiO_3 -based mineral in the Ural Mountains that he dubbed “perovskite” in honour of a Russian mineralogist, Lev von Perovski. Charles Fritts invented primary solar cells in 1883, who created the junction by sandwiching a small layer of the semiconductor selenium between gold and another metal, despite the

efficiency being clearly under 1%. It was not until 1954 that Daryl Chapin, Calvin Fuller, and Gerald Pearson created the first silicon-based solar cell with a 6% efficiency at Bell Laboratories.^{1,2} Additionally, researchers at Bell Labs found that photovoltaic cells became progressively more sensitive to light by utilizing the doping process. In 1957, Egyptian specialist Mohamed M. Atalla employed thermal oxidation for silicon surface passivation, which has been crucial in creating high-efficiency solar cells ever since.³ ⁴ (Some intro of other types of solar cells – GaAs, CdTe, ..) Solar cells were first used as an alternative power source in space on the Vanguard satellite launched in 1958 by the United States, with massive wing-shaped solar arrays composed of 9600 Hoffman solar cells on Explorer 6 launched one year later. Finally, large solar farms were built in the United States starting in the 1980s, for example, in 1983 they established over 16 megawatts capacity solar farms.

1.1 Characteristics of Solar Cells

1.1.1 Solar Irradiance

The sun is the primary energy source for everyone and everything on Earth. The solar spectrum has several absorption peaks, as illustrated in Figure 1. 3. As solar radiation travels through the Earth's atmosphere, it is absorbed and scattered. This leads to a weakening of solar irradiation before it reaches the Earth's surface. Various atmospheric gases further influence the absorption and scattering of solar radiation by air particles. Solar irradiation is filtered by oxygen gas (O₂), ozone (O₃), and nitrogen gas when the wavelength is less than 300 nm (N₂). Water vapour (H₂O) and carbon dioxide will absorb the majority of the infrared spectrum (CO₂). Water vapour (H₂O) exhibits absorption peaks at wavelengths of 900 nm, 1100 nm, 1400 nm, and 1900 nm.

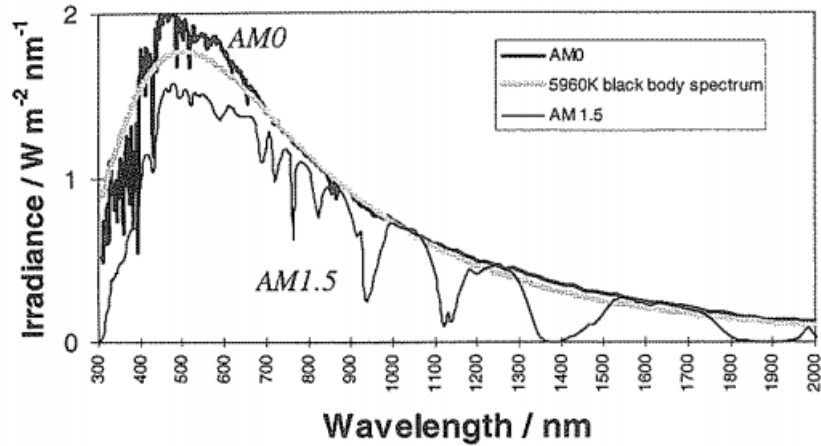


Figure 1. 3 The electromagnetic spectrum Extra-terrestrial (Air Mass 0) solar spectrum (black line) compared with the 5760 K black body spectrum reduced by the factor of 4.6×10^4 (thick grey line) and with the standard terrestrial (Air Mass 1.5) spectrum (thin grey line).⁵

The quantification of solar radiation attenuation in the atmosphere employs the air mass index ($n_{AirMass}$), as depicted in (Figure 1. 4) ⁵:

$$n_{AirMass} = \frac{\text{optical path length to sun}}{\text{optical path length if sun directly overhead}}$$

$$= \frac{\frac{d_{atm}}{\sin\gamma}}{d_{atm}} = \frac{1}{\sin\gamma_s} = \text{cosec}\gamma_s \quad (1.1)$$

Where γ_s represents the elevation angle from the Earth to the sun, while d_{atm} is the atmospheric depth.

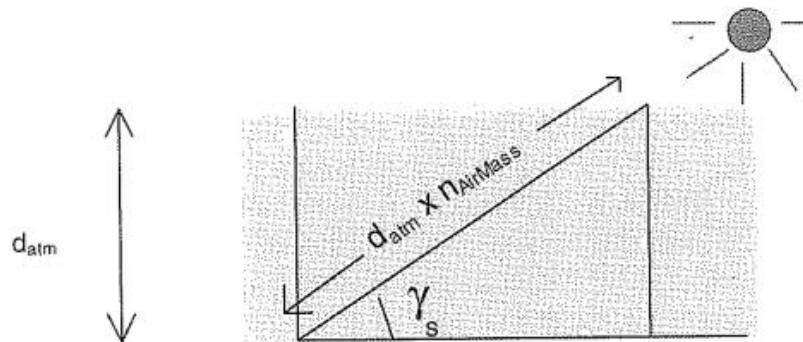


Figure 1. 4 The angle of elevation from Earth to the sun in air mass.⁵

For standard territorial test conditions, the air mass index (AM1.5 or Air Mass 1.5) is typically used, and its corresponding angle of elevation of the sun from the Earth is 42° . AM1.5G is the standard spectrum at the Earth's surface, with both direct and diffused radiations (G means global, including both direct and diffused components). AM1.5D has only direct radiation. To estimate AM1.5 radiation intensity, a common approach is to reduce the AM0 spectrum by 28%, accounting for 18% absorption and 10% scattering. The global spectrum surpasses the direct spectrum by 10%, resulting in an approximate power level of 970 W/m^2 for AM1.5G. However, the standard AM1.5G spectrum is established at 1kW/m^2 for ease of reference and to accommodate solar radiation variability.

1.1.2 Solar Energy Conversion Methods

Energy conversion can be classified into three distinct categories. The first type is photovoltaic energy conversion, which is based on the flow of voltage and current produced by the movement of electrons or radiation. These electric powers are then used to drive the load. This type of energy conversion is commonly observed in semiconductor materials, which generate electricity from light absorption, such as solar cells. The second method is solar thermal energy conversion. Solar radiation generate heat and a simple application is solar water heaters. The solar thermal energy can be effectively stored in proper media, most commonly salt in large solar thermal plants, in which the concentrated solar radiation raises the temperature to make the salt into molten salt that can flow and store the thermal energy until the thermal energy converts into other forms via heat exchange, for example, drive engine to generate electricity.

Lastly, photochemical energy conversion involves turning solar energy into carbohydrates. For example, chloroplasts use sunlight to synthesize glucose through biochemical reactions - photosynthesis.

1.1.3 The Working Principle

Three basic optical processes characterize the cooperation of a photon and an electron. (Figure 1. 5) ⁶ Upon incidence of light (photons) on a semiconductor material, such as silicon and perovskite, the electrons in the material can absorb the energy of the photons. If the energy of the photon energy is equal to or greater than the band gap of the material (the minimum energy needed for an electron to transition from the valence band to the conduction band), the electron will become excited from its initial energy level (valence band) to a higher energy level (conduction band), resulting in the creation of a hole in the original energy level. This mechanism underlies the working principle of photodetectors and solar cells, enabling the conversion of optical radiation into electrical energy. Secondly, in LEDs, electrons in the conduction band can spontaneously return to an unfilled state in the valence band, which converts electrical energy into optical radiation. Lastly, two coherent photons can be transmitted by stimulating the discharge of the other comparative photon during the recombination of the incoming photon. This procedure forms the basis of lasers. These three processes are fundamental to modern optoelectronics and essential to advancing a wide range of technologies.

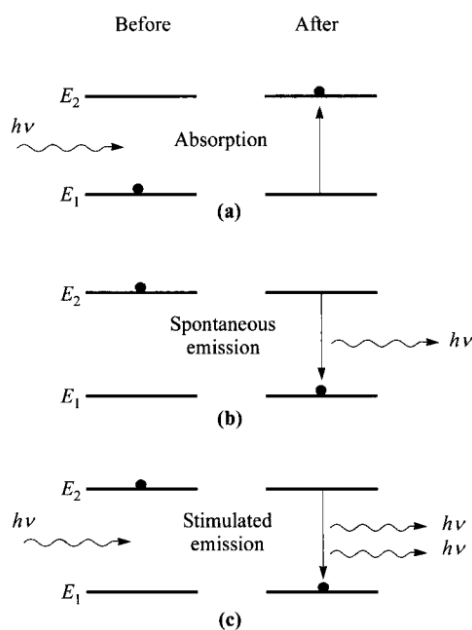


Figure 1. 5 The three fundamental optical processes between two energy levels. The dark spot reveals the state of the electron. ⁶

1.1.4 Prerequisites for Ideal Solar Cells

Band Gap

When a photon carries enough energy to surpass the bandgap, an electron can jump through excitation from the filled state to an unoccupied state in the conduction band. On the contrary, as illustrated in Figure 1. 6, the electron cannot transit from the valence band to the conduction band if the photon's energy is insufficient to overcome the band gap. Additionally, the absorption of each incident photon creates a pair of an electron and a hole. Visible photons can activate electrons in semiconductors with band gaps between 0.5 and 3 eV. For instance, at 300K, silicon has a bandgap of 1.12eV, and gallium arsenide (GaAs) has 1.42eV. The Shockley-Queisser limit, also known as the detailed-balance limit, proposes that the maximum conversion efficiency attainable is ~33% under AM1.5G 1-sun illumination. This efficiency limit is due to competition between recombination and thermodynamic losses. When a solar cell with a single bandgap has a 1.4eV bandgap, the theoretical limiting efficiency is calculated to be ~33% in AM 1.5, as demonstrated in Figure 1. 7 and confirmed by more precise calculations.

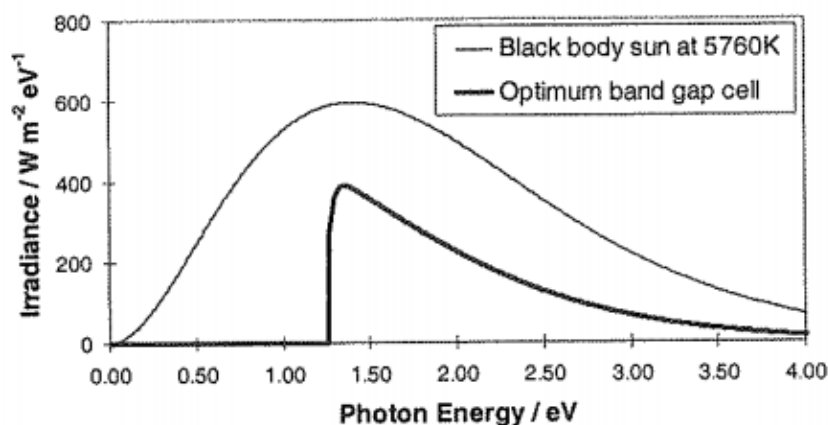


Figure 1. 6 Power spectrum of a black body sun at 5760 K and power available to the optimum band gap cell. ⁵

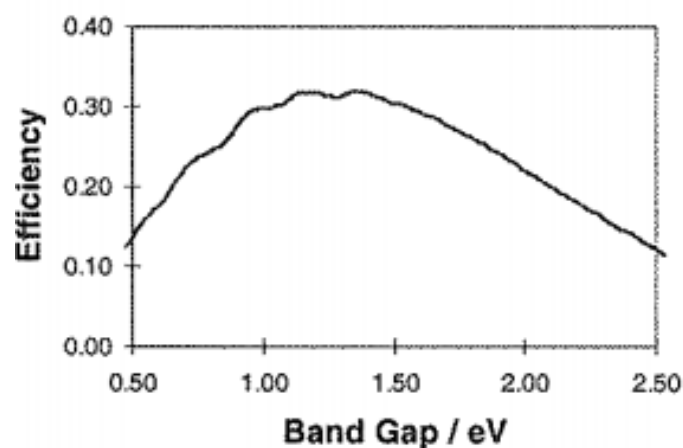


Figure 1. 7 Thermodynamic theoretical limiting efficiency for a single band gap solar cell in AM 1.5. ⁵

Absorption

The efficiency of photovoltaic cells heavily depends on the interactions that occur as light propagates through their material composition, including absorption, reflection, and transmission phenomena. The absorption of light is particularly crucial as it directly influences the conversion efficiency of solar cells, determining how much light energy can be absorbed by the cell material and converted into electrical energy.

The absorption coefficient, a pivotal physical parameter, quantifies the ability of the material to absorb light by measuring the rate of light intensity attenuation per unit length. This physical quantity reflects the capability of the material to absorb light energy within a relatively thin layer thickness. A high absorption coefficient indicates a significant capacity for light energy absorption. This coefficient is significantly impacted by various material-specific properties, such as its chemical composition, crystalline architecture, and electronic bandgap width.

The Beer-Lambert law, also known as Beer's law, Lambert's law, Bouguer's law, or the Bouguer-Lambert-Beer law, is a fundamental principle of light absorption that applies to all electromagnetic radiation and all absorbing substances, including gases, solids, liquids, molecules, atoms, and ions. The Beer-Lambert law serves as the quantitative basis for spectrophotometry, colorimetric analysis, and photometric colorimetry.

When a monochromatic light beam strikes the surface of an absorbing material, and then travels through a specific thickness of the material, the transmitted light's intensity diminishes because some of the light energy is absorbed by the material. The greater the concentration and thickness of the absorbing material, the more pronounced the reduction in light intensity, as described by Eq. 1.2:

$$A = \log_{10} \left(\frac{I_0}{I} \right) = K \cdot c \cdot l \quad (1.2)$$

Where A represents the absorbance of the solution, indicating the extent of light absorption by the solution. K is a coefficient, which could refer to either the absorption coefficient or the molar absorption coefficient. C represents the concentration of the absorbing substance, measured in units of g/L or mol/L. l stands for the thickness of the absorbing substance, typically measured in centimeters. I is the intensity of transmitted light, I_0 is an incident intensity. Increasing the thickness of the active layer to deepen the optical width makes it simple to achieve high absorption of light with incident light energy more remarkable than the bandgap. Typically, the thickness of semiconductors ranges from tens to hundreds of microns to ensure complete absorption.

Carriers Separation

In order to generate an electric field and induce a current, electrons must be evenly distributed, or their densities must be in a gradient. For example, the creation of a P-N junction using two different materials results in an unbalanced distribution of electrons. Furthermore, the efficiency of power conversion is highly dependent on the quality of the junction. Therefore, it is essential to minimize the loss of electrical potential energy when separating carriers.

Carriers Transport

While transporting the charge from the interior circuit to the exterior successfully, it is vital to reduce both parallel and series resistance and minimize carriers that recombine as well as contaminants and defects.

Load Resistance

It must reach its peak at the maximum power point to optimize the load resistance. However, it cannot be utilized if the working voltage is below 1 volt. In order to increase the voltage, solar cells should be combined in series within a module and further linked in parallel and series to form an array.

1.2 Solar Cell Equivalent Circuit

The power of cells is hindered by contact resistance and leakage current at their edges. These similar effects are present in the circuit shown in Figure 1. 8, where parasitic resistance occurs in series (R_s) and parallel (R_{sh}).

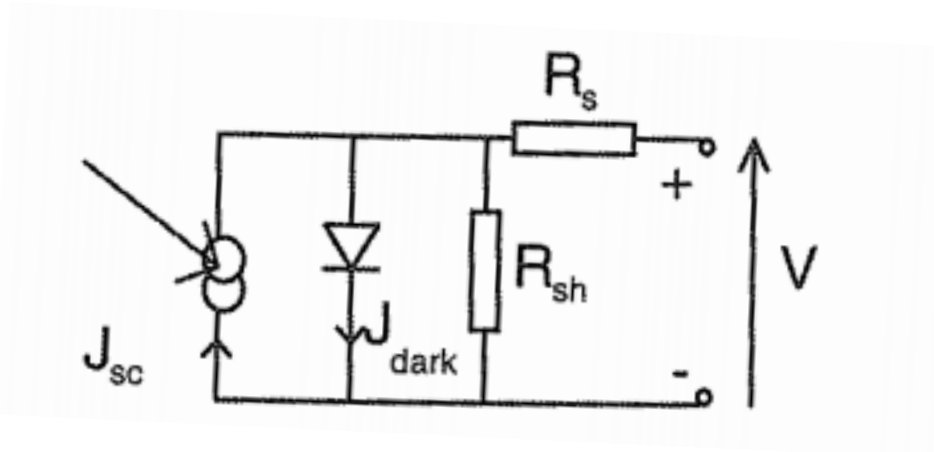


Figure 1. 8 The solar cell equivalent circuit with series and parallel resistance. ⁵

1.2.1 Ideal P-N junction

The operation of solar cells is based on the photovoltaic effect of a semiconductor P-N junction. In this process, both the current on the n side and the current on the p side traverse the space charge region of the P-N junction before converting into the diffusion current (J_{diff} in Eq. 1.3), which results in the minority carrier diffusion shown in Figure 1. 9.

$$J_{diff}(V) = J_{diff}^0 \left[\exp\left(\frac{qV}{k_B T}\right) - 1 \right] \quad (1.3)$$

Where J_{diff}^0 is the reverse saturation diffusion current density, A/cm².

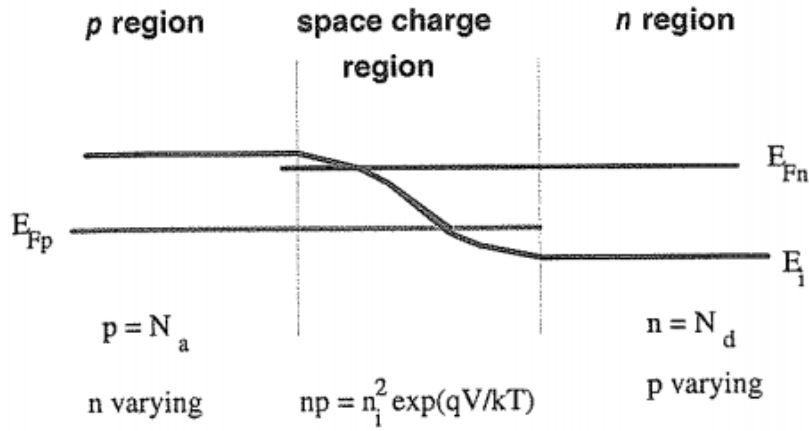


Figure 1. 9 Intrinsic and Quasi Fermi levels and intrinsic potential in the P-N junction under depletion approximation. ⁵

Moreover, Eq. 1.4 might be used to determine the current from the space charge zone (depletion region). Besides that, Eq. 1.4 displays the entire dark current.

$$J_{scr}(V) = J_{scr}^0 \left[\exp\left(\frac{qV}{2k_B T}\right) - 1 \right] \quad (1.4)$$

$$J_{dark}(V) = J_{diff}^0 \left[\exp\left(\frac{qV}{k_B T}\right) - 1 \right] + J_{scr}^0 \left[\exp\left(\frac{qV}{2k_B T}\right) - 1 \right] + J_{rad}^0 \left[\exp\left(\frac{qV}{k_B T}\right) - 1 \right] \quad (1.5)$$

Where J_{scr}^0 is the reverse saturation current density of the space charge region, A/cm² and J_{rad}^0 are the reverse saturation radiative current density.

Since the diffusion lengths of indirect gap semiconductors like silicon are longer than the depletion width, there is hardly any recombination in the space charge region. Consequently, the equation (Eq. 1.6), comparable to the Shockley diode equation for an ideal diode (Eq.1.12), could be used without considering the current in the space charge region and the radiation current. This formula is frequently used to explain the dark current of solar cells.

$$J_{dark}(V) \approx J_{diff}^0 \left[\exp\left(\frac{qV}{k_B T}\right) - 1 \right] \quad (1.6)$$

For the direct gap semiconductors with wide depletion width, the dark current is given by:

$$J_{dark}(V) \approx J_{scr}^0 \left[\exp\left(\frac{qV}{2k_B T}\right) - 1 \right] \quad (1.7)$$

Each of these currents plays a critical role in semiconductor device operation, and is essential for comprehending their behavior and performance characteristics.

1.2.2 Non-Ideal P-N Junction and Parasitic Resistances

The dark current weakly depends on the bias voltage for non-ideal diode performance. The equation can be rewritten as follows to quantify the dark current using the ideality factor (m):

$$J_{dark}(V) = J_0 \left[\exp\left(\frac{qV}{mk_B T}\right) - 1 \right] \quad (1.8)$$

$$J = J_{sc} - J_{dark}(V) = J_{sc} - J_0 \left[\exp\left(\frac{qV}{mk_B T}\right) - 1 \right] \quad (1.9)$$

J_{sc} is the short circuit current, and J_0 is the reverse saturation non-ideal diode current density. The series resistance derives from the resistance of materials, two surface contact electrodes, and leading wires. The leakage current between contacts with different polarities and at the edges of cells is where the parallel resistance originates. Substituting the series and parallel resistance in Eq.1.10:

$$J = J_{sc} - J_0 \left[\exp\left(\frac{qV + JAR_s}{kT}\right) - 1 \right] - \frac{V + JAR_s}{R_{sh}} \quad (1.10)$$

1.3 Solar Cell Critical Parameters

Three categories could be used to categorize photonic devices: firstly, devices operate as light sources. They could convert electrical energy into optical radiation, for instance, the light-emitting diode (LED) and the diode laser. They could generate optical radiation by converting electrical energy, such as the light-emitting diode (LED) and the diode laser. Besides, devices work as detectors. They were capable of differentiating optical signals, like photodetectors. Additionally, devices like solar cells could convert optical radiation into electrical energy.

1.3.1 Current

Photocurrent

The quantum efficiency (QE) of the device when illuminated at a short circuit and the flux density of incident photons are both factors that affect the photocurrent (J_{ph}) that is generated by the solar cell. It can be shown as follows:

$$J_{ph} = J_{sc} = q \int_0^{\infty} QE(E)b_s(E, T_s)dE \quad (1.11)$$

The flux density of incident photons, denoted by the symbol $b_s(E, T_s)$, is the number of photons with incident energy from E to $E+dE$ on a unit area in a given time. And q is the charge of electronic, and J_{sc} is the short circuit current density.

Dark Current

There is a potential difference between the two contact electrodes of solar cells under a given voltage. Then, as a result of the diode property of solar cells, this potential difference produced a dark current, the direction of which is the opposite of the photocurrent. Due to the asymmetric ability to separate charges, photovoltaic devices like diodes may function as rectifiers in the dark. When a solar cell is under forward bias rather than reverse bias, its current is significantly greater. The Shockley diode equation describes the dark current density of an ideal diode as follows:

$$J_{\text{dark}}(V) = J_0 \left[\exp\left(\frac{qV}{k_B T}\right) - 1 \right] \quad (1.12)$$

Where:

J_0 is the density of the reverse saturation current under the reverse bias; it is less than the breakdown voltage current. A/cm^2 is the unit. $q = 1.6 \times 10^{-19} \text{C}$ is the electrical charge. $k_B = 8.62 \times 10^{-5} \text{eV}/\text{K} = 1.38 \times 10^{-23} \text{J}/\text{K}$ is Boltzmann's constant. T is ambient temperature, and if it is room temperature, $T = 300\text{K} = 27^\circ$. As previously stated, $k_B T = 0.0259 \text{eV}$.

Furthermore, as shown in Figure 1. 10 and with the formula below, the total current of solar cells is the sum of the dark current and the short circuit photocurrent.

$$J(V) = J_{sc} - J_{\text{dark}}(V) \quad (1.13)$$

For the ideal diode, from equation 1.12:

$$J = J_{sc} - J_{\text{dark}}(V) = J_{sc} - J_0 \left[\exp\left(\frac{qV}{k_B T}\right) - 1 \right] \quad (1.14)$$

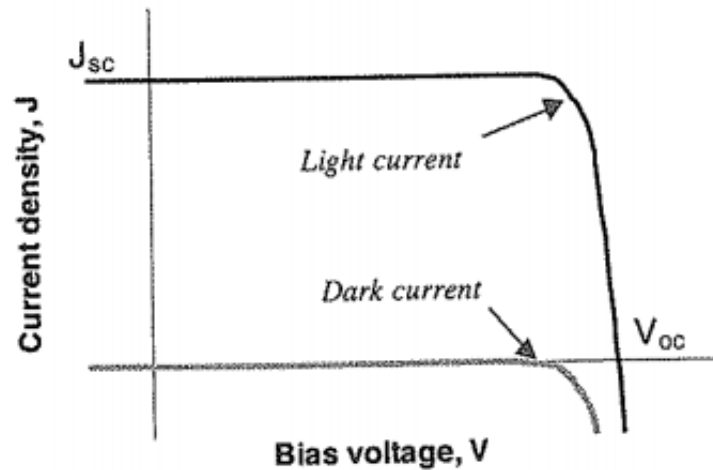


Figure 1. 10 Solar cell characteristics for current and voltage under light and in the dark.⁵

1.3.2 Open Circuit Voltage

J_{SC} is the short circuit current, and J_0 is the reverse saturation current density. When the solar cell is disconnected from the circuit, the current through the device is zero ($J(V)=0$), and the dark current is equal to the short circuit photocurrent, $J_{ph}=J_{SC}=J_{dark}$. The voltage between the two contact electrodes is the open circuit voltage, $V \rightarrow V_{OC}$, also known as the photo-voltage V_{ph} .

The Shockley-Queisser limit (SQ limit), also known as the photovoltaic limit or single-junction photovoltaic limit, is a theoretical model proposed by William Shockley and Hans Queisser in 1961. It defines the theoretical maximum efficiency of a single-junction solar cell, representing the highest energy conversion efficiency achievable under ideal conditions. The SQ limit serves as a crucial theoretical framework characterizing the theoretical maximum efficiency of a single-junction solar cell. It is based on an idealized scenario where each absorbed photon generates a single electron-hole pair and all non-radiative recombination processes are ignored. The SQ limit is primarily governed by the photon energy and the semiconductor bandgap. It assumes that the open-circuit voltage (V_{oc}) of the solar cell can reach its theoretical maximum, meaning that all charge carriers release energy exclusively through the radiative recombination mechanism.

The V_{oc} in equation 1.15 is derived from the intrinsic properties of semiconductor materials under thermal equilibrium, representing the potential difference formed across the p-n junction in the absence of externally photogenerated charge carriers. The term $\ln\left(\frac{N_c N_v}{n_i^2}\right)$ indicates the doping level and intrinsic material characteristics that influence carrier concentrations in the equilibrium state.

The open circuit voltage (V_{oc}) of an ideal solar cell under the conditions of illumination and assuming purely radiative recombination, can be derived using Equation 1.16, which is derived as:

$$V_{OC} = \frac{E_g}{q} - \frac{kT}{q} \ln\left(\frac{N_c N_v}{n_i^2}\right) \quad (1.15)$$

$$V_{OC} = \frac{kT}{q} \ln \left(\frac{J_{SC}}{J_0} + 1 \right) \quad (1.16)$$

Notably, the short circuit current is proportional to the incident light intensity, and thus, the open circuit voltage is logarithmically proportional to the light intensity.

If the voltage is less than zero ($V < 0$), the device consumes power, and the reverse saturation current density is minimal due to the unidirectional conduction characteristic of a diode. On the other hand, the photocurrent is proportional to the light intensity, making it suitable for use as a photodetector. If the voltage is between zero and the open circuit voltage, the product of the voltage and the current are positive, indicating that the solar cell is working and converting light into electricity. When the bias voltage is larger than the open circuit voltage, confusing. This scenario implies that a light-emitting diode is operating, and power is being consumed.

This equation 1.15 presumes that recombination is exclusively radiative and ideal, disregarding non-radiative processes. In practice, the actual Voc frequently falls below this theoretical value due to losses arising from Shockley-Read-Hall recombination, Auger recombination, surface recombination, and other non-ideal factors.

In the field of solar photovoltaics, open-circuit voltage loss (Voc loss) is a critical performance that significantly influences the energy conversion efficiency of solar cells. A comprehensive understanding of Voc loss requires careful consideration of the various physical processes within the solar cell, particularly radiative and non-radiative losses.

Radiative losses arise from the photon emission that occurs during the recombination of electron-hole pairs, leading to light emission. Although this mechanism generates light, not all emitted photons are utilized due to optical losses or inefficiencies, resulting in energy loss. This process is fundamentally dictated by quantum mechanics and is an inevitable form of energy dissipation intrinsic to any photovoltaic device, with its probability increasing alongside charge carrier concentration. In the SQ model, only radiative recombination exists. In ideal photovoltaic materials, effective photon recycling can minimize such losses. The open-circuit voltage associated with radiative losses can be expressed by the following

formula. However, these losses exert a negligible direct influence on open-circuit voltage (V_{oc}).

$$V_{OC}^{rad} = \frac{kT}{q} \ln \left(\frac{J_{SC}}{J_0} + 1 \right) \quad (1.17)$$

Conversely, non-radiative losses critically impact solar cell performance, arising from non-radiative recombination of photogenerated charge carriers within the bulk or at the surface, thereby diminishing charge separation efficiency and V_{oc} . The open-circuit voltage of non-radiative losses can be determined using the following formula 1.16. Shockley-Read-Hall (SRH) recombination is a prominent non-radiative process, involving the recombination of charge carriers through defect states or impurities located within the bandgap of semiconductor materials. Non-radiative losses involve not only SRH recombination but also Auger recombination, where energy is transferred to neighboring electrons, exciting them to higher energy states, and surface recombination, which occurs at surfaces or interfaces that lack proper passivation. These mechanisms dissipate energy as heat through lattice vibrations rather than emitting photons, directly reducing V_{oc} and significantly affecting photovoltaic device performance.

$$V_{OC}^{non-rad} = \frac{kT}{q} \ln \left(\frac{J_0 + J_{NR}}{J_0} \right) \quad (1.18)$$

J_{NR} is the density of non-radiative recombination.

In contrast to radiative losses, non-radiative losses can often be reduced through improved material engineering and surface passivation. Although radiative losses indirectly influence V_{oc} reduction by modulating the generation rate of photogenerated carriers, their direct impact on efficiency is relatively limited. In perovskite solar cells, V_{oc} degradation is primarily linked to non-radiative losses, whereas radiative losses influence V_{oc} indirectly by affecting carrier generation. The overall formula for V_{oc} loss combines radiative and non-radiative losses, and the total open-circuit voltage loss can be expressed by the following equations 1.19 or 1.20.

$$\Delta V_{oc} = V_{oc,ideal} - V_{oc,actual} \quad (1.19)$$

$$\Delta V_{oc} = V_{OC}^{rad} + V_{OC}^{non-rad} \quad (1.20)$$

Therefore, reducing non-radiative losses can significantly improve Voc performance in solar cells and thus enhance overall energy conversion efficiency. This strategy is particularly crucial for optimizing perovskite solar cell performance due to its high potential for minimizing non-radiative recombination processes.

1.3.3 Efficiencies

The quantum efficiency (QE) of solar cells is defined as the probability of electrons transitioning into the external circuit during the incidence of photons with energy E . This parameter is crucial in describing the performance of solar cells, as it is related to the absorption coefficient of the material and the charge separation and collection efficiency, among other factors ⁵.

The connection between wavelength (λ) and photon energy E can be expressed through the Planck constant (h) and the speed of light in vacuum (c) as:

$$E = \frac{hc}{\lambda} \quad (1.21)$$

where $h = 4.135 \times 10^{-15} eV \cdot s = 6.625 \times 10^{-34} J \cdot s$ and $c = 3.0 \times 10^{10} cm/s = 3.0 \times 10^8 m/s$ is the speed of light in a vacuum. More conveniently, the energy of photons can be expressed in electron volts (eV) as:

$$E/eV = \frac{1240}{\lambda/nm} \quad (1.22)$$

Power Conversion Efficiency

Figure 1. 11 shows the current density - voltage characteristic curve (black) and the power density - voltage typical curve (grey) of an ideal cell. The power density of cells can be defined as

$$P = JV \quad (1.23)$$

When cells operate at the maximum power point, the power is P_m , and the corresponding voltage and current density are V_m and J_m , respectively. The fill factor is given by:

$$FF = \frac{J_m V_m}{J_{sc} V_{oc}} \quad (1.24)$$

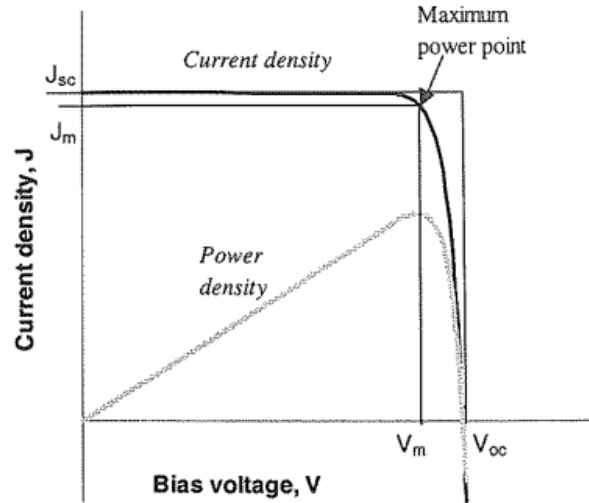


Figure 1. 11 The current density - voltage characteristic curve (black) and the power density - voltage typical curve (grey) of an ideal cell. ⁵

The power conversion efficiency (η) is identified with the power density at the maximum power point and the incident light power density (P_s).

$$\eta = \frac{J_m V_m}{P_s} \quad (1.25)$$

If we substitute the fill factor in Eq. 1.30, the power conversion efficiency is shown as:

$$\eta = \frac{J_{sc} V_{oc} FF}{P_s} \quad (1.26)$$

The current density, open circuit voltage, fill factor, and power conversion efficiency are all critical parameters to the performance of a solar cell. Standard test conditions (STC) specify that solar cells are tested under the Air Mass 1.5 spectrum, a temperature of 25°C, and an incident power density of 1000 W/m².

Chapter 2 Perovskite Solar Cells

Perovskites, which generally refer to compounds with perovskite crystal structures (ABX_3), have a fascinating history that traces back to 1839. During his travel to Russia, Gustav Rose stumbled upon a new $CaTiO_3$ -based mineral in the Ural Mountains. In honor of the Russian mineralogist Levvon Perovski, this mineral was named "perovskite."

The A cation has a larger radius, such as Cs^+ , $CH_3NH_3^+$ (MA^+), and $NH_2CH=NH_2^+$ (FA^+), and its primary function is lattice charge compensation. A does not fundamentally change the structure of the energy band but leads to lattice distortion due to the size of the ion. In general, the larger the ion radius, the larger the cell expansion and the smaller the band gap. Smaller ions are easier to enter the network of PbI_6^{2-} and form a stable perovskite structure. On the contrary, ions with a larger radius may lead to an unstable perovskite structure.

The B cation has a smaller radius, such as Pb^{2+} , Sn^{2+} , Ti^{4+} , and Bi^{3+} , and is often used instead of Pb, which is toxic and not environmentally friendly. The ionic radius of Sn is 1.35 Å, similar to Pb, and the C anion in the structure of ABX_3 is typically Cl^- , Br^- , I^- , O_2^- , as shown in Figure 2. 1.

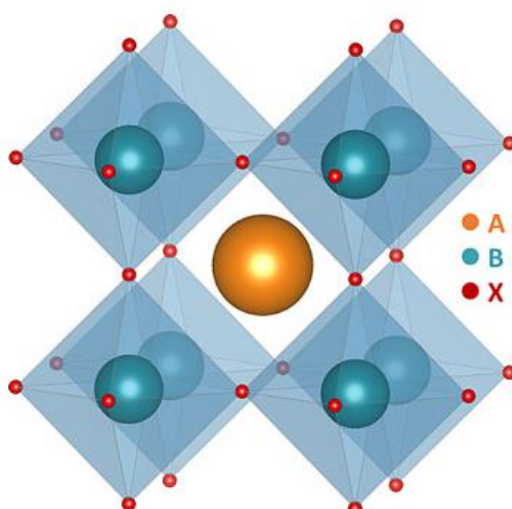


Figure 2. 1 perovskite structure.source: <https://www.x-mol.com/news/13131>.

In 1994, organic-inorganic halide perovskite appeared in optoelectronics when researchers in Watson Research Center (Yorktown Heights, N.Y.) produced light-emitting devices using luminescent organic-inorganic halide perovskites. Two years later, Boeing North America (Seal Beach, Calif.) created nonlinear optical crystals from cesium-germanium halide salts with perovskite structures. In 1999, Murase Chikao et al. suggested rare earth oxide with a perovskite structure as the active layer of a solar cell. Cite references for all these events – original sources

Ten years later, Tsutomu Miyasaka et al. fabricated a dye-sensitized solar cell by placing a thin perovskite layer as a sensitizer on a TiO₂ mesoporous electron transport layer. This started the use of hybrid perovskite in solar cell, although the PCE was just 3.8%, and the stability was very poor - only a few minutes with liquid corrosive electrolyte.⁷ In 2011, Park et al. moved a big step forward realizing a solid-state dye-sensitized solar cell with Spiro-OMeTAD as a solid-state electrolyte, and improved the solid DSSC with perovskite sensitizer to 9% PCE and also promise of possible stable solar cell. Since then, scientists on perovskite based solar cells started focusing more on the solid-state transport layer to overcome stability issues.⁸ In 2012, Henry Snaith and Mike Lee improved the efficiency of perovskite solar cells beyond 10% in a more stable manner using a solid-state hole transporter instead of a mesoporous TiO₂ electron transporter.⁹⁻¹¹ After breaking the 10% mark, the progress of perovskite solar cells became increasingly exciting. In 2013, Burschka et al. achieved dye-sensitized solar cells with efficiencies greater than 15%.¹² During the same year, Olga Malinkiewicz et al. and Liu et al. demonstrated a thermal co-evaporation technique for planar and PN junction architecture perovskite solar cells, increasing efficiency to more than 12% and 15%, respectively.¹³⁻¹⁵ Perovskite solar cells have also been manufactured in an inverted architecture, with the electron transport layer above and the hole transport layer beneath the perovskite active layer. This configuration is similar to that of the regular organic solar cell.¹⁶ In 2014, Yang Yang et al. established perovskite solar cells with planar thin-film architecture one year before the efficiency improved to 19.3%. Since 2015, advancements in deposition techniques have pushed the efficiency of perovskite solar cells to over 26%. (Figure 2. 2)¹⁷

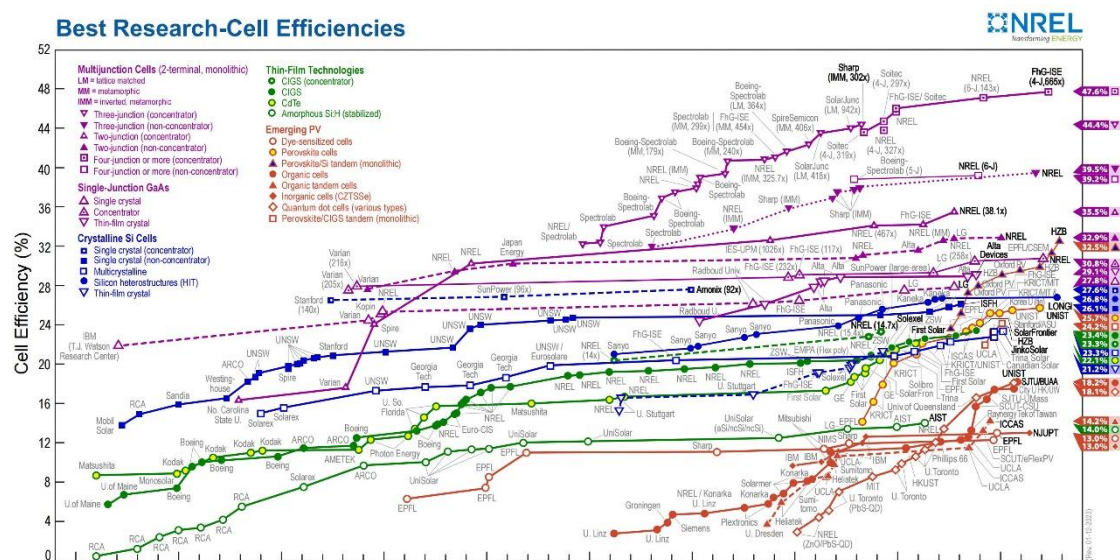


Figure 2. 2 Best research-cell efficiencies between 1975 and 2023. ¹⁸

2.1 Device Structure and Components of Perovskite Solar Cells

There are several device structures of perovskite based solar cells, as shown in Figure 2. 3, including the mesoporous and planar structures. The mesoporous structure is composed of transparent conductive glass (FTO, ITO), an electron transport layer, a mesoporous electron transport layer, a perovskite absorbing layer, a hole transport layer, and electrodes. The traditional mesoporous structure utilizes TiO_2 as the mesoporous material, which acts as a scaffold for absorbent materials, increasing the amount of adsorption and transferring electrons. However, the thickness of the mesoporous layer adopted from transitional DSSC is often above 500nm, which leads to decreased efficiency for carrier collection. Additionally, high-temperature sintering is required to fabricate the DSSC type mesoporous layer, which is detrimental to the preparation of large-area devices and manufacturing process / cost.

On the other hand, the planar structure does not include a mesoporous skeleton but has the perovskite layer in direct contact with p-type and n-type semiconductors on both sides. The planar structure is favourable for large-area devices and the realization of flexible perovskite solar cells. There are two types of planar structure batteries: conventional and inverted. In the conventional structure solar cell, the

incident light from TCO side goes from the electron transport layer, through the perovskite layer, to the hole transport layer. Conversely, in the inverted structure solar cell, the incident light goes through the hole transport layer first and then the perovskite layer to reach the electron transport layer.

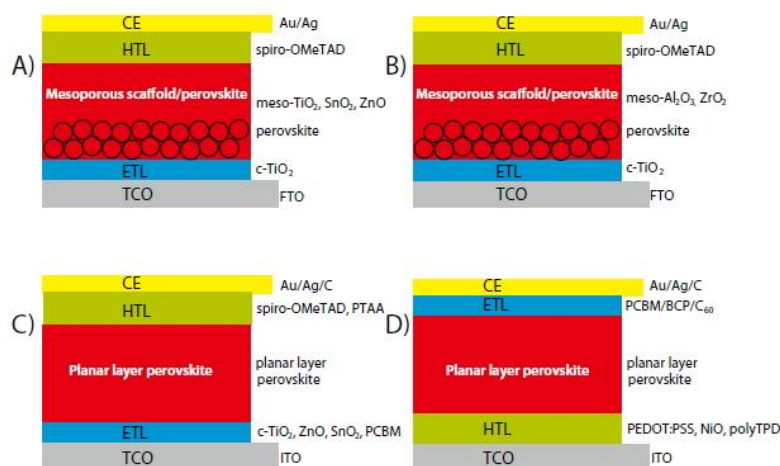


Figure 2. 3 The structure of perovskite solar cells.

source:<https://www.sigmaaldrich.com/china-mainland/technical-documents/articles/material-matters/hybrid-halide-perovskites-based-solar-cells.html>

Figure 2. 3 shows the components of a typical rigid perovskite solar cell, including a conductive glass substrate (ITO or FTO), an electron transport layer (ETL), a perovskite absorbing layer, a hole transport layer (HTL), and electrodes (e.g. Au, Ag, or Al). Each layer performs a specific function in the device.

2.1.1 ITO/FTO glasses

The conductive glass substrates serve as transparent conductive electrode (TCE) and substrates, allowing incident solar light to enter the cell.

2.1.2 The hole transport layer (HTL)

The primary function of the hole transport layer is to extract and collect hole carriers from the perovskite active layer and transfer them to the positive electrode

while effectively blocking the electron carriers. To achieve this, the HOMO of the materials in the HTL must be higher/shallower than the HOMO (valence band) of the perovskite material in the active layer, and the Lowest Unoccupied Molecular Orbital (LUMO) in this layer should also be higher than the LUMO (conduction band) of the perovskite materials in the active layer as shown in Figure 2. 5. Spiro-OMeTAD is a classical & commonly used HTL material, but its synthesis involves many steps and is difficult to purify, making it expensive, and the requirement of lithium salt doping also makes it not stable. Therefore, finding a more efficient, stable, and readily synthesizable HTL material for commercial solar cells is crucial.

In the context of inverted-structure perovskite solar cells, the utilization of hole transport materials (HTMs) such as poly(3,4-ethylenedioxythiophene) (PEDOT), poly(triarylamine) (PTAA), and nickel oxide (NiOx) is prevalent. References... NiOx, a HTL shown effectiveness in organic solar cell time, in particular, demonstrates a notable capacity for Ni²⁺ vacancy formation due to the presence of O²⁻ interstitials, classifying it as a p-type semiconductor with superior chemical robustness and a high degree of hole mobility, recorded at an impressive rate of 47.05 cm²/(V·s). The manipulation of the work function of NiOx, tunable within the ambit of 4.5 to 5.6 eV by modulating the concentrations of O²⁻ interstitials or Ni²⁺ vacancies facilitates a seamless energetic integration with the perovskite's band structure. Furthermore, the elevated conduction band energy level of NiOx (-1.8 eV) acts as an effective blockade against electron leakage from the perovskite layer to the anode, significantly contributing to the enhancement of the device's photovoltaic efficiency.

2.1.3 The active layer

The perovskite active layer is the very core of PSC. It adsorbs solar light, generates weakly bonded electron-hole pairs that dissociate to carriers and eventually generate electricity. The AL will be discussed in more detail in section 2.2.

2.1.4 The electron transport layer (ETL)

In transporting electrons, the ETL collects them from the perovskite active layer before their transfer to the electrode while ensuring that the hole carriers are effectively blocked. One consideration for effective transport is that the LUMO of electron transport materials must be lower than the conduction band of perovskite materials. For optimal transport, electron transport materials typically require a high electron affinity and ionic potential, and their energy level must match that of the perovskite active layer. Common materials used as electron transport layers include SnO_2 , ZnO , and TiO_2 . (as shown in Figure 2. 4).

In the architecture of inverted perovskite solar cells, the electron transport layer (ETL) materials prevalently employed encompass C_{60} , [6,6]-Phenyl C_{61} butyric acid methyl ester (PC_{61}BM), and Indene- C_{60} bisadduct (ICBA). Notably, PC_{61}BM demonstrates an optimal alignment of its lowest unoccupied molecular orbital (LUMO) energy level with the conduction band of methylammonium lead iodide ($\text{CH}_3\text{NH}_3\text{PbI}_3$), facilitating efficient exciton dissociation across the interfaces of the perovskite material, PC_{61}BM , and poly(3,4-ethylenedioxythiophene) polystyrene sulfonate (PEDOT). The film thickness of PC_{61}BM typically maintained below 100 nm, significantly augments the carrier lifetime, thereby enhancing carrier transport and collection efficacy. – Make it professional for thesis

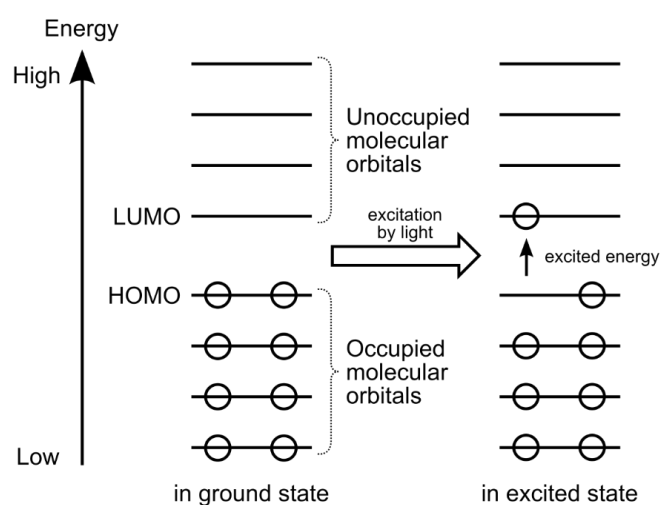


Figure 2. 4 Diagram of HOMO and LUMO molecular orbitals.

source: https://en.wikipedia.org/wiki/HOMO_and_LUMO

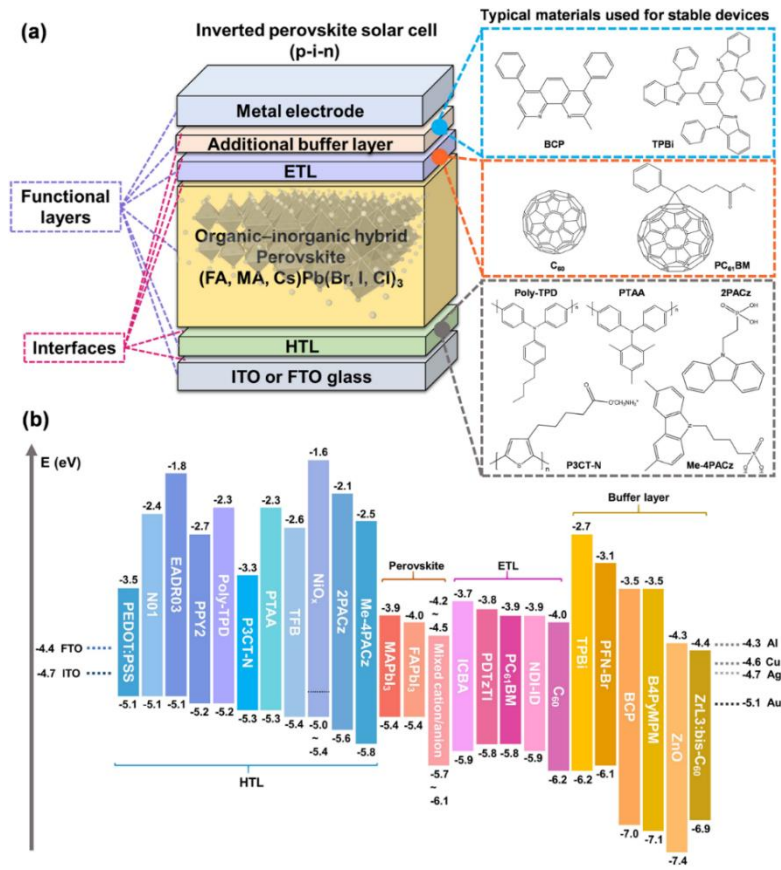


Figure 2. 5 The materials of each functional layer of perovskite solar cells.

2.2 Photovoltaic Materials of The Perovskite Active Layer

Perovskite structures can be assessed for stability using the tolerance factor, which is calculated using equation 2.1:

$$t = \frac{r_A + r_x}{\sqrt{2}(r_B + r_x)} \quad (2.1)$$

Here, t refers to the tolerance factor, while r_A , r_B , and r_X are the ionic radius of A, B and X, respectively.

The stability of the perovskite structure (ABX₃) is maintained within a tolerance factor range of 0.8 to 1, with deviations from this range leading to the failure of the perovskite layer. (Figure 2. 6) Notably, solar cells become less sensitive to light under these conditions. For example, CH₃NH₃PbI₃ (MAPbI₃), the most commonly reported

perovskite material, has a tolerance factor (t) of 0.834, indicating structural stability. Additionally, MAPbI₃ exhibits low defect density in single crystal form, typically ranging from 10⁹ to 10¹⁰ cm⁻³, while electron and hole mobility was found to be around 10cm²/(V•s) and diffusion length exceeding 100nm. Furthermore, MAPbI₃ has properties that make it suitable for a solar cell application, including a direct bandgap with a bandgap energy of 1.55 eV, a high extinction coefficient, and efficient visible light absorption (the absorption edge is 800nm). In particular, visible light absorption is over 90% when the thickness of the MAPbI₃ layer is between 300nm and 400nm and increases to over 99% at a thickness of around 600nm. This absorption ability is significantly greater than that of crystalline silicon. However, the material suffers from poor stability in humid or high-temperature conditions and is susceptible to damage when exposed to prolonged light exposure. This means these devices with MAPbI₃ materials easily decompose in the air.

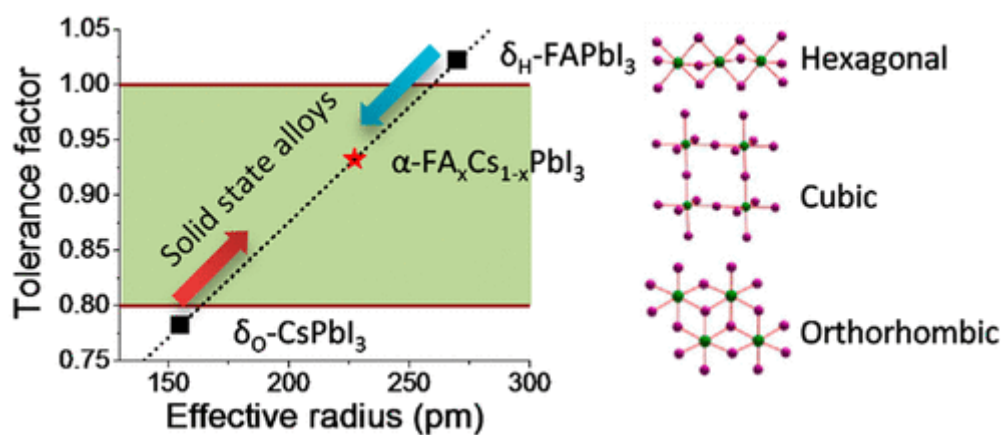


Figure 2. 6 Exploring the Relationship between Tolerance Factor and Crystal Structure in Perovskite Materials.²⁰

The absorption of incident light in photovoltaic devices is greatly influenced by perovskite, which is essential for achieving high efficiency. To attain a wide absorption bandgap is crucial; otherwise, the efficiency will decline due to a low open-circuit voltage.

Mixed perovskite materials have become more sought after because of their adjustable bandgap, high absorption coefficient, long carrier diffusion length, and

high defect tolerance. Presently, most mixed perovskite materials, such as $\text{FA}_{1-x}\text{MA}_x\text{PbI}_y\text{Br}_{1-y}$, with an efficiency of over 25.7%, are widely used as the absorption layer of perovskite cells. FAPbI_3 , known as $\text{HC}(\text{NH}_2)_2\text{PbI}_3$, has a bigger ionic radius of 2.2 Å (1 Å = 10^{-10}m) than MA, whose ionic radius is 1.8 Å, resulting in a narrower bandgap of 1.48 eV, with a spectral response that extends to 850 nm—consequently, its short-circuit current is more significant than that of MAPbI_3 . However, FAPbI_3 has a smaller open-circuit voltage due to the narrow bandgap. It has two phases: one phase, the α - FAPbI_3 phase (the black phase), and has photovoltaic properties. And the other phase, the δ - FAPbI_3 phase, is a yellow phase and lacks such properties. In terms of solar cells, the ideal bandgap of the active layer is 1.34 eV, but few perovskite materials come close to achieving it. If MA is replaced by Cs, an all-inorganic perovskite (CsPbI_3) forms, leading to a bandgap of 1.74 eV. However, it is unstable at room temperature and highly sensitive to humidity changes. Michael Grätzel mixed MA with FA, resulting in $\text{MA}_x\text{FA}_{1-x}\text{PbI}_3$, which prevented the formation of the δ - FAPbI_3 phase.²¹ Furthermore, by combining MA with Cs ($\text{Cs}_x\text{MA}_{1-x}\text{PbI}_3$), the defect density of MAPbI_3 was reduced, leading to longer carrier diffusion lengths.

2.3 Perovskite Nucleation and Crystal Growth Mechanisms

2.3.1 Perovskite Nucleation

The initial formation of the perovskite crystal structure within the precursor solution, known as perovskite nucleation, signifies the commencement of the crystal growth process. This phase is crucial as it determines the quality, size, and distribution of perovskite grains in the final thin film.

Classical nucleation theory explains that nucleation is initiated when the precursor concentration in a solution reaches or surpasses a critical threshold known as supersaturation. This triggers the formation of tiny clusters of ions, called nuclei. The energy required for the formation of a nucleus is calculated by equation 2.2, in which ΔG_s is the surface free energy, ΔG_v is the bulk free energy, r is the radius of the nucleus, γ is the surface free energy per unit area.

The precursor supersaturation in solution boosts the chance of nucleation, which is affected by factors including solvent evaporation rate, temperature, and precursor concentration. The rate of nucleation is influenced by solution composition, temperature, humidity, and environmental conditions. It can be described by equation 2.3, in which N is the number of nuclei, A is the pre-exponential factor, k_B is the Boltzmann constant, N_A is Avogadro's number, S is the level of super-saturation, and T is the temperature.^{51.74} The nucleation rate is strongly dependent on the level of supersaturation state, temperature, and surface free energy of ink.

$$\Delta G = \Delta G_s + \Delta G_v = 4\pi r^2 \gamma + \frac{4}{3} \pi r^3 \Delta G_v \quad (2.2)$$

$$\frac{dN}{dt} = A \exp \left[-\frac{16\pi\gamma^3 V_m^2}{3k_B^3 T^3 N_A^2 (\ln S)^2} \right] \quad (2.3)$$

Controlling the nucleation process is crucial for achieving high-quality perovskite thin films with minimal defects. Therefore, the introduction of an antisolvent, rapid solvent evaporation, additives, solvent mixtures, and temperature regulation techniques are essential. Understanding the intermediate phases in nucleation is also vital as it allows for controlling the size and morphology of the final perovskite crystals, which directly impacts grain size and film quality.

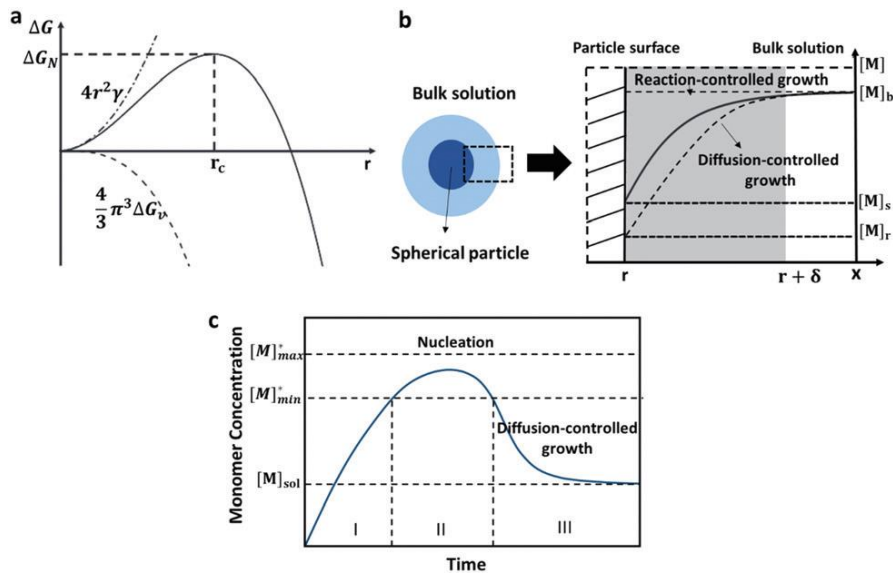


Figure 2. 7 The diagram illustrates the dynamics of nucleation and growth.^{51.74}

2.3.2 Perovskite Growth Mechanisms

Crystal growth in solution includes two main processes: (1) the migration of monomers from the bulk solution to the crystal surface and (2) their subsequent reaction on the surface. The initial step, involving monomer diffusion, is governed by Fick's First Law as equation 2.4

$$J = 4\pi r^2 D \frac{dC}{dx} \quad (2.4)$$

where J is the total flux of monomers, r is the particle radius, D is the diffusion coefficient, and C is the monomer concentration at a distance (x) from the surface.

Surface reactions on particles consume monomers at a rate equal to the total flux of monomers, as per mass balance. This consumption rate is related to particle growth.

$$J = 4\pi r^2 k(C_i + C_r) \quad (2.5)$$

In this equation, k represents the surface reaction rate, C_i signifies the solute concentration at the particle/solution interface, and C_r denotes the solubility of particles with a radius of r .

2.4 Basics of Perovskite Solvent Engineering

Solvent engineering in perovskite technology is targeted at producing uniform and high-quality perovskite thin films through the precise manipulation of nucleation and crystallization processes during solution processing. This approach not only improves the efficiency of perovskite solar cells but also helps in minimizing the occurrence of defects. Some key techniques involved in solvent engineering include the antisolvent technique, mixed solvent systems, gas-assisted crystallization, solvent annealing, hot-casting, Lewis acid-base adduct, and solvent washing.

The antisolvent technique involves the addition of an antisolvent (such as toluene or chlorobenzene) to reduce the solubility of perovskite precursors, which rapidly

induces crystallization. By applying the antisolvent to the wet film after spin-coating, film uniformity is enhanced, pinholes are reduced, and device performance is improved.

By adjusting the solvent mixture, nucleation and crystallization behavior can be modified, leading to optimized thin-film morphology and grain size. The use of a mixed solvent system, which combines solvents like dimethylformamide (DMF) and dimethyl sulfoxide (DMSO), enhances the solubility of precursors and improves control over nucleation and growth.

Dimethyl sulfoxide (DMSO), with a sulfinyl group (S=O) attached to two methyl groups, has a high boiling point of 189°C, which slows down its evaporation. This property allows it to form stable coordination complexes with lead ions, thus stabilizing precursor solutions. DMSO's remarkable solubility and low toxicity make it a preferred solvent in organic-inorganic hybrid perovskite solar cell manufacturing. It can dissolve perovskite precursor materials or act as a reaction medium. Additionally, DMSO serves as a surface modifier, crucially affecting the fabrication of perovskite films. By incorporating DMSO into perovskite solutions, it modulates the interaction with the substrate surface, enhancing the adhesion and crystalline quality between the perovskite film and the substrate, ultimately improving device stability and performance.

During perovskite film formation, DMSO can influence the crystalline structure and orientation of the film, playing a significant role in optimizing the optoelectronic performance of the devices. Through its molecular structure and solvent properties, DMSO interacts with perovskite precursors, influencing growth mechanisms and the lattice arrangement of perovskite crystals. This interaction can produce crystals with varied orientations and morphologies, impacting key performance metrics like light absorption and photovoltaic conversion efficiency. DMSO's dual role as both a solvent and surface modifier is crucial for controlling the morphology, structure, and performance of perovskite films, providing a technical foundation for efficient and stable perovskite solar cells.

On the other hand, dimethylformamide (DMF) contains a formamide group ($\text{N}(\text{CH}_3)_2\text{C}=\text{O}$) that facilitates strong hydrogen bonding. With a lower boiling point of 153°C , DMF evaporates quickly. As a highly polar aprotic solvent, it dissolves organic cations and inorganic salts like lead halides (e.g., PbI_2). Its high solubility ensures a homogeneous precursor solution, aiding uniform thin-film deposition. By coordinating with lead ions to form complexes, DMF stabilizes solutions and prevents the premature precipitation of precursors. Intermediate complexes formed between DMF and PbI_2 impact nucleation and growth rates. The moderate evaporation rate of DMF supports controlled crystallization, yielding larger grains with reduced boundaries, and enhancing film quality.

However, DMF forms less stable complexes with lead halides than DMSO, which establishes strong complexes that stabilize intermediate phases, slowing nucleation and improving crystallization control. DMF's weaker coordination accelerates crystallization. DMSO's slower evaporation facilitates controlled crystallization and the growth of larger grains. In contrast, DMF's faster evaporation can lead to smaller grains. The gradual solvent removal by DMSO improves crystallinity and encourages the development of larger grains, while DMF's rapid evaporation may cause more defects but speeds up processing. When combined, DMSO and DMF complement each other: DMSO enhances crystallization control through strong coordination complexes and slow evaporation, while DMF efficiently dissolves organic cations and precisely regulates crystallization kinetics.

2.5 Perovskite Solar Cell Deposition Techniques

It is essential to increase the degree of compactness, control crystallization, and reduce the roughness of thin films to enhance the generation and separation of photo carriers. Conversely, when the roughness levels are exceptionally high, and there are numerous pinholes, the absorbance and photocurrent are likely to decrease, resulting in an increase in leakage current and a decrease in shunt resistance. Solar cell manufacturing can be classified into five main categories: dip coating, spin coating, slot-die coating, doctor blading, and bar coating. (as illustrated in Figure 2. 10)

2.5.1 Spin Coating

Spin coating is a widely used conventional deposition method for high-efficiency small-area devices. The perovskite precursor solution can be manufactured by mixing perovskite chemicals with different solvents. This precursor solution is then deposited onto the transport layer using the spin-coating process at a given speed, as shown in Figure 2. 8.

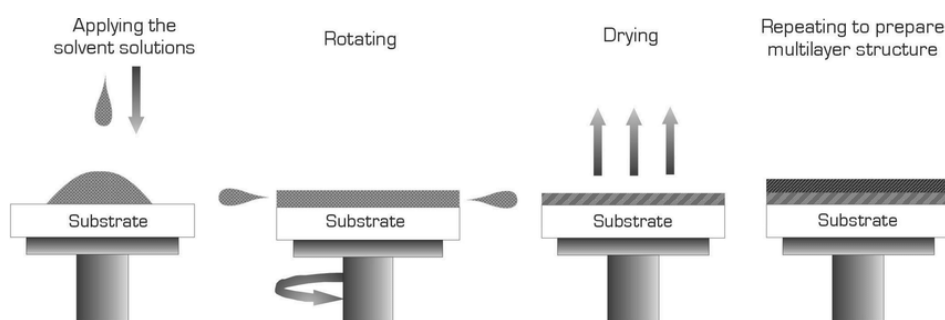


Figure 2. 8 The process of the deposition using the spin coating method.²²

The spin coating technology has a number of advantages. One of the main advantages of the spin coating method is its ability to coat small and flat substrates effectively, with faster drying times when compared to the doctor-blading method. However, this method has significant limitations, as it is unsuitable for large-scale production due to the limited size of substrates that can be coated. Setting up is also increasingly costly, and the solution wastage is higher than the doctor-blading method.

2.5.2 Doctor Blading

The doctor-blading technique (Figure 2. 9) presents a cost-effective and practical solution for industrial-scale and large-scale production. It generates less waste than the spin coating technique while providing a relatively low installation cost. One drawback of this process is its slower drying time. However, this can be remedied by heating or gas quenching or by solvent engineering such as ethyl alcohol. This paper will focus on relevant research that examines the doctor-blading process for its

potential application to our study. Our investigation will concentrate on this particular approach.

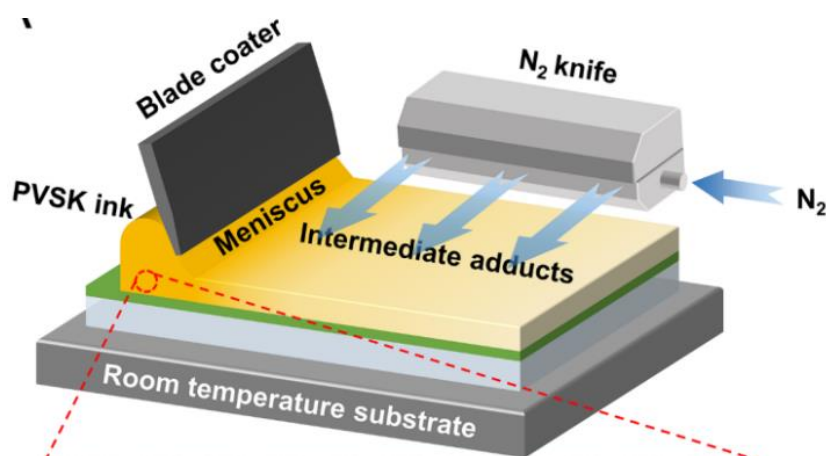


Figure 2. 9 The process of the deposition using the doctor blading method.

Doctor Blading is a simple and effective technique for thin-film deposition, commonly used in solar cells, printed electronics, and displays. This method involves spreading a precursor solution onto a substrate using a blade, with the film thickness being controlled by several parameters: the gap between the blade and substrate, the viscosity of the solution, and the speed of the blade. The technique is noted for its versatility, cost-effectiveness, and scalability for large areas. However, it does present challenges such as edge effects.

One of the primary advantages of doctor blading is its simplicity and adaptability, which make it suitable for a diverse range of materials, including organics and nanoparticles. Its scalability for industrial production is another significant benefit, although maintaining uniformity over large areas remains a challenge.

In comparison to other deposition methods like spin coating, doctor blading offers greater flexibility but may suffer from thickness variability, especially on larger substrates. Despite these issues, the technique is particularly useful in applications such as photovoltaics, printed electronics, and display manufacturing. Nonetheless, doctor blading faces competition from other techniques like slot die coating, which, although more complex, is better suited for large-scale, continuous production.

In summary, while doctor blading is a simple, adaptable, and cost-effective method for thin-film deposition, it does have limitations in terms of uniformity and material efficiency. Its suitability for a wide range of materials and applications makes it a valuable technique.

2.5.3 Slot-die coating

Slot Die Coating, also known as Slot Casting, is a high-precision technique widely used for large-area coatings in industries like photovoltaics and printed electronics. The process operates by distributing liquid material evenly through a slot die, which is meticulously designed to control the coating thickness. This control is influenced by factors including flow rate, substrate speed, and liquid viscosity. The core of the process is the precise control of parameters such as the gap between the die and substrate, as well as the liquid viscosity, to ensure uniform coatings ranging from nanoscale to microscale.

This technique offers several advantages, including high precision, material efficiency, and the capability to coat large areas, making it highly suitable for industrial-scale production. However, it also comes with challenges, such as high initial equipment costs, complex liquid handling requirements, and edge effects that can affect uniformity. Compared to other coating methods like Spin Coating and Doctor Blade Coating, Slot Die Coating excels in material utilization and thickness control, particularly for applications requiring large-scale, uniform coatings.

Despite these advantages, challenges such as maintaining consistency in coating thickness due to edge effects or mismatched flow rates and substrate speeds must be addressed through precise process control. Addressing these factors is critical to achieving high-quality coatings in industrial applications.

2.5.4 Bar coating

Bar coating is a similar technique to doctor blading that involves dispersing excess solution over the substrate using a rod. The bar is a helical thin film applicator comprised of a long cylindrical bar with wire spiraling around it. The thickness of the

film is determined by the amount of solution passing through the gaps between the wire and substrate. This technique is low-cost and easy to set up, and it allows us to change the properties of the film (such as thickness) without altering the chemical properties of the materials. Bar coating can uniformly coat large areas of soft or flexible substrates, but any contamination of the system may result in striations in the wet film. Also, gradients cannot be generated throughout the film as the rod is dragged near the base. Additionally, the coating velocity is very slow.

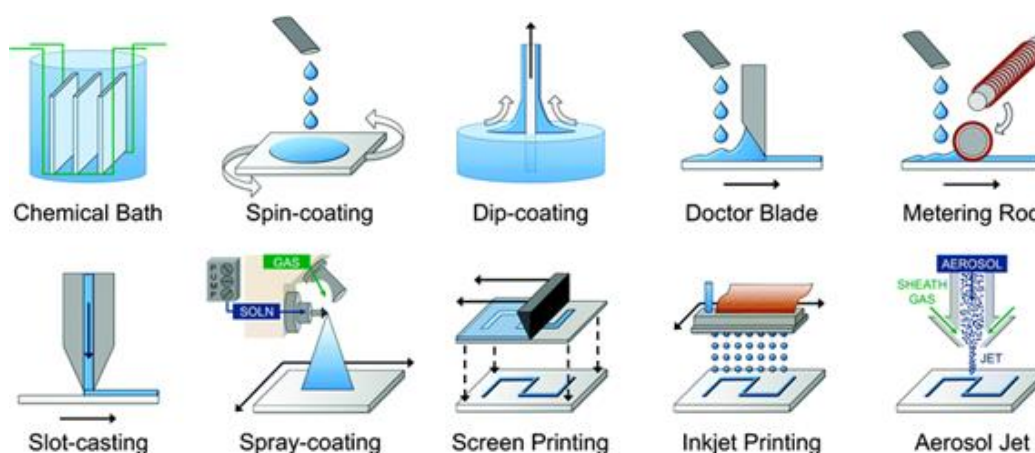


Figure 2. 10 Deposition methods of perovskite solar cells

Source: <https://images.app.goo.gl/dziPpSVKKJZktbaLA>.

2.6 Material characterization and application

There are numerous methods for characterizing material structures, and new ways continue to emerge. This article will introduce a few fundamental techniques frequently encountered. In terms of its objectives, material structure characterization primarily relies on three essential components: chemical composition analysis, structural determination, and morphological observation.

2.6.1 Chemical Composition Analysis

Some prevalent techniques used in the chemical analysis of materials are mass spectrometry, UV-Visible and infrared spectroscopy, gas and liquid chromatography, nuclear magnetic and electron spin resonance, X-ray fluorescence spectroscopy, Auger

and X-ray photoelectron spectroscopy, secondary ion mass spectrometry, electron and atomic probes, and laser probes. For example, mass spectrometry is a fundamental means to identify unknown organic compounds by providing information on their molecular weight and elemental composition. The composition features of polymeric materials may be efficiently presented in chromatography, notably in pyrolysis gas chromatography (PGC). Combining it with mass spectrometry, infrared spectroscopy, thin-layer chromatography, gel chromatography, and other techniques has substantially broadened its range of uses. Because of its widespread use and numerous advantages, infrared spectroscopy plays a particular and essential role in characterizing polymer materials. The ease of the testing process is one of its most significant advantages.

Furthermore, the availability of a large number of recognized compounds with their infrared spectra and distinct frequencies of functional groups assists in the convenient interpretation of the testing results. While infrared (IR) spectroscopy is widely utilized in polymer chemistry analysis, nuclear magnetic resonance (NMR) spectroscopy offers distinct benefits for evaluating polymer configurations, conformations, isomeric identification, and copolymer composition. NMR spectroscopy is particularly effective in identifying the qualitative and quantitative design of copolymers as well as their sequence structures. It is a powerful complement to IR spectroscopy in polymer investigation.

Fourier-Transform Infrared Spectroscopy (FTIR)

Analysis of the infrared spectrum may be used to identify and distinguish between distinct chemical species and examine the molecular structure and chemical bonding. Because infrared spectra are so distinctive, they may be compared to the spectra of standardized chemicals for analysis and identification. There are already a number of published collections of standardized infrared spectra, which may be saved in a computer for comparison and retrieval for analysis and identification. The characteristic wavenumbers of chemical bonds can be employed for quantitative research and to differentiate between types of compounds. The characteristic wavenumber of the same functional group in various molecules might vary within a limited range due to the

interaction between neighbouring functional groups in a molecule. Furthermore, infrared spectra have several applications in the research of polymer configuration, conformation, and mechanical characteristics, as well as in physics, astronomy, meteorology, remote sensing, biology, and medicine.

The theoretical basis for the determination of a compound's structure through infrared spectroscopy lies within the absorbance spectrum. Such a spectrum results from the absorption of specific wavelengths of infrared light when the molecules of a compound vibrate. Additionally, the wavelength of the infrared light absorbed by the vibration of a chemical bond relies on two factors - the bond kinetic constant and the folded mass of the atoms connected at both ends. These factors, in turn, depend on the structural characteristics of the molecule.

When the frequency of the vibration or rotation of a functional group in the substance molecule is the same as that of the infrared light, the substance absorbs infrared light with continuous wavelengths. The molecule changes from its ground state to a higher vibrational energy level as a result of the absorbed energy. Therefore, based on knowledge of the relative vibrations of atoms and molecular rotation inside the molecule, infrared spectroscopy is fundamentally a way to ascertain the structure of a chemical molecule and identify compounds. When the molecule is activated, the vibration of the atomic bonds within each group determines the characteristic frequency of functional groups in complex compounds. Most organic molecules' infrared spectra predominantly reflect the vibrations of the four components C, H, O, and N. And after studying the infrared spectra of different substances, it was determined that vibrations of the same type of bond had comparable frequencies. For instance, compounds containing methyl groups exhibit absorption peaks with frequencies ranging from 2800-3000 cm^{-1} , representing the characteristic frequency of the methyl group. However, the frequency of the same type of functional group varies depending on the chemical environment, resulting in frequency shifts.

The infrared radiation spectrum is classified into three regions based on their wavenumbers: the near-infrared region (10000-4000 cm^{-1}), the mid-infrared region (4000-400 cm^{-1}), and the far-infrared region (400-10 cm^{-1}). Typically, the mid-infrared

area is the most commonly utilized for spectroscopy because the majority of chemical bond vibrations occur within this region, resulting in molecular vibrational spectroscopy, frequently referred to as infrared spectroscopy.

There are four absorption divisions in the mid-infrared spectrum. The first frequency range is from 4000 to 2500 cm^{-1} . This region is the X-H stretching vibration zone, where X is the O, N, C and S atoms in alcohols, phenols, carboxylic acids, amines, imines, amides, acrylamides, alkynes, alkenes, aromatic rings, alkanes, thiols, etc. The stretching vibrations of triple bonds ($\text{C}\equiv\text{C}$, $\text{C}\equiv\text{N}$, $\text{N}\equiv\text{N}$), cumulative double bonds ($\text{C}=\text{C}=\text{C}$, $\text{N}=\text{C}=\text{O}$, $-\text{N}=\text{C}=\text{S}$), and X-H (X is B, P, I, As, Si, etc.) are present in the second peak area (2500-1900 cm^{-1}). The peak zone of stretching vibrations of double bonds ($\text{C}=\text{O}$, $\text{C}=\text{C}$, $\text{C}=\text{N}$, $\text{N}=\text{O}$, etc.) is located in the third peak region (1900-1500 cm^{-1}). The stretching vibration of the X-C (X \neq H) bond and different bending deformation swing vibrations of numerous groups may be found in the spectrum's fourth peak area (1500-600 cm^{-1}).

2.6.2 Structure determination

The majority of methods for determining material structure rely primarily on diffraction methods. These techniques include X-Ray Diffraction, Electron Diffraction, Neutron Diffraction, Mössbauer Spectroscopy, and γ Ray Diffraction, with X-ray diffraction being the most frequently and commonly applied. This technique encompasses Debye powder photographic analysis, high-temperature, room-temperature, and low-temperature diffraction instruments, back-reflection and transmission Laue photography and four-circle diffractometers for determining single crystal structures.

X-Ray Diffraction (XRD)

When a monochromatic X-ray is focused onto a crystal, the electric field created by the periodic variation of the X-ray causes the electrons around the atoms in the

crystal to vibrate, turning each electron into a secondary wave source that emits spherical electromagnetic waves. The frequencies of the emitted spherical waves are consistent with the incident X-ray. The scattering waves from the electrons on the atoms in the crystal, known as coherent scattering or diffraction, can interfere with each other and accumulate based on the periodicity of the crystal structure. Only certain crystals can result in interference and diffraction when the angle of incidence satisfies the Bragg equation(as below 2.6)

$$n\lambda = 2d\sin\theta \quad (2.6)$$

Where n is the diffraction order ($n=1$ is first order, $n=2$ is second order, $n=3$ is third order), λ is the wavelength of the incident wave, d is the interplanar spacing in the atomic lattice, and θ is the angle between the incident wave and the scattering plane.

The XRD spectrum provides information on the material's bulk structure as it indicates that only specific crystals can produce interference and diffraction when the angle of incidence satisfies the Bragg equation. The basic principle of X-ray diffraction is that the scattered rays from crystal planes are enhanced when the path difference is an integer multiple of the wavelength. The lower beam will travel a certain distance further than the upper beam due to the diffraction effect when two atoms scatter the same wavelength and phase. The radiation interference occurs when this distance is equal to a multiple of the radiation wavelength. This phenomenon leads to radiation interference, known as Bragg diffraction. (Figure 2. 11) The crystal cell size, shape, and orientation determine the distribution pattern of the diffraction line. The intensity of the diffraction beams depends on the species of the atoms and their position in the crystal cell.

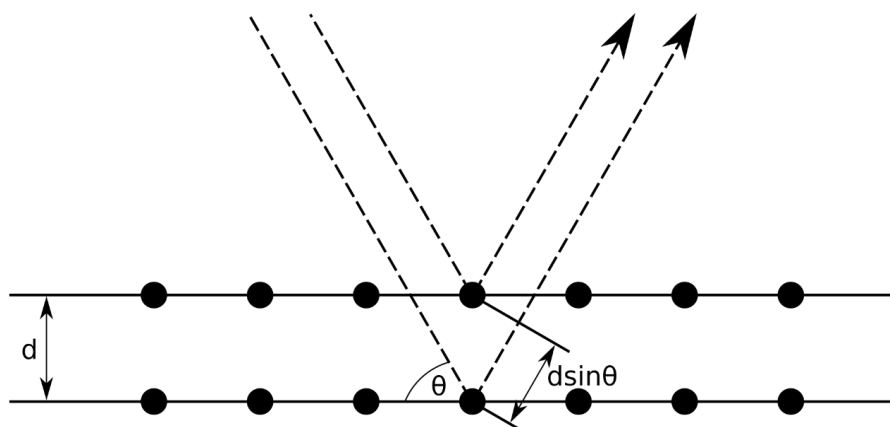


Figure 2. 11 Bragg Diffraction

Source: <http://en.wikipedia.org/wiki/File:DiffractionPlanes.png>.

The XRD can be used for both qualitative and quantitative analysis because the crystal surface spacing varies for different crystals. Each crystal substance corresponds to its unique diffraction pattern, making it impossible for two crystals to have precisely the same diffraction pattern. The phase composition of the sample can be qualitatively analyzed by comparing the X-ray diffraction spectra of the sample to be measured with those of the standard material. On the other hand, the quantitative analysis of the phase composition, crystallinity, and grain size of the sample can be completed by analyzing and calculating the diffraction intensity of the sample. The quantitative analysis methods of phase content mainly include the Rietveld full spectrum refinement quantitative method and the K value method (also known as the RIR method). The principle of the K value method is that Various substances and aluminum oxide(Al_2O_3) are mixed according to the weight ratio of 1:1, and the ratio K of the integral intensity of the most substantial diffraction peak of the two is defined as the RIR value (as the equation 2.8). In the daily, the percentage content of each component (the mass fraction of sample) w_i in the mixed sample is calculated by equation 2.7.

$$K = \left(\frac{I_i}{I_s} \right)_{1:1} \quad (2.7)$$

I_i and I_s are the integral intensity of the diffraction peak for the sample and reference, respectively.

$$w_i = \frac{I_i W_s}{I_s K} \quad (2.8)$$

W_s is the the mass fraction of the reference.

The following helpful information could be obtained in the qualitative analysis of XRD: First, whether the sample is amorphous or crystal-based could be determined. Amorphous samples have no peak and lack fine spectrum peak structure, while crystals exhibit rich spectral line characteristics. Additionally, the size and shape of the crystal cell could be obtained by assessing whether the crystal cell expands or contracts according to the Scherrer formula (as below 2.9). When X-rays incident on a small crystal, the diffraction line will diffuse and widen. Consequently, the X-ray diffraction band becomes more expansive as the crystal grain size decreases.

What's more, the phase composition of the sample also could be determined by the qualitative analysis of XRD, which is one of its most important uses. Suppose the composition elements or groups of the crystalline substance are different or their structure varies. In that case, the number of diffraction peaks, degree, relative intensity, and the shape of the diffraction peak show differences in their diffraction spectra. The XRD standard database includes JCPDS (PDF cards), ICSD, CCDC, etc. The software for analyzing XRD patterns includes Jade, Xpert Highscore, etc. Additionally, the relative crystallinity (X_c) of the sample can be determined by comparing the crystalline area (A_c) obtained from integrating the more substantial diffraction peak with that (A_g) of the amorphous region. (as in equation 2.9).

$$D_{hkl} = \frac{k\lambda}{\beta \cos\theta_{hkl}} \quad (2.9)$$

Where β is the full width at half maximum, k is the shape factor, for spherical particles, k is 1.075, and for cubic crystals, k is 0.9. Typically, k is 1. D_{hkl} only represents the grain size in the normal direction of the crystal plane and has nothing to do with the

grain size in other directions. When the grain is a single crystal, the average grain size measured is the grain size. When the grain is polycrystalline, the average grain size of all the grains that make up a single grain is measured.

$$X_c = \frac{A_c}{A_c + A_g} \quad (2.10)$$

A_c is the crystalline area of the diffraction peak. A_g is the amorphous area.

2.6.3 Morphology observation

The morphology of materials is primarily observed using microscopes and optical microscopes, which is the most commonly employed method. However, the ability to monitor materials at a sub-micron and sub-molecular level has been made possible through the use of scanning electron microscopy (SEM) and transmission electron microscopy (TEM). SEM has proven to be particularly valuable in analyzing the fracture morphology of materials. In recent years, improvements in SEM resolution have enabled direct observation of the spherulite size perfection in some crystalline polymers, as well as the size and distribution of dispersed phases in blends and the miscibility relationship between continuous phases. On the other hand, TEM, although requiring more complex sample preparation, is highly useful in studying defects and interactions in crystal materials.

Scanning Electron Microscopy (SEM)

The Scanning Electron Microscope (SEM) is an analytical instrument that uses secondary electron and backscattered electron signals to obtain various physical and chemical properties of the sample itself. Its magnification can reach hundreds of thousands of times, and its resolution can reach the nanometer level. Through its vacuum system, electron beam system, and imaging system, the SEM provides information on the morphology, composition, crystal structure, electronic structure, and internal electric or magnetic field of the sample. Due to advancements in science and

technology, the SEM has become an essential tool in the field of morphology and composition analysis.

Resolution is the most critical performance index of SEM. At present, the resolution of the secondary electronic image of a tungsten filament in a scanning electron microscope (SEM) ranges from 3nm to 6nm. However, achieving this resolution is not a daily occurrence and is considered only an acceptance indicator. It becomes quite challenging to reach a resolution of 6 nm when using a tungsten filament SEM under customary working conditions, particularly when taking photographs of ordinary samples. With a resolution of 6 nm, clear photos can be taken at magnifications exceeding 50,000 times. The instrument magnification range is 100-20,000 times, and conventional samples can be photographed up to 8-10,000 times. However, samples with poor conductivity or magnetic properties may not appear evident at magnifications greater than 8,000 times. When observing the morphological characteristics of an example, it is essential to select the appropriate magnification for photography. It is not that the larger the magnification, the better. This is because, at magnifications of tens of thousands of times, many samples lack fine surface morphology, making it difficult to obtain clear photos. Moreover, at high magnifications, the sampling area is tiny, only covering a small portion of the sample surface, which leads to a lack of representativeness.

When performing SEM energy spectrum analysis, it is essential to note that this technique can typically only measure elements from C onwards, including C itself. Studying B elements is sometimes possible, although it is not recommended or allowed. When preparing the sample for Energy Dispersive X-ray spectroscopy (EDS) analysis, it is crucial to consider the test position and the elements to be measured. It should be noted that the element being tested does not coincide with the base component. For instance, if the C element is being tested, the sample should not be dispersed onto a base containing C; instead, it can be distributed onto a silicon wafer or tinfoil. Similarly, caution should be exercised when measuring Si elements to avoid sample preparation on silicon wafers. In order to ensure that a clear image is obtained, samples with poor conductivity or strong magnetism are generally gold-plated and then tested.

2.7 Research motivation and objectives

2.7.1 Primary Challenges and Research Motivation

The energy crisis and environmental degradation represent formidable challenges confronting the advancement of modern civilization. The attributes of photovoltaic technology, encompassing its environmental benignity, inherent safety, and the sustainability of its resources, are increasingly underscored as critical advantages in addressing these global issues.

The advent of photovoltaic technologies has precipitated a heightened integration of energy storage solutions capable of transducing solar irradiance into electrical power. This advancement has also resulted in the development and evolution of solar cells through three generations. Initially, solar cells were made of crystalline silicon, which included polysilicon, monocrystalline, and ribbon silicon. Subsequently, they were transformed into thin-film solar cells, such as cadmium telluride or silicon thin-film cells. Recent advancements in thin-film technology have given rise to perovskite, inorganic, and organic solar cells. Perovskite solar cells offer the best stability and efficiency compared to organic solar cells, which can be decomposed at high temperatures and humidity due to the presence of organic ions. Perovskite solar cells have the potential to become a viable option for clean and sustainable energy production.

Currently, silicon-based photovoltaic cells maintain a predominant share of approximately 95% within the solar energy market, yet their peak technological efficiency does not surpass the 30% threshold. According to the latest findings from 2024, significant advancements in the efficiency of perovskite solar cells have been documented. Experimental investigations reveal that perovskite-only cells exhibit an efficiency of around 26%, whereas perovskite-silicon tandem cells, which amalgamate traditional silicon substrates with perovskite compounds, have achieved efficiencies over 33% under controlled laboratory conditions. However, the pathway to commercialization of perovskite solar technology is obstructed by challenges pertinent to their prolonged stability, scalability, and the formulation of manufacturing processes

capable of dependably fabricating devices at reduced costs, necessitating further advancements in materials science and engineering to surmount these barriers.

2.7.2 Research objectives

The present research aims to generate highly efficient, stable perovskite photovoltaic devices. The following are the specific objectives:

1. To significantly enhance the stability of perovskite films and devices under conditions of moisture, thermal stress, and light exposure by developing a water-resistant barrier on the surface of the perovskite.
2. To enhance the efficiency of perovskite films, particularly when dealing with larger areas, it is necessary to ensure their compactness and uniformity while minimizing non-radiative recombination. This can be achieved by effectively controlling the intermediate solvent-complex phases during perovskite crystallization.
3. To improve the moisture resistance of perovskite films and devices and enhance the long-term operational stability of PSCs under ambient conditions by using a comprehensive co-polymerization technique.

2.7.3 Thesis outline

Chapter 1 provides an introduction to the solar cell, covering its history, principles, and parameters. This includes solar irradiance, different types of solar energy conversion methods, the essential optical processes involved, prerequisites for ideal solar cells, as well as information on photocurrent, dark current, open circuit voltage, and efficiencies.

Chapter 2 reviews the understanding of perovskite solar cells, including their typical structure, the photovoltaic components found in the active layer, and the deposition techniques used, such as spin coating and doctor blading.

Chapter 3 In order to facilitate room-temperature meniscus coating of superior perovskite films, we showed the integration of a multifunctional zwitterionic surfactant into perovskite ink. By investigating the perovskite crystallization process in situ, We emphasized the beneficial effects of the surfactant on film formation, crystallization

kinetics, defect passivation, and moisture barrier defense, in addition to enabling greater efficiencies of 22% (0.04 cm² active area) and 21% (0.8 cm²) across perovskite compositions and device topologies. Furthermore, this strategy's universality and adaptability markedly improved stability under various aging circumstances.

Chapter 4 To partially replace the traditional hazardous solvent for high-performance room-temperature blade-coated PSCs and modules, we developed a simple and effective green solvent engineering (GSE) technique by adding green solvent, ethyl alcohol (EtOH), into the perovskite ink. We systematically investigated and offered fundamental knowledge of perovskite crystallization kinetics in this printing-friendly technology to identify the real-time perovskite structure development and phase-transition route during solidification.

Chapter 5 In order to cause a regulated co-polymerization at the perovskite surface and GBs, our study showed how cross-linkable agents might be incorporated asynchronously. We added divinyl sulfone (DVS), a brand-new cross-linking initiator, to the perovskite precursor solution. Maintaining the kinetic balance between perovskite nucleation and crystal development, DVS manipulated intermediate-dominated perovskite crystallization, producing high-quality perovskite films with low defect density. The pre-embedded cross-linking initiator sparked the three-dimensional co-polymerization into a controlled macro reticular structure, but more critically, it was initiated by a post-treated nucleophilic glycerine (gly) reagent.

Chapter 6 outlines the thesis and future development prospects of perovskite solar cells.

Chapter 3 Zwitterionic-Surfactant-Assisted Room Temperature Coating of Efficient Perovskite Solar Cells

3.1 Introduction

Over the past decade, organic-inorganic hybrid perovskite (OIHP) materials (such as methylammonium lead halides MAPbX_3 , where $X = \text{I, Br, or Cl}$) have attracted increasing attention in the photovoltaic research community due to their outstanding and tunable electronic and optical properties, such as tunable energy levels through compositional engineering, ambipolar charge transport with long diffusion length ($>1 \mu\text{m}$) and lifetime, excellent light-absorption coefficient ($\approx 10^5 \text{ cm}^{-1}$), and high defect tolerance.²³⁻²⁵ The performance of laboratory-scale perovskite solar cells (PSCs) has improved tremendously, reaching a certified power conversion efficiency (PCE) up to 25.2%. Superior to other high-efficiency photovoltaic materials, such as silicon and gallium arsenide (GaAs), perovskite polycrystalline films can be deposited in a facile solution process, which is in favor of high-throughput and low-cost printing techniques for scale-up manufacture of PSCs.²⁶⁻³⁰

Although very promising, most of the reported high-efficiency PSCs are fabricated by spin-coating methods so far, especially by one-step spin coating associated with antisolvent drop-casting to precipitate the intermediate phase of the perovskite complex.³¹⁻³³ However, this deposition technique makes it difficult to prepare uniform and high-quality perovskite films in relatively large areas, and it cannot be compatible with industrial-level manufacturing.³⁴⁻³⁶ In order to address this issue, scalable deposition techniques have recently attracted massive interest from the commercialization point of view. Many efforts have been devoted to printing techniques of perovskite photovoltaic films into larger areas, including spray coating,^{37,38} slot-die coating,^{39,40} doctor-blade coating,^{41,42} and so on. Blade coating, also known as a knife or bar coating, is a simple, cost-efficient, and roll-to-roll-compatible meniscus-coating

technique for optoelectronic device fabrication. Meanwhile, in order to control the drying dynamics of perovskite ink, hot-casting,^{42,43} vacuum-flashing,^{44,45} and gas-quenching post-treatments^{46,47} have also been involved to replace the conventional antisolvent drop casting. Phase-transition pathways from the disordered perovskite precursor to the polycrystalline perovskite thin films throughout the ink-drying process have been well investigated and gleaned into the role of fluid dynamics in meniscus-coating techniques.^{43,48-51} Until now, PCEs of the blade-coated PSCs have rapidly climbed up to 21% for small-area devices ($\sim 0.1 \text{ cm}^2$), $\sim 20\%$ for 1.0 cm^2 devices, and 16.4% for large perovskite modules (63.7 cm^2).^{47,52,53} However, these results still lag behind the performance of small-area PSCs deposited by spin coating.

Additive engineering in perovskite precursors has been well-established in spin-coated PSCs.^{27,33,54-57} However, coating-friendly multifunctional additives specially designed for scalable deposition of perovskite films toward higher-performance PSCs still lack detailed investigations. It is a significant challenge to coat uniform and fully covered perovskite films on a hydrophobic hole transport layer (HTL), such as poly[bis(4-phenyl)(2,4,6-trimethylphenyl)amine (PTAA), because of the non-wetting surface toward perovskite precursor solution (commonly in polar solvent, e.g., N, N-dimethylformamide [DMF] and dimethyl sulfoxide [DMSO]).⁵⁸ The hydrophobic nature of PTAA HTL reduces the adhesion of perovskite ink, inducing severe shrink and pin-hole issues of the blade-coated perovskite films. In the printing industry, surfactants with long alkyl chains are essential additives to fine-tune the surface energy of printing ink for high-quality printed films. This concept has also expanded to published electronics research to improve the coverage and quality of electronic films. Very recently, blade coating of the perovskite ink containing a minimal amount of surfactants (dozens of ppm) on a preheated substrate ($\geq 140^\circ\text{C}$) has been demonstrated to be an efficient and high-throughput deposition technology for high-quality perovskite films in a large area, representing a breakthrough in the field.⁵⁹ However, most of the high-performance blade-coated PSCs are involved with high-temperature hot-casting post-treatment, which hinders their applications, particularly in flexible photovoltaic

modules. The evaluated processing temperature leads to simultaneous fast solvent evaporation and crystal growth, which makes detailed perovskite crystallization study intractable and process control harder. Perovskite wet films in high-temperature coating always suffer from inherent Be´nard–Marangoni convection and, thus, yield inhomogeneous films with island microstructures.⁶⁰ In our opinion, room-temperature (RT) coating of large-area and high-quality perovskite films incorporated with multifunctional surfactants in a well-controlled manner is more desirable for future PSC manufacture.

In this study, we demonstrate the RT meniscus coating of high-quality perovskite photovoltaic films incorporated with a multifunctional sulfobetaine-based zwitterionic surfactant, tetradecyl dimethyl (3-sulfopropyl)ammonium hydroxide inner salt (TAH) (Figure 3.1). Besides hydrophobic (water-fear) and hydrophilic (water-friend) terminal groups, zwitterionic surfactants also carry both positively and negatively charged functionalized groups connected with a covalent bond. Their unique characteristics enable them to distinguish from other common organic additives and display special performance in large-scale coating.⁶¹ We in situ investigate the nucleation kinetics of the intermediate complex and its transition to the perovskite during the ink-drying and annealing process, respectively, using the time-resolved X-ray scattering and UV-vis absorption technologies. The coating-friendly TAH not only helps to improve the adhesion of perovskite ink to the underlying hydrophobic transport layer, thus constructing a compact and smooth perovskite film with full coverage even on RT substrate but also finely modulates the perovskite crystallization kinetics, inducing better crystallinity and dominant out-of-plane orientation. Moreover, functionalized zwitterionic moieties have a solid capability to passivate the positively and negatively charged defects at the perovskite surface and grain boundaries (GBs) simultaneously.^{62,63} This strategy can be applied across perovskite compositions and device architectures with enhanced PCEs up to 22% for both the inverted structure MAPbI₃-based and conventional-structure-mixed triple-cation (CsFAMA) PSCs, with significant open-circuit voltage (V_{OC}) enhancement. Upscaling the active area to 0.8 cm² still maintains a superior efficiency of over 21%. In addition, during the perovskite

formation process, TAH has been shown to self-assemble at the perovskite surface, especially the upper surface, with hydrophobic long tails pointing outside and spontaneously forming a moisture barrier with alkyl chains intertwining. This approach significantly enhances the stability of both perovskite films and devices under the conditions of moisture stress (60% relative humidity⁶⁴), high-temperature stress (80°C), or continuous illumination in the ambient atmosphere.

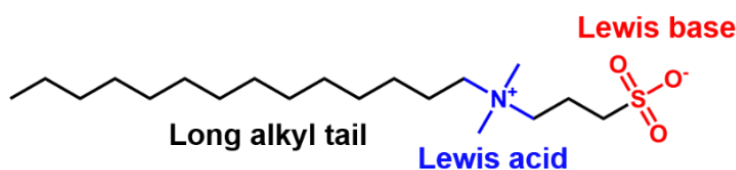


Figure 3. 1 The molecular structure of TAH.

3.2 Results and Discussion

3.2.1 Perovskite Film Deposition and Morphology

The RT meniscus-guided blade-coating technique used in this study is illustrated in Figure 3. 2A. The perovskite precursor solution was swiped linearly by a film applicator, resulting in a wet perovskite film on the PTAA-coated indium tin oxide (ITO) substrate. The perovskite precursor solution with highly disordered ions requires additional energy to re-orientate, and this freezes their motion, assembling them into a highly ordered crystal lattice. Thus, the formation of an intermediate adduct with a less-disordered state in lower entropy can facilitate its crystallization into a superior feature. In this study, enlightened by the intermediate protocol, we separated the precursor film deposition from subsequent thermal annealing in a well-controlled manner, thus allowing an RT process. A laminar nitrogen knife subsequently quenched the as-prepared perovskite wet film in the direction parallel to the substrate. Functionally similar to the conventional antisolvent drop-casting in the spin-coating technique, this nitrogen-quenching post-treatment induces instant super-saturation of the precursor solution and facilitates fast nucleation of the ordered perovskite intermediate adducts

(Figure 3. 3), which helps to trigger the formation of ultra-smooth perovskite films in large areas after proper thermal annealing.^{46,65,66}

Figure 3. 2C shows the photographs of the blade-coated perovskite films with different amounts of TAH- on PTAA-coated ITO substrate after thermal annealing. De-wetting problem of perovskite ink on the PTAA layer prevents the deposition of high-quality perovskite films with uniform and pinhole-free grains in the inverted p-i-n structured PSCs. In our study, the pristine perovskite ink first spreads over the substrate by the film applicator but shrinks quickly during the quenching process, leaving partially uncovered perovskite film after annealing. The de-wetting problem can be solved when a small amount (e.g., 0.1 wt %) of TAH surfactant is incorporated into the perovskite ink. The severe shrink phenomenon is eliminated during the drying process of the TAH-based perovskite wet film, and the perovskite film displays almost 100% coverage after thermal annealing.

To better understand this process, we measured the contact angles of the corresponding perovskite droplets on the PTAA-coated ITO substrate, as shown in Figure 3. 2D. The pristine perovskite droplet shows a relatively large contact angle of 41.0° on the PTAA layer. The contact angles are monotonically reduced when a small amount of TAH is incorporated into the perovskite ink (from 0 to 0.1 wt %). The droplet containing 0.1 wt % TAH displays excellent wetting contact on PTAA with a contact angle of 19.8°. Due to its amphipathic nature, TAH provides a strong capability to fine-tune the surface energy of the perovskite ink and improves its adhesion to the underlying hydrophobic substrate. According to the relationship between the free energy required for heterogeneous and homogeneous nucleation:^{67,68}

$$G_{\text{Heterogeneous}} = G_{\text{Homogeneous}} * \frac{(2 + \cos \theta)(1 - \cos \theta)^2}{4} \quad (3.1)$$

where θ is the contact angle on the solid/liquid interface. The wetting contact of TAH-based perovskite ink on PTAA results in a lower energy barrier for forming

heterogeneous nucleation, which benefits the formation of uniform and high-quality perovskite films with full coverage.

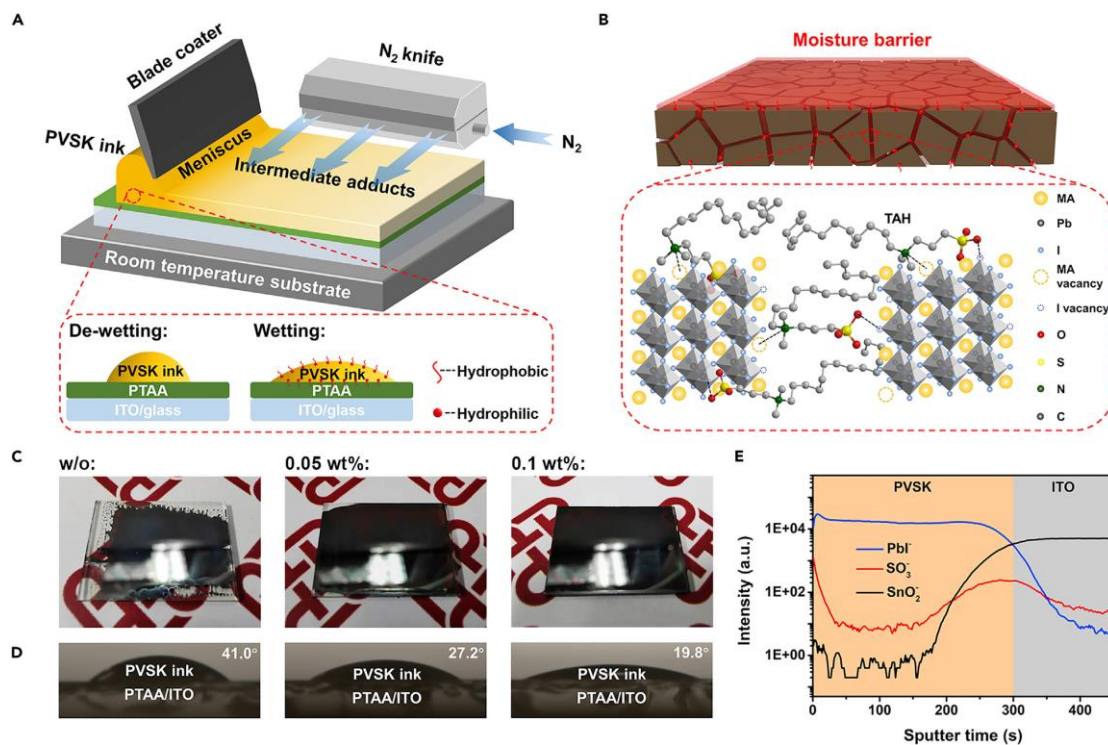


Figure 3. 2 Perovskite Film Deposition and Morphology. (A) Schematic illustration of the zwitterionic surfactant-assisted meniscus coating at room temperature. (B) Schematic illustration of the coordinate interaction between TAH and charged defects at the perovskite surface and GBs and spontaneous formation of moisture barrier. (C) Photographs of the blade-coated perovskite films with different amount of TAH on PTAA-coated ITO substrates. (D) Contact angles of the corresponding perovskite ink droplets on PTAA-coated ITO substrates. (E) ToF-SIMS depth-profile analysis in the TAH-incorporated perovskite film.



Figure 3. 3 Photographs of the as-cast perovskite films with different amounts of TAH before thermal annealing.

Figure 3. 4 shows the top-view scanning electron microscopy (SEM) images of the annealed MAPbI₃-based perovskite films incorporated with different amounts of TAH. In the pristine perovskite, a large number of pinholes can be observed at GBs, mainly due to the de-wetting problem and severe shrink of perovskite wet film during the ink-drying process. On the contrary, the ink incorporated with 0.05 and 0.1 wt % TAH significantly suppresses the formation of pinhole and constructs a compact perovskite film with dense and uniform grains. We also performed cross-sectional SEM combined with energy-dispersive X-ray spectroscopy (EDX) in the pristine and TAH-incorporated perovskite films, which were blade-coated on PTAA/ITO substrates (Figure 3. 5). Both perovskite films show a similar thickness of ~400 nm. While compared with the pristine film, TAH-based perovskite film displays much improved physical contact with closer adhesion to the underlying PTAA/ITO substrate, which likely indicates that TAH modifies the perovskite ink/PTAA interface and enhances the affinity to the underlying hydrophobic transport layer. According to the cross-sectional EDX mapping, the stronger intensity of the S Ka1 signal derived from TAH was clearly detected at the perovskite upper surface, and the intensity decreased into the bulk.

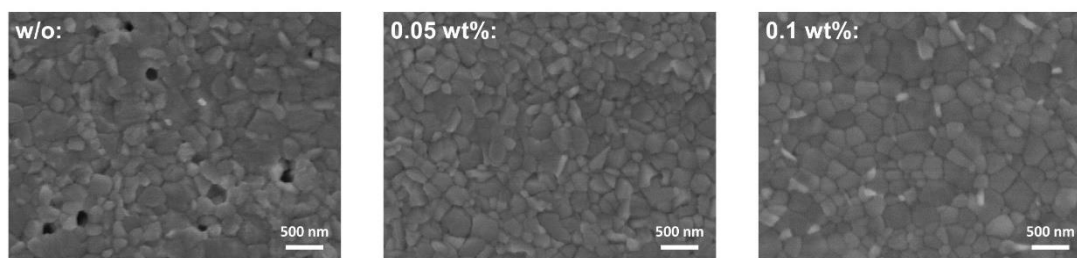


Figure 3. 4 SEM images of the blade-coated perovskite films with different amount of TAH on PTAA/ITO substrate. Scale bar: 500 nm.

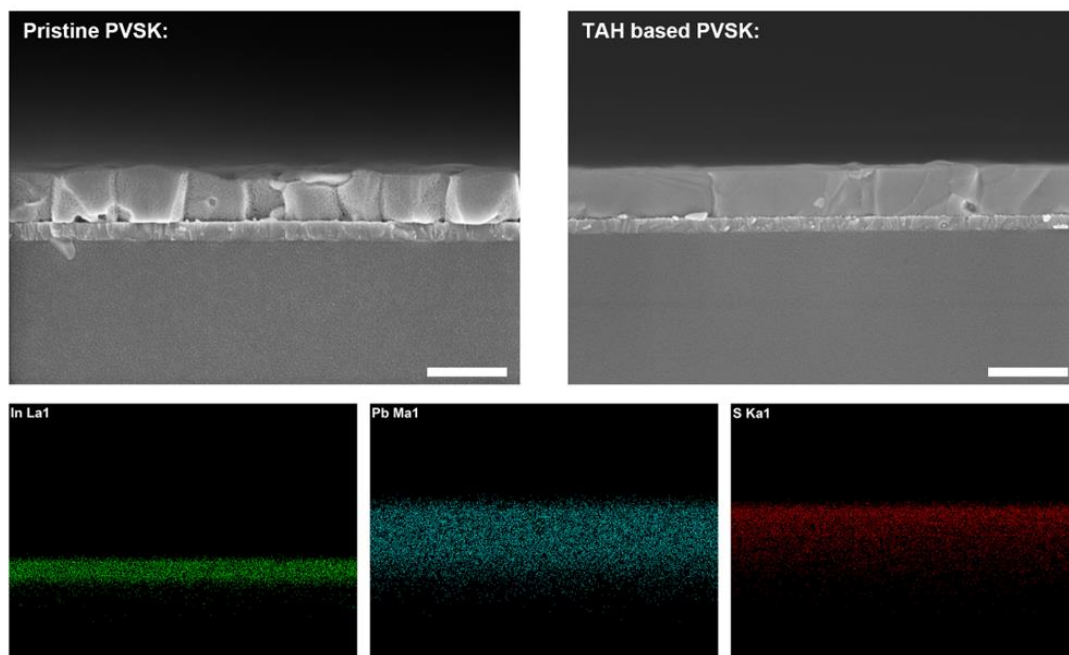


Figure 3. 5 Cross-sectional SEM images of the pristine and TAH-based perovskite films blade-coated on PTAA/ITO substrate and corresponding EDX mapping. Scale bar: 500 nm

In order to investigate TAH distribution in the bulk perovskite more precisely, we further conducted time-of-flight secondary ion mass spectrometry (ToF-SIMS) (Figure 3. 2E). Uniform signal of PbI^- throughout the whole thickness represented the bulk perovskite. A strong signal of SO_3^- derived from TAH was detected at the perovskite upper surface, which became two orders of magnitude lower at ~ 50 nm into the bulk (~ 35 s sputtering time). While deeper into the perovskite, a moderate amount of TAH was observed close to the PVSK/ITO interface, which was still much lower than that at the upper surface of the perovskite. According to the cross-sectional EDX and ToF-SIMS results, we can conclude that TAH prefers to self-assemble at the perovskite surface, especially at the upper surface, due to its amphipathic nature, which spontaneously forms a moisture barrier and facilitates inner encapsulation (Figure 3. 2B). We further measured the roughness of blade-coated perovskite films on the PTAA layer using atomic force microscopy (AFM), as shown in Figure 3. 6. The root mean square roughness (R_q) in the pristine perovskite is calculated to be 26.8 nm (area of $3 \mu\text{m} \times 3 \mu\text{m}$). With the incorporation of TAH surfactant from 0 to 0.1 wt %, the blade-

coated perovskite becomes much smoother and pin-hole free, with reduced R_q of 18.4 nm for 0.05 wt % and 16.3 nm for 0.1 wt % TAH, which also coincides well with the cross-sectional SEM images. TAH-based perovskites also display slightly stronger UV-vis absorption (Figure 3. 7A), which is mainly attributed to the improved coverage and quality of perovskite films. At the same time, the TAH additive does not affect the band gap of respective perovskite films. Both the pristine and TAH-based perovskite have an almost identical band gap of 1.59 eV (Figure 3. 7B).

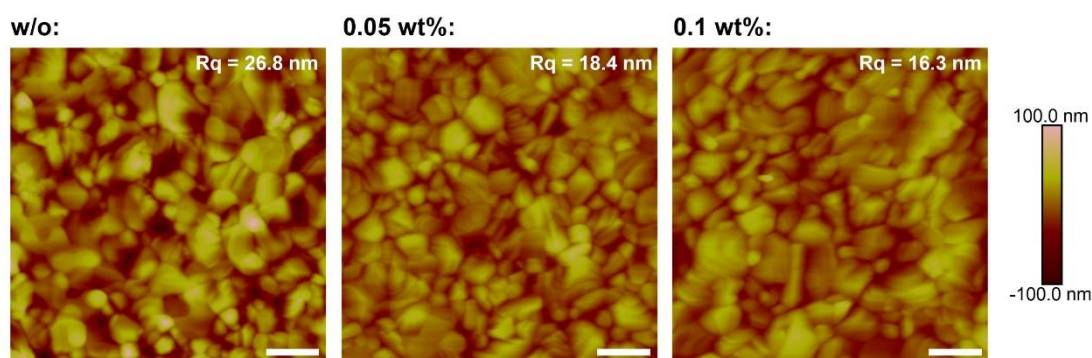


Figure 3. 6 AFM height images of the blade-coated perovskite films with different amount of TAH. Scale bar: 500 nm.

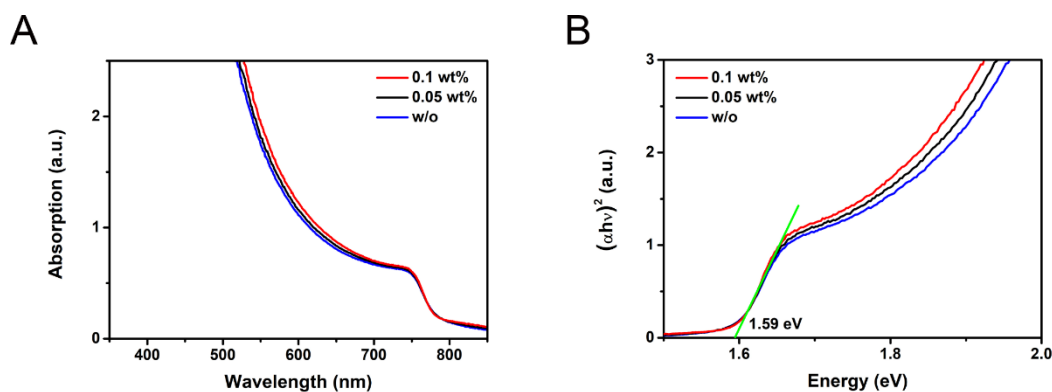


Figure 3. 7 (A) UV-vis absorption spectra of the perovskite films with different amounts of TAH. (B) Tauc plots as a function of $(\alpha h\nu)^2$ vs energy for the respective perovskite films. The band gap can be determined via linear extrapolation of the leading edges of the $(\alpha h\nu)^2$ curve to the baseline.

3.2.2 Perovskite Crystallization and Orientation

X-ray diffraction (XRD) measurement was performed to investigate the role of TAH in perovskite crystallization and grain orientation. We first isolated the intermediate phase and measured the XRD patterns of the as-cast perovskite films before thermal annealing (Figure 3. 8). For the pristine perovskite, three prominent peaks located at $2\theta = 6.5^\circ$, 7.2° , and 9.2° can be assigned to the $(MA)_2Pb_3I_8 \cdot 2DMSO$ intermediate phase, and one peak located at 14.08° represents the tetragonal $MAPbI_3$ phase.^{31,69} In comparison, the as-cast TAH-based perovskite film displays a new diffraction peak located at 9.48° , but the signal of tetragonal perovskite is missing. The new peak does not belong to any known intermediate solvate.^{70,71} Thus, we speculate that MAI-PbI₂-TAH, as a possible intermediate phase, is also precipitated during ink-drying. This result suggests that besides DMSO, TAH also induces extra coordination with perovskite precursors and retards the unfavored quick formation of perovskite at the early stage, which is coincident well with the film color in the as-cast perovskite (Figure 3. 3).

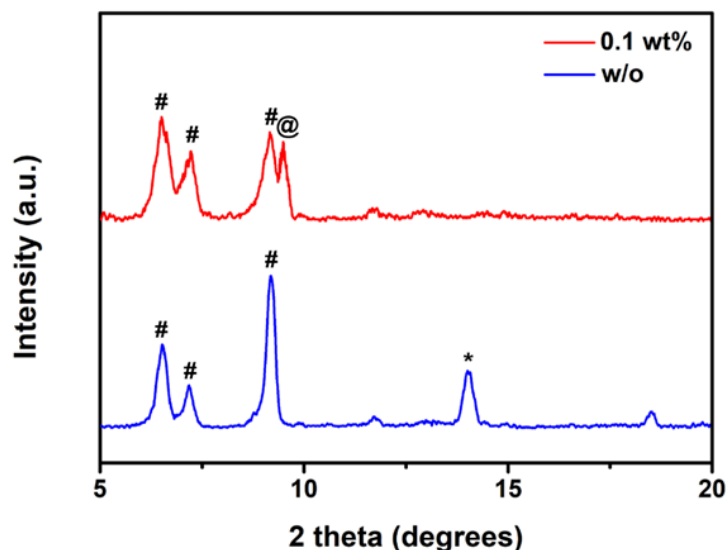


Figure 3. 8 XRD patterns of the as-cast pristine and TAH incorporated perovskite films before annealing.

In order to gain further insights into the crystallization dynamics with the incorporation of TAH, synchrotron-based in-situ grazing-incidence wide-angle X-ray scattering (GIWAXS) measurements were performed throughout the drying process of the perovskite ink with different concentrations of TAH.⁷² The two-dimensional (2D) GIWAXS patterns were measured at 1 s per frame, and the data collection lasted for 100 s until the scattering patterns were nearly unchanged, as shown in Figure 3.10. The corresponding intensity profiles and false-color intensity maps versus q and frame numbers are summarized in s 3. 9A and B, respectively. For the pristine perovskite, A scattering halo centered at $q \approx 0.4 \text{ \AA}^{-1}$ originates from the perovskite precursor solution at the early stage. It gradually shifts to higher q due to the removal of DMF molecules.^{49,70} After ~ 21 s of drying, the scattering ring of the precursor solution disappears, followed by the presence of a few sharp scattering peaks located at $q = 0.468, 0.515, \text{ and } 0.654 \text{ \AA}^{-1}$ (Figure 3. 9B and Figure 3. 10), which are assigned to the $(\text{MA})_2\text{Pb}_3\text{I}_8 \cdot 2\text{DMSO}$ intermediate phase.^{31,69,73} For the perovskite ink containing 0.05 wt% TAH, similar scattering peaks appear as early as ~ 16 s during the drying process (Figure 3. 10 and Figure 3. 11), indicating a faster nucleation rate.

Furthermore, when the TAH concentration is increased to 0.1 wt%, it takes an even shorter time of ~ 11 s to nucleate the intermediate complex. In the meantime, three new scattering peaks at $q = 0.550, 0.564, \text{ and } 0.674 \text{ \AA}^{-1}$ were observed (Figure 3. 9B and Figure 3. 10). The strong scattering signal at $q = 0.674 \text{ \AA}^{-1}$ is well agreed with the new peak located at $2\theta = 9.48^\circ$ measured from XRD (Figure 3. 8), which is likely related to the new intermediate adduct of MAI-PbI₂-TAH. Based on XRD and in-situ GIWAXS results, it is indicated that TAH tends to accelerate the nucleation process of the intermediate phases, which might arise from its extra and stronger coordinate interaction with perovskite precursor compared with DMSO. Such the faster nucleation kinetics of the intermediate complex is beneficial for the formation of dense perovskite grains.

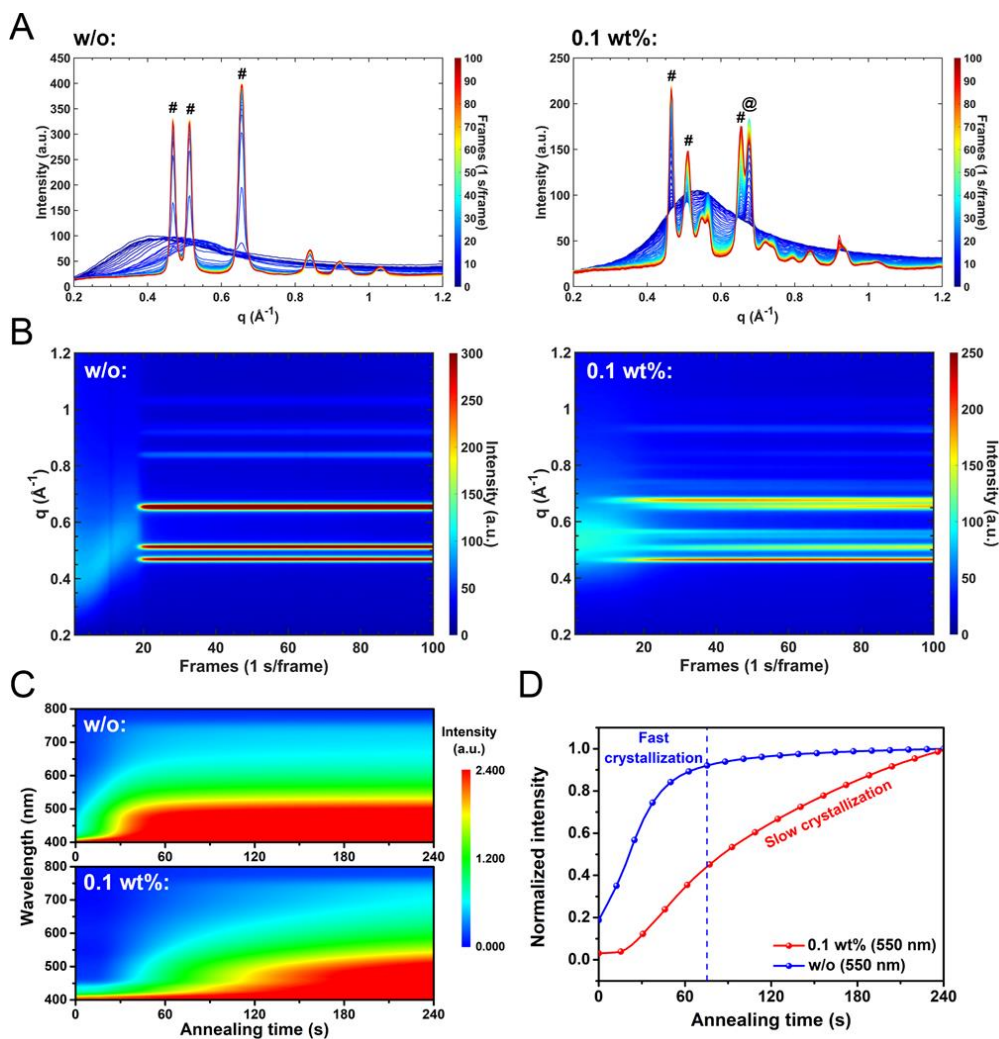


Figure 3.9 Crystallization Dynamics of the Intermediate Complex and Perovskite. (A) In-situ GIWAXS intensity profiles measured within 100 frames during the drying process of the perovskite inks without (left) and with 0.1 wt% TAH (right). (B) In-situ GIWAXS false-color intensity maps versus q and frame numbers during the drying process of the corresponding perovskite inks. (C) In-situ UV-vis absorption spectra as a function of annealing time for the perovskite without and with 0.1 wt% TAH annealed at 100 °C. (D) Time-resolved UV-vis absorption intensity at the wavelength of 550 nm for the corresponding perovskite films annealed at 100 °C.

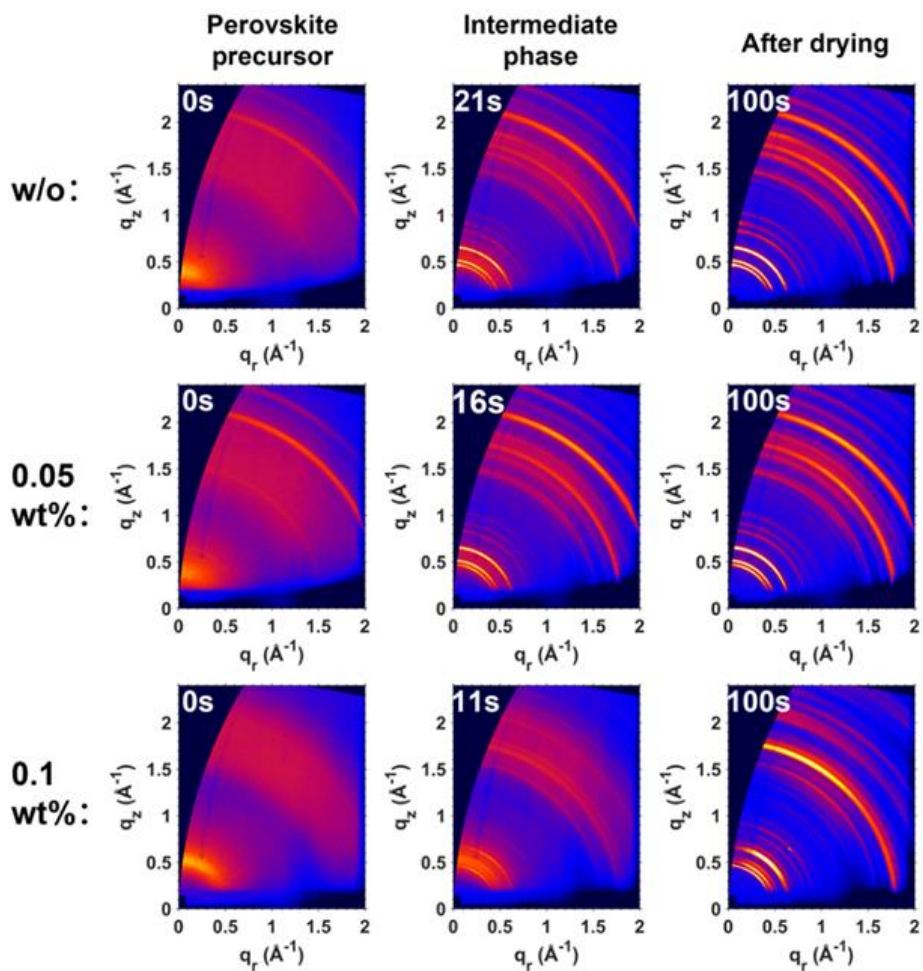


Figure 3. 10 2D GIWAXS patterns of the respective perovskite inks at different crystallization stages versus drying time.

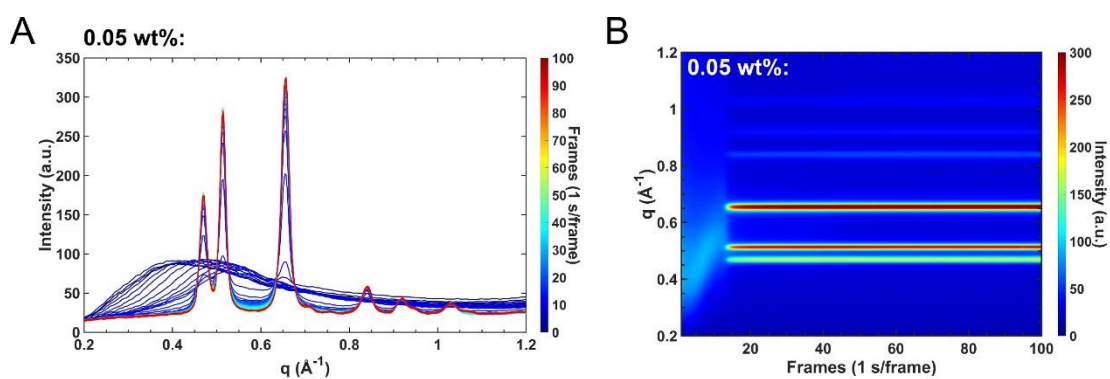


Figure 3. 11 (A) In-situ GIWAXS intensity profile and (B) the corresponding false-color intensity map versus q and frame numbers during the drying process of the 0.05 wt% TAH incorporated perovskite ink.

The transparent intermediate complex of $(\text{MA})_2\text{Pb}_3\text{I}_8 \cdot 2\text{DMSO}$ and MAI-PbI₂-TAH was converted into dark brown perovskite after thermal annealing (100 °C). We in situ studied the perovskite crystal growth during the annealing process with a time-resolved UV-vis absorption spectroscopy system. Figure 3. 9C shows the color mapping of the UV-vis spectra as a function of annealing time for the perovskite without and with 0.1 wt% TAH. We extracted the absorption intensity at the wavelength of 550 nm and plotted it as a function of annealing time (Figure 3. 9D). In the pristine perovskite, the relatively unstable intermediate adduct with DMSO coordination leads to unfavored quick crystal growth of perovskite within 75 s during the annealing process, which induces a discontinuous and inhomogeneous film morphology. On the contrary, the crystal growth is obviously retarded in TAH-incorporated perovskite since extra energy is required to decompose the relatively stable intermediate adduct with $\text{Pb}^{2+}\text{-SO}_3^-$ coordination bonds, which is transformed into the black perovskite phase even beyond 240 s. Such slow crystal growth during thermal annealing in the TAH-based perovskite allows the randomly formed nuclei to adjust their orientation to minimize the total Gibbs free energy and grow in a thermodynamically preferential orientation.⁷⁴

The crystal structure of the annealed perovskite with different amounts of TAH was also analyzed, as shown in Figure 3.12A. They all display similar diffraction patterns, with sharp peaks typical for the tetragonal MAPbI₃ phase. All of them show strong signals at $2\theta = 14.08^\circ$, 28.40° , and 31.86° , assigned to the (110), (220), and (310) planes, respectively. Several minor signals at 19.98° , 23.46° , 24.48° , 34.95° , 40.65° , 42.60° , and 43.17° , were assigned to (112), (211), (202), (312), (224), (411), and (314) planes respectively.⁷⁵ A small PbI₂ diffraction peak at $2\theta = 12.67^\circ$ is also observed in all three samples because of 5 mol% excess PbI₂ in the perovskite precursor recipe. It has been suggested that a moderate residual of excess PbI₂ can passivate the defects at perovskite surface and GBs and thus enhance the device performance. With the increased TAH concentration from 0 to 0.1 wt%, there is no shift for the diffraction peaks, revealing that TAH does not permeate into MAPbI₃ crystal lattice to induce a phase transition or form particular 2D structure at perovskite surface and GBs. Compared with the pristine perovskite, TAH-based perovskites show stronger and sharper XRD peaks, with the full

width at half maximum (FWHM) of (110) peak narrowed down from 0.252° to 0.201° (Figure 3. 13). The XRD patterns also display an increased ratio of the intensity between (110) and (112) peaks when incorporated with TAH (7.04 for the pristine, 10.37 for the 0.05 wt %, and 15.75 for the 0.1 wt%), which indicates a prominent (110) orientation (Figure 3. 12A). The improved crystallinity and preferential (110) orientation in TAH-based perovskite films are related to its stronger coordinate interaction and dominated precipitate of MAI-PbI₂-TAH adduct, which can further retard the perovskite crystallization and facilitate high-quality perovskites.

We further analyzed the surface, bulk crystallinity, and crystal orientation of annealed perovskite films with ex-situ GIWAXS measurements. Figure 3. 12B shows the 2D GIWAXS patterns of the pristine and TAH-incorporated perovskite films measured under the incident angles (α_i) of 0.2° and 1° , respectively. The scattering signal from the perovskite surface can be detected with a relatively minor incident angle (e.g., $\alpha_i = 0.2^\circ$, penetration depth $Z_p \approx 100$ nm). In comparison, a large angle of 1° can probe the bulk information of the perovskite ($Z_p \approx 700$ nm, more details in Note 3. 1). Thus, this technique is reliable in distinguishing the surface signal from the bulk signal.⁷⁶ Treatment with TAH (tetradecyldimethyl(3-sulfopropyl)ammonium hydroxide) leads to a decrease in GIWAXS intensity at the film surface, primarily due to the self-assembly of TAH molecules on the perovskite surface. The amphiphilic nature of TAH causes these molecules to accumulate at the film surface, forming a moisture barrier with hydrophobic alkyl chains oriented outward. This accumulation reduces the crystallinity of the top layers of the film, resulting in a weakened GIWAXS signal from the surface. Furthermore, TAH coordinates with lead ions in the perovskite, modulating the crystallization dynamics. This coordination results in slower crystal growth and improved out-of-plane orientation of the perovskite grains. Consequently, while the overall crystallinity of the bulk film is enhanced, the crystallinity near the surface is reduced, which is detected as a decrease in GIWAXS intensity in the surface region.

Figure 3. 12C shows the polar intensity profiles along the (110) ring at $q = 1.00 \text{ \AA}^{-1}$ from the 2D GIWAX patterns of these two types of perovskite films measured at 0.2° and 1° , respectively. The pristine perovskite exhibits almost an isotropic (110) ring in

both surface and bulk patterns. In contrast, the bulk ($\alpha_i = 1^\circ$) (110) ring of the TAH-based perovskite film concentrates along the out-of-plane (q_z) direction. It suggests a relatively dominant out-of-plane orientation with respect to the substrate for the perovskite grains, which is supposed to facilitate charge transport of PSCs in the vertical direction.⁷⁷ On the other hand, without a new scattering ring detected, the surface signal in TAH-based perovskite appears much decreased in intensity than the bulk one (Figure 3. 14), which agreed well with the depth distribution of TAH from EDX and ToF-SIMS results.

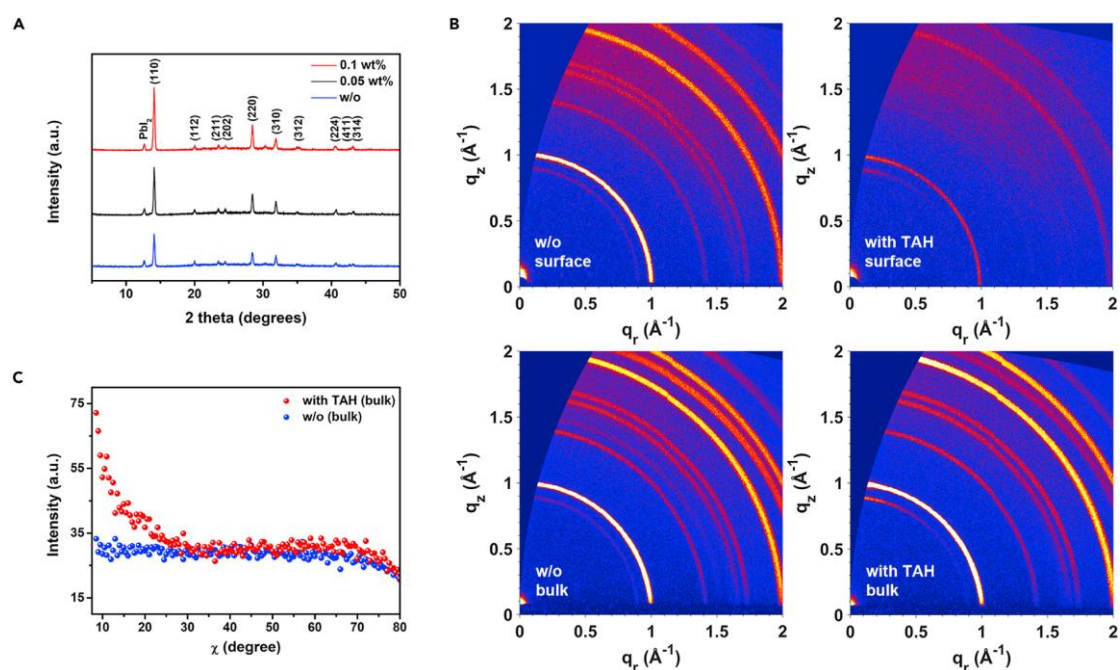


Figure 3. 12 Perovskite Crystallization and Orientation. (A) XRD patterns of the annealed perovskite films incorporated with different amounts of TAH. (B) 2D GIWAXS patterns of the pristine (left) and TAH-incorporated perovskites (right) at the upper surface ($\alpha = 0.2^\circ$) and in the bulk ($\alpha = 1^\circ$). (C) The polar intensity profiles along the (110) ring in the range of $q = 0.95\text{--}1.05 \text{ \AA}^{-1}$ from 2D GIWAXS patterns of the pristine and TAH-incorporated perovskites in the bulk ($\alpha = 1^\circ$).

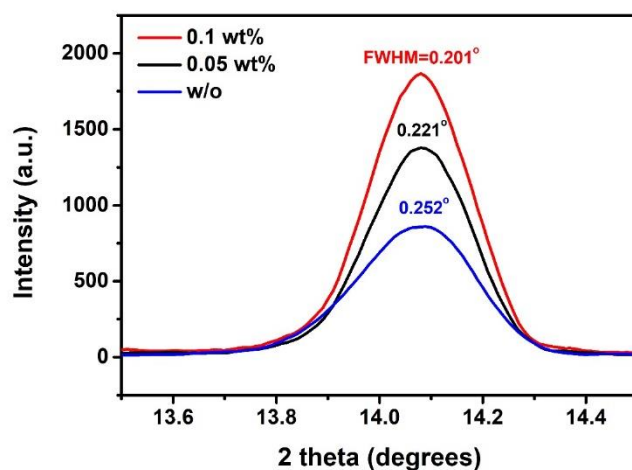


Figure 3. 13 Full width at half maximum (FWHM) of (110) peaks in the perovskite films with different amounts of TAH.

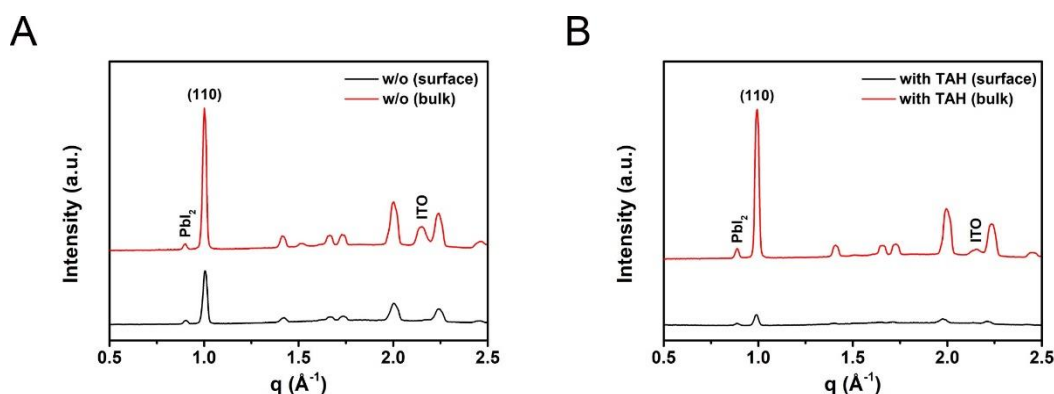


Figure 3. 14 GIWAXS intensity profiles of (A) the pristine and (B) TAH-incorporated perovskites at the upper surface (black curve, $\alpha_i = 0.2^\circ$) and in the bulk (red curve, $\alpha_i = 1^\circ$), respectively.

3.2.3 Charged Defects Passivation

In order to investigate the charge recombination dynamics, steady-state photoluminescence (PL) and time-resolved photoluminescence (TRPL) decay measurements were performed on the quartz substrate. Figure 3. 15A shows the steady-state PL spectra of the respective perovskite films with different amounts of TAH. Compared with the pristine perovskite, 0.05 wt% TAH incorporated perovskite exhibits stronger PL intensity by a factor of 320%, and the 0.1 wt% TAH-based film further increases the PL intensity to a level of over 640%. In addition, TAH-based perovskite

films show a blue-shifted PL peak (770 nm for 0.05 wt% and 768 nm for 0.1 wt%) compared with the pristine perovskite (774 nm). We also measured the photoluminescence quantum yields (PLQYs) in the perovskite films with different amounts of TAH. As shown in Figure 3. 16A, compared with the pristine perovskite (3.08%), TAH-incorporated perovskite film displays much higher PLQYs up to 5.94% for 0.05 wt % and 10.21% for 0.1 wt % TAH. Significantly enhanced PLQYs and blue-shifted PL peaks confirm the suppression of trap-assisted non-radiative recombination at perovskite surface and GBs induced by TAH.

TRPL decays of the corresponding perovskite films are shown in Figure 3. 15B. Fitting the experimental data with the bi-exponential function:

$$I(t) = A_1 \exp\left(-\frac{t}{\tau_1}\right) + A_2 \exp\left(-\frac{t}{\tau_2}\right) \quad (3.2)$$

Yields two decay times (e.g., τ_1 and τ_2); the fitting parameters are summarized in Table 3. 1. The fast decay lifetime (τ_1) is likely related to the charge-trapping process at the perovskite surface, while the slow decay lifetime (τ_2) represents the de-trapping or recombination process in bulk. It should be noted that the excitation fluence in our study is very low ($\leq 5 \text{ nJ/cm}^2$), which only generates a much lower density of free carriers ($2.4 \times 10^{14} \text{ cm}^{-3}$) compared with that of trap states. In this condition, TRPL decay mainly responds to the trapping and nonradiative recombination behaviors (Figure 3. 15, Table 3. 1 and Table 3. 2, more details in Note 3. 2). Compared with the pristine perovskite film with a relatively short lifetime (99.26 ns), TAH-based perovskites exhibit a prolonged average lifetime (217.07 ns for 0.05 wt% and 344.78 ns for 0.1 wt% TAH), which indicates better quality of perovskite crystal with the lower density of trap states. Moreover, the proportion of the fast decay is significantly reduced when TAH is incorporated into the perovskite (55.9% for the pristine, 17.8% for 0.05 wt%, and 7.1% for 0.1 wt% TAH), which further confirms the strongly suppressed non-radiative recombination at perovskite surface (Table 3. 1).

Note 3. 1 GIWAXS distinguishes the surface signal from the bulk signal.

Ex-situ GIWAXS measurement (Cu X-ray source, 8.05 keV, 1.54 Å) was carried out under two incident angles ($\alpha_i = 0.2^\circ$ and 1° respectively). The penetration depth (Z_p) into perovskite (X-ray absorption coefficient $\approx 26 \text{ mm}^{-1}$) with $\alpha_i = 0.2^\circ$ can be calculated to be $\sim 100 \text{ nm}$ and $\sim 700 \text{ nm}$ with $\alpha_i = 1^\circ$.⁷⁸ In the GIWAXS intensity profiles (Figure 3.12), neither the pristine nor the TAH-based perovskites showed any diffraction signal of ITO ($q = 2.15 \text{ \AA}^{-1}$) with $\alpha_i = 0.2^\circ$. While a 1° incident X-ray could penetrate the whole thickness of perovskite, we detected the ITO signal ((222) plane, $q = 2.15 \text{ \AA}^{-1}$) both in the pristine and TAH-based perovskite films. Therefore, this technique is reliable for distinguishing the surface signal from the bulk signal.⁷⁹

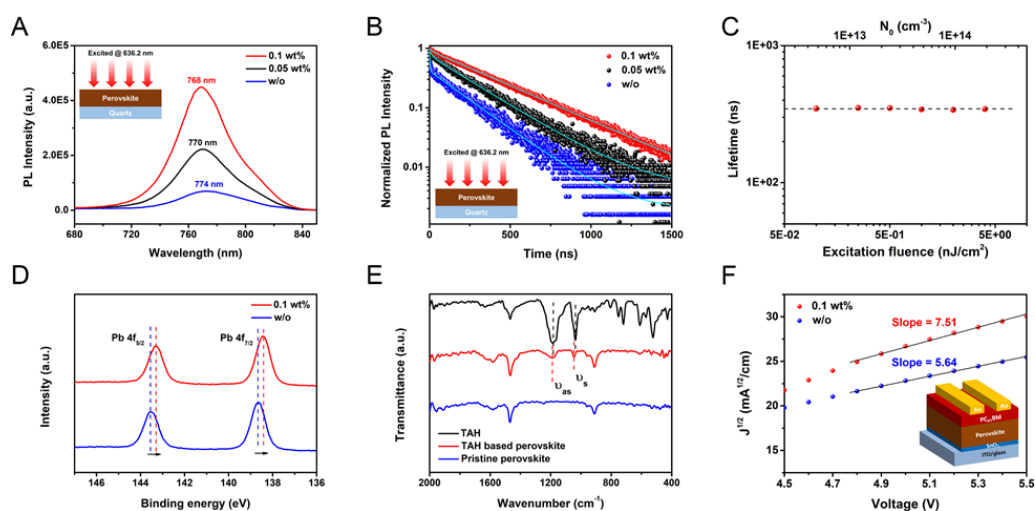


Figure 3. 15 Charged Defects Passivation. (A) Steady-state PL spectra of the perovskite films with different amounts of TAH. All the samples were prepared on quartz substrates excited with a 636.2 nm laser. (B)TRPL decays of the respective perovskite films. All the samples were prepared on quartz substrates excited with a 636.2 nm laser. (C)Excitation intensity dependence of the PL lifetime in the TAH incorporated perovskite film. (D)XPS Pb 4f spectra of the pristine and 0.1 wt% TAH incorporated perovskites. (E)FITR spectra of the pure TAH, pristine perovskite, and TAH-based perovskite films. (F)SCLC analysis of the pristine and TAH-incorporated perovskite films (fitting the slope in the trap-free regime). Inset: structure of electron-only device.

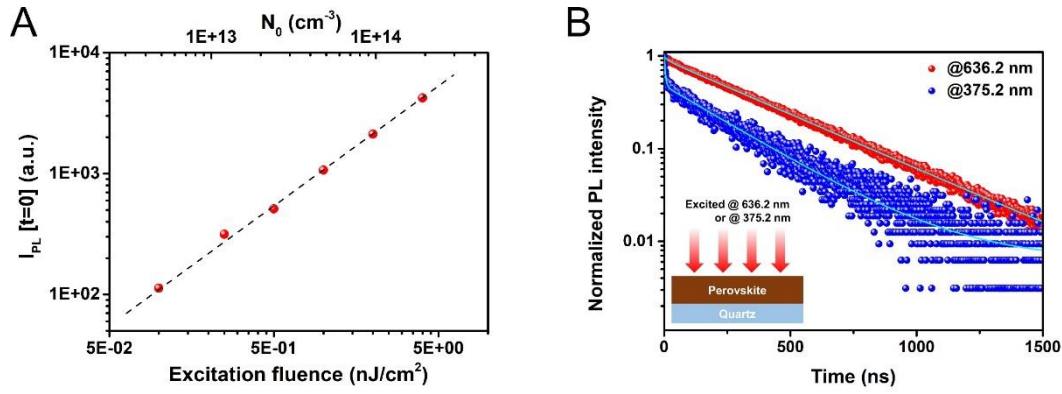


Figure 3. 16 (A) Excitation fluence dependence of the initial PL intensity just after the excitation in the TAH-incorporated perovskite film. (B) TRPL decay in the TAH incorporated perovskite with the excitation of 636.2 and 375.2 nm, respectively.

Table 3. 1 Fitting parameters of the bi-exponential decay function in TRPL spectra of the perovskites with different amount of TAH.

TAH concentration (wt%)	A_1	τ_1 (ns)	A_2	τ_2 (ns)	Average decay time ^a τ (ns)
w/o	0.52	3.33	0.41	220.92	99.26
0.05	0.16	19.06	0.74	259.88	217.07
0.1	0.07	22.89	0.91	369.54	344.78

^aAverage decay time is calculated according to the equation: $\tau = (A_1\tau_1 + A_2\tau_2)/(A_1 + A_2)$.

Table 3. 2 Fitting parameters of the bi-exponential decay function in fluence-dependent TRPL spectra of the TAH incorporated perovskite excited at 636.2 nm (0.1 to 4 nJ/cm²).

Excitation fluence (nJ/cm ²)	A_1	τ_1 (ns)	A_2	τ_2 (ns)	Average decay time ^a τ (ns)	Initial PL intensity [t=0] (a.u.)
0.1	0.25	28.92	0.59	482.54	347.53	113
0.25	0.18	23.13	0.69	436.94	351.32	315
0.5	0.16	24.27	0.77	418.11	350.35	513

1	0.15	24.58	0.81	401.90	342.94	1070
2	0.11	23.02	0.84	381.92	340.36	2123
4	0.07	22.89	0.91	369.54	344.78	4222

^aAverage decay time is calculated according to the equation: $\tau = (A_1\tau_1 + A_2\tau_2)/(A_1 + A_2)$.

Note 3. 2 Calculation of the initial density photogenerated carrier in TRPL.

The initial density photogenerated carriers N_0 in TRPL, when excited with 636.2 nm picosecond pulsed diode laser (EPL-635, ~ 5 nJ/cm²), can be estimated using the following equation:⁸⁰

$$N_0 = \frac{A(\lambda) \times F}{E_{ph}(\lambda) \times W} \quad (3.3)$$

In which F is the total incident fluence at excitation wavelength $\lambda = 636.2$ nm (~ 5 nJ/cm²), photon energy $E_{ph}(\lambda) \approx 3.12 \times 10^{-10}$ nJ, perovskite film thickness $W = 400$ nm; $A(\lambda)$ is the overall absorbance, which can be estimated using the following equation:

$$A(\lambda) = 1 - R - T = (1 - e^{-\alpha(\lambda) \cdot W}) \cdot (1 - R) \quad (3.4)$$

R and T are the reflectance and transmittance, respectively, and $\alpha(\lambda)$ is the absorption coefficient. For MAPbI₃-based perovskite, the overall absorbance is calculated to be $A(636.2 \text{ nm}) \approx 0.92$ with the $\alpha(636.2 \text{ nm}) \approx 5 \times 10^4 \text{ cm}^{-1}$.⁸¹ Therefore, N_0 can be calculated to be $2.4 \times 10^{14} \text{ cm}^{-3}$, which is much lower than the density of trap states measured in TAS analysis.

Fluence-dependent TRPL decay for the sample of TAH-incorporated perovskite was performed in order to reveal the PL lifetime and initial PL intensity right after the excitation of a 636.2 nm pulsed laser as a function of its fluence (Figure 3. 17C and Figure 3. 18A). The initial PL intensity exhibited a linear dependence on the excitation fluence, and the PL lifetime remained almost constant (Table 3.2), which confirmed low excitation fluence (≤ 5 nJ/cm²) in TRPL mainly triggered the trapping and nonradiative recombination behaviors of photogenerated carriers.

We also performed wavelength-dependent TRPL measurement with the excitation at 375.2 nm (EPL-375) and 636.2 nm (EPL-635) pulsed laser, respectively, as shown in Figure 3.14B. Compared with the 636.2 nm laser ($Z_p = 1/\alpha \approx 500$ nm), the penetration depth (Z_p) of the 375.2 nm laser is

much lower (~50 nm). Therefore, TRPL with the excitation at 375.2 nm mainly reflected the signal at the perovskite upper surface. We compared the fitting parameters of the TAH-incorporated perovskite under these two conditions (Table 3.3). The 375.2 nm excitation displayed a much higher proportion of fast decay (53.9%) compared with that at 636.2 nm (7.1%), which further indicates the rapid decline (τ_1) is likely relevant to surface recombination. In contrast, the slow decay (τ_2) originates from the deeper sub-surface region or in the bulk.⁸²

Table 3. 3 Fitting parameters of the bi-exponential decay function in TRPL spectra of the TAH incorporated perovskite excited at 375.2 and 636.2 nm (4 nJ/cm²), respectively.

Excitation wavelength (nm)	A ₁	τ_1 (ns)	A ₂	τ_2 (ns)	Average decay time ^a τ (ns)
375.2	0.55	4.58	0.47	267.43	125.70
636.2	0.07	22.89	0.91	369.54	344.78

^aAverage decay time is calculated according to the equation: $\tau = (A_1\tau_1 + A_2\tau_2)/(A_1 + A_2)$.

Several measurements were carried out to verify the interaction between the zwitterionic moieties in TAH and charged defects in the perovskite. We first conducted X-ray photoelectron spectroscopy (XPS) to investigate the coordinate interaction. Figure 3. 19 shows the typical XPS survey for the pristine and TAH-incorporated perovskites. In order to confirm whether there is a remnant of TAH in the annealed perovskite film, we examined the O 1s XPS spectra in these two samples. While negligible O 1s signal in the pristine perovskite, a prominent O 1s peak at 532.3 eV was detected in the TAH-incorporated perovskite, which confirmed the existence of TAH after thermal annealing. In addition, both the Pb 4f_{7/2} and Pb 4f_{5/2} peaks (at 138.7 and 143.6 eV, respectively) detected in the pristine perovskite are shifted to the direction with lower binding energy by ~0.3 eV in the 0.1 wt% TAH based perovskite (Figure 3. 15C). Such a negative shift of Pb 4f signal indicates the decreased cationic charge of under-coordinated Pb²⁺ within the perovskite, which is likely due to the donation of

lone pair electrons within the sulfonate groups (SO_3^-) in TAH through the coordinate interaction.^{83,84}

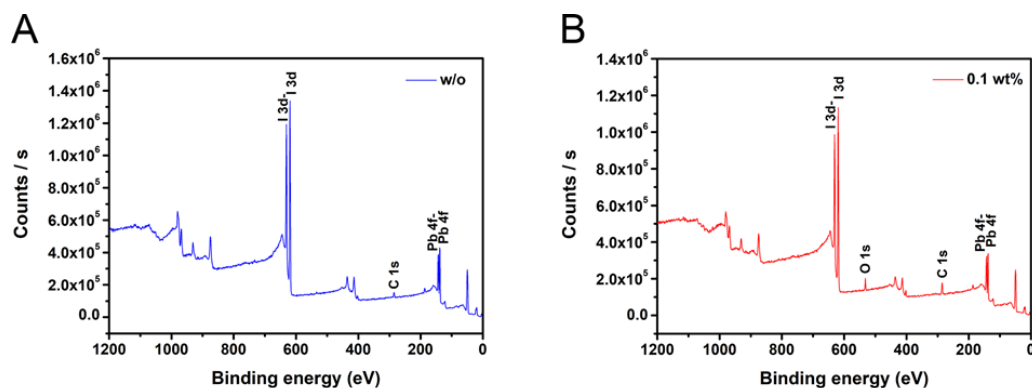


Figure 3. 19 XPS survey for (A) the pristine and (B) 0.1 wt% TAH incorporated perovskites.

Fourier transform infrared spectroscopy (FTIR) was also performed to confirm this interaction between sulfonate zwitterion and under-coordinated Pb^{2+} in the annealed perovskite films, as shown in Figure 3. 15E. The FTIR spectrum for the pure TAH film shows two peaks at ~ 1035 and 1184 cm^{-1} , representing the symmetric and asymmetric stretching vibrations of $\text{S}=\text{O}$ (ν_s and ν_{as}) in SO_3^- .⁸⁵ These two peaks shift to a higher wavenumber of ~ 1045 and 1190 cm^{-1} , respectively, when TAH is incorporated into the perovskite. In comparison, these vibration signals of $\text{S}=\text{O}$ cannot be detected in the pristine perovskite, indicating the volatility of DMSO during the annealing process. The increased wavenumber of $\text{S}=\text{O}$ stretching vibration stems from the decreased spatial symmetry of SO_3^- in TAH after coordinating interaction with under-coordinated Pb^{2+} . Thus, the symmetric and asymmetric stretching vibrations become harder. This result indicates the coordination between sulfonate groups in TAH and under-coordinated Pb^{2+} in the perovskite even after the thermal annealing, confirming its strong capability to passivate charged defects at perovskite surface and GBs.

Space charge limited current (SCLC) analysis based on electron-only devices with the structure of ITO/ SnO_2 /PVSK/ PC_{61}BM /Au was carried out to estimate the electron trap density (N_t) and electron mobility (μ_e), respectively, in different regimes, as shown

in Figure 3. 15F. The trap-filled limit voltage (V_{TFL}) determined as the onset voltage of the TFL regime ($n > 3$) can be used to calculate N_t with the equation:

$$N_t = \frac{2\varepsilon_0\varepsilon_r V_{TFL}}{qL^2} \quad (3.5)$$

In which ε_0 is the vacuum permittivity, ε_r is the relative permittivity of perovskite, which can be taken as the value of 18 for MAPbI₃ from previous work,⁸⁶ and L is the thickness of the perovskite film. Compared with the pristine perovskite ($N_t = 1.28 \times 10^{16} \text{ cm}^{-3}$), TAH-incorporated perovskite film has a relatively lower trap density ($N_t = 0.94 \times 10^{16} \text{ cm}^{-3}$), which confirms TAH's efficient passivation of charged defects at perovskite surface and GBs. Charge transport property in the perovskite films incorporated with TAH can also be estimated in the trap-free regime ($n = 2$) with the equation:⁸⁷

$$J = \frac{9\mu_e\varepsilon_0\varepsilon_r V^2}{8L^3} \quad (3.6)$$

Compared with the pristine perovskite $\mu_e = 2.2 \times 10^{-2} \text{ cm}^2 \text{ V}^{-1} \text{ s}^{-1}$, TAH-incorporated perovskite exhibits higher electron mobility of $3.9 \times 10^{-2} \text{ cm}^2 \text{ V}^{-1} \text{ s}^{-1}$ in the vertical direction, mainly due to the significantly improved film quality with higher crystallinity and relatively preferential out-of-plane orientation.

3.2.4 Photovoltaic Device Performance

We fabricated inverted p-i-n PSCs through a meniscus-guided blade coating technique using the perovskite ink incorporated with zwitterionic surfactant TAH. The inverted PSCs are assembled with the structure of ITO/PTAA/TAH-MAPbI₃/PC₆₁BM/bathophenanthroline (BCP)/Ag, where a ~400 nm thick uniform and pinhole-free perovskite film is sandwiched between PTAA HTL and PC₆₁BM electron transport layer (ETL). (

Figure 3. 20A).

Figure 3. 20B shows the schematic energy level diagrams of corresponding components in the p-i-n PSCs, which are calculated from ultraviolet photoelectron spectra (UPS), as shown in

Figure 3. 21. Band structure parameters are also summarized in Table 3.4. Compared with the pristine perovskite, the work function, HOMO, and LUMO energy levels of TAH-based perovskite are shifted up to 0.09, 0.12, and 0.12 eV, respectively, which might be attributed to the formation of interfacial dipole induced by TAH at the upper surface of perovskite (Figure 3. 22).

The photovoltaic parameters of MAPbI₃-based perovskite incorporated with different amounts of TAH are summarized in Table 3. 5. With the increase of TAH concentration from 0 to 0.2 wt%, the V_{OC} is significantly and monotonically enhanced from 1.067 V to 1.131 V. This clearly shows the TAH's excellent capability to passivate charged defects at perovskite surface and GBs. The short-circuit current density (J_{SC}) and fill factor (FF) begin to drop when more (0.2 wt%) TAH is incorporated, which indicates the devices with excess TAH start to suffer from inferior charge extraction and transport due to the extra alkyl chain assembled at the surface and GBs of perovskite films (Figure 3. 23A). This is not a drawback, as 0.1 wt% TAH already enables high-quality coating of perovskite films. Figure 3. 23A shows the J - V curves of the champion devices with and without TAH. An anti-reflection (AR)MgF₂ film is deposited on the incident side of the ITO/glass substrate to improve the transmittance of substrates (Figure 3. 23B). The control devices based on pristine MAPbI₃ show a maximum PCE of 19.34%, with a V_{OC} of 1.067 V, a J_{SC} of 23.27 mA/cm², and an FF of 77.90%.

In comparison, the devices incorporated with 0.1 wt% TAH in the ink exhibit the highest efficiency, with a maximum PCE up to 22.07%, an obviously enhanced V_{OC} of 1.126 V, a J_{SC} of 24.13 mA/cm², and an FF of 81.22%. The improved photovoltaic performance is mainly attributed to the high-quality perovskite films with high crystallinity and preferred orientation, as well as the efficient passivation of charged defects at both perovskite surface and GBs assisted with zwitterionic surfactant TAH. The integrated J_{SC} from external quantum efficiency (EQE) measurement for the control and TAH-based devices are 22.06 and 23.13 mA/cm², respectively (

Figure 3. 20D), which are consistent with those measured from $J-V$ curves.

Figure 3. 24 A and B show the hysteresis behavior in $J-V$ curves for the PSCs with and without TAH under forward and reverse scanning, respectively. Generally, hysteresis is ascribed to the interfacial capacitance, which originates from unbalanced charge extraction, high density of trap states at the perovskite surface, and ion migration. The TAH-based device shows negligible hysteresis in $J-V$ curves with a hysteresis index $((PCE_{\text{Reverse}} - PCE_{\text{Forward}})/PCE_{\text{Reverse}})$ of barely 0.4%, which is lower than that of the control device (2.1%). The elimination of the hysteresis effect is mainly attributed to the efficient passivation of charged defects at perovskite surface and GBs. Figure 3. 24C shows the steady-state photocurrent outputs and stabilized PCEs for the devices with and without TAH, which are measured under their maximum power points (MPPs). The TAH-based device exhibits a stabilized photocurrent of 22.86 mA/cm² at 0.96 V bias, with a stabilized efficiency of 21.95%, which is consistent with the efficiency from the $J-V$ curves. The control device exhibits a relatively lower stabilized photocurrent of 21.31 mA/cm² at 0.90 V bias, with a stabilized efficiency of 19.18%.

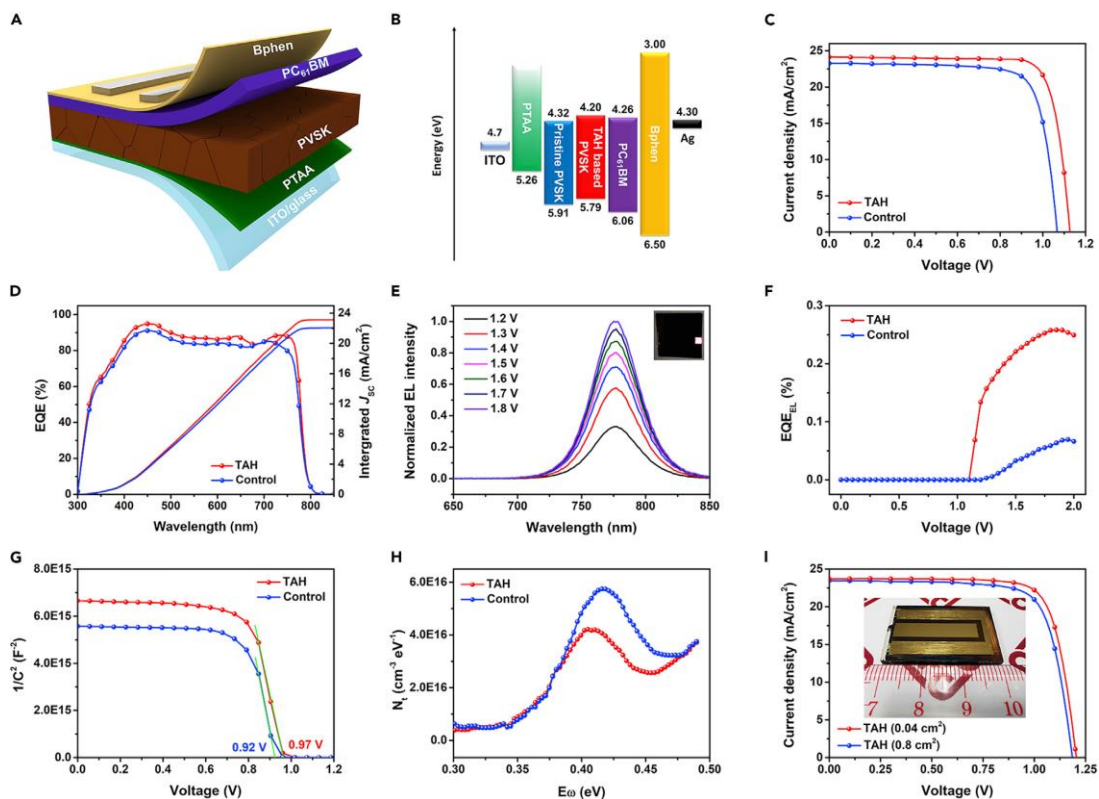


Figure 3. 20 Perovskite Solar Cells Performance. (A) Schematic device architecture of the inverted p-i-n PSCs. (B) Energy-level diagrams of corresponding components in the inverted p-i-n PSCs. (C) J-V curves of the best-performance control and TAH-based devices with p-i-n structure. (D) EQE spectra and integrated JSC values for the control and TAH-based devices. (E) EL spectra for the TAH-based device under voltage bias from 1.2 to 1.8 V. Inset: a photograph showing a TAH-based PSC operating as an LED (active area: 0.04 cm²) with visible red emission. (F) EQEEL as a function of the applied voltage bias for the control and TAH-based PSCs operating as LEDs. (G) Mott-Schottky plots in the control and TAH-based devices. (H) Nt distribution as a function of defect energy level E_d for the control and TAH-based devices, as measured in the TAS method. (I) J-V curves of the best-performance TAH-based PSCs with 0.04 and 0.8 cm² active area in the conventional n-i-p structure. Inset: a photograph showing a 0.8 cm² device.

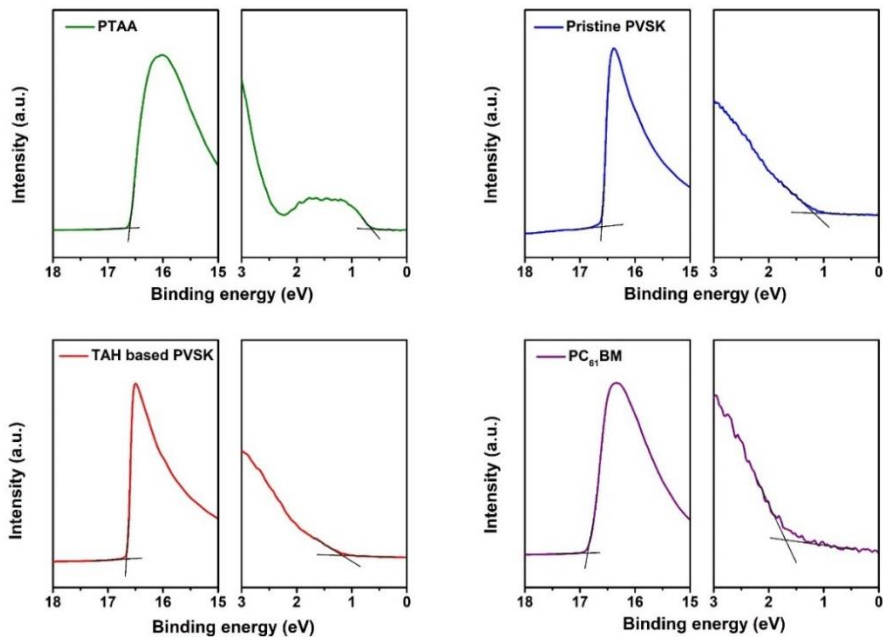


Figure 3. 21 UPS spectra of PTAA, pristine MAPbI₃, TAH based MAPbI₃ and PC₆₁BM respectively.

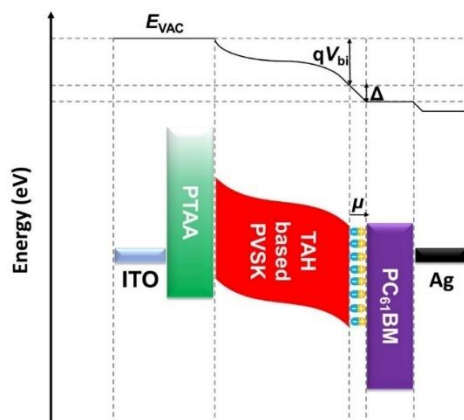


Figure 3. 22 Energy band structure of a complete p-i-n structured PSCs under short-circuit condition and vacuum level offset due to the interfacial dipole.

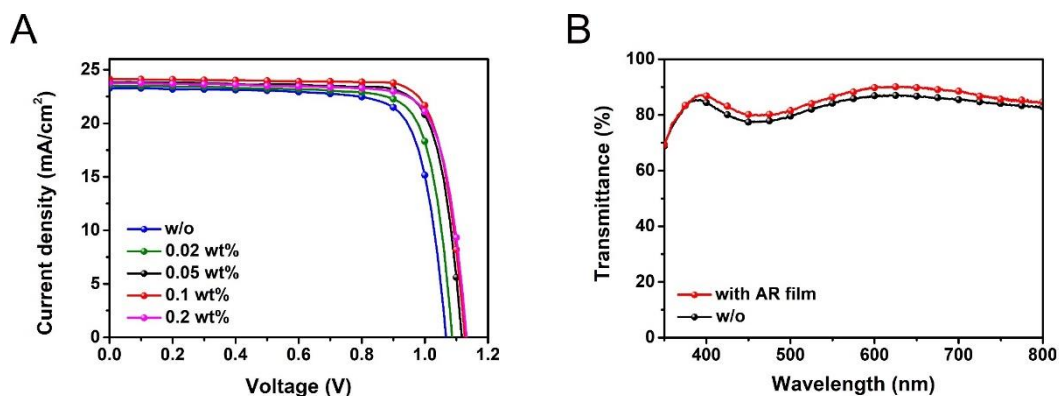


Figure 3. 23 (A) J-V curves of the best-performance TAH-based devices under different concentrations. (B) Transmittance of ITO/glass substrates with and without AR film.

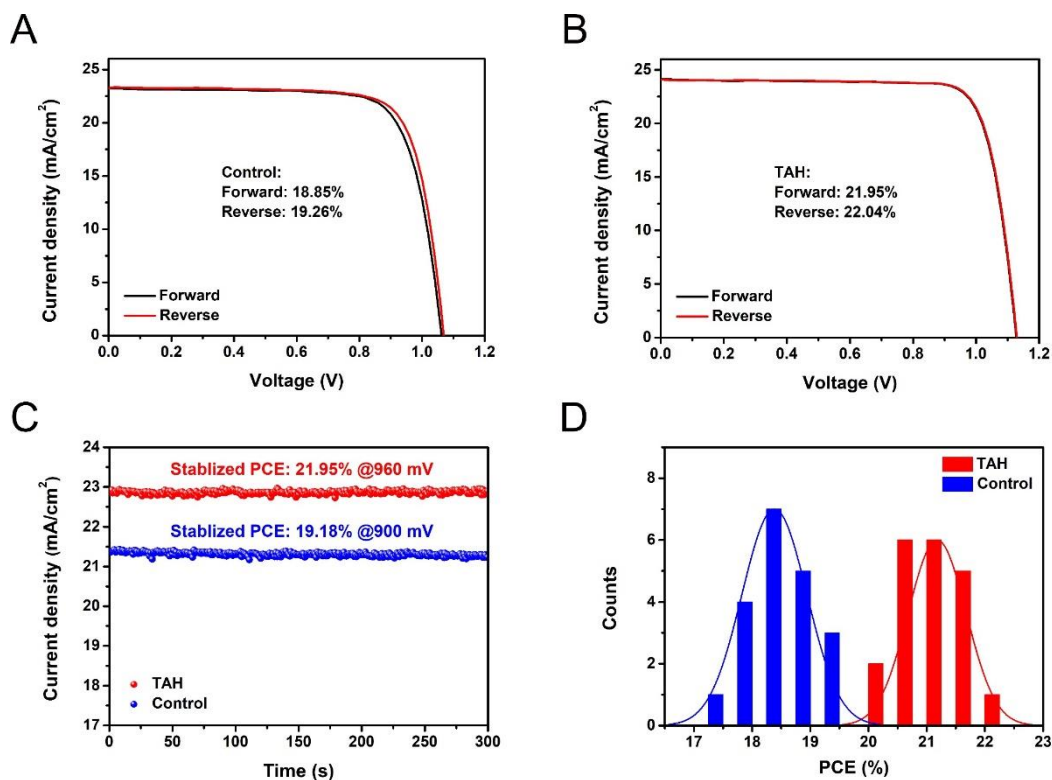


Figure 3. 24 Hysteresis effect in J-V curves under different scanning directions for the representative (A) control and (B) TAH based device. (C) Steady-state photocurrent outputs and stabilized PCEs under MPP for the control and TAH based devices. (D) PCEs histogram of 20 control and TAH based devices.

Table 3. 4 Band structure of PTAA, pristine MAPbI₃, TAH-based MAPbI₃, and PC₆₁BM

Materials	Bandgap (eV)	$E_{\text{cut-off}}$ (eV)	$E_{\text{edge-on}}$ (eV)	Work function (eV)	HOMO energy level (eV)	LUMO ^a energy level (eV)
PTAA	3.30	16.60	0.64	-4.62	-5.26	-1.96
Pristine MAPbI ₃	1.59	16.52	1.21	-4.70	-5.91	-4.32
TAH based MAPbI ₃	1.59	16.61	1.18	-4.61	-5.79	-4.20
PC ₆₁ BM	1.80	16.86	1.70	-4.36	-6.06	-4.26

^aLUMO energy level is calculated from HOMO and optical bandgap.

Table 3. 5 Photovoltaic parameters of the blade-coated inverted p-i-n PSCs incorporated with different amounts of TAH.

TAH concentration (wt%)	V_{OC} (V)	J_{SC} (mA cm ⁻²)	FF (%)	PCE (%)	
				Average ^a	Best
w/o	1.067	23.27	77.90	18.38 ± 0.56	19.34
0.02	1.088	23.52	79.12	19.48 ± 0.50	20.24
0.05	1.120	23.85	80.14	20.57 ± 0.43	21.41
0.1	1.126	24.13	81.22	21.18 ± 0.50	22.07
0.2	1.131	23.74	79.33	20.52 ± 0.37	21.30

^a.Average value and standard deviation are calculated from 20 devices.

To understand the mechanism behind the significantly improved V_{OC} in the TAH-based devices, we measured the external quantum efficiency of electroluminescence (EQE_{EEL}) for a complete PSC operating as a light-emitting diode (LED) in forward voltage bias, which has been extensively utilized to estimate the V_{OC} deficit.⁸⁸ For the purpose of evaluating V_{OC} , the EQE_{EEL} is measured when the injection current (dark recombination current) equals the J_{SC} under simulated 1-sun illumination. A large

EQE_{EL} indicates a large ratio of injection current, resulting in photoemission, suggesting low non-radiative recombination. The theoretical radiative limit of V_{OC} ($V_{\text{OC,rad}}$) can be calculated from the reciprocity relation between the photovoltaic external quantum efficiency (EQE_{PV}) and EQE_{EL} according to equation 3.7:^{89,90}

$$V_{\text{OC,rad}} = \frac{k_{\text{B}}T}{q} \ln \left(\frac{\int \text{EQE}_{\text{PV}}(E) \times \phi_{\text{AM1.5}}(E) dE}{\int \text{EQE}_{\text{PV}}(E) \times \phi_{\text{BB}}(E) dE} + 1 \right) = \frac{k_{\text{B}}T}{q} \ln \left(\frac{J_{\text{SC}}}{J_0^{\text{rad}}} + 1 \right) \quad (3.7)$$

In which $\phi_{\text{AM1.5}}$ and ϕ_{BB} refer to the solar AM 1.5 spectrum and the black-body radiation spectrum at 300 K, respectively, and J_0^{rad} refers to the radiative emission photocurrent density in the dark. Following the detailed balance model, $V_{\text{OC,rad}}$ has been calculated to be 1.30 V for MAPbI_3 with a bandgap of 1.59 eV.⁹¹ In a real PSC, additional non-radiative recombination loss should be considered according to the equation 3.8^{26,92}

$$V_{\text{OC}} = V_{\text{OC,rad}} - \Delta V_{\text{OC,nr}} = V_{\text{OC,rad}} + \frac{k_{\text{B}}T}{q} \ln \text{EQE}_{\text{EL}} \quad (3.8)$$

In which $\Delta V_{\text{OC,nr}}$ refers to the non-radiative recombination loss, and EQE_{EL} refers to the external quantum efficiency of electroluminescence under an injection current density equal to J_{SC} . As shown in

Figure 3. 20E and F, we tested the control and TAH-based PSCs operating as LEDs under voltage bias from 0 to 2 V. The TAH-based device starts to work under 1.1 V voltage bias. It shows an EQE_{EL} of 0.14% at a driving current equal to the J_{SC} (Figure 3. 25), corresponding to a $\Delta V_{\text{OC,nr}}$ of 170 mV. The calculated V_{OC} in the TAH-based device (1.13 V) agrees well with the V_{OC} measured in the J - V curve (~ 1.13 V). In comparison, the control device shows a much lower EQE_{EL} of 0.0044% at a driving current equal to the J_{SC} , corresponding to a much higher $\Delta V_{\text{OC,nr}}$ of 260 mV. This result indicates that non-radiative recombination in the TAH-incorporated perovskite has been

significantly suppressed mainly because of its strong coordinate interaction with the charged defects.

Mott-Schottky (M-S) analysis was carried out to estimate the V_{bi} of the control and TAH-based devices, as shown in

Figure 3. 20G. The relationship between the junction capacitance and DC voltage bias can be described by the equation 3.9:⁹³

$$\frac{A^2}{C^2} = \frac{2(V_{bi} - V)}{q\varepsilon_0\varepsilon N} \quad (3.9)$$

In which A is the active area of the device, q is the elementary charge, ε_0 and ε refer to vacuum and relative permittivity, respectively, N refers to the impurity doping density, and V refers to the applied DC voltage. V_{bi} can be calculated using the intercept of the linear regime of the M-S plot with the x-axis. The fitting result shows a larger V_{bi} for the TAH-based device (0.97 V) compared with the control device (0.92 V), which follows a trend similar to the V_{OC} measured in the J - V curves. In TAH-incorporated perovskite, TAH prefers to anchor at the upper surface of perovskite, which induces the formation of the interfacial dipole with its negative moieties (SO_3^-) towards perovskite and positive moieties (NH_4^+) towards outside. This dipole is aligned with the direction of the built-in field in PSCs. The superposition of the built-in field and the interfacial dipole leads to a greater local electric area, which enhances the V_{bi} (Figure 3. 26).⁹⁴

The NH_4^+ (ammonium) cation in the TAH zwitterion plays a critical role in enhancing its interaction with perovskite materials. This cation contributes significantly to surface passivation by interacting with negatively charged defect sites, such as halide vacancies, thereby reducing surface defects and suppressing non-radiative recombination. Consequently, these interactions improve the electronic properties of the film. Additionally, The zwitterionic nature of TAH, characterized by NH_4^+ as the positively charged group and sulfonate (SO_3^-) as the negatively charged group, facilitates self-assembly on the perovskite surface. The NH_4^+ anchors the TAH molecule to the surface, while the hydrophobic alkyl chain extends outward, forming a moisture

barrier that protects the perovskite from degradation in humid conditions. Furthermore, the interaction between NH_4^+ and perovskite ions stabilizes the crystal structure during formation, leading to better film morphology and more uniform crystallization. In summary, NH_4^+ in TAH is crucial for defect passivation, moisture resistance, and stabilization of perovskite films.

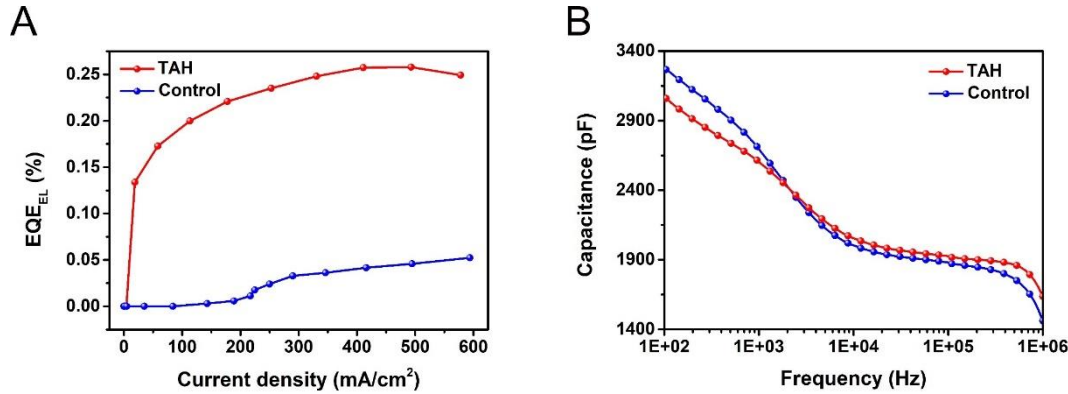


Figure 3. 25 (A) EQE_{EL} as a function of the driving current density for the control and TAH-based PSCs when operating as LEDs. (B) Capacitance spectra as a function of AC frequency for the control and TAH-based devices..

We further quantitatively estimated the energetic distribution of trap density (N_t) using temperature-dependent admittance spectroscopy (TAS) combined with Mott-Schottky analysis.^{95,96} Figure 3. 26B displays the capacitance spectra as a function of AC frequency for the control and TAH-based devices, applied by an AC voltage of 50 mV with a frequency decrease from 10^6 to 100 Hz (Note 3. 3). As shown in

Figure 3. 20H, for the control devices, the energetic trap density distribution peak is $5.74 \times 10^{16} \text{ cm}^{-3} \text{ eV}^{-1}$ centered at the energy depth of 0.42 eV, while that of the TAH-based devices is reduced to $4.21 \times 10^{16} \text{ cm}^{-3} \text{ eV}^{-1}$ located at 0.40 eV. The energetic distribution of trap states can be fitted by Gaussian distribution, and the integrated N_t for the control devices is calculated to be $6.83 \times 10^{15} \text{ cm}^{-3}$, which is 1.27 times larger than that of the TAH based devices ($5.36 \times 10^{15} \text{ cm}^{-3}$). TAS result suggests that deep trap states at the surface of pristine perovskite are efficiently suppressed with the incorporation of TAH in the perovskite ink.

Note 3. 3 Temperature-dependent admittance spectroscopy analysis.

Thermal-dependent admittance spectroscopy (TAS) is a well-established and effective technique to quantitatively characterize both shallow and deep defects, which has been widely applied for understanding defects in organic solar cells and PSCs. The energy level of trap states can be derived using the equation 3.10:

$$\omega_0 = \beta T^2 \exp\left(\frac{-E_a}{k_B T}\right) \quad (3.10)$$

In which ω_0 is the characteristic transition (attempt to escape) angular frequency, β is a temperature-independent parameter, E_a is the defect activation energy, k_B is the Boltzmann constant, and T is temperature. The derivative of the capacitance spectra can be used to define ω_0 . According to this equation, the value of E_a and β can be determined through the Arrhenius plot of characteristic angular frequency.⁹⁷ The energetic profile of trap density of states (N_t) can be derived from the angular frequency-dependent capacitance according to the equation:3.11:

$$N_t(E_\omega) = -\frac{V_{bi}}{eW} \frac{dC}{d\omega} \frac{\omega}{k_B T} \quad (3.11)$$

In which V_{bi} is the built-in potential, W is the depletion width, C is the capacitance, and ω is the applied angular frequency. In the case of PSCs, the demarcation energy E_ω can be determined by the applied angular frequency through the equation 3.12:

$$E_\omega = k_B T \ln\left(\frac{\beta T^2}{\omega}\right) \quad (3.12)$$

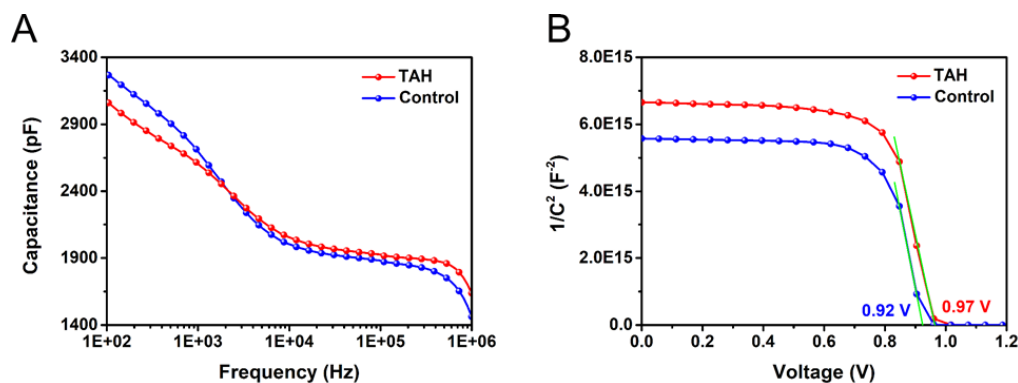


Figure 3. 26 (A) Capacitance spectra as a function of AC frequency for the control and TAH-based devices. (B) Mott–Schottky plots for the corresponding devices.

In order to examine the universality of additive engineering using TAH zwitterionic surfactant in the meniscus coating of different types of PSCs, we investigated the mixed triple-cation perovskite (CsFAMA) system in the conventional n-i-p architecture. Figure 3. 27 and Table 3. 6 show the J - V curves and photovoltaic parameters of the best-performing control and TAH-based devices with conventional n-i-p planar structure of FTO/SnO₂/TAH-PVSK/Spiro-OMeTAD/Au. Compared with the control devices, 0.1 wt% TAH-based devices exhibit superior photovoltaic performance with simultaneous increases in V_{OC} , J_{SC} , and FF, yielding a maximum PCE of up to 22.20%. This significant improvement is coincident well with the trend in inverted p-i-n devices. It should be noted that a very high V_{OC} of up to 1.205 V is obtained for the TAH-based devices, corresponding to a small V_{OC} deficit of 0.405 V for ~1.61 eV bandgap of triple-cation mixed perovskite. Large-area PSCs are crucial for the development of low-cost perovskite modules. We also blade-coated perovskite films in relatively large areas with a dimension of 3 cm × 2 cm (

Figure 3. 20) and built the conventional architecture PSCs with enlarged active area from 0.04 to 0.8 cm².

Figure 3. 20I displays the J - V curves of the champion TAH incorporated PSCs with 0.8 cm² active area, which shows a superior PCE of 21.02% and a stabilized PCE of 20.93% under MPP of 0.98 V (Table 3. 6 and Figure 3. 27).

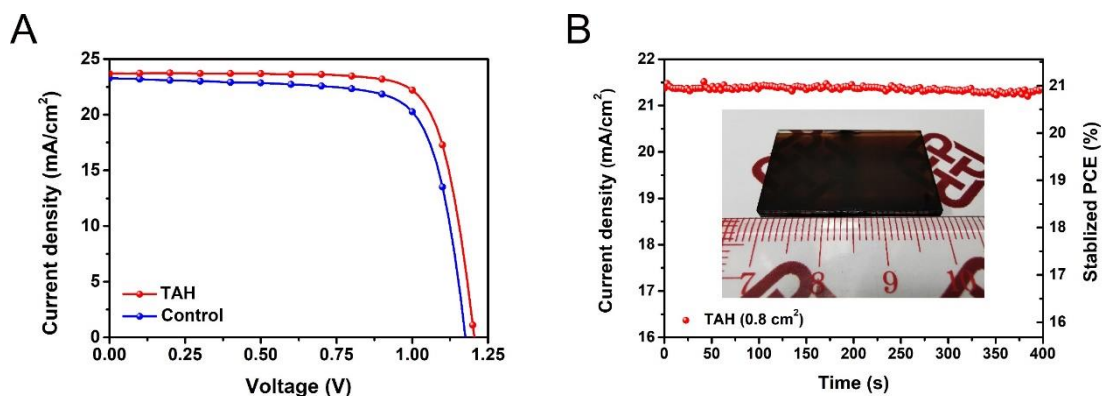


Figure 3. 27 (A) J - V curves of the best-performance control and TAH-based devices in conventional n-i-p architecture (0.04 cm^2 active area). (B) Steady-state photocurrent output and stabilized PCE under MPP at 0.98 V bias for the TAH-based n-i-p device (0.8 cm^2 active area). Inset: photograph of a blade-coated perovskite film on an FTO substrate with a $3 \text{ cm} \times 2 \text{ cm}$ dimension.

Table 3. 6 Photovoltaic parameters of the blade-coated PSCs in conventional n-i-p structure.

Condition (active area)	V_{OC} (V)	J_{SC}^a (mA cm^{-2})	FF (%)	PCE (%)	
				Average ^b	Best
w/o (0.04 cm^2)	1.175	23.28	74.06	19.60 ± 0.42	20.26
0.1 wt% TAH (0.04 cm^2)	1.205	23.68	77.79	21.46 ± 0.47	22.20
0.1 wt% TAH (0.8 cm^2)	1.186	23.45	75.59	19.88 ± 0.65	21.02

^aAR MgF₂ films are deposited on the incident side of the ITO/glass substrate.

^bAverage value and standard deviation are calculated from 10 devices.

We summarized the state-of-the-art PCEs as a function of processing temperature for the deposition of perovskite photovoltaic films through different scalable printing techniques published in the previous works, as shown in Figure 3. 28; Table 3. 7. It is worth noting that this work (red star, RT coating) reaches one of the highest records for the upscaling coated PSCs (substrate temperature from RT to 150°C), not limited to RT-coated ones. Compared with our previous work (red dot), here we focus on the perovskite ink multifunctional formulation and achieve a significant increase of PCEs from 20% to over 22%.⁴⁶ As far as we know, this work is also among the top performances for the MAPbI₃-based PSCs, regardless of the deposition methods. This result suggests an efficient and universal additive strategy using TAH zwitterionic

surfactant in the RT meniscus coating of perovskite films for both the inverted and conventional structured devices in relatively large areas.

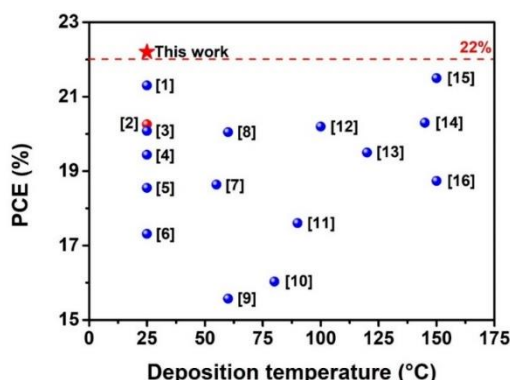


Figure 3. 28 State-of-the-art PCEs of the upscaling coated PSCs under different deposition temperatures summarized from previous works.

Table 3. 7 State-of-the-art PCEs of the upscaling coated PSCs under different deposition temperatures summarized from previous works.

Reference	PCE (%)	Deposition temperature (°C)	Active area (cm ²)	Deposition technique
This work	22.20	25	0.04	Doctor blading
	21.02		0.8	
52	21.30	25	0.08	Doctor blading
	16.40		63.7	
46	20.26	25	0.06	Doctor blading
	18.76		1	
47	20.08	25	0.09	Air blading
	19.12		1	
98	19.44	25	0.12	Doctor blading
	13.85		16	
29	18.55	25	0.12	Doctor blading
	17.33		1.2	

99	17.31	25	0.15	Slot-die coating
100	18.64	55	0.04	Inkjet printing
	17.74		2.02	
48	20.05	60	0.1	Doctor blading
101	15.57	60	0.1	Slot-die coating
102	16.03	60-80	0.1	Ultrasonic spray
	13.09		1	
103	17.60	90	1	Soft-cover deposition
58	20.20	100	0.08	Doctor blading
104	19.50	120	NA	Doctor blading
59	20.30	145	0.075	Doctor blading
	15.30		33	
53	21.50	150	0.08	Doctor blading
	20.00		1.1	
50	18.74	150	0.09	Doctor blading
	17.06		1	

3.2.5 Water-Resistant Perovskite Films and Device Stability

Organic-inorganic halide perovskites are highly sensitive to moisture and can be decomposed readily in high-humidity environments. In order to examine the water-resistant performance of perovskite with the TAH strategy, we first measured the static water contact angles on the surface of pristine and 0.1 wt% TAH incorporated perovskite (Figure 3. 29). TAH-incorporated perovskite surface exhibits a relatively larger water contact angle (42.6°) compared with that on the pristine perovskite (33.9°). The dynamic dissolving process of water droplets on the surface of these two perovskites was also recorded, as shown in Figure 3. 30A. When contacted with a water droplet, the pristine perovskite is immediately decomposed to PbI_2 , while the TAH-incorporated perovskite film surface becomes much more water-resistant. Considering the amphipathic nature of TAH molecules, this result indicates that TAH molecules prefer to self-assemble on the upper surface of perovskite with the hydrophobic alkyl chains intertwining, inducing the formation of a waterproof barrier and facilitating inner encapsulation.¹⁰⁵

This agrees with the GIWAXS result. The moisture stability of the pristine and TAH-incorporated perovskite films was studied by exposing them to a relatively high RH of $60 \pm 10\%$ at $25 \pm 5^\circ\text{C}$ for 14 days. The evolution of the perovskite phase was tracked by XRD, as shown in Figure 3. 29. For the pristine perovskite, the XRD pattern appears with two prominent peaks at 8.5° and 10.5° after 14 days of aging, which can be assigned to a perovskite hydrate $(\text{CH}_3\text{NH}_3)_4\text{PbI}_6 \cdot 2\text{H}_2\text{O}$. This hydrate is a pale yellow crystalline solid, and it has been suggested that the transition from MAPbI_3 to $(\text{CH}_3\text{NH}_3)_4\text{PbI}_6 \cdot 2\text{H}_2\text{O}$ hydrate occurs readily upon exposure to humid air.¹⁰⁶ The intensity of the PbI_2 diffraction peak at 12.6° also increases in the pristine perovskite, suggesting apparent decomposition into PbI_2 . In comparison, the diffraction pattern of TAH-incorporated perovskite is almost identical after exposure to high RH over 14 days, and only a trace amount of perovskite hydrate can be detected. The superior moisture stability of TAH-based perovskite is mainly attributed to the self-assembly and intertwining of hydrophobic alkyl chains at the perovskite upper surface.

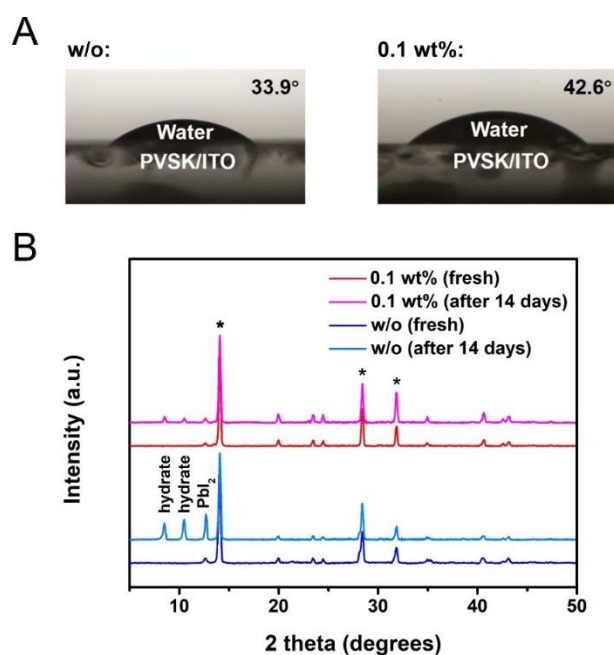


Figure 3. 29 (A) Contact angles of the water droplet on the surface of pristine and TAH-based perovskite films. (B) Evolution of the perovskite phase for the pristine and TAH-incorporated perovskite films exposed under 25 ± 5 °C and $60 \pm 10\%$ RH for over 14 days.

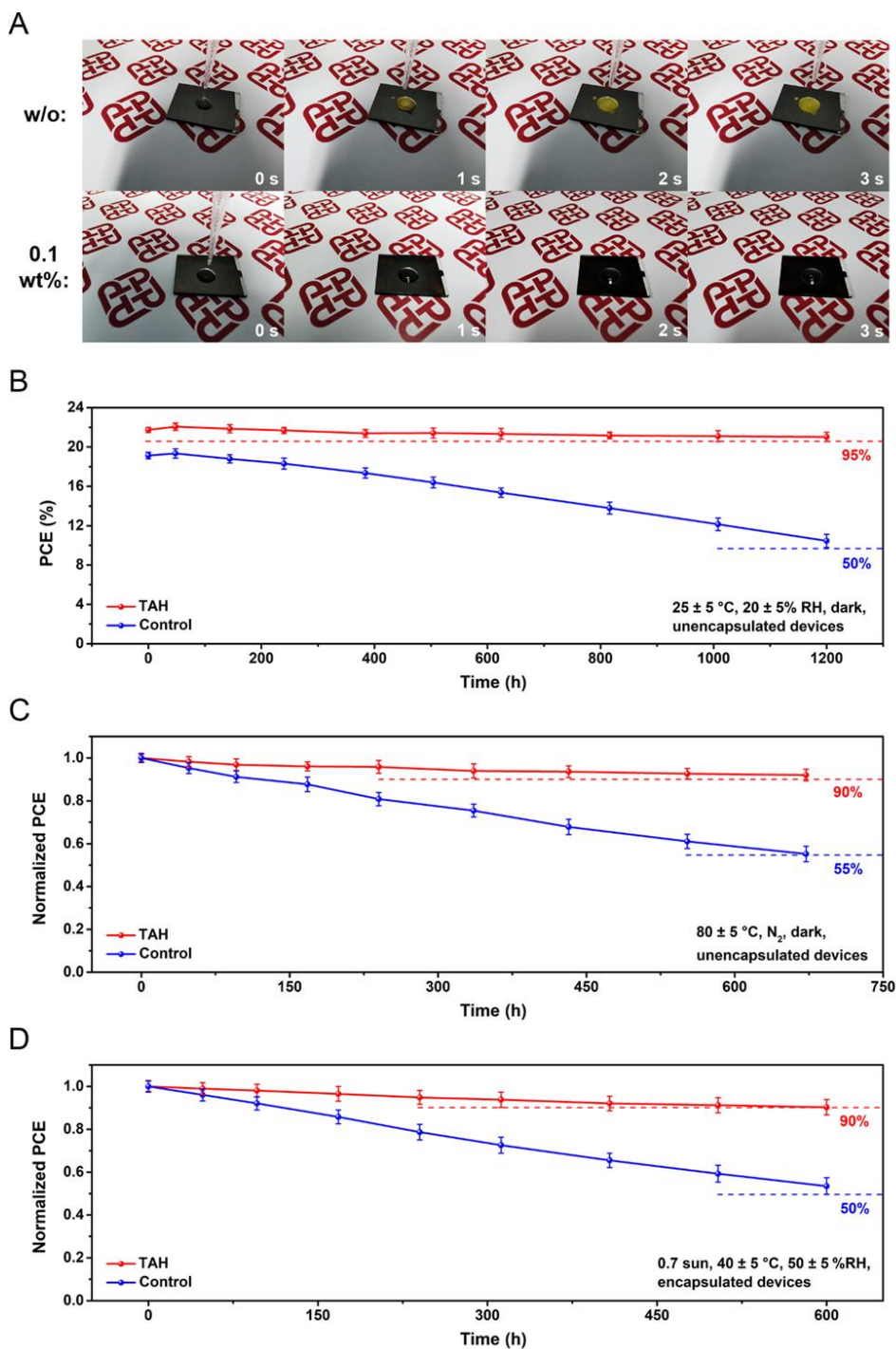


Figure 3. 30 Water-Resistant Perovskite Films and Device Stability. (A) Dynamic dissolving process of a water droplet on the surface of pristine and TAH-incorporated perovskite films. (B) Ambient stability of the unencapsulated devices shelved under $25^{\circ}\text{C} \pm 5^{\circ}\text{C}$ and $20\% \pm 5\% \text{RH}$. Data were represented as the mean value and the standard deviation from 10 samples in each condition. (C) Thermal stability of the unencapsulated devices at $80^{\circ}\text{C} \pm 5^{\circ}\text{C}$ in a nitrogen atmosphere. Data were represented as the mean value and the standard deviation from 5 samples in each condition. (D)

Light stability of the encapsulated devices exposed under continuous 0.7 sun illumination at $40^{\circ}\text{C} \pm 5^{\circ}\text{C}$ and $50\% \pm 5\%$ RH. Data were represented as the mean value and the standard deviation from 5 samples in each condition.

MAPbI₃ is the original but less stable perovskite composition in most high-efficiency PSCs. Inverted p-i-n structured MAPbI₃-based PSCs were used to evaluate the device stability with this multifunctional additive strategy. The ambient storage, thermal stressing, and light illumination stability of the blade-coated devices were investigated in detail under different aging conditions, as shown in Figure 3. 30. The ambient stability of the unencapsulated devices was tracked under $25 \pm 5^{\circ}\text{C}$ and $20 \pm 5\%$ RH. TAH-based devices offer much better shelf stability, retaining an average PCE of over 21% (96.7% of initial PCE) after 1200 h. In comparison, the control devices only maintain an average PCE of 10.5% (54.7% of initial PCE) under the same condition. Thermal stability was recorded during the aging process of the control and TAH-based devices at 80°C in the glovebox. TAH-based devices display superior thermal stability, maintaining 92.0% of their initial value on average after 672 h aging, compared to only 55.2% for the control device. Light illumination stability of the encapsulated devices was also examined under continuous illumination at $40 \pm 5^{\circ}\text{C}$ and $50 \pm 5\%$ RH. After 600 h light soaking under 0.7 sun, TAH-based devices keep an average of 90.3% of their initial efficiency, which is much higher than the control devices (53.5%). Since the charged defects at the perovskite surface and GBs are one of the main reasons for the accelerated deterioration in moisture, the enhanced stability of TAH-based devices under different aging conditions is mainly attributed to the efficient defects passivation as well as the robust, water-resistant barrier at perovskite surface with the assist of TAH strategy.

3.3 Conclusion

In summary, we have demonstrated a facile multifunctional zwitterionic surfactant strategy incorporated into the perovskite ink, successfully enabling room-temperature

meniscus coating of high-quality perovskite photovoltaic films. TAH facilitates dense perovskite films with full coverage, modulates perovskite crystallization and orientation, neutralizes charged defects, and self-assembles a waterproof barrier at the perovskite surface. The universality and versatility of this strategy not only enable the enhanced efficiencies of over 22% (0.04 cm² active area) and 21% (0.8 cm²) across perovskite compositions and device architectures but also promote the moisture, thermal, and light illumination stability simultaneously. Further understanding of the role of functionalized surfactants in the large-scale printing of perovskite polycrystalline films offers a new pathway towards scalable manufacture of perovskite-based optoelectronic devices with superior performance and stability.

3.4 Experimental Procedures

Materials

Unless stated otherwise, chemicals and solvents were obtained commercially and were used without further purification, including tetradecyl dimethyl (3-sulfopropyl) ammonium hydroxide inner salt (TAH) (Tokyo Chemical Industry, 98.0%), lead iodide (PbI₂) (TCI, 99.99%), methylammonium iodide (MAI) and methylammonium chloride (MACl) (Xi'an Polymer Light Technology Corp., 99.5%), poly[bis(4-phenyl)(2,4,6-trimethylphenyl)amine (PTAA) ($M_n \leq 6000$, Xi'an Polymer Light Technology Corp.), PC₆₁BM (99.5%, Solenne BV) and bathophenanthroline (BCP) (98%, Alfa Aesar). All solvents, including N, N-dimethylformamide (DMF) (99.8%, anhydrous), dimethyl sulfoxide (DMSO) (99.9%, anhydrous), chlorobenzene (99.8%, anhydrous), toluene (99.8%, anhydrous) and 2-propanol (99.5%, anhydrous) were purchased from Sigma-Aldrich.

Device Fabrication

Laser-patterned ITO/glass substrates (sheet resistance $\approx 12 \Omega$ per square) were pre-cleaned using an ultrasonicator and subjected to ultraviolet–ozone treatment for 20 min. For the inverted p-i-n structured PSCs, the PTAA hole transport layer (HTL) was spin-coated on the pre-cleaned ITO substrate using the PTAA solution (5 mg/mL in toluene) at 5000 rpm and annealed at 100 °C for 10 min. MAPbI₃-based perovskite precursor

solution was prepared with 1.15 M PbI_2 , 1.1 M MAI, and 0.05 M MAI dissolved in the mixture solvent of DMF and DMSO (9:1, v:v). We prepared the TAH's mother solution in the mixture solvent of DMF and DMSO (9:1, v:v, 20 mg/mL) and stirred it overnight. According to different concentrations of TAH in perovskite precursor solution (0, 0.02, 0.05, 0.1, and 0.2 wt%), we added 0, 16, 40, 80, and 160 μL of TAH mother solution into 1 mL perovskite precursor solution respectively and stirred the mixture solution for one h. A small droplet of perovskite ink (5 μL) was dripped on the substrate and swiped linearly by a film applicator at the speed of 10 mm/s. The gap between the blade coater and substrate was set as 100 μm . A laminar nitrogen knife was installed right next to the blade substrate with the flow parallel to the substrate. The as-prepared wet perovskite film was gas-quenched by the nitrogen knife with the fixed nitrogen blow rate of 40 m/s (calibrated using the Testo 416 flowmeter) in order to remove the extra precursor solution and induce the precipitate of perovskite intermediate adducts. The intermediate films were transferred onto a hotplate and annealed at 100 $^\circ\text{C}$ for 30 min. PC_{61}BM electron transport layer (ETL) was spin-coated on the top of perovskite film using PC_{61}BM solution (20 mg/mL in chlorobenzene). The inverted devices were finished by thermal evaporating an 80 nm thick Ag counter electrode under a 10^{-6} Torr pressure. For the conventional n-i-p structured PSCs, a thin layer of SnO_2 nanoparticles was spin-coated onto the pre-cleaned ITO substrate using a SnO_2 colloidal dispersion solution in water (5 wt%) at 5000 rpm and annealed at 150 $^\circ\text{C}$ for 30 min in ambient atmosphere. Mixed triple-cation (CsFAMA) perovskite precursor solution was prepared with 1.2 M PbI_2 , 1.1 M FAI, 0.2 M PbBr_2 , 0.2 M MABr, and 0.05 M CsI dissolved in the mixture solvent of DMF and DMSO (8:2, v:v). Spiro-OMeTAD HTL was spin-coated on the top of perovskite using its solution (80 mg/mL in chlorobenzene) with 29 μL of tBP and 17.5 μL of Li-TFSI (520 mg/mL in acetonitrile). Finally, thermal evaporation deposited an 80 nm thick Au electrode using a shadow mask to pattern the electrodes. We encapsulated the devices in the nitrogen glovebox. Epoxy resin AB glue (Super Glue Corp.) was used for device edge sealing with a cover glass. The devices were further dried at room temperature for 10 min to allow complete solidification of the AB glue.

Characterizations

The film morphology of the perovskite was examined using a high-resolution field emission SEM (JEOL JSM-6335F). AFM height images were obtained using a Bruker Multimode 8 scanning probe microscope (tapping mode). ToF-SIMS depth analysis was conducted using Model TOF-SIMS V, ION-TOF GmbH with pulsed primary ions from a Cs⁺ (3 keV) liquid-metal ion gun and a Bi⁺ pulsed primary ion beam for the analysis (25 keV). Crystalline structure was investigated on a Rigaku SmartLab X-ray diffractometer with Cu K α radiation in a step of 0.01° and θ -2 θ scan mode from 5° to 50°. GIWAXS was carried out using a Xeuss 2.0 SAXS/WAXS laboratory beamline with a Cu X-ray source (8.05 keV, 1.54 Å) and a Pilatus3R 300K detector. In-situ GIWAXS was conducted by a 23A minor- and wide-angle X-ray scattering beamline at the National Synchrotron Radiation Research Center (NSRRC), Hsinchu, Taiwan. The wavelength of the X-ray was kept at 1.239 Å (10 keV), and a C9728DK area detector collected the time-resolved scattering signals. The incident angle was kept at 2° to enhance the signal resolution with a frame exposure time of 1 s. The in-situ UV-vis absorption spectra were obtained using an F20-UVX spectrometer (Filmetrics, Inc.) equipped with tungsten halogen and deuterium light sources (Filmetrics, Inc.). UV-vis absorption spectra were measured by using a UV-vis spectrophotometer (CARY5000, Varian). Steady-state PL and TRPL transient decay spectra were measured using a PL spectrometer (Edinburgh Instruments, FLS920) with the excitation source of 636.2 nm picosecond pulsed diode laser (EPL-635, ~5 nJ/cm²) and detected at 780 nm. PLQYs were measured using a commercialized PLQY system (LQ-100, Enli Technology Co. Ltd., Taiwan), which consists of a 405 nm LED excitation source (0.65 mW/cm²), a polytetrafluoroethylene (PTFE) integrating sphere, a H-sCMOS 2048 multichannel spectrometer, and optical fibers. The integration time was set as 300 ms. FTIR spectra were measured with an attenuated total reflection (ATR) spectrometer (PerkinElmer Spectrum 100, USA) from 4000 to 400 cm⁻¹ with a resolution of 4 cm⁻¹. UPS and XPS measurement was carried out by a VG ESCLAB 220i-XL surface analysis system equipped with a monochromatic Al K X-ray source (1486.6 eV) in a vacuum of 3.0 × 10⁻⁸ Torr. J-V curves were obtained using a Keithley 2400 Source Meter under

standard AM 1.5 G illumination (Enli Technology Co. Ltd., Taiwan) and a standard KG-5 Si diode calibrated the light intensity for the completed devices. Both forward (from -0.2 to 1.2 V) and reverse scanning (from 1.2 to -0.2 V) were performed with a delay time of 100 ms. Small-area devices have an active area of 0.04 cm² confined by the crossed area of the counter electrode and ITO stripe. Relatively large-area devices have an active area of 0.8 cm². An anti-reflection (AR) MgF₂ film is deposited on the incident side of the ITO/glass substrate. EQE spectra were measured with a QE-R 3011 EQE system (Enli Technology Co. Ltd., Taiwan) using 100 Hz chopped monochromatic light ranging from 300 to 850 nm. The EL EQE spectra were recorded by an LED photoluminescence quantum yield measurement system (Enli Tech LQ-100) equipped with the Keithley 2400 Source Measure Unit. Mott–Schottky analysis was examined using a CHI660e electrochemical workstation at 100 kHz with the DC bias potential ranging from 0 to 1.3 V under dark conditions. Admittance spectra were obtained using an impedance analyzer (Hioki E. E. Corp., Model 3532-50 LCR HiTESTER). An AC modulation of an amplitude of 50 mV was superimposed at the frequency decreased from 103 to 0.1 kHz in the dark.

Chapter 4 Manipulating Crystallization Kinetics in High-Performance Blade-Coated Perovskite Solar Cells via Cosolvent-Assisted Phase Transition

4.1 Introduction

Photovoltaic (PV) technology directly converts solar energy into electricity, offering a clean, sustainable solution to overcome the challenge of ever-increasing global energy. In the past decade, solar cells based on organic–inorganic halide perovskites (OIHPs) have attracted increasing attention and have been regarded as the candidate for the third generation of PV technology due to their outstanding and tunable optoelectronic properties.^{11,23,24,107,108} Most importantly, the ionic nature of OIHPs provides good solubility in common polar aprotic solvents, which enables facile and versatile solution-processed coating techniques at low temperatures.^{17,29,31,109} The performance of laboratory-scale perovskite solar cells (PSCs) has made tremendous strides, reaching a certified power conversion efficiency (PCE) of up to 25.7%, which is comparable with crystalline silicon PV. It surpasses technologies like copper indium gallium selenide, cadmium telluride, and so on.¹¹⁰⁻¹¹³

In contrast to other conventional PV technologies, minimizing the PCE loss of PSCs remains challenging when scaling up the device area from cells to modules (CTM loss).^{33,114,115} Manipulating the perovskite solidification process, including nucleation and crystal growth, plays a critical role in controlling the film morphology and thus affects the resultant PV performance, especially over a large area.¹¹⁶⁻¹¹⁸ Blade coating has been demonstrated as a facile and effective printing-friendly technique for upscaling perovskite thin films and devices.^{41,42,119-121} Hot-casting has been widely involved during the blade coating process to accelerate the drying kinetics of perovskite inks. In contrast, the evaluated processing temperature induces the inherent Bénard–

Marangoni convection within the perovskite wet films, bringing potential energy-consuming concerns for future mass manufacture.^{60,122}

A solvent is a medium to dissolve the perovskite precursors. Its characteristics (e.g., boiling point, viscosity, vapor pressure, polarity, coordination ability) are directly linked to the film-forming process regardless of coating techniques. For the more desired upscaling methods processed at room temperature, concerning their intrinsic slow-drying kinetics, rapid removal of the solvent is the prerequisite to generating dense nuclei and promoting the homogeneity of perovskite films.^{46,52,123} On the other hand, using polar aprotic solvents with high toxicity (e.g., N, N-dimethylformamide, DMF) may also bring underlying problems to our environment and health.¹²⁴ Therefore, developing green and more volatile solvent systems is essential for the scale-up and future commercialization of PSCs.

Delicate control of the intermediate solvent-complex phases during the perovskite crystallization is critical to improving the crystal quality and eliminating defects.^{73,125} There have been observations of interesting residual-solvent-assisted mass transport/diffusion and reconstruction of perovskite precursor during the aging/ripening process of as-cast intermediate films across different perovskite compositions, which was shown to facilitate the formation of desired perovskite phase and optimal film morphology via ex-situ techniques.^{126,127} However, deep insights into the structural transformation that occurred in this magic transition process are missing so far. There is no in situ crystallization kinetics study to diagnose the whole perovskite phase-transition pathway and manipulate the balance between nucleation and grain growth rate, especially under room-temperature printing-friendly technique.^{74,128}

In this work, we demonstrated a facile and effective ethyl alcohol (EtOH) cosolvent (ECS) strategy by incorporating EtOH into perovskite ink for high-performance room-temperature blade-coated PSCs and modules. We systematically investigated the whole perovskite structural evolution and crystallization pathway using real-time X-ray scattering and UV-vis absorption techniques. We proved the incorporation of EtOH into the solvent system triggered rapid nucleation with dense perovskite/intermediate

nuclei and promoted the formation of an FA-based precursor solvate ($\text{FA}_2\text{PbBr}_4 \cdot \text{DMSO}$) during the trace-solvent-assisted transition (TSAT) process, which was confirmed by density functional theory (DFT) calculations. This exciting phase transition process was beneficial to manipulating the balance between nucleation and crystal growth to form a homogenous and compact perovskite film. In the blade-coated PSCs, this strategy effectively suppressed the nonradiative recombination and improved the PCE up to 22.51% (0.04 cm² device area) and 20.37% (0.98 cm²) in a 1.60 eV perovskite system. The remarkable performances are further validated in a 1.54 eV perovskite system with the enhanced PCE up to 23.19% (0.04 cm²), 21.04% (0.98 cm²) and 18.95% (2.7 cm², 3-subcells minimodules). A maximum V_{OC} of 1.205 V was achieved in this system, corresponding to the V_{OC} deficit as low as 335 mV, which agreed well with the measured nonradiative recombination loss ($\Delta V_{OC, nr}$, 77 mV) from external quantum efficiency of electroluminescence (EQE_{EL}). This result represents one of the highest records for the blade-coated PSCs in both small-area devices and minimodules. More importantly, this strategy significantly enhanced the device's stability under different aging conditions.

4.2 Results and Discussion

We dissolved the triple-cations perovskite precursors (CsFAMA) into the host DMF solvent. Lewis basic dimethyl sulfoxide (DMSO) was subsequently incorporated into the solution with a 1:1 molar ratio to the perovskite precursors. For the ECS approach, different ratios (0 to 40%, v:v) of EtOH were used to replace the host solvent of DMF (e.g., 9:1 means the volume ratio between DMF and EtOH is 9:1 unless stated otherwise). From 10:0 to 8:2, the mixed solvent can totally dissolve the perovskite precursor (Figure 4. 1). The meniscus-guided blade-coating technique was used to deposit perovskite thin films on the room-temperature substrate (Figure 4. 2A). A film applicator linearly swiped the small droplet of perovskite ink at the blading speed of 10 mm s⁻¹. It fell into the Landau–Levich region, which indicated the film was still wet after blading.^{129,130} A laminar nitrogen knife was installed right next to the blade substrate at an angle of 20° to the substrate. The as-prepared wet precursor film was

immediately gas-quenched by nitrogen blowing to partially remove the extra solvent and induce the nucleation of the perovskite/intermediate mixture. We first in situ studied the nucleation kinetics of perovskite ink during the gas-quenching process with time-resolved UV-vis absorption spectroscopy, as shown in Figure 4. 2B. For the pristine perovskite ink (10:0), the as-prepared film was still wet within the first ≈ 17 s of gas quenching with neglectable UV-vis absorption above 400 nm. The nucleation of perovskite/intermediates began at ≈ 17.6 s, along with the broadening of absorption spectra and the increase of their intensity. By contrast, for the ECS-based perovskite ink, the nucleation started earlier at 11.2 and 8.4 s for the 9:1 and 8:2 ink, respectively (Figure 4. 2C, D).

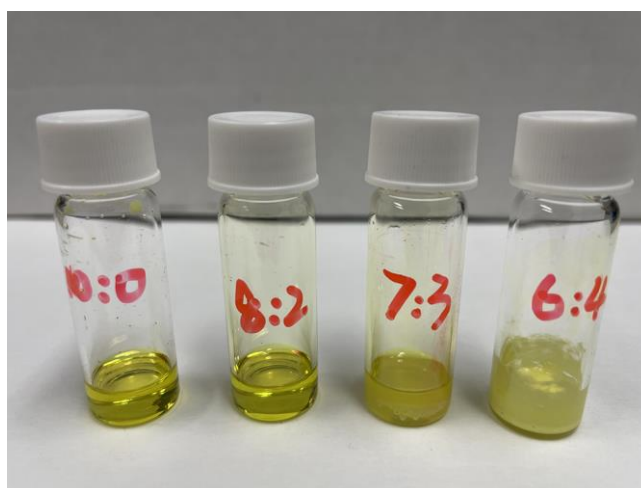


Figure 4. 1 Perovskite precursor ink in the mixed solvent system with different volume of DMF and EtOH (e.g., 8:2 means volume ratio of DMF/EtOH is 9:1)..

In the classical nucleation theory, the nucleation of particles is triggered by the supersaturation state of the precursor solution. The nucleation rate can be described by equation 4.1, in which N is the number of nuclei, A is the pre-exponential factor, k_B is the Boltzmann constant, N_A is Avogadro's number, S is the level of super-saturation, and T is the temperature.^{51,74} The nucleation rate is strongly dependent on the level of

supersaturation state, temperature, and surface free energy of ink. In our study, the vapor pressure of EtOH, DMF, and DMSO are 5.95, 0.36, and 0.06 kPa at 20 °C (Table 4. 1). According to Raoult's law,¹³¹ the vapor pressure of the 10:0, 9:1, and 8:2 mixed solvent systems were calculated to be 0.33, 0.99, and 1.61 kPa, respectively (see Note 4. 1 and Table 4. 2). Considering the identical nitrogen blowing speed (40 m s⁻¹), the higher vapor pressure of the mixed solvent system induced a faster nucleation rate, which was coincident with the result from the first derivative of UV-vis absorption intensity (Figure 4. 2D). As a result, the solvent engineering with EtOH triggered rapid precipitation of perovskite nanocrystals and intermediate complex, thus forming a high density of nuclei after gas quenching, which agreed well with the X-ray diffraction (XRD) patterns for the as-cast intermediate films (Figure 4. 3).

$$\frac{dN}{dt} = A \exp \left[- \frac{16\pi\gamma^3 V_m^2}{3k_B^3 T^3 N_A^2 (\ln S)^2} \right] \quad (4.1)$$

Table 4. 1 Summary of the related solvent properties.

Solvent	Vapor pressure at 20 °C [kPa]	Density [g/mL]	Molar mass [g/mol]
EtOH	5.95	0.79	46.07
DMF	0.36	0.95	73.10
DMSO	0.06	1.10	78.73

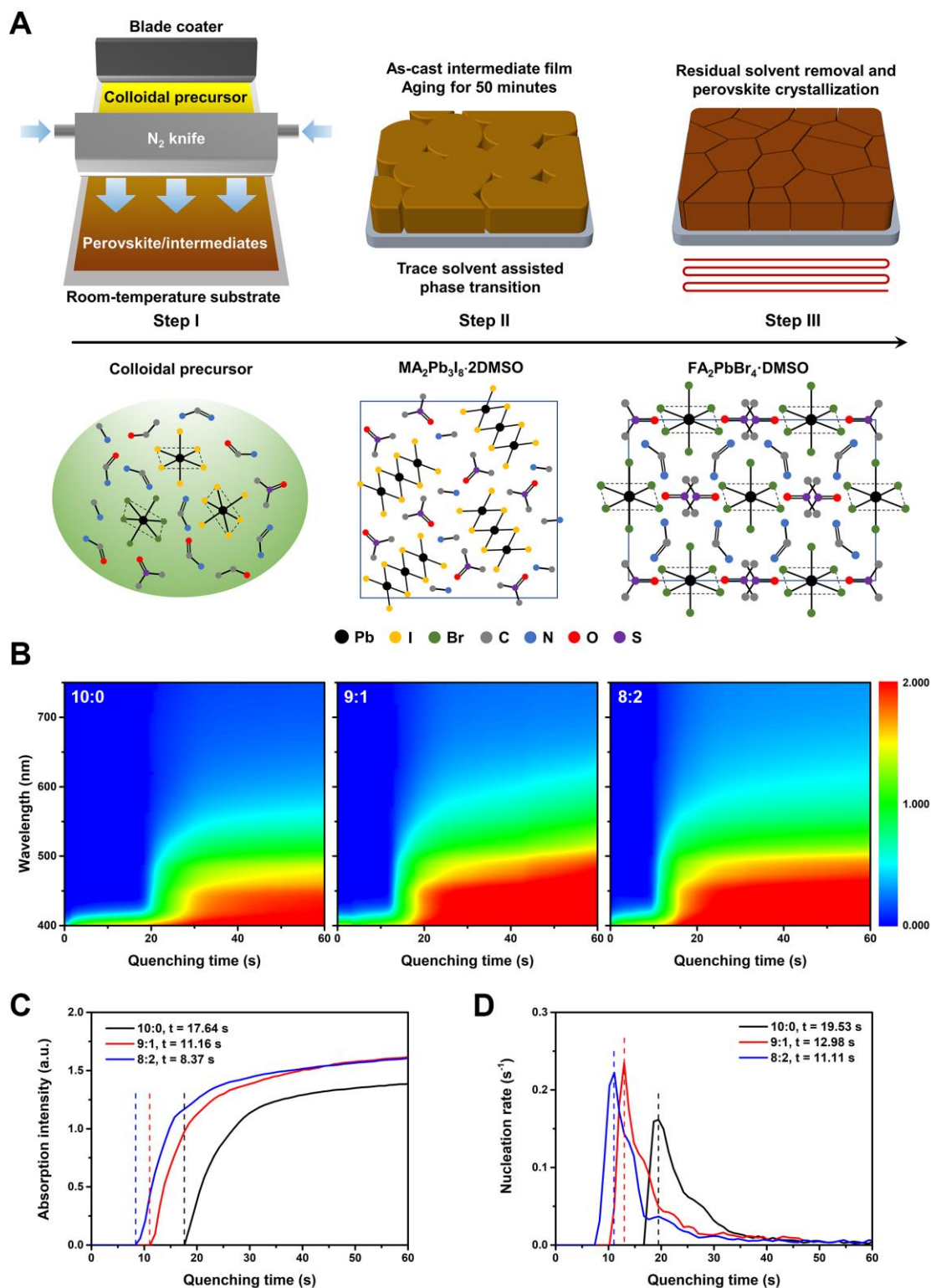


Figure 4. 2 (A) Schematic illustration of the nitrogen-quenching-assisted room-temperature blade coating technique (step I), trace-solvent-assisted phase transition (step II), and thermal annealing (step III). Crystal structure of the involved intermediate phases. (B) In situ UV-vis absorption spectra as a function of gas-quenching time for the perovskite wet films fabricated by the ink with

different volume ratios of DMF/EtOH. (C) UV–vis absorption intensity evolution at the wavelength of 500 nm during the gas quenching. (D) Corresponding nucleation rates are calculated by their first derivative.

Table 4. 2 Calculation of the vapor pressure of the mixed solvent systems.

Mixed solvent system (DMF/EtOH, v:v)	Mixed vapor pressure at 20 °C [kPa]
10:0	0.33
9:1	0.97
8:2	1.58

Note 4. 1 Vapor pressure calculation of the mixed solvent system.

The relationship between the vapor pressure and the corresponding concentration in an ideal solvent mixture obeys Raoult's law. It states that the partial vapor pressure of each component in a perfect mixed solvent at a given temperature is equal to the product of the mole fraction of the pure component multiplied by their corresponding vapor pressure. The partial vapor pressure is calculated according to Supplemental Equation 1, and the total vapor pressure is equal to the sum of the individual vapor pressures according to Equation 3.3.

$$P_A = \chi_A P_A^0, \quad P_B = \chi_B P_B^0 \quad (4.2)$$

$$P_{total} = P_A + P_B = \chi_A P_A^0 + \chi_B P_B^0 + \dots \quad (4.3)$$

$$\chi_A = \frac{\text{moles of } A}{\text{total number of moles}} \quad (4.4)$$

Where P_{total} is the total vapor pressure of the mixed solvent; χ_A is the molar fraction of component A ; P_A^0 is the vapor pressure of pure solvent A at the given temperature; P_A and P_B are the partial vapor pressures of the components A and B .

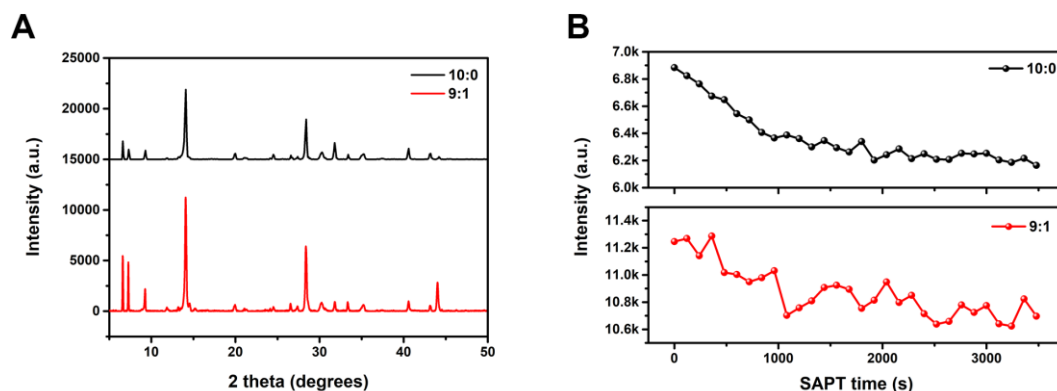


Figure 4. 3 (A) XRD patterns for the as-prepared perovskite/intermediate films after gas quenching. (B) Evolution for the perovskite (100) peak at $2\theta = 14.06^\circ$ during the SAPT process.

After gas quenching, the as-cast intermediate films were kept in the glovebox at room temperature for one hour before thermal annealing. The residual solvent (e.g., DMF, DMSO, and EtOH) in the films was expected to assist the mass transport and diffusion of perovskite precursors, thus facilitating film reconstruction and phase transition. Time-resolved XRD was performed to analyze the perovskite structure evolution and crystallization pathway to offer a deep insight into this TSAT process. Figure 4. 4A shows the false-color intensity mapping versus 2θ and time for the TSAT of fresh intermediate films from the 10:0 and 9:1 ink. These two films both show three diffraction peaks located at $2\theta = 6.58^\circ$, 7.26° , and 9.26° , corresponding to the intermediate phase of MA-based precursor solvate ($\text{MA}_2\text{Pb}_3\text{I}_8 \cdot 2\text{DMSO}$).^{69,73} Besides, They both show the prominent peak located at $2\theta = 14.06^\circ$, corresponding to the (100) plane for cubic perovskite, which confirms the coexistence of intermediate complex and polydisperse perovskite nanocrystals.¹³² The evolution of intermediate complexes and (100) perovskite diffraction peak was tracked during the TSAT process. It should be noted that the 9:1 film displays a prominent diffraction peak located at $2\theta = 15.20^\circ$ at the beginning, and its intensity increases along with the TSAT process. On the contrary, this peak intensity is much lower for the 10:0 film (Figure 4. 4B). This characteristic peak belongs to the (002) plane of $\text{FA}_2\text{PbBr}_4 \cdot \text{DMSO}$ adduct (orthorhombic, $\text{Pca}2_1$).¹³³ No DMF-based solvent complexes are observed despite the host solvent being DMF, mainly due to the more vital Lewis essential coordination

ability of DMSO than DMF.¹³⁴ A slight decrease of the (100) perovskite peak was also observed in both 10:0 and 9:1 films (Figure 4. 3B). Real-time XRD analysis during the TSAT process confirms a partial reconstruction and transformation of the metastable perovskite nuclei through the concatenation of nanostructures, forming The incorporation of EtOH facilitates the formation of a new FA-based precursor solvate during the TSAT process.

To further investigate the interaction between FA₂PbBr₄·DMSO and EtOH, we conducted the DFT calculation to reveal its structural change and electronic modulations. First, we compared the electronic distributions of FA₂PbBr₄·DMSO without and with EtOH. For the pristine FA₂PbBr₄·DMSO, the bonding orbitals are mainly located at the Pb sites, while Br sites dominate the antibonding orbitals. Meanwhile, DMSO partially contributes to the bonding orbitals (Figure 4. 4C). On the contrary, the incorporation of EtOH into FA₂PbBr₄·DMSO lattice strongly affects its structure and electronic distribution (Figure 4. 4D). The bonding orbitals shift toward the distorted [PbBr₆] octahedron, induced by EtOH, which further disassociates the Pb-O bond between Pb and DMSO. We additionally analyze the effect of EtOH on the bond length distributions (Figure 4. 4E). The incorporation of EtOH does not affect N-H and C-H bonds, while Pb-O bonds are evidently reduced due to EtOH. Meanwhile, the Pb-Br bond length distribution change also reveals the distortion of [PbBr₆] octahedron. To further display the electronic structures of the adduct, we plotted the projected partial density of states (PDOS). At the initial interaction with the precursor PbBr₂, we notice both DMSO and EtOH only induce limited change to the electronic structures (Figure 4. 5A). The conduction band minimum (CBM) and valence band maximum (VBM) are mainly contributed by Br-4p and Pb-6p orbitals, respectively. As the precursor concentration increases, EtOH plays a significant role in forming FA₂PbBr₄·DMSO and the further conversion to perovskite. For the pristine FA₂PbBr₄·DMSO, the CBM and VBM are dominated by Pb-6p and Br-4p, respectively, which are consistent with the conventional perovskite materials (Figure 4. 4F). We notice a bandgap between the CBM and VBM, indicating that DMSO does not induce

apparent modulation to the electronic structures. In comparison, EtOH generates strongly perturbed electronic structures of the adduct (Figure 4. 4G), inducing several gap states contributed Pb-6p and EtOH-s,p orbitals between the CBM and VBM. Moreover, the s,p orbitals of FA and DMSO are both modulated slightly due to the formation of hydrogen bonds between precursor and EtOH. We further carried out the energetic calculation during the formation of $\text{FA}_2\text{PbBr}_4 \cdot \text{DMSO}$. A small amount of EtOH increases the stability of the adduct, facilitating the reaction of precursor solvate (Figure 4. 5B). The energy evolutions from the initial precursor PbBr_2 toward $\text{FA}_2\text{PbBr}_4 \cdot \text{DMSO}$ are strongly related to the existence of EtOH (Figure 4. 4H). As the precursor concentration increases, we notice strong Pb-O bonds lead to a higher energy cost of 1.13 eV, whereas EtOH significantly decreased the total energy to -2.07 eV. For the agglomeration of $\text{PbBr}_2 \cdot \text{DMSO}$ to $\text{Pb}_2\text{Br}_4 \cdot 2\text{DMSO}$ and finally, toward $\text{FA}_2\text{PbBr}_4 \cdot \text{DMSO}$, EtOH promotes its formation by lowering the energy barrier from 3.14 to 0.90 eV, and the final energy release from -1.96 to -4.21 eV, respectively. This result strongly proves that EtOH can promote the whole agglomeration process from the $\text{PbBr}_2 \cdot 2\text{DMSO}$ complex to the final adduct of $\text{FA}_2\text{PbBr}_4 \cdot \text{DMSO}$.

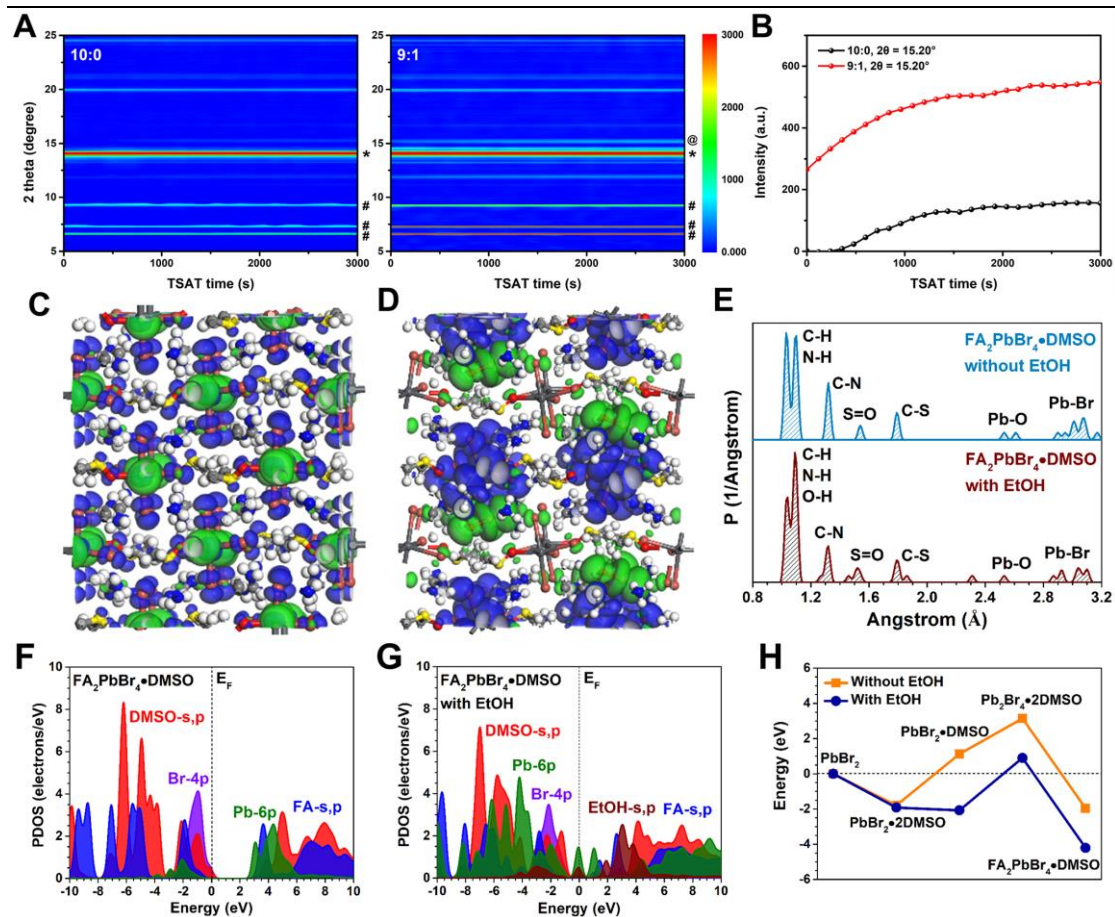


Figure 4. 4 (A) In situ XRD false-color intensity maps during the TSAT process for the perovskite/intermediate films fabricated by the 10:0 and 9:1 ink, respectively, where * represents cubic perovskite phase; # represents MA₂Pb₃I₈·2DMSO; @ represents FA₂PbBr₄·DMSO. (B) XRD intensity evolution for the FA-based adduct (FA₂PbBr₄·DMSO) at 2θ = 15.20° during the TSAT process. C, D) 3D contour plot of electronic distributions of FA₂PbBr₄·DMSO. (C) and FA₂PbBr₄·DMSO incorporated with EtOH. (D), in which dark gray balls = Pb, brown balls = Br, blue balls = N, red balls = O, yellow balls = S, light gray balls = C, and white balls = H; the blue isosurfaces represent bonding orbitals, and the green isosurfaces represent antibonding orbitals. E) Bond length distributions of FA₂PbBr₄·DMSO without/with EtOH. F, G) PDOS of FA₂PbBr₄·DMSO. (F) and FA₂PbBr₄·DMSO incorporated with EtOH. (G) and (H) Energy change of the structural evolution from PbBr₂ to FA₂PbBr₄·DMSO.

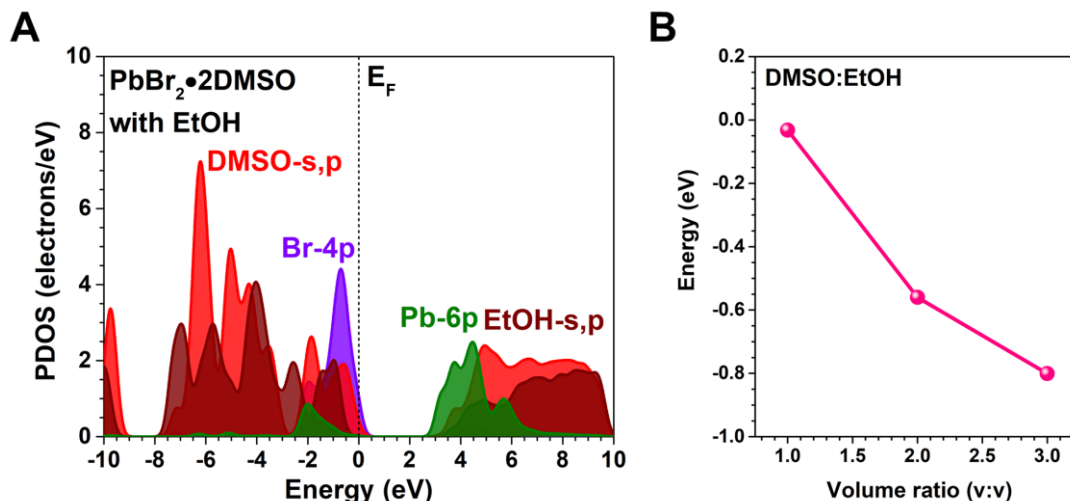


Figure 4. 5 (A) Projected partial density of states (PDOS) for the $\text{PbBr}_2 \cdot 2\text{DMSO}$. (B) The formation energy of $\text{FA}_2\text{PbBr}_4 \cdot \text{DMSO}$ as a function of the volume ratio between DMSO and EtOH.

After the TSAT process, the mixed perovskite/intermediate film was transferred onto the hotplate to induce the second-order phase transition and crystal growth. We further in situ studied the crystal growth kinetics using the time-resolved XRD technique. Figure 4. 6A and B shows the XRD false-color intensity maps versus 2θ and annealing time for the perovskite films fabricated by the 10:0 and 9:1 ink, respectively. When tracking the evolution of intermediate complexes and (100) perovskite peak during thermal annealing, we found the crystal growth in ECS-based perovskite films was obviously retarded (Figure 4. 6C and D). The pristine perovskite film shows an intensity increase of (100) prominent peak during the first ≈ 500 s thermal annealing. Then, it remains unchanged, which means the crystal growth occurs at the first ≈ 500 s of thermal annealing in the pristine perovskite film, while the crystal growth in the ECS-based perovskite film takes over 1000s. The average crystal growth rates of the pristine and ECS-based perovskite films were calculated to be 2.43 and 1.57 s^{-1} , respectively, which mainly result from the formation of a new FA-based precursor solvate ($\text{FA}_2\text{PbBr}_4 \cdot \text{DMSO}$) during the TSAT process. It requires extra energy to dissociate these stable intermediate complexes into plumbiodide fragments upon the removal of residual solvent and recrystallize into cubic perovskite phase in thin films.¹³² It has been widely reported that a slow crystallization process improves the perovskite film quality

with higher crystallinity and fewer defects.^{74,77} We also emphasize the significant role of the TSAT process discussed above in manipulating the crystal growth kinetics and thus constructing high-quality perovskite films, with the comparison of the corresponding XRD intensity evolution for the 9:1 based perovskite films with and without TSAT (Figure 4. 6B; Figure 4. 7). The film without TSAT shows a relatively faster average crystal growth rate (2.24 vs 1.57 s⁻¹).

Figure 4.6E shows the crystal structure of the annealed perovskite films from the inks with different volume ratios between DMF and EtOH. All the samples display similar diffraction patterns, with a set of sharp peaks corresponding to the cubic perovskite phase (*Pm3m*). With the increase of EtOH volume ratio from 0% to 20%, the XRD patterns show an increased proportion of the intensity between (100) at $2\theta = 14.06^\circ$ and (111) at $2\theta = 24.48^\circ$ from 62.1 to 86.7, suggesting a more preferential (100) orientation. Compared with the pristine perovskite, the ECS-based perovskite film shows stronger and sharper XRD peaks, with the full width at half maximum (FWHM) of (100) peak narrowed down from 0.219° to 0.206° (Figure 4. 6F). Grazing incidence wide-angle X-ray scattering (GIWAXS) analysis also presents a highly oriented perovskite film under the ECS strategy, with discrete spots at the main scattering ring ($q = 0.95\text{--}1.05 \text{ \AA}^{-1}$) along q_z and q_r axes (Figure 4. 8). The improved crystallinity and preferential orientation for the ECS-based perovskite films are highly related to the fine regulation of the balance during the solidification process through accelerating perovskite/intermediate nucleation and retarding the crystal growth rate.

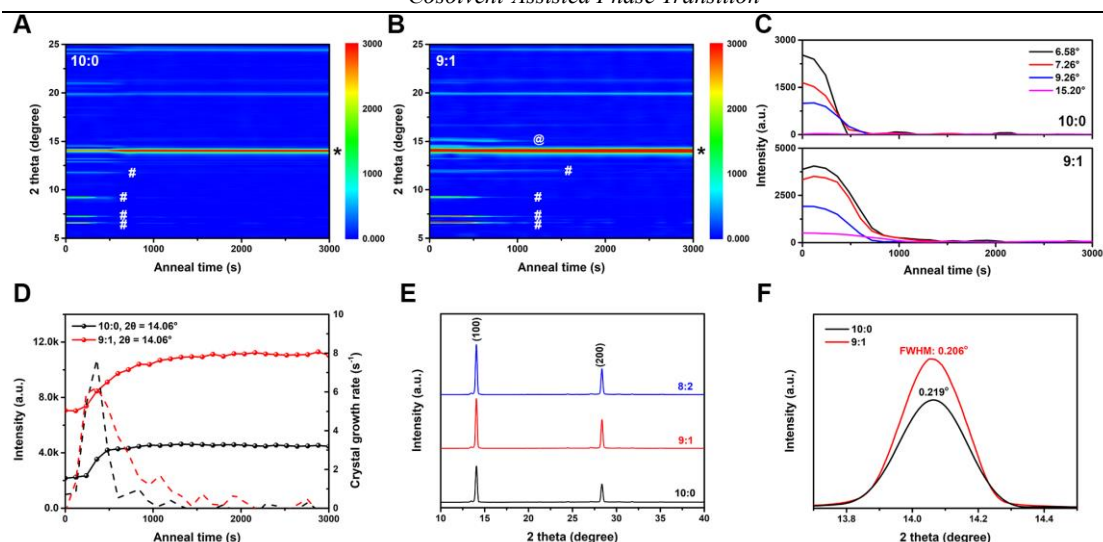


Figure 4. 6 In situ XRD false-color intensity maps versus 2θ and annealing time for the perovskite films fabricated by the ink with 10:0 (A) and 9:1 (B) volume ratios of DMF/EtOH, in which * represents cubic perovskite phase; # represents $\text{MA}_2\text{Pb}_3\text{I}_8 \cdot 2\text{DMSO}$; @ represents $\text{FA}_2\text{PbBr}_4 \cdot \text{DMSO}$. (C) XRD intensity evolution for the intermediate phases at $2\theta = 6.58^\circ$, 7.26° , 9.26° , and 15.20° , respectively, during the annealing process. (D) XRD intensity evolution for the perovskite main peak at $2\theta = 14.06^\circ$ and corresponding crystal growth rates. (E) XRD patterns of the annealed perovskite films fabricated by the inks with different volume ratios between DMF and EtOH. (F) FWHM of (100) peak for the corresponding perovskite films.

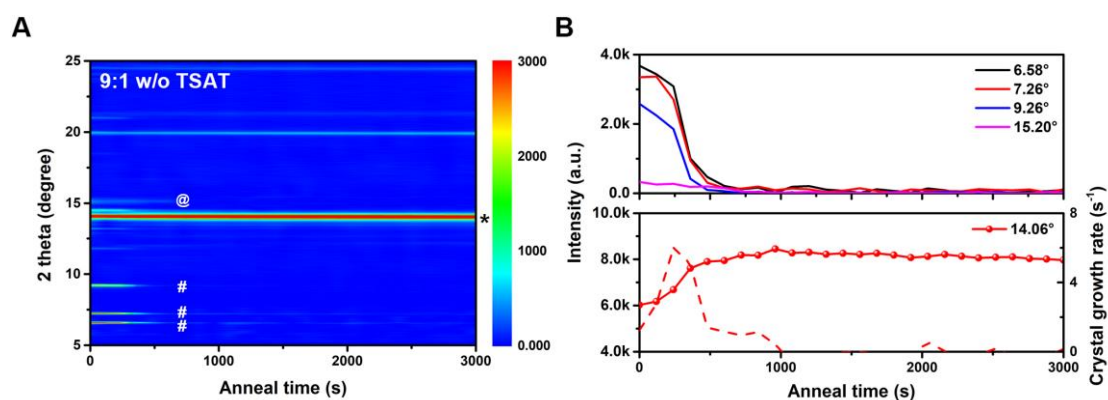


Figure 4. 7 (A) In-situ XRD false-color intensity map versus 2θ and annealing time for the 9:1 based perovskite films without trace solvent assisted transition process (TSAT), in which * represents cubic perovskite phase; # represents $\text{MA}_2\text{Pb}_3\text{I}_8 \cdot 2\text{DMSO}$; @ represents $\text{FA}_2\text{PbBr}_4 \cdot \text{DMSO}$. (B) XRD intensity evolution of the intermediate phases at $2\theta = 6.58^\circ$, 7.26° , 9.26° and 15.20° , and the

perovskite main peak at $2\theta = 14.06^\circ$, respectively. The crystal growth rate is calculated from the first derivative of the corresponding intensity.

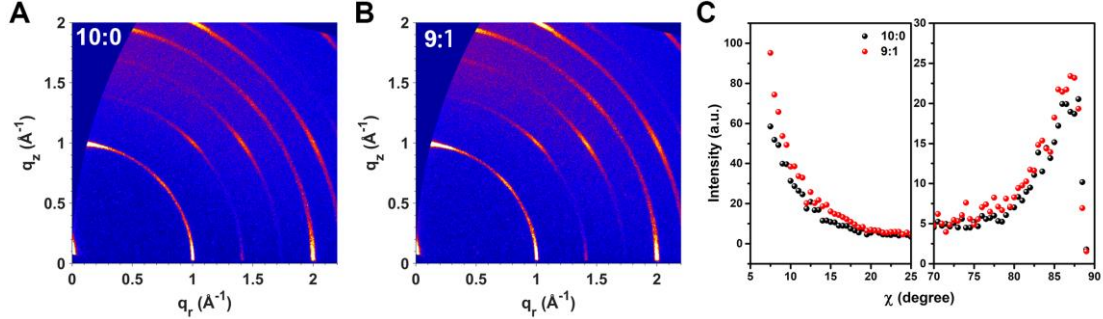


Figure 4.8 2D GIWAXS patterns of the corresponding perovskite films fabricated by the inks with (A) 10:0 and (B) 9:1 volume ratio of DMF and EtOH. (C) The polar intensity profiles along the (100) ring in the range of $q = 0.95\text{--}1.05 \text{ \AA}^{-1}$ from 2D GIWAXS patterns.

We further performed steady-state (SSPL) and time-resolved photoluminescence (TRPL) to investigate the charge recombination behavior. Figure 4.9A shows the SSPL spectra of the respective perovskite films from the 10:0, 9.5:0.5, and 9:1 ink. Compared with the pristine one, ECS-based samples exhibit films are shown in Figure 4.9B. Fitting the experimental data with the bi-exponential function 4.5 and the fitting parameters are summarized in Table 4.3 of the Supporting Information. It should be noted that the excitation fluence in our study is very low ($\approx 5 \text{ nJ cm}^{-2}$), which only generates a much lower density of free carriers ($2.4 \times 10^{14} \text{ cm}^{-3}$) compared with that of trap states ($\approx 10^{18} \text{ cm}^{-3}$). TRPL decay mainly responds to trapping and nonradiative recombination behavior in this condition. The corresponding perovskite films by the 10:0, 9.5:0.5, and 9:1 ink show an average lifetime of 89.17, 359.91, and 581.29 ns, respectively. This result suggests a decreased nonradiative recombination for the ECS-based samples mainly due to the lower trap density.

$$I(t) = A_1 \exp\left(-\frac{t}{\tau_1}\right) + A_2 \exp\left(-\frac{t}{\tau_2}\right) \quad (4.5)$$

We fabricated the conventional n-i-p PSCs assembled with the structure of ITO/SnO₂/perovskite/spiro-OMeTAD/Au through a gas-quenching-assisted blade-coating technique, in which a ≈ 700 nm thick monolithically grained perovskite film is sandwiched between 30 and 200 nm thickness of SnO₂ and spiro-OMeTAD, respectively (Figure 4. 10A). An ≈ 1.60 eV triple-cations-based perovskite system was used in this study (Figure 4. 10B), in which the ECS-based film is shown to be constructed by compacted crystal grains with slightly smaller grain sizes (Figure 4. 10C). Ultraviolet photoelectron spectra (UPS) results proved that the ECS approach did not significantly affect the band structure of perovskite (Figure 4. 11 and Table 4. 4). Figure 4.9C shows the $J-V$ curves of the corresponding champion devices fabricated by the inks with different volume ratios between DMF and EtOH, and the photovoltaic parameters are summarized in Table 4. 5. With the volume ratio of EtOH increased from 0 to 10%, the open-circuit voltage (V_{OC}) is significantly enhanced from 1.183 to 1.218 V, which indicates the ECS approach is applicable to print high-quality perovskite films with lower defect density. Among them, ECS-based PSCs prepared by the 9:1 ink demonstrate the highest efficiency up to 22.18% (average: $21.88\% \pm 0.36\%$) in small-area devices (0.04 cm^2 device area) (Figure 4. 12A).

Further increasing the EtOH volume ratio displays a trend to deteriorate the fill factor (FF) and PCE, mainly due to the unbalanced solubility of EtOH toward organic and metallic moieties, thus causing the nonstoichiometric issue. The ECS approach is also validated when upscaling the device area toward 0.98 cm^2 , with a relatively small deviation in PCEs (Figure 4. 12B). The integrated values of J_{SC} are calculated to be 21.98 and 22.26 mA cm^{-2} for the control and ECS-based PSCs from the EQE spectra (Figure 4.12C), which is well agreed with the J_{SC} measured from $J-V$ curves (mismatch $< 5\%$). Figure 4. 12D shows the steady-state photocurrent density and stabilized PCE measured under maximum power point. The ECS-based device exhibits a steady photocurrent density of $\approx 22 \text{ mA cm}^{-2}$ at 1 V bias, with a stabilized PCE up to 22.00%, consistent with the PCE from $J-V$ curves. The pristine and ECS-based perovskites display identical photovoltaic bandgap (E_g^{IP}) of 1.60 eV (Figure 4. 13),

which agrees well with that measured from the Tauc plot of UV-vis absorption. It should be noted that the control and ECS-based devices without TSAT both exhibit relatively inferior performance compared with their counterparts with TSAT (Figure 4. 14 and Table 4. 6), which highlights the decent regulation of perovskite crystallization is highly related to the resultant device performance. Figure 4. 15 shows the $J-V$ curves under forward and reverse scanning for the representative control and ECS-based PSCs. Hysteresis index (HI) was calculated using equation 4.6, summarized in Table 4. 7 of the Supporting Information. All the ECS-based PSCs show a negligible hysteresis effect ($\approx 0.5\%$ HI), which is lower than that of the control devices ($\approx 1.3\%$ HI). The elimination of hysteresis in $J-V$ curves is mainly attributed to lower trap density in perovskites under the ECS approach.

$$HI = \frac{PCE_{\text{reverse}} - PCE_{\text{forward}}}{PCE_{\text{reverse}}} \quad (4.6)$$

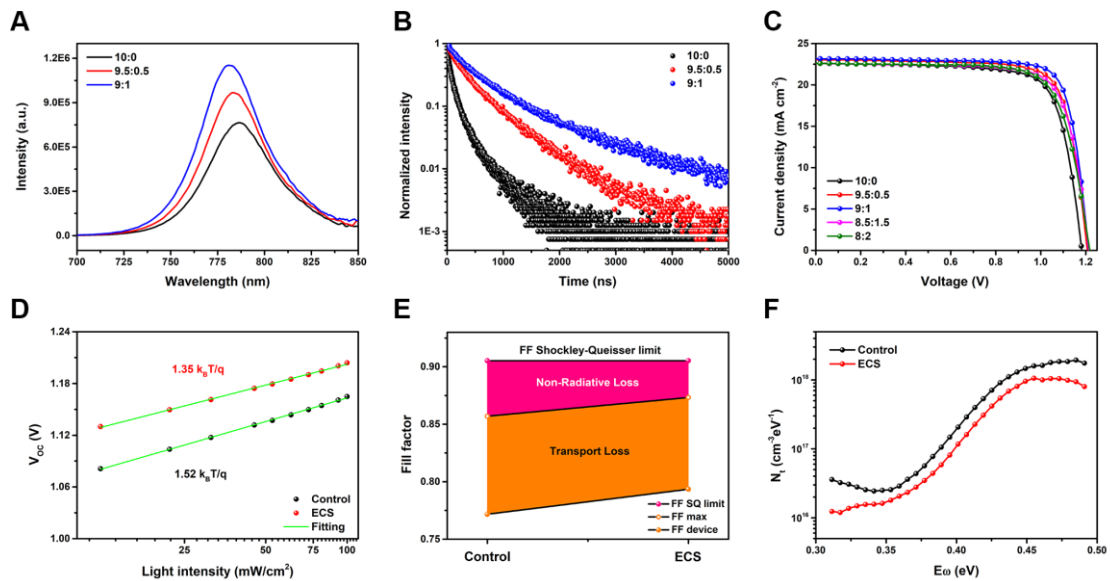


Figure 4. 9 (A) Steady-state PL spectra of the perovskite films fabricated by the ink with different volume ratios between DMF and EtOH. All samples were prepared on quartz substrates with the excitation at 636.2 nm. (B) TRPL decays of the corresponding perovskite films. (C) $J-V$ curves of the champion blade-coated PSCs in a 1.60 eV perovskite system (0.04 cm^2 device area) from the ink with different volume ratios between DMF and EtOH. (D) Plot of the light intensity-dependent V_{OC} for the control and ECS-based devices. (E) Fill factor limitation is composed of nonradiative

loss (pink area) and transport loss (orange area). (F) Energetic trap density distribution for the control and ECS-based devices measured by admittance spectroscopy.

Table 4. 3 Fitting parameters of the bi-exponential decay function in TRPL spectra for the perovskite films fabricated by the ink with different volume ratios between DMF and EtOH.

DMF/EtOH v:v	A ₁	τ ₁ [ns]	A ₂	τ ₂ [ns]	Average decay time ^{a)} τ [ns]
10:0	0.62	35.04	0.36	182.39	89.17
9.5:0.5	0.51	158.50	0.46	583.21	359.91
9:1	0.57	271.45	0.39	1034.13	581.29

^{a)}Average decay time was calculated according to the equation: $\tau = (A_1\tau_1 + A_2\tau_2)/(A_1 + A_2)$.

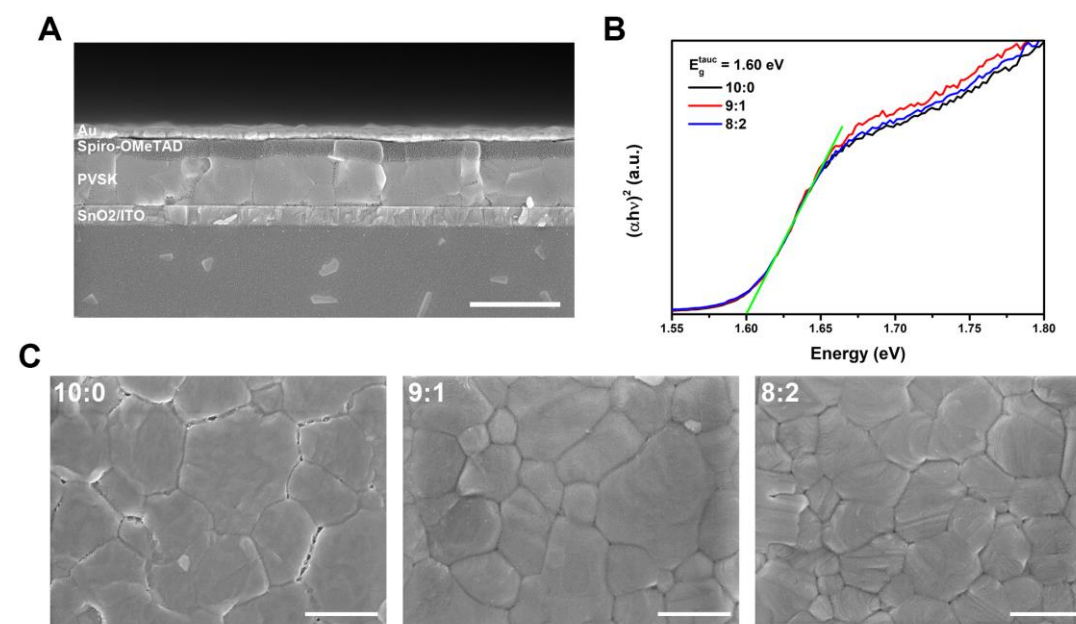


Figure 4. 10 (A) Cross-sectional SEM images of the conventional n-i-p PSCs assembled with the structure of ITO/SnO₂/perovskite/spiro-OMeTAD/Au; scale bar: 1 μm. (B) Tauc plots as a function of $(\alpha h\nu)^2$ vs. energy for the CsFAMA-based perovskite films fabricated by the ink with different volume ratios between DMF and EtOH. The band gap can be determined via linear extrapolation of the leading edges of the $(\alpha h\nu)^2$ curve to the baseline. (C) Top-view SEM images of the corresponding perovskite films by the 10:0, 9:1, and 8:2 inks, respectively; scale bar:1 μm.

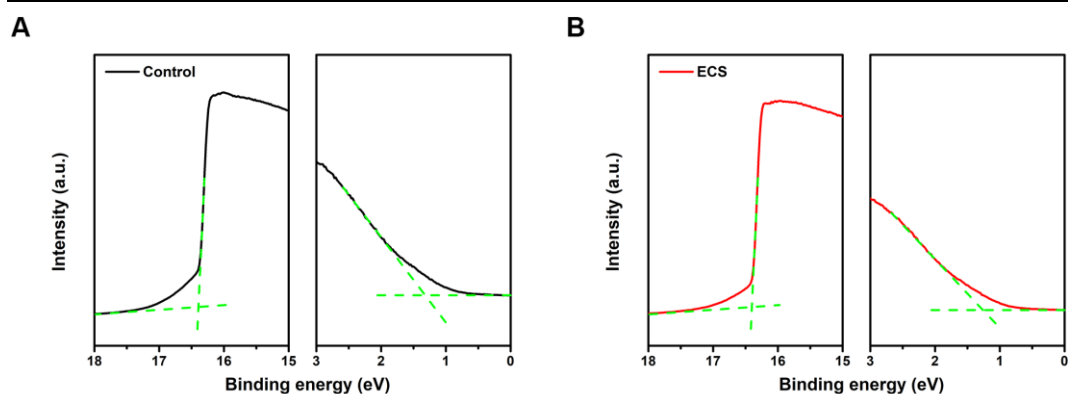


Figure 4. 11 UPS spectra of the control and ECS-based perovskite films.

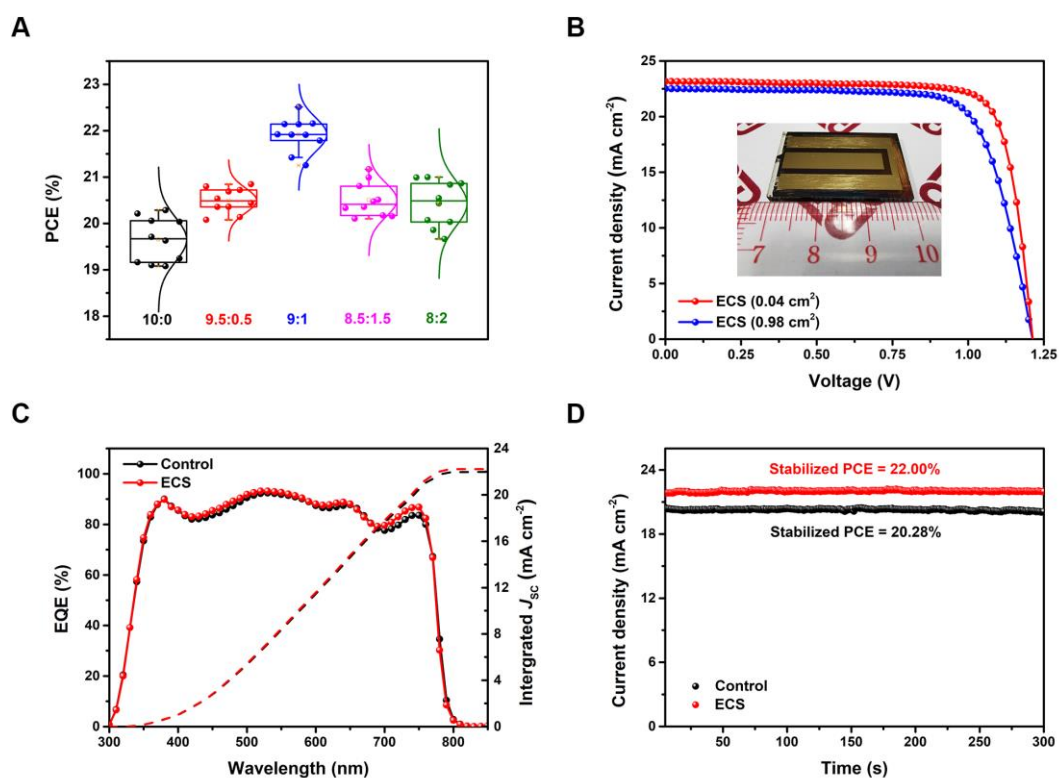


Figure 4. 12 (A) PCE distribution of the blade-coated PSCs from the ink with different volume ratios of DMF/EtOH. (B) J - V curves of the best-performance ECS-based devices with device areas of 0.04 and 0.98 cm^2 , respectively. (C) EQE spectra of the control and ECS-based devices. (D) Steady-state photocurrent output and stabilized PCEs for the control and ECS-based devices.

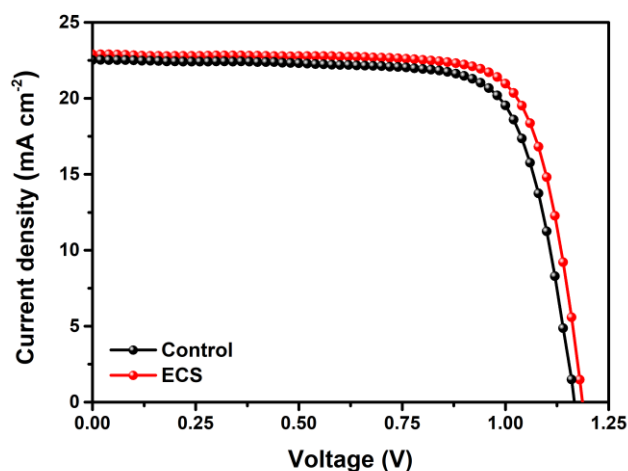


Figure 4.13 J - V curves of the representative control and ECS-based devices without TSAT.

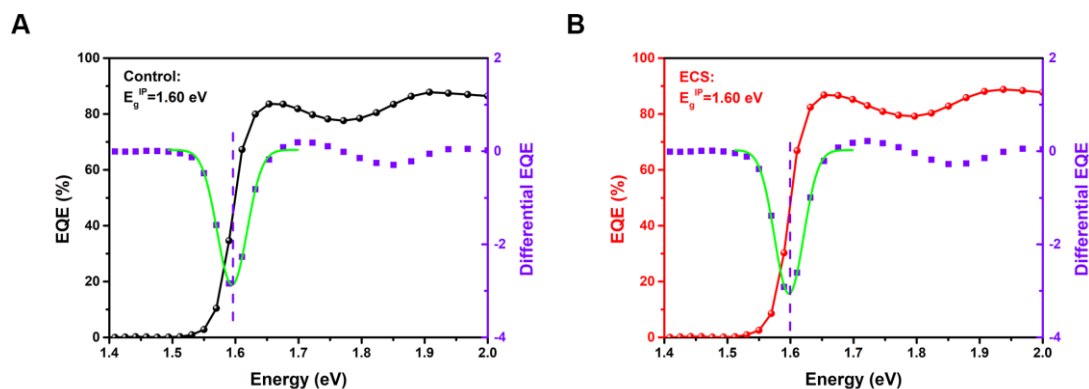


Figure 4.14 Calculation of the bandgap for the control (A) and ECS-based perovskite films through EQE spectra. The maximum differential value of EQE can determine E_g^{IP} .

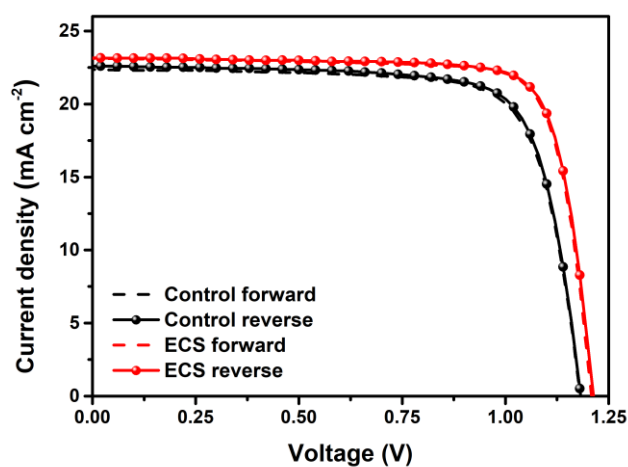


Figure 4.15 J - V curves under forward and reverse scanning for the representative control and ECS-based devices.

Table 4. 4 Band structure of the control and ECS-based perovskite films.

Conditions (DMF/EtOH v:v)	Bandgap ^a [eV]	$E_{\text{cut-off}}$ [eV]	$E_{\text{edge-on}}$ [eV]	Work function [eV]	HOMO energy level [eV]	LUMO energy level [eV]
Control (10:0)	1.60	16.39	1.32	4.83	6.15	4.55
ECS (9:1)	1.60	16.40	1.27	4.82	6.09	4.49

Table 4. 5 Photovoltaic parameters of the control and ECS-based devices with different volume ratios between DMF and EtOH.

Perovskite bandgap [eV]	DMF/EtOH v:v	Device area [cm ²]	V_{oc} [V]	J_{sc} [mA cm ⁻²]	FF [%]	Average PCE ^a [%]	Maximum PCE [%]
1.60	10:0	0.04	1.182	22.60	76.18	19.78 ± 0.48	20.35
	9.5:0.5	0.04	1.207	23.06	77.78	20.65 ± 0.42	21.66
	9:1	0.04	1.213	23.16	80.09	21.88 ± 0.36	22.51
		0.98	1.213	22.50	74.66	19.32 ± 0.60	20.37
	8.5:1.5	0.04	1.215	22.58	77.01	20.51 ± 0.37	21.12
	8:2	0.04	1.218	22.59	75.25	20.43 ± 0.49	20.71
1.54	10:0	0.04	1.173	24.07	75.26	20.43 ± 0.46	21.25
	9:1	0.04	1.192	24.01	81.04	22.60 ± 0.35	23.19
		0.98	1.193	23.98	73.54	20.52 ± 0.61	21.04
		2.7	3.501	7.57	71.50	17.76± 0.83	18.95

Table 4. 6 Photovoltaic parameters of the representative control and ECS-based devices without TAST.

Conditions (DMF/EtOH, v:v)	V_{OC} [V]	J_{SC} [mA/cm ²]	FF [%]	PCE [%]
Control (10:0)	1.167	22.52	76.24	20.04
ECS (9:1)	1.186	22.89	77.22	20.96

Table 4. 7 Photovoltaic parameters for the representative control and ECS-based PSCs ($E_g=1.60$ eV) under forward and reverse scanning.

Conditions (DMF/EtOH, v:v)	Scan direction	V_{OC} [V]	J_{SC} [mA cm ⁻²]	FF [%]	PCE [%]	HI ^{a)} [%]
10:0	F	1.181	22.37	75.97	20.08	1.33
	R	1.182	22.60	76.18	20.35	
9.5:0.5	F	1.202	23.13	77.65	21.59	0.32
	R	1.207	23.06	77.78	21.66	
9:1	F	1.209	23.12	80.16	22.40	0.49
	R	1.213	23.16	80.09	22.51	
8.5:1.5	F	1.214	22.59	76.85	21.07	0.23
	R	1.215	22.58	77.01	21.12	
8:2	F	1.214	22.56	75.20	20.59	0.54
	R	1.218	22.59	75.25	20.71	

We identify the origins of increased V_{OC} in the ECS-based devices by quantifying the dominating recombination mechanisms to analyze the fundamental mechanism underlying charge recombination and V_{OC} deficit. We examined the EQE_{EEL} for a complete PSC operating as a light-emitting diode (LED) in forward voltage bias.²⁶ According to the reciprocity relation between EQE_{PV} and EQE_{EEL}, The theoretical radiative limit of V_{OC} ($V_{OC,rad}$) can be calculated through equation 4.7 in which $\Phi_{AMI.5}$ and Φ_{BB} refer to the solar AM 1.5G spectrum and the black-body radiation spectrum at 300 K, respectively.⁹⁰ $V_{OC,rad}$ was calculated to be 1.31 V for a 1.60 eV perovskite system from a detailed balance model.⁹¹ Thus, the V_{OC} difference between the control and ECS-based devices should originate from the nonradiative recombination loss

($\Delta V_{OC,nr}$), which can be calculated from the EQE_{EL} at the injection current density equal to J_{SC} with the equation 4.8. The ECS-based device shows a relatively higher EQE_{EL} of 1.82% at the injection current density comparable to J_{SC} , corresponding to a $\Delta V_{OC,nr}$ of 104 mV (Figure 4. 16A–C). By contrast, the control devices display a higher $\Delta V_{OC,nr}$ of 138 mV ($EQE_{EL} = 0.50\%$). V_{OC} deficit analysis agrees well with the measured value from the J – V curves. This result suggests that the ECS strategy efficiently suppresses the nonradiative recombination in the bulk perovskite (Figure 4. 16D).

$$V_{OC,rad} = \frac{k_B T}{q} \ln \left(\frac{\int EQE_{PV}(E) \times \phi_{AM1.5}(E) dE}{\int EQE_{PV}(E) \times \phi_{BB}(E) dE} + 1 \right) = \frac{k_B T}{q} \ln \left(\frac{J_{SC}}{J_0^{rad}} + 1 \right) \quad (4.7)$$

$$\Delta V_{OC,nr} = -\frac{k_B T}{q} \ln EQE_{EL} \quad (4.8)$$

We further measured the light intensity– V_{OC} relationship in the range from 12.23 to 100 mW cm^{–2}, as shown in Figure 4. 9D.^{135,136} The ideality factor (n) is correlated with the slope of the V_{OC} versus light intensity in the natural logarithm scale. The ECS-based devices show a smaller ideality factor of 1.35 compared with the control devices ($n = 1.52$), suggesting the suppressed trap-assisted recombination. On the other hand, the FF loss between the Shockley–Queisser limit (FF_{SQ}) and the measured FF from J – V curves compose two parts—nonradiative loss and charge transport loss. Following the detailed, balanced model, FF_{SQ} is calculated to be 90.53% in the 1.60 eV perovskite system, and the maximum FF (FF_{max}) without charge transport loss can be calculated through the Equation 4.9.¹³⁷ As shown in Figure 4. 9D, E, the enhanced V_{OC} and FF for the ECS-based devices mainly come from the suppression of nonradiative recombination.

$$FF_{max} = \frac{v_{oc} - \ln(v_{oc} + 0.72)}{v_{oc} + 1}, v_{oc} = \frac{V_{oc}}{\frac{nk_B T}{q}} \quad (4.9)$$

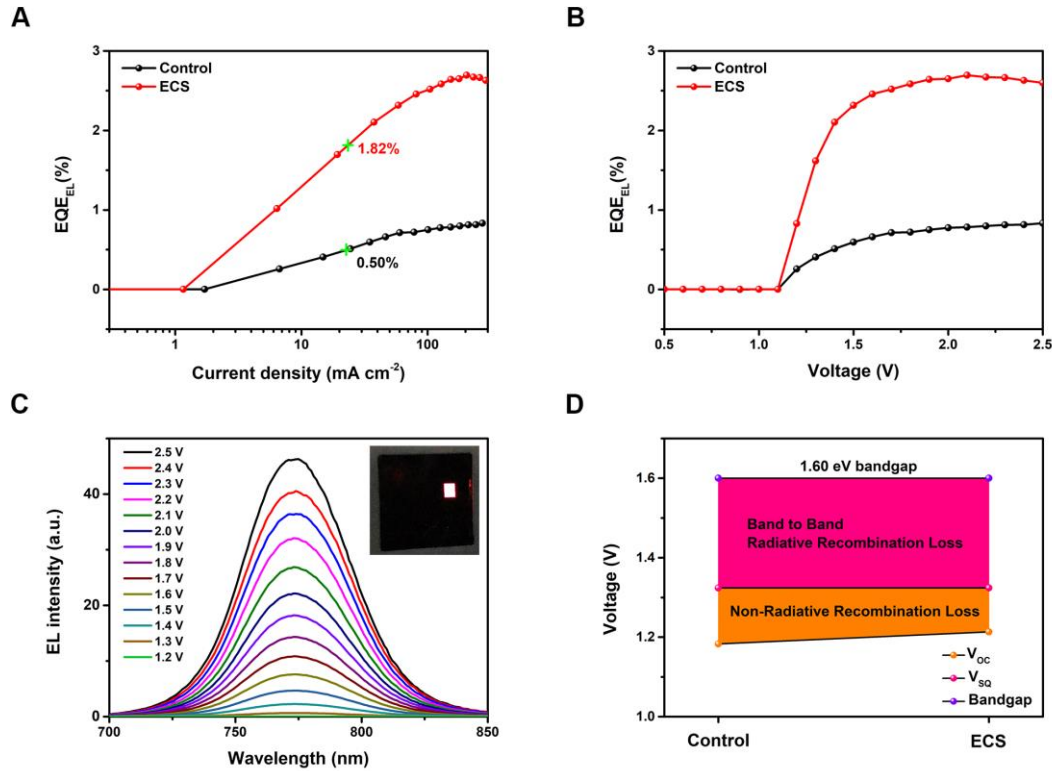


Figure 4. 16 EQE_{EL} as a function of the injection current density (A) and applied voltage bias (B) for the control and ECS-based PSCs when operating as LEDs. (C) EL spectra for the representative ECS-based device under voltage bias from 1.2 to 2.5 V; inset is a photograph showing an ECS-based PSC operating as an LED (device area: 0.04 cm²) with visible red emission. (D) V_{OC} deficit from band-to-band radiative and non-radiative recombination loss for the control and ECS-based devices, respectively.

Thermal admittance spectroscopy (TAS) was further performed to quantitatively estimate the energetic distribution of trap density (N_t) under an AC voltage with the frequency decreased from 10⁶ to 100 Hz according to equation 4.10 in which V_{bi} is the built-in potential, W is the depletion width, C is the capacitance, and ω is the applied angular frequency.⁹⁵⁻⁹⁷ V_{bi} and W could be estimated through the Mott-Schottky analysis for a PSC device. The demarcation energy (E_ω) is calculated from equation 4.11, where β is a temperature-independent parameter from the Arrhenius plot. As shown in Figure 4. 9F, the ECS-based devices display a relatively lower N_t (6.43×10^{16} cm⁻³) compared with the control devices (1.15×10^{17} cm⁻³). TAS result agrees well

with the trap density analysis in the space charge limited current method, in which the ECS-based devices also show much lower trap density (Figure 4. 17).

Electrochemical impedance spectroscopy was carried out to extract more information about the charge transport and recombination behavior in PSCs.^{138,139} Figure 4. 18A, B shows the Nyquist plots for the control and ECS-based devices, respectively, measured at DC bias from 0.7 to 1 V and AC bias frequency from 10^6 to 100 Hz. The inset of Figure 4. 18A represents the equivalent circuit for the simulation of charge transfer and the recombination process, in which R_S is defined as the series resistance of devices, and R_{rec} represents the recombination resistance in the bulk perovskite, which is inversely related to the recombination rate of photogenerated carriers. In contrast to the control devices, the ECS-based devices show smaller R_S , which is highly related to the enhanced FF value measured from $J-V$ curves (Figure 4. 18C). On the other hand, the higher R_{rec} in the ECS-based devices is responsible for the lower recombination rate of photogenerated carriers in the bulk perovskite, which is in accordance with the enhanced V_{OC} , as mentioned before (Figure 4. 18D).

$$N_t(E_\omega) = -\frac{V_{bi}}{eW} \frac{dC}{d\omega} \frac{\omega}{k_B T} \quad (4.10)$$

$$E_\omega = k_B T \ln\left(\frac{\beta T^2}{\omega}\right) \quad (4.11)$$

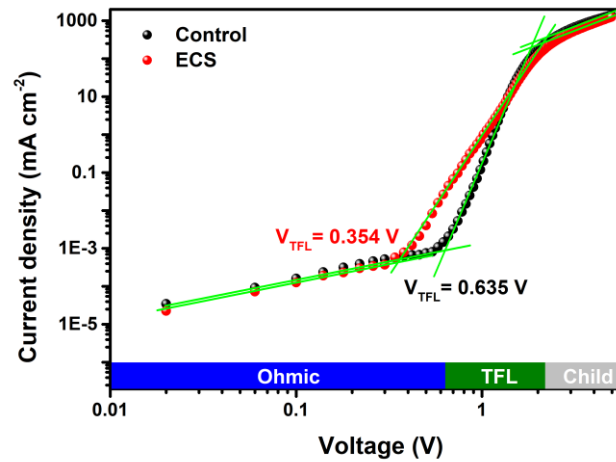


Figure 4. 17 SCLC analysis for the electron-only devices based on the pristine and ECS-based perovskite films.

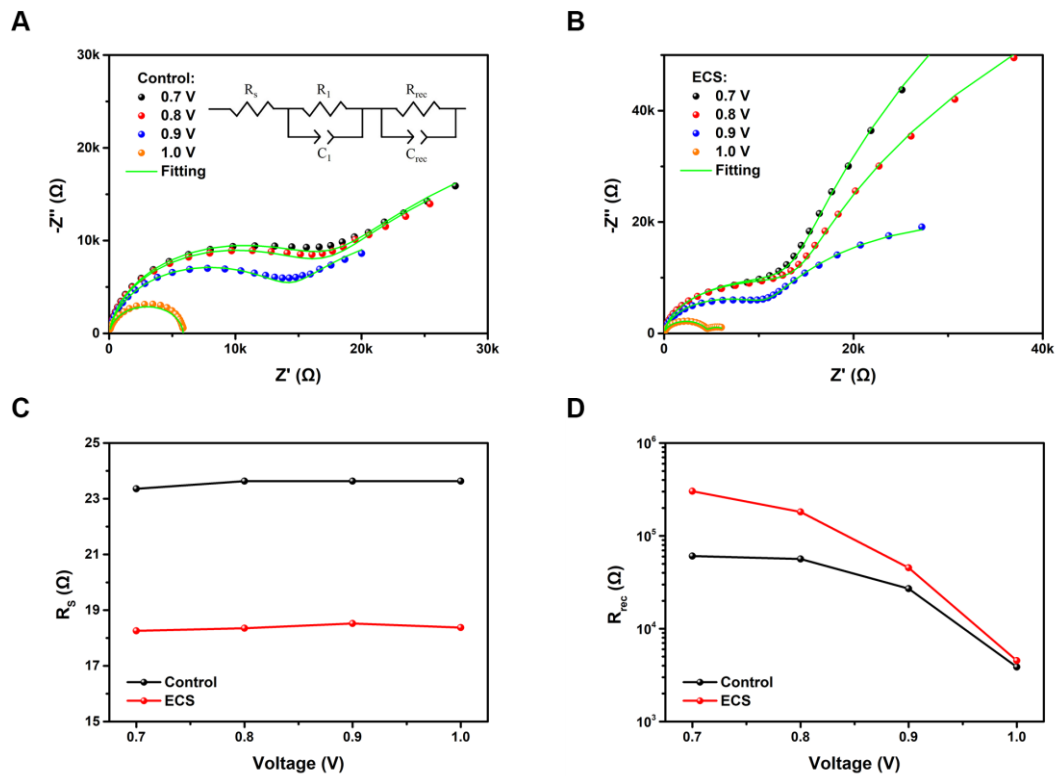


Figure 4. 18 Nyquist plots of the control (A) and ECS-based devices (B) in the dark under 0.7 to 1.0 V bias voltage, respectively. Inset: equivalent circuit for the simulation of charge transfer and recombination process. The relationship between bias voltage and (C) R_S and (D) R_{rec} .

FA-dominated perovskites with a bandgap closer to the Shockley–Queisser limit are the state-of-the-art photoactive materials in PSCs, which deliver higher efficiency in principle. We further proved this strategy in an ≈ 1.54 eV FA-dominated perovskite system, $\text{Cs}_{0.03}(\text{FA}_{0.97}\text{MA}_{0.03})_{0.97}\text{Pb}(\text{I}_{0.97}\text{Br}_{0.03})_3$, and achieved a maximum PCE up to 23.19% for the ECS-based devices (0.04 cm^2 device area), which is superior to that of the control devices (21.25%) (Figure 4. 19A). ECS-based devices also show a negligible hysteresis effect in J – V curves (0.34% HI), lower than that of the control devices (0.71% HI), summarized in Table 4. 8. The integrated values of J_{SC} are calculated to be 23.55 mA cm^{-2} for the ECS-based PSCs from the EQE spectra, which agrees well with the J_{SC} value from the J – V curves (Figure 4. 19B). More importantly, when upscaling the device area, we achieved the maximum PCEs of 21.04% and 18.95% for the ECS-based device (0.98 cm^2) and minimodule (2.7 cm^2 , 3-subcells), respectively,

through the room-temperature blade-coating technique (Figure 4. 19C). This result represents one of the highest records for the blade-coated perovskite solar cells (PSCs) in both small-area devices and minimodules, corresponding to a relatively small CTM loss of $1.59\% \text{ cm}^{-2}$ (equation 4.12).¹⁴⁰⁻¹⁴² which indicates the great potential for future commercialization using the ECS strategy (Figure 4. 19D).^{29,52,59,98,143-146} It should be noted that we achieved a maximum V_{OC} of 1.205 V in this perovskite system, corresponding to an excellent V_{OC} deficit as low as 335 mV (Figure 4. 20), which is even closer to the values for the state-of-the-art inorganic PV technologies. In order to analyze the V_{OC} deficit, we performed the EQE_{EL} spectra for the complete devices operating as an LED. The ECS-based device exhibits an EQE_{EL} up to 5.13% at an injection current density equal to 24.01 mA cm^{-2} , corresponding to a $\Delta V_{OC,nr}$ of 77 mV, which is lower than that for the control device (100 mV). As far as we know, the $\Delta V_{OC,nr}$ of 77 mV is among the lowest values in all reported PSCs (Table 4. 9).

$$\text{CTM loss} = \frac{\text{PCE}_{\text{cell}} - \text{PCE}_{\text{module}}}{\text{Area}_{\text{module}} - \text{Area}_{\text{cell}}} \quad (4.12)$$

In addition to the device performance, the long-term stability under different aging conditions is of great importance for PSC technology. Figure 4. 19F shows the long-term shelf stability of the unencapsulated devices under ambient environment ($25 \pm 5 \text{ }^\circ\text{C}$, $20\% \pm 5\% \text{ RH}$). The ECS-based devices offer much better shelf stability, maintaining 93.4% of its initial PCE after $\approx 1500 \text{ h}$. In comparison, the control devices only keep 59.8% of their initial value under the same aging condition. In addition, the thermal stability test was conducted on an $80 \pm 5 \text{ }^\circ\text{C}$ hotplate in the glovebox. The ECS-based devices display superior thermal stability, retaining over 90% of their initial efficiency after $\approx 500 \text{ h}$ aging, compared with only $\approx 60\%$ for the control devices. It is well-known that shallow defects. (with low migration activation energy) at perovskite surface and grain boundaries initialize the permeation of moisture and oxygen into the perovskite films to accelerate the degradation of PSCs.^{62,147} ECS strategy significantly

improved the long-term stability of devices, mainly due to the improved crystal quality and significantly decreased shallow N_t (see Figure 4. 9F) in the resultant perovskite films through the fine regulation of nucleation and crystal growth.

4.3 Conclusion

We have demonstrated a practical ECS approach by incorporating green and volatile solvent EtOH into the perovskite ink to partially replace the conventional polar aprotic and toxic solvents (e.g., DMF) for efficient room-temperature blade-coated PSCs. We systematically studied perovskite crystallization dynamics to diagnose the real-time perovskite structural evolution and phase-transition pathway. We highlighted the critical role of EtOH during the TSAT process. Real-time XRD technique and DFT calculations uncovered the residual EtOH facilitated the formation of a FA-based precursor solvate during the TSAT process, which is critical to forming the homogenous and compact perovskite film. This strategy was proven to regulate the perovskite solidification process through accelerating perovskite/intermediate nucleation and retarding the crystal growth rate, thus improving film quality with higher crystallinity, preferential orientation, and lower density of trap states. The universality and versatility of this strategy not only enhanced the efficiencies in small-area devices and minimodules with low V_{OC} deficit but also improved their stability under different aging conditions. The plan is, therefore, applicable for the future industrial manufacture of high-performance perovskite solar modules in an eco-friendly and cost-effective way.

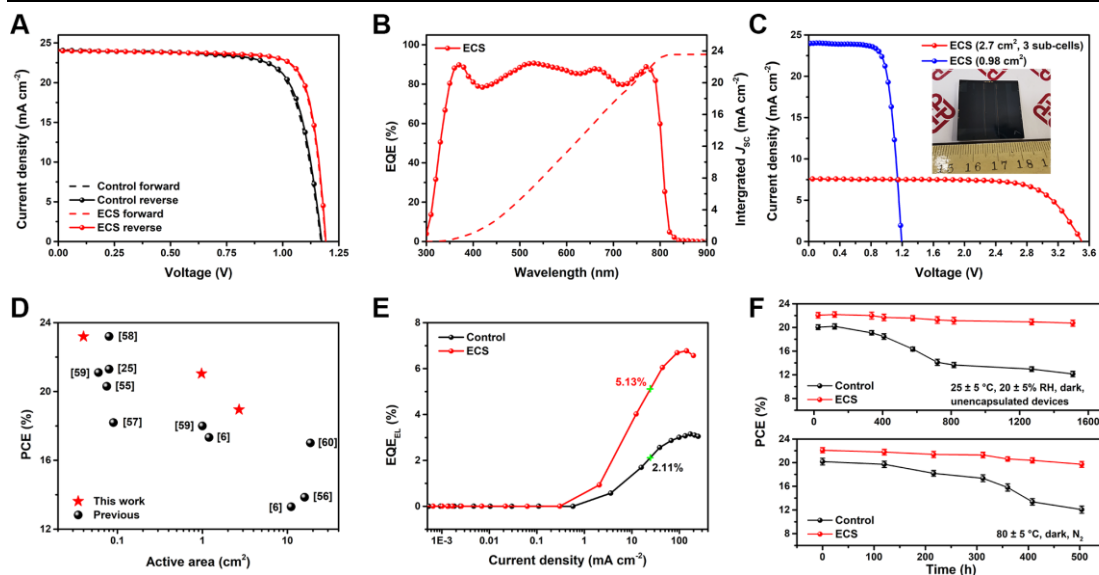


Figure 4. 19 (A) J - V curves of the champion control and ECS-based PSCs in a 1.54 eV perovskite system from forward and reverse scan directions. (B) EQE spectrum of the ECS-based devices with an integrated J_{SC} of 23.55 mA cm^{-2} . (C) J - V curves of the champion ECS-based device (0.98 cm^2 device area) and minimodule (2.7 cm^2 , 3-subcells). (D) Comparison of the state-of-the-art PCEs from the previous relevant works as a function of device area.¹⁴⁶ (E) EQE_{EL} as a function of the injection current density for the control and ECS-based PSCs when operating as LEDs. (F) Long-term stability for the control and ECS-based devices under different aging conditions.

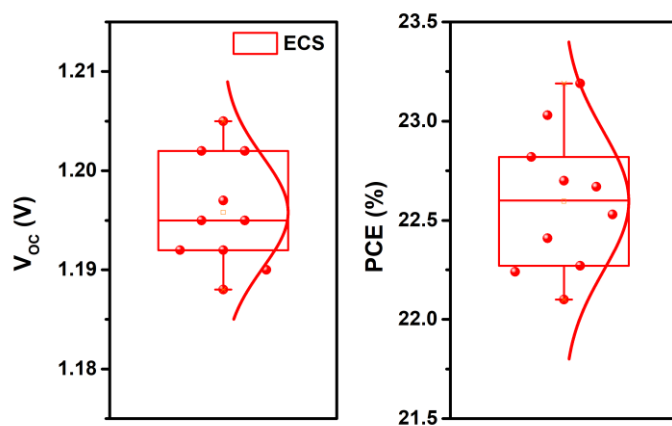


Figure 4. 20 V_{oc} (left) and PCE (right) distribution for ten representative ECS-based devices in a 1.54 eV perovskite system.

Table 4. 8 Photovoltaic parameters for the representative control and ECS-based PSCs ($E_g=1.54$ eV)

under forward and reverse scanning.

Conditions (DMF/EtOH, v:v)	Scan direction	V_{OC} [V]	J_{SC} [mA cm ⁻²]	FF [%]	PCE [%]	HI ^{a)} [%]
10:0	F	1.170	24.13	74.72	21.10	0.71
	R	1.173	24.07	75.26	21.25	
9:1	F	1.190	24.16	80.38	23.11	0.34
	R	1.192	24.01	81.04	23.19	

^{a)}Hysteresis index (HI) was calculated from the equation: $HI = \frac{PCE_{reverse} - PCE_{forward}}{PCE_{reverse}}$

Table 4. 9 Summary of the state-of-the-art values of V_{OC} deficit and non-radiative recombination loss ($\Delta V_{OC,nr}$) reported in other relevant works.

Perovskite bandgap E_g [eV]	Maximum V_{OC} [V]	V_{OC} deficit [V]	$\Delta V_{OC,nr}$ ^{b)} [V]	Reference
1.56	1.17	0.39	NA	148
1.57	1.18	0.39	NA	149
1.54	1.161	0.379	0.112	150
1.57	1.195	0.375	NA	118
1.53	1.18	0.35	0.070	151
1.516	1.173	0.343	NA	152
1.56	1.225	0.335	NA	153
1.54	1.205	0.335	0.077	This work
1.51	1.18	0.330	NA	154
1.536	1.21	0.326	0.074	155
1.53	1.21	0.32	0.060	156
1.53	1.22	0.31	0.054	113

^{a)} V_{OC} deficit was calculated from $E_g/q - V_{OC,max}$; ^{b)} $\Delta V_{OC,nr}$ was estimated using the EQE_{EL} at the injection current density equal to J_{SC} with the equation: $\Delta V_{OC,nr} = -\frac{k_B T}{q} \ln EQE_{EL}$.

4.4 Experimental Section

Materials: Unless stated otherwise, chemicals and solvents were obtained commercially and were used without further purification, including lead iodide (PbI₂)

(Sigma-Aldrich, 99.99%), lead(II) bromide (PbBr₂) (Sigma-Aldrich, 99.999%), formamidinium iodide (FAI) (Greatcell Energy), methylammonium bromide (MABr) (Greatcell Energy), and methylammonium chloride (MACl) (Sigma-Aldrich, ≥98%). All solvents, including DMF (99.8%, anhydrous), DMSO (99.9%, anhydrous) and EtOH (anhydrous, ≤0.005% water) were purchased from Sigma-Aldrich.

Device Fabrications: Laser-patterned ITO/glass substrates (sheet resistance $\approx 12 \Omega \text{ sq}^{-1}$) were washed with a detergent solution, distilled water, acetone, and isopropanol, respectively. After ultraviolet–ozone treatment for 20 min, the thin layer of self-synthesized SnO₂ solution was spin-coated onto the precleaned ITO substrate at 4000 rpm for 30 s and annealed at 200 °C for 60 min in an ambient atmosphere. Mixed triple-cation (CsFAMA) perovskite precursor solution ($E_g = 1.60 \text{ eV}$) was prepared with 1.2 M PbI₂, 1.1 M FAI, 0.2 M PbBr₂, 0.2 M MABr, and 0.05 m CsI dissolved in DMF. Lewis basic DMSO was subsequently incorporated into the solution with a 1:1 molar ratio to perovskite precursor. For the ECS-based ink, different ratios (0 to 40%, v:v) of EtOH was used to replace the host solvent of DMF (e.g., 9:1 means volume ratio of DMF/EtOH is 9:1, unless stated otherwise). The Cs_{0.03}(FA_{0.97}MA_{0.03})_{0.97}Pb(I_{0.97}Br_{0.03})₃ perovskite precursor solution ($E_g = 1.54 \text{ eV}$) was prepared using the mixed powders of FAI:MABr:MACl:PbBr₂:PbI₂ (molar ratio: 1.41:0.04:0.4:0.04:1.47) in DMF, blended with CsI (1.5 M; 3% volume ratio) stock solution. Lewis basic DMSO was subsequently incorporated into the solution with a 1:1 molar ratio to perovskite precursor. For the room-temperature blade-coated PSCs, an automatic wire-bar coater (RK PrintCoat Instruments, K paint type) was employed in a humidity-control ambient environment. (30% ± 5% RH). A small droplet of perovskite ink was dripped on the substrate and swiped linearly by an adjustable film applicator (BEVS 1806B/100) at the blading speed of 10 mm s⁻¹. The gap between the film applicator and substrate was set as 100 μm. A laminar nitrogen knife (Wells Corp., 150 mm width) was installed right next to the blade substrate with the flow at 20° to the substrate. The as-prepared wet perovskite film was gas-quenched by the nitrogen knife with the fixed nitrogen blow rate of 40 m

s⁻¹ (calibrated using the Testo 416 flowmeter) in order to remove the extra precursor solution and induce the precipitate of perovskite intermediate adducts. The as-prepared perovskite films were later transferred onto the hotplate at 120 °C for 60 min in the controlled ambient air (20–30% relative humidity). BABr/IPA solution (2 mg mL⁻¹) was spin-coated onto the perovskite films at 5000 rpm and annealed at 100 °C for 10 min. Spiro-OMeTAD solution (80 mg mL⁻¹ in chlorobenzene) with 29 μL of Tbp and 17.5 μL of Li-TFSI (520 mg mL⁻¹ in acetonitrile) was prepared and deposited onto the perovskite films through spin-coating. Finally, an 80 nm thick Au electrode was thermally evaporated on top of the device through a shadow mask to pattern the electrodes.

Characterizations: DFT calculations were carried out within CASTEP packages. The generalized gradient approximation and Perdew–Burke–Ernzerhof was utilized to describe the exchange-correlation energy. The plane-wave basis cutoff energy was set to 380 eV by considering the ultrafine quality. The ultrasoft pseudopotentials with the Broyden–Fletcher–Goldfarb–Shannon algorithm were selected for all the geometry optimizations. The coarse quality of the k-point set was used for the energy minimizations. Meanwhile, the convergence criteria of the geometry optimizations were set as follows: Hellmann–Feynman forces on the atom should be less than 0.001 eV Å⁻¹; the total energy difference and interionic displacement should be less than 5 × 10⁻⁵ eV per atom and 0.005 Å, respectively. Crystalline structure was explored on a Rigaku SmartLab X-ray diffractometer with Cu Kα radiation in a step of 0.01° and θ–2θ scan mode from 5° to 50°. AFM height images were examined using a Bruker Multimode 8 scanning probe microscope (tapping mode). Film morphology of the perovskite was measured using a high-resolution field emission SEM (TESCAN VEGA3). GIWAXS was investigated using a Xeuss 2.0 SAXS/WAXS laboratory beamline with a Cu X-ray source (8.05 keV, 1.54 Å) and a Pilatus3R 300K detector. The in situ UV–vis absorption spectra were measured using an F20-UVX spectrometer (Filmetrics, Inc.) equipped with tungsten halogen and deuterium light sources (Filmetrics, Inc.). UV–vis absorption spectra were measured by using a UV–vis

spectrophotometer (CARY5000, Varian). Steady-state PL and TRPL transient decay spectra were measured using a PL spectrometer (Edinburgh Instruments, FLS920) with the excitation source of 636.2 nm picosecond pulsed diode laser (EPL-635, $\approx 5 \text{ nJ cm}^{-2}$) and detected at 780 nm. UPS measurement was carried out by a VG ESCLAB 220i-XL surface analysis system equipped with a monochromatic Al K α X-ray source (1486.6 eV) in a vacuum of 3.0×10^{-8} Torr. For the completed devices, J - V curves were obtained using a Keithley 2400 Source Meter under standard AM 1.5 G illumination. (Enli Technology Co. Ltd., Taiwan), and the light intensity was calibrated by a standard KG-5 Si diode. Both forward (from -0.2 to 1.25 V) and reverse scanning (from 1.25 to -0.2 V) were performed with a delay time of 100 ms. The test areas (0.04, 0.98, and 2.7 cm^2) were typically defined by a metal mask with an aperture aligned with the active area. EQE spectra were measured with a QE-R 3011 EQE system (Enli Technology Co. Ltd., Taiwan) using 210 Hz chopped monochromatic light ranging from 300 to 850 nm. The EL EQE spectra were recorded by an LED photoluminescence quantum yield measurement system (Enli Tech LQ-100) equipped with Keithley 2400 Source Measure Unit.

Chapter 5 Highly stable perovskite solar cells with 0.30 voltage deficit enabled by a multi-functional asynchronous cross-linking

5.1 Introduction

Photovoltaic (PV) technology has shown great potential in offering a clean and sustainable solution to the issue of global energy scarcity in recent years. The interest in organic-inorganic hybrid perovskite materials has grown due to their advantageous characteristics, such as high charge carrier mobility and lifetime, tuneable bandgaps, high absorption coefficient, and good solubility in common polar aprotic solvents.¹⁵⁷⁻¹⁵⁹ These materials have been widely used in various optoelectronic and electronic applications, including solar cells, light-emitting devices, lasers, and photodetectors. Among them, solar cells based on organic-inorganic halide perovskites (OIHPs) have emerged as a leading technology in the field of emerging photovoltaics, which is comparable with crystalline silicon, gallium arsenide (GaAs), copper indium gallium selenide (CIGS), cadmium telluride (CdTe) technologies and so on.

The intrinsic stability of the perovskite layer and its interfaces remains the primary challenge in commercializing perovskite solar cells (PSCs) despite the significant advancements in laboratory-scale PSCs, achieving certified power conversion efficiency (PCE) over 26.0%.¹⁶⁰ This challenge mainly arises from the fragile and ionic nature of halide perovskite materials, which make them highly sensitive and reactive toward the ambient environment.¹⁶¹⁻¹⁶³ Solution deposition of perovskite thin films would spontaneously induce high concentrations of intrinsic defects (e.g., halide vacancies, under-coordinated lead cations) at perovskite surface and grain boundaries (GBs). Such defects are likely to be detrimental to the device performance (e.g., open-circuit voltage, V_{OC}) and would accelerate the perovskite degradation under ambient atmosphere.¹⁶⁴ It's well recognized that delicate control of perovskite formation and

crystallization kinetics (nucleation and crystal growth rate) is of great significance to mitigate these defects to a great extent.^{165,166}

The interfacial strain caused by lattice distortion of the microscopic perovskite crystal structure directly affects its optoelectronic properties and accelerates perovskite degradation as well. Strain engineering has been developed as a novel approach to further enhance the performance (e.g., V_{OC}) and operational stability of devices.¹¹ So far, this field is still lack of reports reaching 95% of the S-Q limit in V_{OC} . The soft and elastic nature of polymer is highly valuable in regulating residual strain during perovskite formation, and provide intrinsic moisture resistance.¹²⁻¹⁴ Whereas, due to strong coordinate interaction with perovskite precursors, polymer-based complexes are easy to precipitate from perovskite solutions when incorporated in large amounts for regulation.¹⁵⁻¹⁷ An alternative approach is to incorporate cross-linkable ligands into perovskite precursor solutions or through an antisolvent technique and trigger in-situ polymerization under the stimulus of thermal or ultraviolet during or after the solidification of perovskite films.¹⁸⁻²⁰ So far, most related works synchronously fed monomers into perovskites and induced spontaneous but uncontrollable polymerization, which might cause uncertainty of perovskite precursor stoichiometry and colloidal size, thus disrupting the delicate perovskite crystallization process. There is a lack of synergy works that implement delicate perovskite crystallization manipulation and provide all-around protection of perovskites.

Crosslinking methods commonly employed in the stabilization of perovskite crystal structures can be broadly categorized into small molecule crosslinking and polymer crosslinking. Small molecule crosslinking utilizes agents such as diamines or dicarboxylic acids, which react with organic cations present in the perovskite crystals to form chemical bonds. This process significantly enhances the stability of the perovskite crystal structure. This process significantly enhances the stability of the perovskite crystal structure. For example, 1,3-propanediamine (PDA) can crosslink with methylammonium cations, effectively reducing ion migration within the perovskite layer and improving the stability of the device.

Polymer crosslinking, such as with polyethyleneimine (PEI) or polyvinyl alcohol (PVA), plays a crucial role in enhancing the stability of perovskite crystals by forming a dense network structure. This network significantly reduces the vulnerability of the perovskite layer to moisture and oxygen. The crosslinking reactions occur between the organic or inorganic components of the perovskite crystals. However, most current research in this area involves the simultaneous injection of monomers into the perovskite matrix, triggering spontaneous but uncontrolled polymerization. This lack of control can lead to uncertainties in the stoichiometry of the perovskite precursors and the size of colloidal particles, thereby disrupting the precise crystallization process of the perovskite material.

The lack of effective crystallization control frequently introduces defects into the perovskite film, compromising its structural integrity and optoelectronic performance. Furthermore, current research in perovskite materials lacks synergistic strategies that can simultaneously fine-tune the crystallization process while providing comprehensive protection to the perovskite. Typically, existing approaches focus either on enhancing the stability of the perovskite film or on promoting crystallization, but they overlook achieving both objectives simultaneously in a single process. This indicates a significant gap in the ability to regulate perovskite crystallization dynamics while constructing an effective protective system, which is crucial for improving the long-term stability and high performance of perovskite solar cells.

This work demonstrated the asynchronous incorporation of cross-linkable agents to trigger a controllable co-polymerization at perovskite surface and GBs (Figure 5. 1A). We pre-embedded a new cross-linking initiator, divinyl sulfone (DVS), into perovskite precursor solution. As a co-solvent with low coordination ability (low donor number, DN), DVS implemented the intermediate-dominated perovskite crystallization manipulation through a favoured FAI-DVS-based solvate transition, keeping the kinetic balance between perovskite nucleation and crystal growth and thus delivering high-quality perovskite films with low defect density. More importantly, the pre-embedded cross-linking initiator triggered the three-dimensional co-polymerization into a

controllable macro reticular structure through a post-treated nucleophilic glycerine (gly) reagent. The copolymer scaffolds passivated the intrinsic defects at the perovskite surface and GBs and released the residual strain at the near-surface region. As a result, we achieved a maximum PCE of 25.22% (certified 24.6%) with a maximum V_{OC} of 1.229 V (0.301 V deficit in 1.53 eV bandgap perovskite), coincident with the measured non-radiative recombination loss of only 52.5 mV from ELEQE. These values are among the best in all reported FA-dominated perovskite systems. This all-around copolymerization significantly enhanced the moisture resistance of perovskite films and devices and achieved the long-term operational stability of PSCs under ambient conditions ($T_{90} > 1800$ h).

5.2 Result and discussion

The cross-linking initiator, DVS, was firstly incorporated into perovskite precursor solution as a co-solvent and mixed with the primary solvent DMF in an appropriate volume ratio (0 to 20%, v:v). The conventional solvent system (DMF/DMSO=5:1, v:v) was used for comparison. It should be noted that the crystallization kinetics of perovskite film is not only determined by the boiling point, viscosity, and vapour pressure of solvent systems but also highly affected by the coordinate chemistry within the perovskite ink, as well as the intermediate phase transition.

Donor number (DN) is a quantitative measurement of the Lewis basicity of a solvent that evaluates its coordinate interaction with Lewis acid (e.g., PbI_2).¹⁷⁴ In order to study the precursor chemistry within the DVS-based solvent system, we first examined the DN of DVS by ^{23}Na nuclear magnetic resonance (NMR) spectroscopy. A series of common organic solvents were selected with reported DN values (Table 5. 1). An appropriate amount of $NaClO_4$ was dissolved into these solvents to prepare a 0.2 M

solution. The DN of DVS was extracted from the linear fitting against ^{23}Na NMR shift to be 17.3 kcal/mol (Figure 5. 1B, Figure 5. 2, Table 5. 1), much lower than the commonly used aprotic organic solvents (e.g., DMSO).

As a result, DVS is a low Lewis basic solvent, which exhibits weak coordinate interaction with PbI_2 (Figure 5. 3). In contrast, there is a strong interaction between DVS and ammonium iodide (e.g., FAI). We dissolved FAI into DVS, delivering a clear solution but with a different colour compared with the DVS solvent (Figure 5. 3). We observed new diffraction peaks at $2\theta=12.78^\circ$ and 14.19° besides the characteristic peaks of FAI powder when X-ray diffraction (XRD) spectroscopy was performed on the quasi-wet film using FAI in DVS solution (Figure 5. 4), which may indicate a new solvate phase based on FAI-DVS. ^1H NMR result also verifies this chemical interaction (Figure 5. 1C). The hydrogen chemical shifts are located at 7.854 and 8.748 ppm for pure FAI solution, whereas, in FAI/DVS solution, we observe a notable shift and split of the hydrogen signals at 7.845, 8.631 and 8.666 ppm, implying different chemical environment and a strong chemical interaction between DVS and FA^+ .

We analyzed the time-resolved UV-vis absorption spectroscopy during the antisolvent-assisted spin-coating to provide a comprehensive insight into the perovskite crystallization kinetics affected by the DVS pre-embedded precursor solution. Figure 5. 1D shows the two-dimensional pseudo-colour absorption intensity mapping as a function of spin-coating time. We dripped chlorobenzene (CB) upon the surface of the perovskite wet film during spin coating (at 25 s). We found the sample from DVS-based perovskite ink (DMF/DVS=5:1, v:v) shows much faster nucleation kinetics compared

to that from DMSO-based ink (DMF: DMSO=5:1, v:v) (Figure 5. 5). During thermal annealing, the as-cast perovskite films were treated with gly to trigger co-polymerization at the perovskite surface and GBs as well. We used the same technique to quantify the perovskite crystal growth rate in this process. Figure 5. 6A shows the pseudo-colour mapping of the UV-vis absorption spectra as a function of annealing time. The absorption profile at 450 nm was extracted, and the average crystal growth rates were calculated to be 0.073 and 0.061 s⁻¹, respectively, for the control and DVS-gly-based perovskite films (Figure 5. 7).

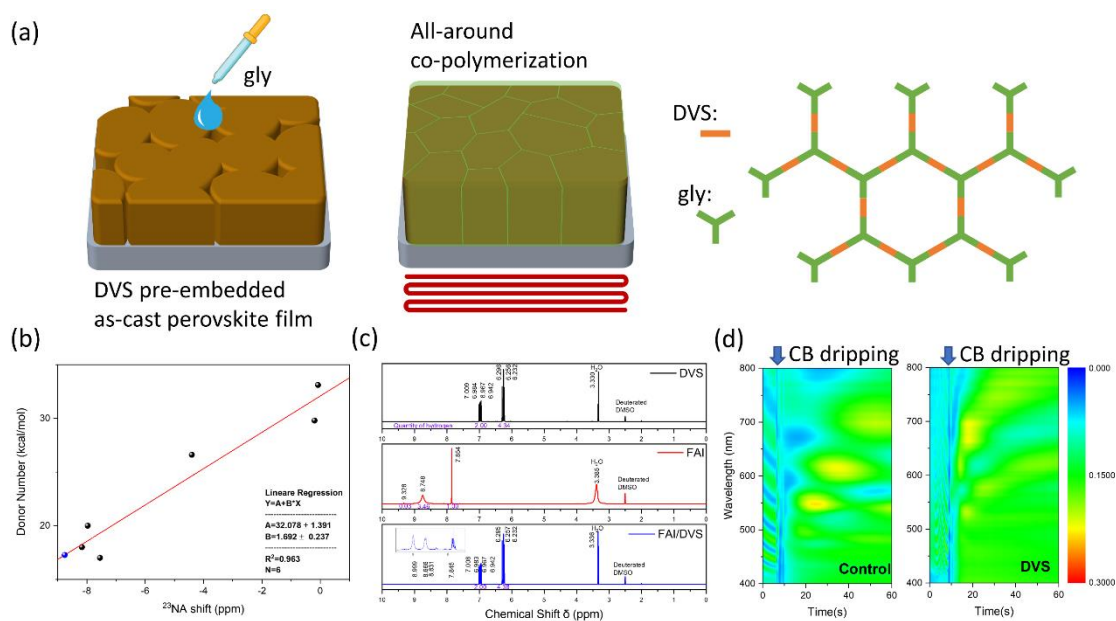


Figure 5. 1 (A) Schematic illustration of intermediate-dominated perovskite crystallization by pre-embedded DVS and all-around co-polymerization protection through the post-treatment of gly. (B) Linear fitting of ²³Na NMR chemical shift and DN of the selected organic solvents to calculate the DN of DVS. (C) ¹H NMR spectra of FAI, DVS, and FAI/DVS into DMSO-d₆ solution, respectively. (D) Two-dimensional pseudo-color absorption intensity mapping as a function of spin-coating time during the in-situ measurement.

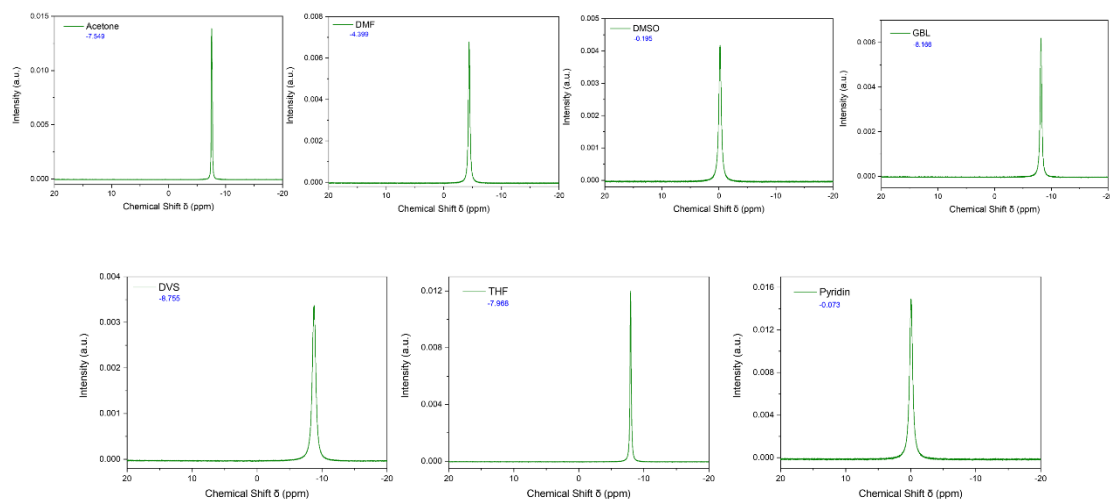


Figure 5. 2 ^{23}Na nuclear magnetic resonance (NMR) spectra for common organic solvents and DVS.

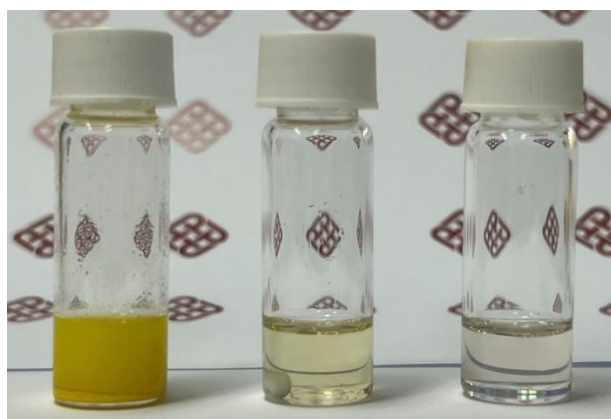


Figure 5. 3 Photo images of PbI_2 power in DVS (left), FAI powder in DVS (middle), and DVS solvent (right)

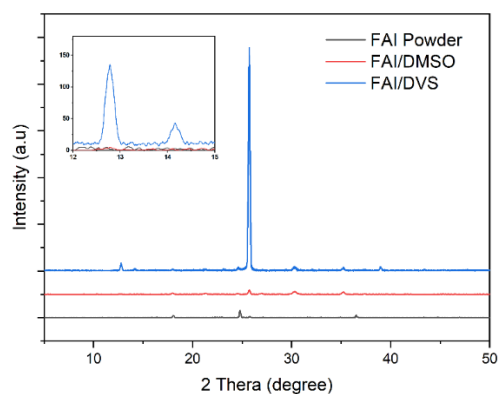


Figure 5. 4 XRD patterns of FAI powder and quasi-wet films by FAI/DMSO and FAI/DVS solutions;

inset: the diffraction peaks of FAI-DVS solvate.

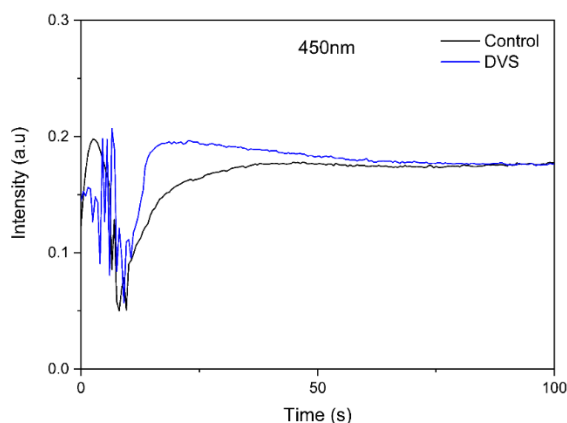


Figure 5. 5 UV-vis absorption intensity evolution at the wavelength of 450 nm during anti-solvent assisted spin coating of the control and DVS-based perovskite inks.

Table 5. 1 ^{23}Na NMR shift for a series of common organic solvents to calculate the DN for DVS.

Solvents	DN (kcal/mol)	^{23}Na shift (ppm)
Acetone	17	-7.549
DMF	26.6	-4.399
DMSO	29.8	-0.195
GBL	18	-8.166
THF	20	-7.968
Pyridin	33.1	-0.073
DVS	17.3	-8.755

We further detailedly diagnosed phase transitions that occurred during the thermal annealing process, using in-situ XRD spectroscopy between the control and DVS-gly-based samples. For the as-cast control sample, besides the characteristic diffraction peaks of cubic FAPbI₃ at $2\theta=14.01^\circ$, 19.88° , 24.39° , and 28.24° , corresponding to (001), (011), (111) and (002) planes, we observed the signal of MAI-PbI₂-DMSO based solvate at $2\theta<10^\circ$ (Figure 5. 6A). For comparison, the as-cast DVS-based perovskite film shows two distinct diffraction peaks at $2\theta=11.51^\circ$ and 24.05° , gradually vanishing

with thermal annealing (Figure 5. 6B, Figure 5. 6C, and Figure 5. 8B). This signal is likely ascribed to the FAI-DVS solvate, which confirms that cubic perovskite nanocrystals and additional FA-based intermediate complex transition co-exist in the DVS-based sample. We extracted the XRD intensity of the perovskite prominent peak at $2\theta=14.01^\circ$ as a function of annealing time, as shown in Figure 5. 6D. There is a pronounced delay of perovskite crystal growth for the DVS-gly-based sample, which is mainly due to the necessary thermal energy to dissociate the intermediate and recrystallize into the cubic perovskite phase, as well as to induce the co-polymerization. It has been well recognized that delayed crystal growth is favoured to form high-quality perovskite films with better crystallinity, more dominated grain orientation, and lower defect density.¹⁷⁵

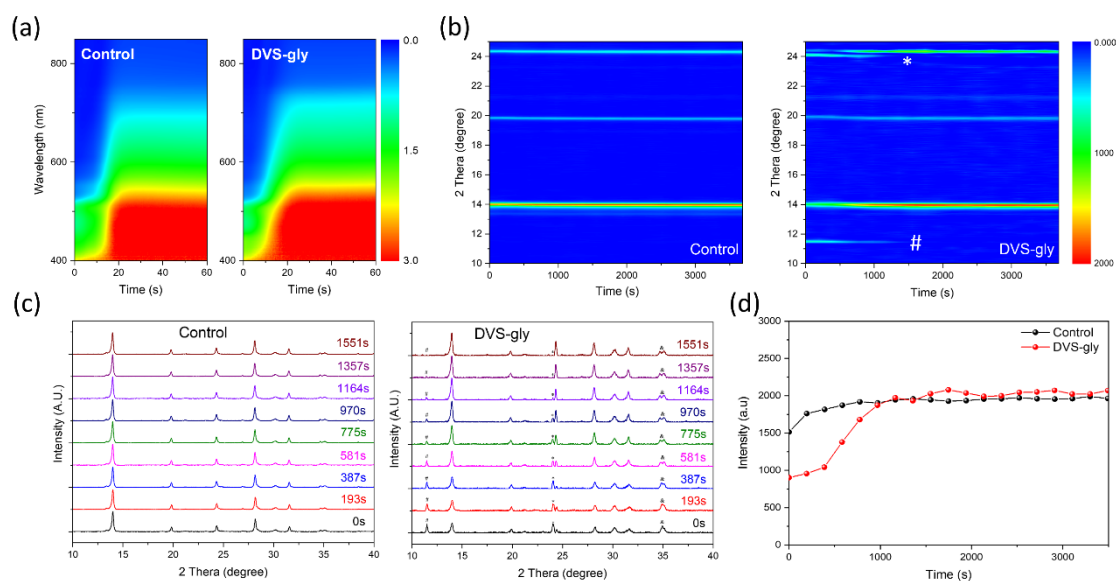


Figure 5. 6 (A) Pseudo-colour mapping of the UV-vis absorption spectra as a function of annealing time. (B) In-situ XRD measurement of the control and DVS-gly based perovskite films during thermal annealing (intermediate phases presented by # and * symbol can be ascribed to FAI-DVS

solvate). (C) Corresponding XRD spectra as a function of annealing time. (D) XRD intensity evolution of the perovskite prominent peak at $2\theta=14.01^\circ$.

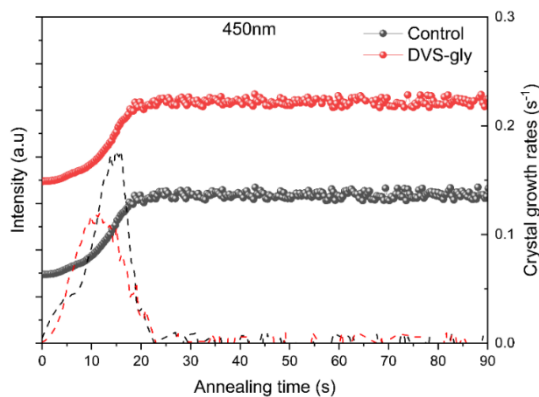


Figure 5. 7 UV–vis absorption intensity evolution at the wavelength of 450 nm and t for the control and DVS-gly based perovskite films during thermal annealing and their corresponding crystal growth rate.

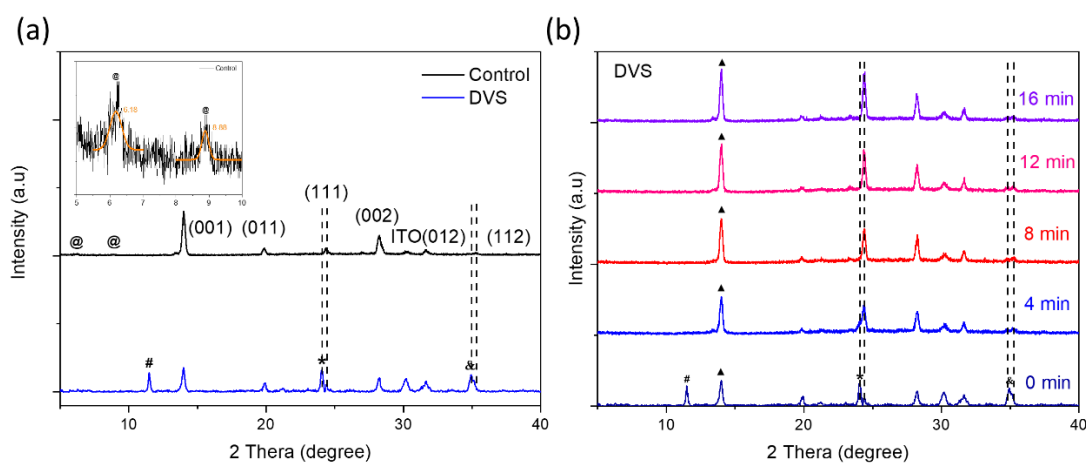


Figure 5. 8 (A) XRD patterns of the as-cast control and DVS-based perovskite films (intermediate phases presented by # and * symbol can be ascribed to FAI-DVS solvate); inset: intermediate phase presented by @ is assigned to MAI-PbI₂-DMSO based solvate. (B) XRD patterns as a function of annealing time for the DVS-based sample in intervals of 4 minutes each (▲ is corresponding to the perovskite central peak).

In our study, the nucleophilic reagent, glycerin (gly), was used for the post-treatment upon the as-cast DVS-embedded perovskite films. Cross-link reaction was precisely controlled by optimizing the molar ratio of glycerol versus DVS (from 0 to 3 mol%) and spin-coating parameters to ensure uniform film coverage without excess residues.

The resulting cross-link scaffold provided superior water resistance, released residual tensile strain near the perovskite surface, and suppressed deep-level defects. Compared with the control device, our strategy significantly improved the overall device performance, especially in open-circuit voltage (V_{oc}) and fill factor (FF). We also demonstrated the device performance dependence on the molar ratio of gly versus DVS, as shown in Figure 5. 9 and Table 5. 2. From 0 to 1.5 mol%, there is a slight improvement in V_{oc} , whereas, further increasing to 3 mol% shows a downtrend in FF values.

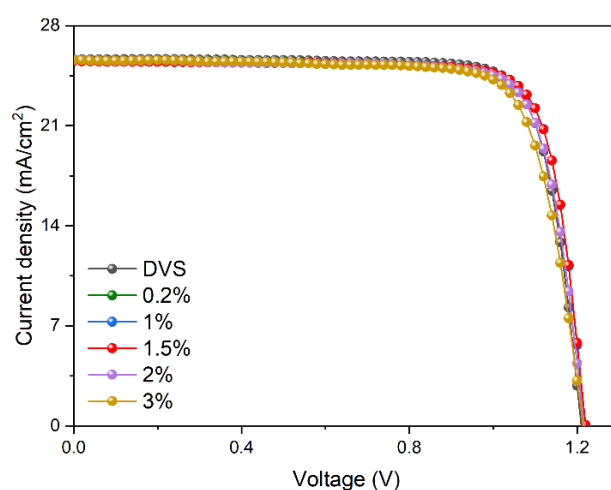


Figure 5. 9. The JV curves at different glycerol concentrations.

Table 5. 3 Photovoltaic parameters at different glycerol concentrations under optimized conditions.

Molar Ratio (Gly:DVS)	V _{oc} (V)	J _{sc} (mA cm ⁻²)	FF (%)	PCE (%)
Only DVS	1.210	25.64	80.83	25.084
0.2%	1.216	25.53	81.23	25.213
1%	1.219	25.54	80.97	25.221
1.5%	1.220	25.51	81.03	25.225
2%	1.217	25.59	79.82	24.857
3%	1.215	25.61	78.20	24.329

Cross-link reaction between the pre-embedded initiator (DVS) and post-treated nucleophilic reagent (gly) was confirmed through Fourier transform infrared spectroscopy (FTIR) and matrix-assisted laser desorption/ionization time-of-flight mass spectrometry (MALDI-TOF-MS). In FTIR, the characteristic signal of DVS with the C=C stretching vibration of $\nu_{C=C}$ at 1610 cm^{-1} was diminished after thermal annealing, while a distinct peak corresponding to the stretching vibration of C-O-C at 1275 cm^{-1} and 830 cm^{-1} appeared (Figure 5. 10A).^{176,177} This result validates the high reactivity in nucleophile-mediated oxa-Michael addition reactions between DVS and gly (Figure 5. 12).¹⁷⁸ It should be noted that this addition reaction is the sole pathway for the controllable co-polymerization into the macro reticular structure. Furthermore, the characteristic peaks of S=O at 1310 and 1132 cm^{-1} are displayed in both the as-cast and post-treated samples, confirming the existence of DVS-gly co-polymer in final perovskite after thermal annealing (Figure 5. 11). MALDI-TOF-MS was further

performed to examine the cross-link reaction, which verifies the presence of a few fragments in the DVS-gly network (Figure 5. 10B, details in Note 5. 1).

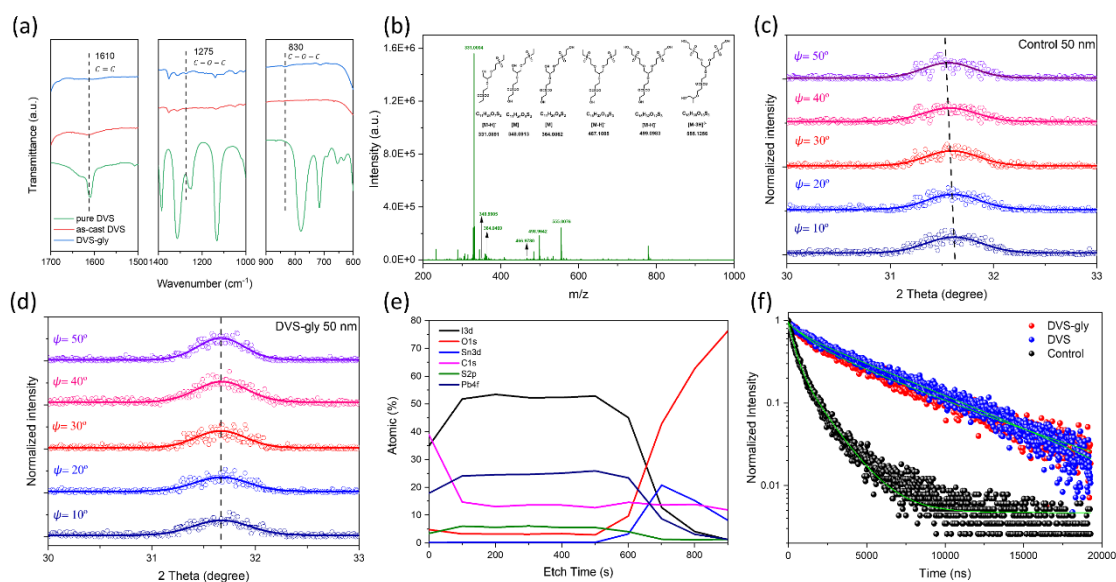


Figure 5. 10 (a) After annealing, FTIR spectra in selected regions for the DVS solvent, as-cast DVS-based perovskite film, and DVS-gly-based perovskite final film. (b) MALDI-TOF-MS measurement for the DVS/gly mixture solution. (c-d) GI-XRD spectra in 2θ - $\sin 2\psi$ mode for (c) control and (d) DVS-gly based perovskite films at near-surface region (50 nm depth), respectively. (e) In-depth XPS spectra for the DVS-gly-based perovskite film. (f) TRPL decay for the control, DVS, and DVS-gly-based perovskite films.

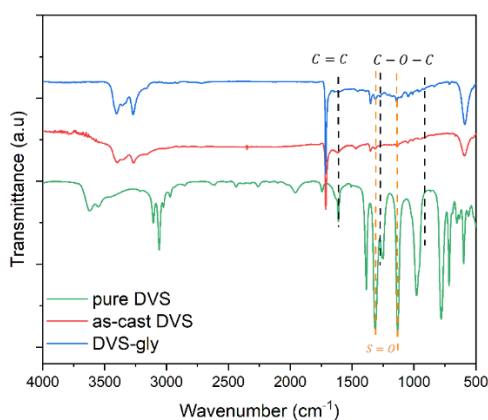


Figure 5. 11 FTIR spectra for the DVS solvent, as-cast DVS-based perovskite film, and DVS-gly-based perovskite final film after annealing.

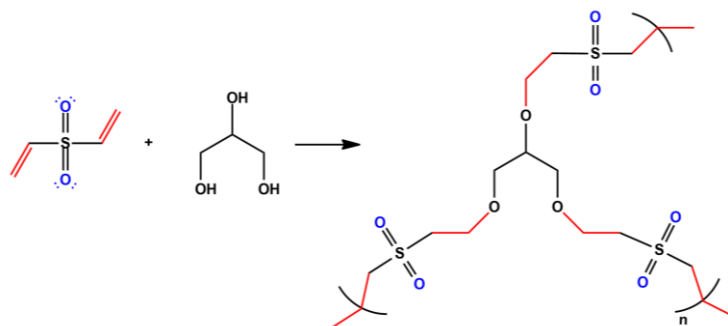


Figure 5. 12 Nucleophile-mediated oxa-Michael addition reactions between DVS and gly.

Note 5. 1 MALDI-TOF-MS data:

$C_{11}H_{24}O_7S_2$ for $[M-H]^-$: calculated 331.0891(m/z); found 331.004 (m/z). $C_{11}H_{24}O_8S_2$ for $[M]$: calculated 348.0913 (m/z); found 348.9905 (m/z). $C_{11}H_{24}O_9S_2$ for $[M]$: calculated 364.0862 (m/z); found 364.0469 (m/z). $C_{15}H_{32}O_{10}S_3$ for $[M-H]^-$: calculated 467.1085 (m/z); found 466.9780 (m/z). $C_{15}H_{32}O_{12}S_3$ for $[M-H]^-$: calculated 499.0983 (m/z); found 498.9642 (m/z). $C_{18}H_{38}O_{13}S_3$ for $[M-3H]^{3-}$: calculated 555.1256 (m/z); found 555.0076 (m/z)

After controllable co-polymerization and perovskite crystal growth, the control, DVS, and DVS-gly-based perovskite films showed identical XRD patterns, and no low-dimensional perovskites or non-perovskites were detected (Figure 5. 13A), corresponding to the characteristic diffraction peaks of cubic $FAPbI_3$, which may indicate that the DVS-gly co-polymer scaffold distributes at perovskite surface and GBs. Among them, the DVS-gly-based perovskite film exhibits the sharpest XRD patterns, with the full width at half maximum (FWHM) of (100) narrowed down from 0.231° to 0.193° , indicating better crystallinity (Figure 5. 13B). Top-view scanning electron microscopy (SEM) image of DVS-gly based perovskite film displays a homogenous

and compact grain, with slightly enlarged GBs (Figure 5. 14), which validates that the DVS-gly scaffold was mainly constructed at perovskite GBs during thermal annealing.

It's well known that the lattice mismatch mainly arises from unfavoured phase transition and perovskite grain propagation, inducing the residual strain and intrinsic defects in final perovskite films and eventually accelerating perovskite degradation.¹⁷³ Here, we performed depth-dependent grazing incident X-ray diffraction (GI-XRD) in $2\theta\text{-sin}^2\psi$ mode to identify the lattice mismatch and analyse the evolution of residual strain across the perovskite film through varying grazing incident angles (Figure 5. 10C and D). The nearly equivalent depth-dependent XRD patterns show that the film had the same cubic phase structure at each depth. We selected two typical regions (50 nm at near perovskite surface and 200 nm in bulk) by varying the appropriate incident angles. The (012) plane at $2\theta=31.6^\circ$ is characteristic for strain analysis due to its high diversity, which is generally adopted to acquire more grain information and alleviate the orientation effect on the linear relationship of $2\theta\text{-sin}^2\psi$ in this method.¹⁷⁹ For the control sample, we observed a pronounced shift of (012) peak to the smaller 2θ along with the increase of instrument tilt angle ψ , which indicates an increase of crystal plane distance $d(012)$ and thus the tensile strain bears at the near-surface region (Figure 5. 10C).

In comparison, the position of the (012) peak almost remained unchanged for the DVS-gly-based perovskite, which suggests that the soft nature of the DVS-gly copolymer scaffold could effectively signify the uneven distribution of residual tensile strain at the near-surface region (Figure 5. 10D). We observed the same function for the

DVS-gly sample in the bulk region (Figure 5. 15), which implies the co-polymer network may penetrate through the whole thickness of perovskite film. In-depth element analysis using X-ray photoelectron spectroscopy (XPS) was further performed to prove that the DVS-gly co-polymer was uniformly distributed across the whole perovskite film, with constant characteristic signals of S and O element within 500 s etching (Figure 5. 10E). These results imply that our strategy provides all-around protection at perovskite surface and GBs.

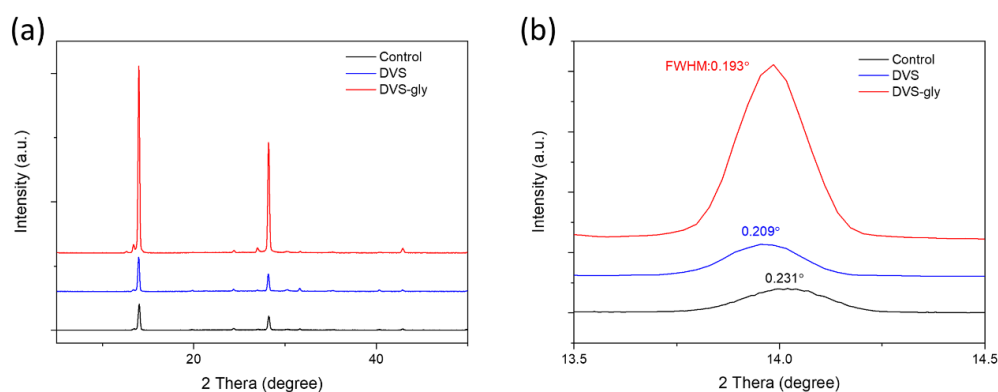


Figure 5. 13 (A) After thermal annealing, XRD patterns of the final control, DVS-based, and DVS-gly-based perovskite films. (B) FWHM of the perovskite prominent peak at $2\theta=14.01^\circ$ for the corresponding samples.

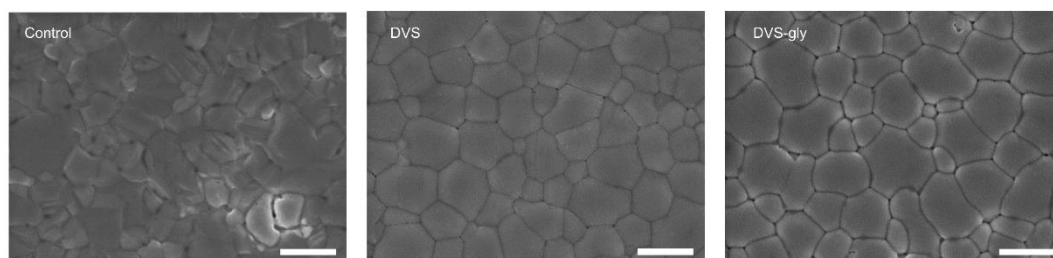


Figure 5. 14 SEM top view images of the control, DVS-based, and DVS-gly-based perovskite films; scale bar: 1 μm .

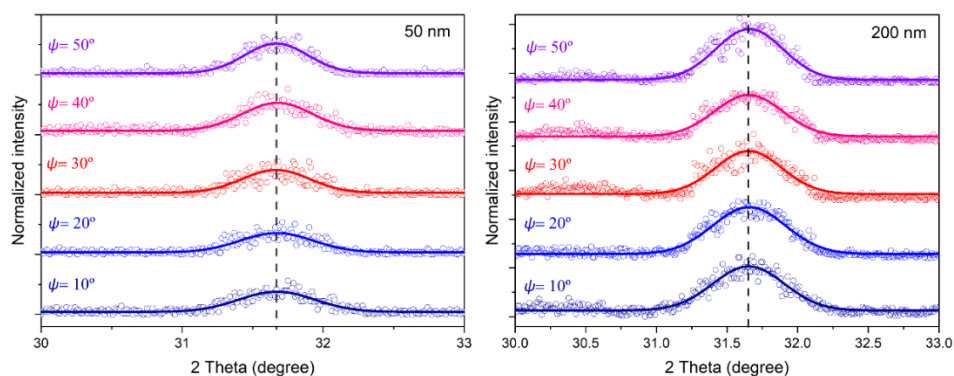


Figure 5. 15 GI-XRD spectra in $2\theta\text{-sin}^2\psi$ mode for the DVS-gly based perovskite films at near-surface region (50 nm depth, left) and in bulk (200 nm depth, right), respectively.

Steady-state and time-resolved photoluminescence (TRPL) spectra were conducted to explore the charge recombination behaviour in the perovskite films. The DVS-gly-based sample shows a much more pronounced and slightly blue-shifted PL peak (805 nm) compared with the control perovskite film (809 nm), which is a sign of a reduced trap density of state (tDOS) near the band tail (Figure 5. 16). TRPL decay spectra were fitted using the bi-exponential function, and the fitting parameters are summarized in Table 5. 4. It should be noted that the excitation fluence in our study is very low ($636.2\text{ nm}, \leq 5\text{ nJ/cm}^2$), which only generates a much lower density of free carriers ($2.4 \times 10^{14}\text{ cm}^{-3}$, much lower than the trap density) compared with that of trap states.¹¹⁹ In this condition, TRPL decay mainly responds to the trap-assisted recombination behaviour in the bulk perovskite. Compared with the control sample (782.88 ns), the DVS and DVS-gly-based samples show a much prolonged lifetime on average (4091.66 and 4682.63 ns, respectively), which indicates that this strategy significantly reduces non-

radiative recombination both through the delicate crystallization manipulation and effective passivation by the co-polymer network (Figure 5. 10F).

We fabricated the conventional n-i-p PSCs assembled with the structure of ITO/SnO₂/perovskite/spiro-OMeTAD/Au, using the perovskite ink mixed with an appropriate amount of DVS (0 to 20%, v:v, regarding the primary solvent DMF). We first examined the work functions of the corresponding perovskite films using ultraviolet photoemission spectroscopy (UPS), as shown in. These samples display a downward trend of work functions (-4.513, -4.629, and -4.691 eV for control, DVS, and DVS-gly-based perovskite films, which may relate to the relief of negatively charged iodine interstitial (I_i⁻) defects.¹⁸⁰ Figure 5. 18 shows the J-V curves of the best-performance devices under different volume ratios of DVS, and Table 5. 5 summarizes their photovoltaic characteristics. Along with the volume ratio DVS from 0 to 20%, V_{OC} values exhibit an increasing trend from 1.200 to 1.229 V. At the same time, J_{SC} almost keeps constant at $\sim 25.2 \text{ mA cm}^{-2}$, which is well agreed with the integrated value from external quantum efficiency (EQE) spectra (Figure 5. 19B, less than 3% mismatch). Among them, devices from the ink with 7% DVS deliver the highest efficiency, with a maximum PCE of 25.08%. More importantly, after co-polymerization through the post-treatment of gly, the DVS-gly-based devices further enhance the efficiency up to 25.22% (certified 24.63%), as shown in Figure 5. 19A, and Figure 5. 20, with a maximum V_{OC} of 1.229 V. The photovoltaic bandgap (E_g^{IP}) of the FA-dominated perovskite used in this work was calculated to be 1.53 eV from the first differential of EQE spectra (Figure 5. 21), corresponding to a V_{OC} deficit as low as 0.301 V. This value is the lowest among

all reported FA-dominated perovskite systems (Table 5. 6). When upscaling the device area, we achieved the maximum PCE of 21.75% for the minimodule (3-subcells, 3.6*3.6 cm² substrate, Figure 5. 23).

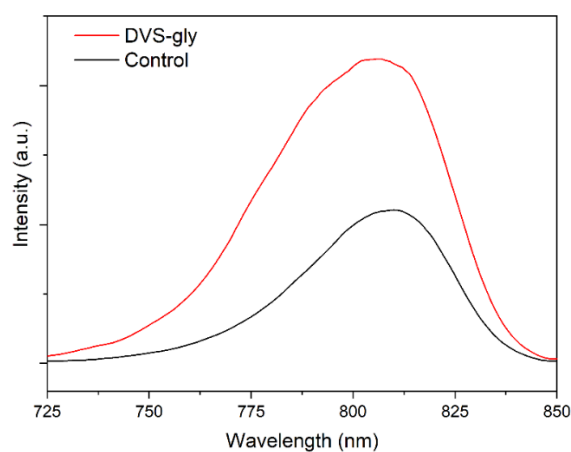


Figure 5. 16. Steady-state PL spectra for the control and DVS-gly-based perovskite films.

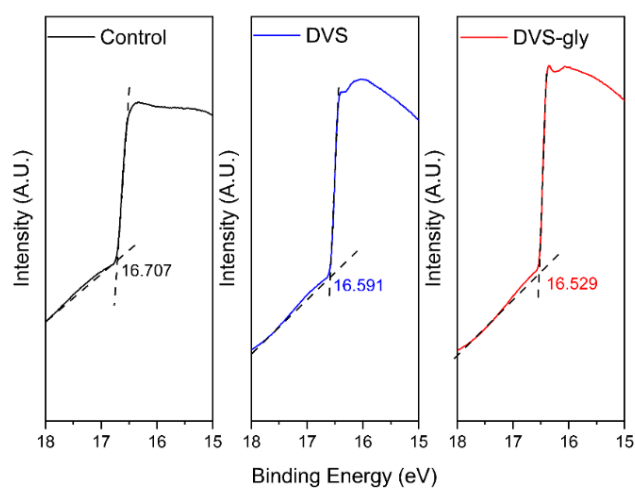


Figure 5. 17. UPS results at the cut-off region for the control, DVS-based, and DVS-gly-based perovskite films.

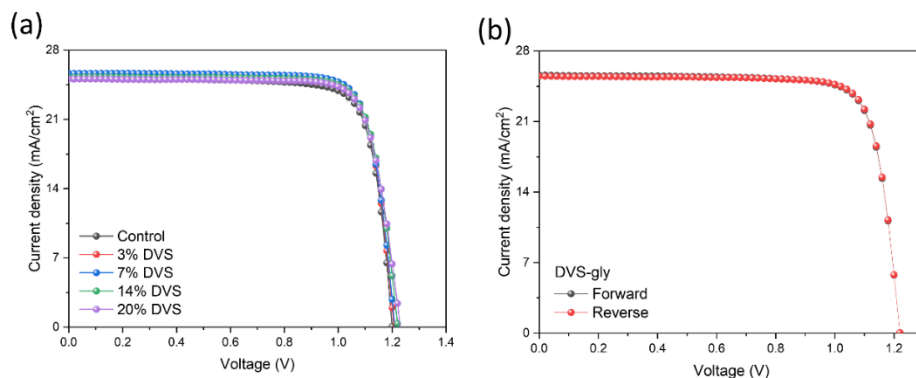


Figure 5. 18 (A) J - V curves for the PSCs based on the ink with different volume ratio of DVS. (B) Representative J - V curves of the DVS-gly-based devices under forward and reverse scanning, respectively.

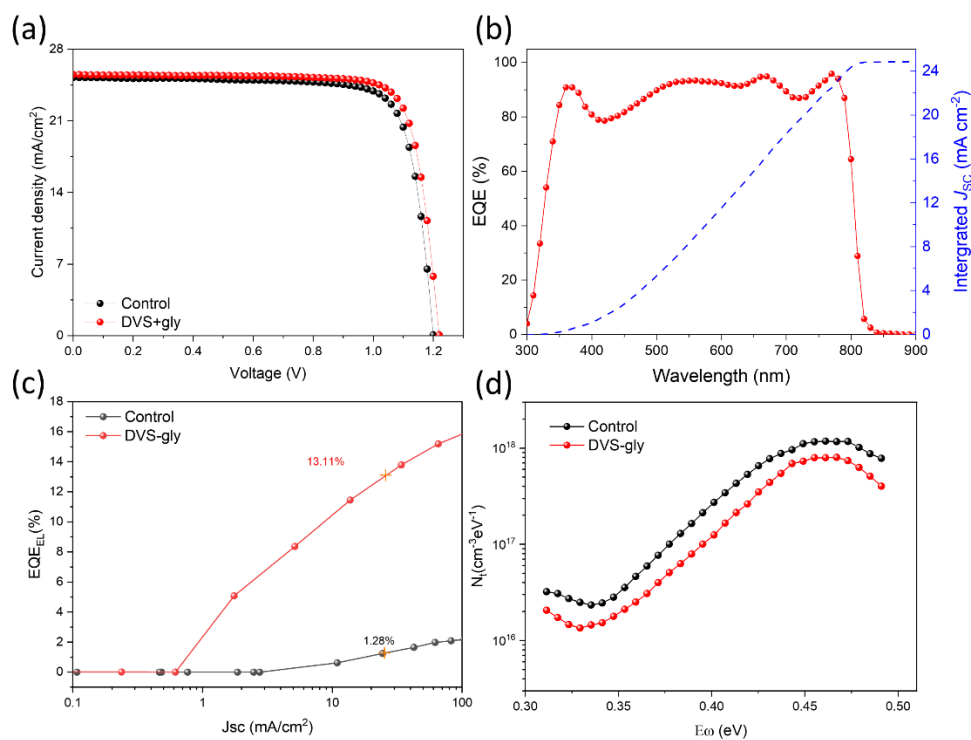


Figure 5. 19 (A) J - V curves of the best-performance control and DVS-gly-based devices. (B) EQE spectrum of the DVS-gly based PSCs. (C) EQE_{EL} as a function of the injection current density to calculate the nonradiative recombination loss. (D) Energetic distribution of trap density for the control and DVS-gly based PSCs measured by admittance spectroscopy.

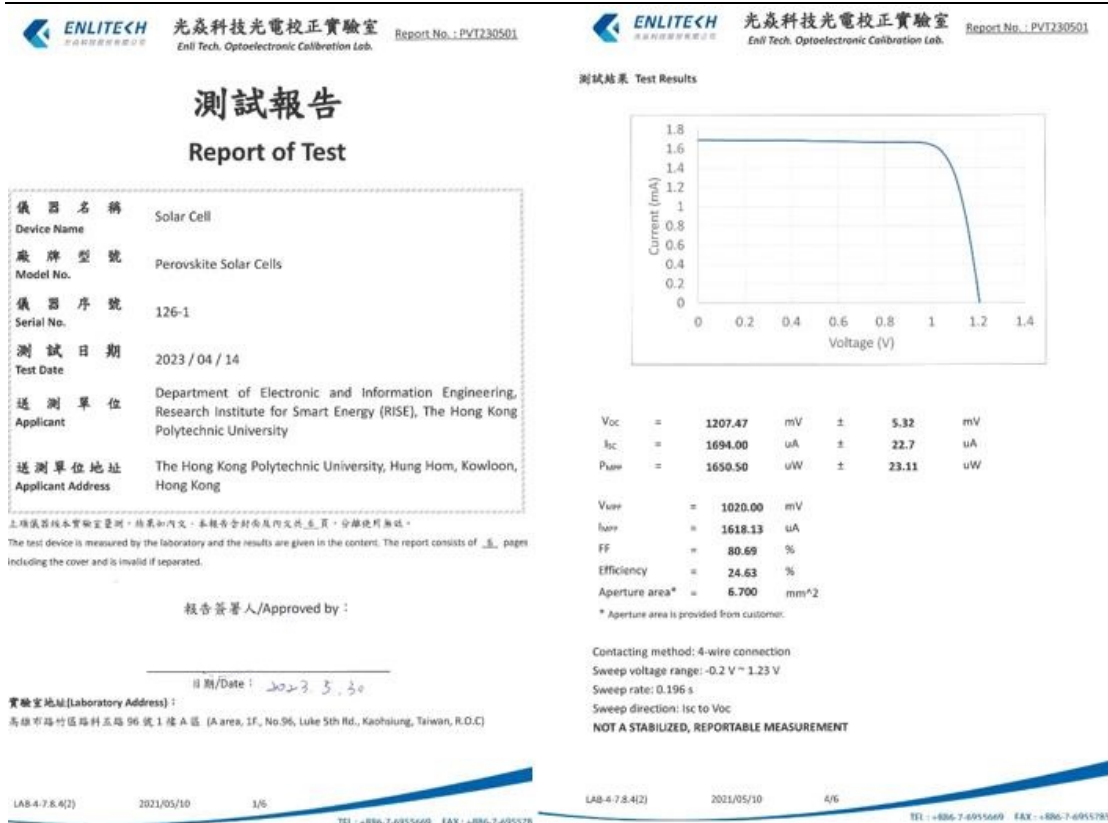


Figure 5. 20. Certified results from an Taiwan Accreditation Foundation (TAF) accredited photovoltaic certification laboratory (Enli Tech. Optoelectronic Calibration Lab., Taiwan). The certified PCE is 24.63% - certified aperture with the area of 0.067 cm².

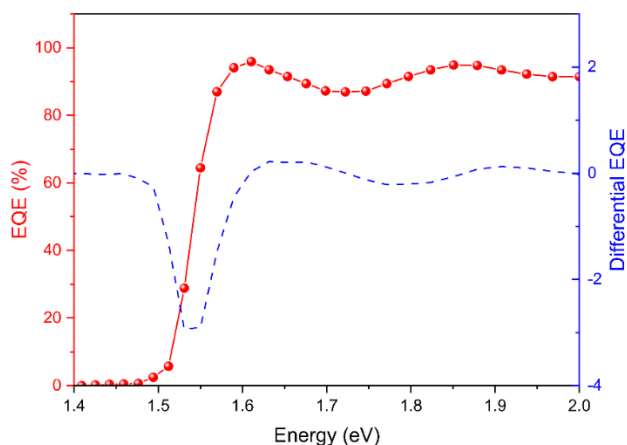


Figure 5. 21 Calculation of the bandgap for the DVS-gly-based perovskite films through EQE spectra. The maximum differential value of EQE can determine E_g^{IP}.

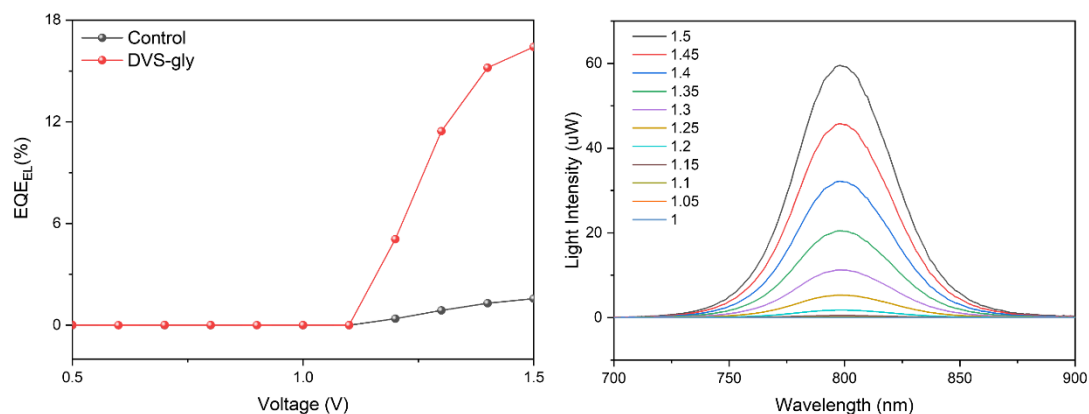


Figure 5. 22 (A) EQE_{EL} as a function of the applied voltage bias for the DVS-gly based PSCs when operating as LEDs. (B) EL spectra for the representative DVS-gly based device under voltage bias from 1 to 1.5 V.

Table 5. 4 Fitting parameters of the bi-exponential decay function in TRPL spectra for the corresponding perovskite films.

Conditions	A ₁	τ ₁ [ns]	A ₂	τ ₂ [ns]	Average decay time ^{a)} τ [ns]
Control	0.623	390.31	0.328	1534.45	782.88
DVS	0.341	1275.96	0.581	5744.05	4091.66
DVS-gly	0.201	910.74	0.725	5728.27	4682.63

^{a)}Average decay time was calculated according to the equation: $\tau = (A_1\tau_1 + A_2\tau_2)/(A_1 + A_2)$.

Table 5. 5 Photovoltaic parameters of the DVS based devices with different volume ratios of DVS into DMF host solvent.

DMF/DVS v:v (%)	V _{OC} (V)	J _{SC} (mA cm ⁻²)	FF (%)	PCE (%)	
				Average	Best
100:0	1.200	25.21	79.77	23.66±0.37	24.14
100:3	1.207	25.57	81.04	24.51±0.30	25.00
100:7	1.210	25.64	80.83	24.80±0.22	25.08
100:14	1.221	25.24	80.46	24.37±0.33	24.80
100:20	1.229	25.08	79.82	24.09±0.35	24.61

Table 5. 6 Summary of the state-of-the-art values of V_{OC} deficit and non-radiative recombination loss ($\Delta V_{OC,nr}$) reported in other relevant works.

Perovskite bandgap E_g [eV]	Maximum V_{OC} [V]	V_{OC} deficit ^{a)} [V]	$\Delta V_{OC,nr}$ ^{b)} [V]	Reference
1.57	1.195	0.375	NA	181
1.53	1.18	0.35	0.070	88
1.516	1.173	0.343	NA	182
1.56	1.225	0.335	NA	153
1.536	1.21	0.326	0.074	109
1.53	1.21	0.32	0.060	183
1.53	1.22	0.31	0.054	184
1.53	1.19	0.34	0.0394	185
1.55	1.208	0.342	NA	186
1.53	1.229	0.301	0.0525	This work

^{a)} V_{OC} deficit was calculated from $E_g/q - V_{OC,max}$; ^{b)} $\Delta V_{OC,nr}$ was estimated using the EQE_{EL} at the injection current density equal to J_{SC} with the equation: $\Delta V_{OC,nr} = -\frac{k_B T}{q} \ln EQE_{EL}$.

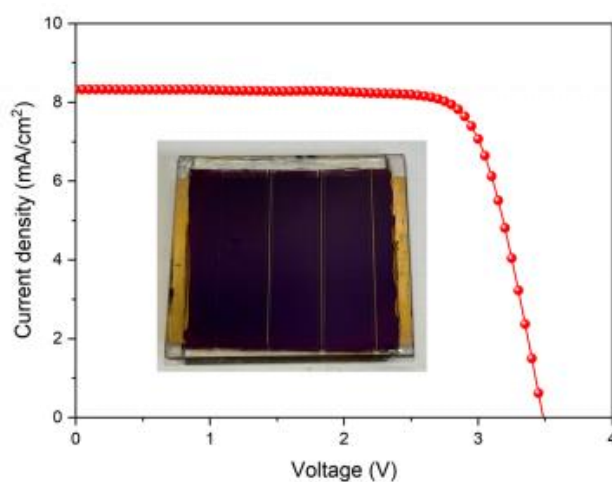


Figure 5. 23. J-V curve for the DVS-gly based minimodule (3-subcells, 3.6*3.6 cm² substrate, active area: 5.85 cm²).

By quantifying the predominated recombination mechanisms, we uncover the increase of V_{OC} in DVS-gly-based devices using the electroluminescence method. We

measured the external quantum efficiency of electroluminescence (EQE_{EL}) when a PSC operating as a light-emitting diode (LED) in forward voltage bias (Figure 5. 19C and Figure 5. 22). The non-radiative recombination loss ($\Delta V_{\text{OC},nr}$) can be derived from the EQE_{EL} at the injection current density equal to J_{SC} .¹⁵¹ Compared with the control device ($\text{EQE}_{\text{EL}}=1.28\%$, $\Delta V_{\text{OC},nr}=113$ mV), The DVS-gly device exhibits a much enhanced EQE_{EL} of 13.11% at the injection current density equal to J_{SC} , corresponding to a $\Delta V_{\text{OC},nr}$ of 52.5 mV, coincident with the V_{OC} deficit from J - V test. This result indicates the hybrid cross-linking significantly suppresses the non-radiative recombination at perovskite surface and GBs, which dominates the V_{OC} enhancement for the DVS-gly-based devices.

Thermal admittance spectroscopy (TAS) was performed to quantitatively estimate the energetic distribution of trap density (N_t) under an AC voltage with the frequency decreased from 10^6 to 100 Hz.⁹⁶ Compared with the control device ($N_t=8.33 \times 10^{16} \text{ cm}^{-3}$), the DVS-gly-based devices display much lower N_t ($5.09 \times 10^{16} \text{ cm}^{-3}$) (Figure 5. 19D). It's well known that deep defects (>0.35 eV here) at perovskite surface and GBs are mainly regarded as the non-radiative recombination center, significantly detrimental to the V_{OC} of PSCs.¹⁸⁷ DVS-gly strategy not only manipulates the delicate crystallization process through the favoured intermediate-dominated transition, delivering high-quality perovskite crystal but also the controllable co-polymerization at perovskite surface and GBs efficiently relieves these intrinsic defects. Our strategy synergistically eliminates the intrinsic deep defects to a great extent and pushes the V_{OC} value close to the radiative limit.

To further study the charge transport/recombination behaviour in PSCs, we performed electrochemical impedance spectroscopy (EIS).¹³⁸ Figure 5. 24A and Figure 5. 24B show Nyquist plots for the control and DVS-gly-based devices under AC bias frequencies from 10^6 to 100 Hz, respectively. The equivalent circuit for simulating charge transfer and recombination is shown in the inset, where R_S is the series resistance of the devices, and R_{rec} is the recombination resistance in the bulk perovskite, inversely related to the rate at which photogenerated carrier recombination. The DVS-gly devices show lower R_S than the control devices, which is highly related to the enhanced FF measured by $J-V$ curves (Figure 5. 24C). More importantly, the higher R_{rec} for the DVS-gly devices is mainly responsible for the reduced recombination rate of photogenerated carriers in the bulk perovskite (Figure 5. 24D), which is in accordance with the enhanced V_{OC} as mentioned before.

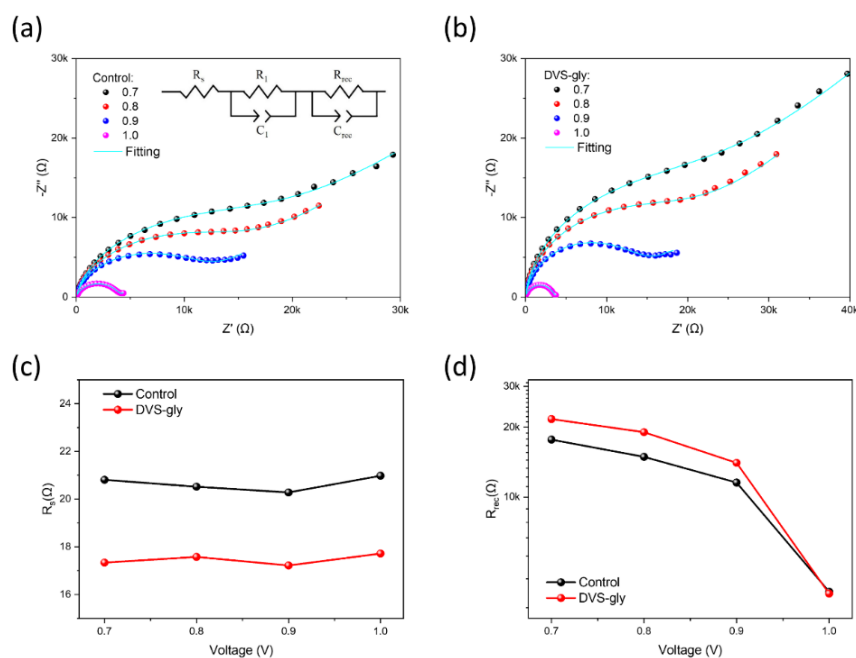


Figure 5. 24 (A-B) Nyquist plots of the control (A) and DVS-gly based PSC (B) in the dark under 0.7 to 1.0 V bias voltage, respectively; Inset: equivalent circuit for the simulation of charge transfer

and recombination process. (C-D) The relationship between bias voltage and (C) R_s and (D) R_{rec} for the corresponding PSCs, respectively.

In addition to the device performance, the long-term stability under various aging conditions, especially the long-term operational stability, is of great significance for the future commercialization of PSC technology. Through inner encapsulation, the DVS-gly co-polymerization strategy provided superior moisture resistance to the perovskite films and devices (Figure 5. 25A and Table 5. 7). The unencapsulated DVS-gly-based perovskite films and devices exhibit much-improved stability directly under water soaking. We monitored the PCE evolution of the encapsulated devices under maximum power point (MPP) and continuous 1-sun illumination (30 ± 5 °C and $60 \pm 5\%$ RH). DVS-gly devices maintained over 90% of their initial PCE after 1800h operation, significantly superior to the control devices (Figure 5. 25B). Besides, we also evaluated the thermal stability and shelf stability of the unencapsulated devices in the glovebox (80 ± 5 °C) and under ambient atmosphere (25 ± 5 °C, $20 \pm 5\%$ RH), respectively (Figure 5. 25C and Figure 5. 25D). DVS-gly devices exhibit both much enhanced thermal stability (maintaining over 91% of their initial efficiency after aging for 408 h) and shelf stability than (holding 98% of their initial PCE over 2300 h) the control devices. It's well known that shallow defects (with low migration activation energy) at perovskite surface and grain boundaries initialize the permeation of moisture and oxygen into the perovskite films to accelerate the degradation of PSCs. The effective

relief of shallow defects and superior moisture resistance through this strategy is responsible for enhanced stability under different aging conditions.¹⁸⁸

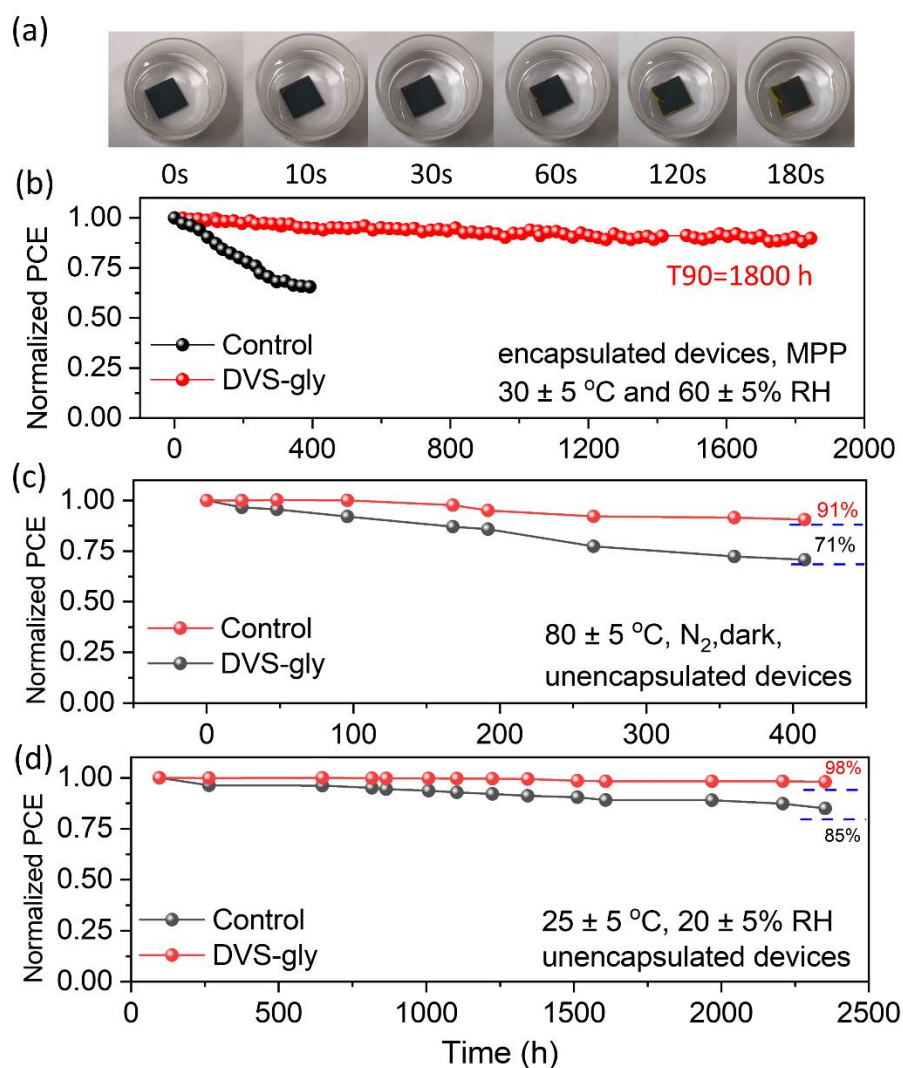


Figure 5. 25 (A) Images of a DVS-gly-based perovskite film directly immersed in water. (b-d) Long-term stability test under (B) MPP tracking (encapsulated devices: 1-sun, $30 \pm 5 \text{ }^\circ\text{C}$, $60 \pm 10\% \text{ RH}$), (C) thermal stress (unencapsulated device: dark, $80 \pm 5 \text{ }^\circ\text{C}$, N_2), (D) shelf storage (unencapsulated device: dark, $25 \pm 5 \text{ }^\circ\text{C}$, $20 \pm 5\% \text{ RH}$).

Table 5. 7 Photovoltaic parameters of unencapsulated devices immersed in water as a function of time.

Control					DVS-gly				
Soaking time (s)	V _{OC} (V)	J _{SC} (mA cm ⁻²)	FF (%)	PCE (%)	Soaking time (s)	V _{OC} (V)	J _{SC} (mA cm ⁻²)	FF (%)	PCE (%)
0	1.191	24.30	80.19	23.21	0	1.209	24.25	81.61	23.92
23	1.188	23.00	77.97	21.31	23	1.205	24.02	81.67	23.64
33	1.135	21.37	75.86	18.40	33	1.204	23.97	80.67	23.28
					150	1.205	23.53	79.99	22.68
					180	1.207	23.39	79.34	22.39

5.3 Conclusion

This work provided an insightful strategy to synergically implement delicate perovskite crystallization manipulation and provide all-around protection at the perovskite surface and GBs during the perovskite forming process. The pre-embedded DVS dominated the FA-based intermediate transition during the delicate manipulation of perovskite crystallization and induced a three-dimensional co-polymerization through gly post-treatment upon as-cast films. We validated that the polymer scaffold passivated the intrinsic defects at the perovskite surface and GBs and released the residual strain at the near-surface region. We achieved superior device performance among the FA-dominated perovskite system. This strategy significantly improved the moisture resistance and enhanced long-term operational stability, which may advance the commercialization of this promising PV technology.

5.4 Experimental Section

Materials:

The following chemicals and solvents were used without further purification: lead iodide (PbI₂) (Sigma-Aldrich, 99.99%), lead(II) bromide (PbBr₂) (Sigma-Aldrich,

99.999%), formamidinium iodide (FAI) (Greatcell Energy), methylammonium bromide (MABr) (Greatcell Energy), and methylammonium chloride (MACl). All of the solvents were bought from Sigma-Aldrich, including Divinyl sulfone (contains 400-600 hydroquinone as an inhibitor, $\geq 6\%$), dimethyl sulfoxide (DMSO), and N, N-dimethylformamide (DMF) (99.8%, anhydrous).

Device fabrication:

FTO/glass substrates with laser patterns (sheet resistance $\approx 12 \Omega$ per square) were cleaned in detergent, distilled water, acetone, and isopropanol, respectively. The FTO glass was submerged in a TiCl_4 solution at 70°C for 60 minutes to produce the TiO_2 by employing the chemical bath deposition process. After that, the FTO substrate was repeatedly cleaned with distilled water and ethanol and dried for 30 minutes at 200°C . After 20 minutes of ultraviolet-ozone treatment, a thin coating of self-produced SnO_2 solution was spin-coated onto the previous TiO_2 layer for 30 seconds at 4000 rpm. Then, it was annealed for 60 mins at 200°C in an ambient atmosphere. The mixed powders of FAI:MABr:MACl: PbBr_2 : PbI_2 (molar ratio=1.41:0.04:0.4:0.04:1.47) in DMF/DMSO (4:1, v:v) were combined with appropriate amount of CsI mother solution (1.5M, in DMSO) stock solution to create the $\text{Cs}_{0.03}(\text{FA}_{0.97}\text{MA}_{0.03})_{0.97}\text{Pb}(\text{I}_{0.97}\text{Br}_{0.03})_3$ perovskite precursor solution (bandgap = 1.53 eV). Different amounts of DVS (0 to 20%, v:v) were incorporated into the perovskite solution in DMF for the DVS-based perovskite ink. After the post-treatment of glycerol, the as-cast perovskite films were transferred into a controlled ambient environment (20%–30% relative humidity, RH) and annealed onto a hotplate at 120°C for 60 mins to facilitate the spontaneous cross-linking and perovskite crystallization. The samples were transferred into the glovebox and spin-coated with BABr (2 mg/mL, IPA) and spiro-OMeTAD (80 mg/mL in CB, 29 μL of tBP, and 17.5 μL of Li-TFSI mother solution), respectively, followed by a 10 mins annealing at 100°C . An 80 nm thick Au electrode was subsequently patterned by thermally evaporating on top of the device using a shadow mask.

Characterizations:

Crystalline structure was explored on a Rigaku SmartLab X-ray diffractometer with Cu K α radiation in a step of 0.01° and θ -2 θ scan mode from 5° to 50°. Perovskite film morphology was examined by a high-resolution field emission scanning electron microscopy (SEM) (TESCAN VEGA3). Grazing-incidence wide-angle X-ray scattering (GIWAXS) was investigated using a Xeuss 2.0 SAXS/WAXS laboratory beamline with a Cu X-ray source (8.05 keV, 1.54 Å) and a Pilatus3R 300K detector. The in-situ UV-vis absorption spectra were measured using an F20-UVX spectrometer (Filmetrics, Inc.) equipped with tungsten halogen and deuterium light sources. Appropriate amounts of FAI, DVS, and FAI/DVS were dissolved into DMSO-d₆ to prepare the sample solutions. Their proton spectra were acquired using a 400 MHz NMR spectrometer. Steady-state photoluminescence (PL) and time-resolved decay spectra were measured using a PL spectrometer (Edinburgh Instruments, FLS920) with the excitation source of 636.2 nm picosecond pulsed diode laser (EPL-635, ~5 nJ/cm²) and detected at 780 nm. The bi-exponential function fitted TRPL decays spectra 5.1. Ultraviolet photoemission spectroscopy (UPS) measurement was carried out by a VG ESCLAB 220i-XL surface analysis system equipped with a monochromatic Al K X-ray source (1486.6 eV) in a vacuum of 3.0×10^{-8} Torr. J-V curves were obtained using a Keithley 2400 Source Meter under standard AM 1.5 G illumination (Enli Technology Co. Ltd., Taiwan) and a standard KG-5 Si diode calibrated the light intensity for the completed devices. Both forward (from -0.2 to 1.25 V) and reverse scanning (from 1.25 to -0.2 V) were performed with a delay time of 100 ms. The test areas (0.04 cm²) are typically defined by a metal mask with an aperture aligned with the active area. EQE spectra were measured with a QE-R 3011 EQE system (Enli Technology Co. Ltd., Taiwan) using 210 Hz chopped monochromatic light ranging from 300 to 850 nm. The EL EQE spectra were recorded by an LED photo-luminescence quantum yield measurement system (Enli Tech LQ-100) equipped with the Keithley 2400 Source Measure Unit. The non-radiative recombination loss ($\Delta V_{OC, nr}$) can be derived from the

EQE_{EL} at the injection current density equal to J_{SC} with equation 5.2. Thermal admittance spectroscopy (TAS) was performed to estimate the energetic distribution of trap density within perovskite films under an AC voltage with the frequency decreased from 10^6 to 100 Hz according to equation 5.3.

$$I(t) = A_1 \exp\left(-\frac{t}{\tau_1}\right) + A_2 \exp\left(-\frac{t}{\tau_2}\right) \quad (5.1)$$

$$\Delta V_{OC,nr} = -\frac{k_B T}{q} \ln EQE_{EL} \quad (5.2)$$

$$N_t(E_\omega) = -\frac{V_{bi}}{eW} \frac{dC}{d\omega} \frac{\omega}{k_B T} \quad (5.3)$$

$$E_\omega = k_B T \ln\left(\frac{\beta T^2}{\omega}\right) \quad (5.4)$$

V_{bi} is the built-in potential, W is the depletion width, C is the capacitance, ω is the applied angular frequency, and β is a temperature-independent parameter from the Arrhenius plot. The Mott-Schottky analysis could calculate V_{bi} and W for a PSC device.

Chapter 6 Summary and Outlook

6.1 Summary

Organic-inorganic halide perovskites-based solar cells have made enormous strides in the last ten years and have become increasingly popular in the scientific and industrial arenas. Minimizing the power conversion efficiency (PCE) loss of perovskite solar cells (PSCs) in comparison to other traditional photovoltaic (PV) technologies, however, remains a significant problem when scaling up the device area from cells to modules. The intermediate solvent-complex phases during perovskite crystallization must be carefully controlled in order to enhance crystal quality and minimize defects in perovskite films across vast regions. As-cast intermediate films' aging/ripening process has been reported in earlier research to result in fascinating residual solvent-aided mass transport/diffusion and reformation of perovskite precursors. In spite of these facts, In-depth understanding of the structural changes taking place throughout this miraculous transition phase is still missing.

First, we have shown how to include a multifunctional zwitterionic surfactant into a perovskite ink easily. This method allows for the meniscus coating of premium perovskite solar films at room temperature. TAH, a surfactant, promotes dense perovskite films with complete covering and modifies the crystallization and orientation of perovskite. Additionally, it self-assembles a waterproof barrier and neutralizes charged defects at the perovskite surface. With regard to perovskite compositions and device designs, the universality and adaptability of this approach not only improve the efficiencies of over 22% (0.04 cm² active area) and 21% (0.8 cm²) but also concurrently support moisture, thermal, and light illumination stability. By better understanding the role of functionalized surfactants in the large-scale printing of perovskite polycrystalline films, this approach opens a new avenue toward the scalable fabrication of perovskite-based optoelectronic devices with more extraordinary performance and stability.

In contrast to conventional devices, the inverted device based on PTAA requires rinsing before depositing the perovskite layer, which makes the procedure more difficult. The doctor-blade coating method was used to swipe the perovskite precursor solution linearly at room temperature after being treated with various ethyl alcohol concentrations to enhance the procedure. We discovered that ethyl alcohol not only speeds up the nucleation of perovskites and produces more compact and uniform perovskite films but also suppresses non-radiative recombination. This was found after investigating the nucleation of perovskite intermediate complex by in-situ X-ray diffraction and time-dependent UV-vis absorption technologies. The stability and efficiency both rise from 20.31% to 22.18% as a result.

Secondly, the integration of ethyl alcohol (EtOH) into perovskite ink for high-performance room-temperature blade-coated perovskite solar cells (PSCs) and modules served as a demonstration of a simple and effective EtOH co-solvent (ECS) technique. Our methodical real-time perovskite crystallization investigation revealed the phase-transition mechanism and delicate perovskite structure evolutions. The formation of an FA-based precursor solvate ($\text{FA}_2\text{PbBr}_4\text{D}\cdot\text{MSO}$) during the trace solvent-assisted transition (TSAT) process, which expertly balanced the balance between nucleation and crystal growth to ensure high-quality perovskite films, was significantly aided by EtOH in the mixed-solvent system, according to both time-resolved X-ray diffraction technique and density functional theory (DFT) calculations. One of the most significant records for blade-coated PSCs in both small-area devices and mini-modules, this method effectively reduced non-radiative recombination and improved efficiency in both 1.54 (23.19%) and 1.60 eV (22.51%) perovskite systems. In the 1.54 eV perovskite system, we attained an outstanding V_{OC} deficit as low as 335 mV, which coincided with the reported non-radiative recombination loss of only 77 mV. Another distinguishing feature of this strategy is improved device stability.

Thirdly, We pre-incorporated divinyl sulfone (DVS), a cross-linking initiator in the perovskite precursor solution. As a co-solvent, DVS's special feature enabled the intermediate-dominated perovskite crystallization manipulation by implementing a preferred FAI-DVS-based solvate transition. Moreover, the post-treatment of the

nucleophilic reagent glycerine (gly) caused the controlled co-polymerization in three dimensions. In addition to releasing the remaining tensile strain, the co-polymer scaffold also passivated the intrinsic defects at the near-surface area. As a consequence, we obtained one of the best maximum PCEs over 25% (certified 24.6%) and maximum V_{OC} (1.229 V and 0.301 V deficit) among all published FA-dominated perovskite systems. This all-around co-polymerization technique greatly improved the moisture resistance of perovskite films and devices, resulting in the long-term operational stability of PSCs under ambient conditions ($T_{90} > 1800$ h).

6.2 Outlook

Perovskite solar cells must satisfy the following requirements to be industrialized: high stability, high photovoltaic performance, and low cost of large-area devices.

Developing deposition technologies is essential for achieving perovskite mass manufacturing and commercialization of solar cells. Several techniques can be utilized to fabricate large-area perovskite solar cells, including spray coating, slot-die coating, and doctor-blade coating. However, compared to small-area (≤ 1 cm²) devices, the efficiency of large-area devices utilizing these coating processes is lower. Therefore, optimizing the structure, critical materials, deposition method, and decreasing series resistance is essential to producing high-performance, large-area perovskite solar cells. I observed that the devices using alcohol had a current density of just 23.16 mA/cm², which has to be increased. More research into additive engineering to control crystal growth in large-area perovskite films generated through doctor blading is required to address the issue of low current density in alcohol-based devices. Methylammonium acetate (MAAc) would be the first option for addition because of its simpler evaporation at low temperatures close to 60 °C, which may help in solvent evaporation and intermediate perovskite phase transition management.

A number of difficulties associated with perovskite stability must be resolved, including temperature, light, and light-related instability. By protecting perovskite solar cells from exposure to air, it is possible to reduce the humidity instability. Optimizing the deposition procedure, the composition of the perovskite films, the bulk, and their

interface is necessary to solve light and thermal stability issues. For example, investigating substances like sulfobetaine-based zwitterionic surfactants, which may provide a robust waterproof barrier at the top of perovskite and significantly improve the durability of perovskite films and devices under moisture, heat, and light stressing conditions, is one strategy.

The large-scale production of perovskite solar cells is currently limited by the high cost and instability of organic hole transport layer (HTL) materials such as Spiro-OMeTAD and PTAA, which are easy to degradation under light, heat, and humidity. Eliminating the HTL can significantly enhance overall device stability, as it removes these sensitive materials from the system. Additionally, the absence of the HTL simplifies the interface between the perovskite layer and the electrode, which can potentially reduce interfacial defects. Therefore, the removal of the HTL not only addresses cost and stability issues but also contributes to improved device performance by minimizing recombination losses.

One of the primary challenges associated with HTL-free designs is the increased risk of short circuits due to the direct interaction between electrons from the perovskite layer and the anode. The absence of the HTL, which typically serves as a barrier to electron transport, increases the risk of short-circuiting.

The utilization of carbon-based electrodes offers a promising solution to this issue. These electrodes not only serve as effective contacts but also exhibit excellent hole selectivity, blocking electron transport and then preventing short circuits. Furthermore, carbon materials are characterized by their stability, low cost, and ease of large-scale production, making them an attractive option for further reducing production costs.

The introduction of a thin buffer layer between the perovskite and the electrode is essential for preventing direct contact between electrons and the anode. This buffer layer is crucial for ensuring that only holes are extracted by the anode, enhancing charge selectivity. Materials such as graphene oxide can serve as effective electron-blocking layers. These materials are typically thin enough not to interfere with hole extraction but are highly effective at blocking electron transport. Additionally, small amounts of

doping at the perovskite or electrode interface can further improve charge selectivity. For instance, introducing a nickel oxide (NiO_x) layer between the perovskite and the anode can serve as a hole-selective contact layer. NiO_x , with its p-type conductivity, promotes hole extraction while blocking electron transport to prevent short circuits. Moreover, NiO_x is stable, low-cost, and enhances device longevity.

HTL-free perovskite solar cells offer significant advantages by reducing material costs, simplifying manufacturing processes, and enhancing long-term stability through the removal of organic hole transport layers. However, a critical challenge that must be addressed is the risk of short circuits between electrons and the anode. To mitigate this issue, several strategies can be employed, such as the use of selective electrode materials, energy level engineering, surface passivation, and interface modification. With these techniques, HTL-free perovskite solar cells have the potential not only to achieve efficiencies comparable to traditional designs but also to offer improved stability and lower production costs.

References

- 1 April 25, 1954: Bell Labs Demonstrates the First Practical Silicon Solar Cell. *APS News. American Physical Society*. **18 (4)** (2009).
- 2 Tsokos, K. A. Physics for the IB Diploma Full Colour. *Cambridge University Press* (2010).
- 3 Black, L. E. New Perspectives on Surface Passivation: Understanding the Si-Al₂O₃ Interface (PDF). *Springer* (2016).
- 4 Lojek, B. History of Semiconductor Engineering. *Springer Science & Business Media*, 120 & 321–323 (2019).
- 5 Nelson, J. *The Physics of solar cells*. (2003).
- 6 S. M. Sze, K. K. N. *Physics of Semiconductor Devices*. Vol. Third Edition (2007).
- 7 Kojima, A. T., Kenjiro; Shirai, Yasuo; Miyasaka, Tsutomu. Organometal Halide Perovskites as Visible-Light Sensitizers for Photovoltaic Cells. *Journal of the American Chemical Society* **131 (17)**, 6050–6051, doi:doi:10.1021/ja809598r (2009).
- 8 Im, J.-H. L., Chang-Ryul; Lee, Jin-Wook; Park, Sang-Won; Park, Nam-Gyu. 6.5% efficient perovskite quantum-dot-sensitized solar cell. *Nanoscale* **3 (10)**, 4088–4093, doi:doi:10.1039/C1NR10867K (2011).
- 9 Lee, M. M. T., J.; Miyasaka, T.; Murakami, T. N.; Snaith, H. J. Efficient Hybrid Solar Cells Based on Meso-Superstructured Organometal Halide Perovskites. *Science* **338 (6107)**, 643–647, doi:doi:10.1126/science.1228604 (2012).
- 10 Hadlington, S. Perovskite coat gives hybrid solar cells a boost. *RSC Chemistry world* (2012).
- 11 Kim, H.-S. L., Chang-Ryul; Im, Jeong-Hyeok; Lee, Ki-Beom; Moehl, Thomas; Marchioro, Arianna; Moon, Soo-Jin; Humphry-Baker, Robin; Yum, Jun-Ho; Moser, Jacques E.; Grätzel, Michael; Park, Nam-Gyu. Lead Iodide Perovskite Sensitized All-Solid-State Submicron Thin Film Mesoscopic Solar Cell with Efficiency Exceeding 9%. *Scientific Reports* **2**, doi:doi:10.1038/srep00591 (2012).
- 12 Burschka, J. P., Norman; Moon, Soo-Jin; Humphry-Baker, Robin; Gao, Peng; Nazeeruddin, Mohammad K.; Grätzel, Michael. Sequential deposition as a route to high-performance perovskite-sensitized solar cells. *Nature* **499 (7458)**, 316–319, doi:doi:10.1038/nature12340 (2013).
- 13 Olga Malinkiewicz, A. Y., Yong Hui Lee, Guillermo Mínguez Espallargas, Michael Graetzel, Mohammad K. Nazeeruddin & Henk J. Bolink. Perovskite solar cells employing organic charge-transport layers. *Nature Photonics* **8 (2)**, 128–132, doi:doi:10.1038/nphoton.2013.341 (2013).
- 14 Liu, M. J., Michael B.; Snaith, Henry J. Efficient planar heterojunction perovskite solar cells by vapour deposition. *Nature* **501 (7467)**, 395–398, doi:doi:10.1038/nature12509 (2013).
- 15 Miodownik, M. *The perovskite lightbulb moment for solar power*, (2014).

- 16 Docampo, P. B., James M.; Darwich, Mariam; Eperon, Giles E.; Snaith, Henry J. Efficient organometal trihalide perovskite planar-heterojunction solar cells on flexible polymer substrates. *Nature Communications* **4**, doi:doi:10.1038/ncomms3761. PMID 24217714 (2013).
- 17 Zhou, H. C., Q.; Li, G.; Luo, S.; Song, T.-b.; Duan, H.-S.; Hong, Z.; You, J.; Liu, Y.; Yang, Y. Interface engineering of highly efficient perovskite solar cells. *Science* **345 (6196)**, 542–546, doi:doi:10.1126/science.1254050 (2014).
- 18 Best Research-Cell Efficiency Chart.2023. <https://www.nrel.gov/pv/cell-efficiency.html>.
- 19 Li, B. & Zhang, W. Improving the stability of inverted perovskite solar cells towards commercialization. *Communications Materials* **3**, doi:10.1038/s43246-022-00291-x (2022).
- 20 Li, Z. *et al.* Stabilizing Perovskite Structures by Tuning Tolerance Factor: Formation of Formamidinium and Cesium Lead Iodide Solid-State Alloys. *Chemistry of Materials* **28**, 284-292, doi:10.1021/acs.chemmater.5b04107 (2015).
- 21 N, P. mixed-organic cation perovskite photovoltaics for enhanced solar-light harvesting. *Angewandte Chemie* **126(12)**, 3215-3221 (2014).
- 22 *Sol gel TiO 2 antireflection coatings for silicon solar cells - Scientific Figure on ResearchGate* https://www.researchgate.net/figure/The-stages-of-the-deposition-thin-films-by-spin-coating-method_fig3_277891167 [accessed 9 Jul, 2020].
- 23 Gratzel, M. The light and shade of perovskite solar cells. *Nat. Mater* **13**, 838-842 (2014).
- 24 Green, M. A., Ho-Baillie, A., and Snaith, H.J. The emergence of perovskite solar cells. *Nat. Photonics* **8**, 506-514 (2014).
- 25 Correa-Baena, J.-P., Abate, A., Saliba, M., Tress, W., Jesper Jacobsson, T., Grätzel, M., and Hagfeldt, A. The rapid evolution of highly efficient perovskite solar cells. *Energy Environ. Sci* **10**, 710-727 (2017).
- 26 Saliba, M., Matsui, T., Domanski, K., Seo, J.-Y., Ummadisingu, A., Zakeeruddin, S.M., Correa-Baena, J.-P., Tress, W.R., Abate, A., Hagfeldt, A., et al. Incorporation of rubidium cations into perovskite solar cells improves photovoltaic performance. *Science* **354**, 206-209 (2016).
- 27 Wu, Y., Xie, F., Chen, H., Yang, X., Su, H., Cai, M., Zhou, Z., Noda, T., and Han, L. Thermally stable MAPbI₃ perovskite solar cells with efficiency of 19.19% and area over 1 cm² achieved by additive engineering. *Adv. Mater* **29**, **1701073** (2017).
- 28 Tan, H., Jain, A., Voznyy, O., Lan, X., de Arquer, F.P.G., Fan, J.Z., Quintero-Bermudez, R., Yuan, M., Zhang, B., Zhao, Y., et al. Efficient and stable solution-processed planar perovskite solar cells via contact passivation. *Science* **355**, 722-726 (2017).
- 29 Yang, M., Li, Z., Reese, M.O., Reid, O.G., Kim, D.H., Siol, S., Klein, T.R., Yan, Y., Berry, J.J., van Hest, M.F.A.M., et al. Perovskite ink with wide processing window for scalable high-efficiency solar cells. *Nat. Energy* **2**, **17038** (2017).

- 30 Yang, G., Chen, C., Yao, F., Chen, Z., Zhang, Q., Zheng, X., Ma, J., Lei, H., Qin, P., Xiong, L., et al. Effective carrier-concentration tuning of SnO₂ quantum dot electron-selective layers for high-performance planar perovskite solar cells. *Adv. Mater* **30**, 1706023 (2018).
- 31 Jeon, N. J., Noh, J.H., Kim, Y.C., Yang, W.S., Ryu, S., and Seok, S.I. Solvent engineering for high-performance inorganic-organic hybrid perovskite solar cells. *Nat. Mater* **13**, 897-903 (2014).
- 32 Xiao, M., Huang, F., Huang, W., Dkhissi, Y., Zhu, Y., Etheridge, J., Gray-Weale, A., Bach, U., Cheng, Y.B., and Spiccia, L. A fast deposition-crystallization procedure for highly efficient lead iodide perovskite thin-film solar cells. *Angew. Chem. Int. Ed. Engl* **53**, 9898-9903 (2014).
- 33 Kim, M., Kim, G.-H., Lee, T.K., Choi, I.W., Choi, H.W., Jo, Y., Yoon, Y.J., Kim, J.W., Lee, J., Huh, D., et al. Methylammonium chloride induces intermediate phase stabilization for efficient perovskite solar cells. *Joule* **3**, 2179-2192 (2019).
- 34 Yang, M., Zhou, Y., Zeng, Y., Jiang, C.S., Padture, N.P., and Zhu, K. Square-centimeter solution-processed planar CH₃NH₃PbI₃ perovskite solar cells with efficiency exceeding 15%. *Adv. Mater* **27**, 6363-6370 (2015).
- 35 Ye, F., Chen, H., Xie, F., Tang, W., Yin, M., He, J., Bi, E., Wang, Y., Yang, X., and Han, L. Soft-cover deposition of scaling-up uniform perovskite thin films for high cost-performance solar cells. *Energy Environ. Sci* **9**, 2295-2301 (2016).
- 36 Chen, H., Ye, F., Tang, W., He, J., Yin, M., Wang, Y., Xie, F., Bi, E., Yang, X., Gratzel, M., et al. A solvent- and vacuum-free route to large-area perovskite films for efficient solar modules. *Nature* **550**, 92-95 (2017).
- 37 Barrows, A. T., Pearson, A.J., Kwak, C.K., Dunbar, A.D.F., Buckley, A.R., and Lidzey, D.G. Efficient planar heterojunction mixed-halide perovskite solar cells deposited via spray-deposition. *Energy Environ. Sci* **7**, 2944-2950 (2014).
- 38 Mohamad, D. K., Griffin, J., Bracher, C., Barrows, A.T., and Lidzey, D.G. Spray-cast multilayer organometal perovskite solar cells fabricated in air. *Adv. Energy Mater* **6**, 1600994 (2016).
- 39 Schmidt, T. M., Larsen-Olsen, T.T., Carlé, J.E., Angmo, D., and Krebs, F.C. Upscaling of perovskite solar cells: fully ambient roll processing of flexible perovskite solar cells with printed back electrodes. *Adv. Energy Mater* **5**, 1500569 (2015).
- 40 Hwang, K., Jung, Y.S., Heo, Y.J., Scholes, F.H., Watkins, S.E., Subbiah, J., Jones, D.J., Kim, D.Y., and Vak, D. Toward large scale roll-to-roll production of fully printed perovskite solar cells. *Adv. Mater* **27**, 1241-1247 (2015).
- 41 Deng, Y., Peng, E., Shao, Y., Xiao, Z., Dong, Q., and Huang, J. Scalable fabrication of efficient organolead trihalide perovskite solar cells with doctor-bladed active layers. *Energy Environ. Sci* **8**, 1544-1550 (2015).
- 42 Yang, Z., Chueh, C.-C., Zuo, F., Kim, J.H., Liang, P.-W., and Jen, A.K.Y. High-performance fully printable perovskite solar cells via blade-coating technique under the ambient condition. *Adv. Energy Mater* **5**, 1500328 (2015).

- 43 Zhong, Y., Munir, R., Li, J., Tang, M.-C., Niazi, M.R., Smilgies, D.-M., Zhao, K., and Amassian, A. Blade-coated hybrid perovskite solar cells with efficiency > 17%: an in situ investigation. *ACS Energy Lett* **3**, 1078-1085 (2018).
- 44 Xiong Li, D. B., 2* Chenyi Yi, 1* Jean-David Décoppet, 1 Jingshan Luo, 1 Shaik Mohammed Zakeeruddin, 1 Anders Hagfeldt, 2 Michael Grätzel 1†. A vacuum flash-assisted solution process for high-efficiency large-area perovskite solar cells. *Science* **353**, 58-62, doi:DOI: 10.1126/science.aaf8060 (2016).
- 45 Kim, G. M., and Tatsuma, T. Semitransparent solar cells with ultrasmooth and low-scattering perovskite thin films. *J. Phys. Chem. C* **120**, 28933-28938 (2016).
- 46 Hu, H., Ren, Z., Fong, P.W.K., Qin, M., Liu, D., Lei, D., Lu, X., and Li, G. Room-temperature meniscus coating of >20% perovskite solar cells: a film formation mechanism investigation. *Adv. Funct. Mater* **29**, 1900092 (2019).
- 47 Ding, J., Han, Q., Ge, Q.-Q., Xue, D.-J., Ma, J.-Y., Zhao, B.-Y., Chen, Y.-X., Liu, J., Mitzi, D.B., and Hu, J.-S. Fully air-bladed high-efficiency perovskite photovoltaics. *Joule* **3**, 402-416 (2019).
- 48 He, M., Li, B., Cui, X., Jiang, B., He, Y., Chen, Y., O'Neil, D., Szymanski, P., Ei-Sayed, M.A., Huang, J., et al. Meniscus-assisted solution printing of large-grained perovskite films for high-efficiency solar cells. *Nat. Commun* **8**, 16045 (2017).
- 49 Munir, R. e. a. Hybrid perovskite thin-film photovoltaics: In situ diagnostics and importance of the precursor solvate phases. *Adv. Mater* **29**, 1604113 (2017).
- 50 Li, J., Munir, R., Fan, Y., Niu, T., Liu, Y., Zhong, Y., Yang, Z., Tian, Y., Liu, B., Sun, J., et al. Phase transition control for high-performance blade-coated perovskite solar cells. *Joule* **2**, 1313-1330 (2018).
- 51 Hu, H. *et al.* Nucleation and crystal growth control for scalable solution-processed organic-inorganic hybrid perovskite solar cells. *Journal of Materials Chemistry A* **8**, 1578-1603, doi:10.1039/C9TA11245F (2020).
- 52 Deng, Y., Van Brackle, C.H., Dai, X., Zhao, J., Chen, B., and Huang, J. Tailoring solvent coordination for high-speed, room-temperature blading of perovskite photovoltaic films. *Sci. Adv.* **5**, eaax7537 (2019).
- 53 Wu, W.-Q., Yang, Z., Rudd, P.N., Shao, Y., Dai, X., Wei, H., Zhao, J., Fang, Y., Wang, Q., Liu, Y., et al. Bilateral alkylamine for suppressing charge recombination and improving stability in blade-coated perovskite solar cells. *Sci. Adv* **5**, 8925 (2019).
- 54 Li, X. *et al.* Improved performance and stability of perovskite solar cells by crystal crosslinking with alkylphosphonic acid omega-ammonium chlorides. *Nat Chem* **7**, 703-711, doi:10.1038/nchem.2324 (2015).
- 55 Zheng, X. *et al.* Dual Functions of Crystallization Control and Defect Passivation Enabled by Sulfonic Zwitterions for Stable and Efficient Perovskite Solar Cells. *Adv Mater* **30**, e1803428, doi:10.1002/adma.201803428 (2018).
- 56 Qin, P. L. *et al.* Stable and Efficient Organo-Metal Halide Hybrid Perovskite Solar Cells via pi-Conjugated Lewis Base Polymer Induced Trap Passivation and Charge Extraction. *Adv Mater* **30**, e1706126, doi:10.1002/adma.201706126 (2018).

- 57 Zhang, F. & Zhu, K. Additive Engineering for Efficient and Stable Perovskite Solar Cells. *Advanced Energy Materials* **10**, doi:10.1002/aenm.201902579 (2019).
- 58 Wu, W. Q. *et al.* Molecular doping enabled scalable blading of efficient hole-transport-layer-free perovskite solar cells. *Nat Commun* **9**, 1625, doi:10.1038/s41467-018-04028-8 (2018).
- 59 Deng, Y. *et al.* Surfactant-controlled ink drying enables high-speed deposition of perovskite films for efficient photovoltaic modules. *Nature Energy* **3**, 560-566, doi:10.1038/s41560-018-0153-9 (2018).
- 60 Pearson, J. R. A. On convection cells induced by surface tension. *Journal of Fluid Mechanics* **4**, 489-500, doi:10.1017/s0022112058000616 (2006).
- 61 Islam, A. *et al.* Zwitterions for Organic/Perovskite Solar Cells, Light-Emitting Devices, and Lithium Ion Batteries: Recent Progress and Perspectives. *Advanced Energy Materials* **9**, doi:10.1002/aenm.201803354 (2019).
- 62 Zheng, X. *et al.* Defect passivation in hybrid perovskite solar cells using quaternary ammonium halide anions and cations. *Nature Energy* **2**, doi:10.1038/nenergy.2017.102 (2017).
- 63 Bi, D. *et al.* Multifunctional molecular modulators for perovskite solar cells with over 20% efficiency and high operational stability. *Nat Commun* **9**, 4482, doi:10.1038/s41467-018-06709-w (2018).
- 64 Viktor Gutmann, E. W. Coordination reactions in non aqueous solutions - The role of the donor strength. (1966).
- 65 Conings, B. *et al.* A Universal Deposition Protocol for Planar Heterojunction Solar Cells with High Efficiency Based on Hybrid Lead Halide Perovskite Families. *Adv Mater* **28**, 10701-10709, doi:10.1002/adma.201603747 (2016).
- 66 Babayigit, A., D'Haen, J., Boyen, H.-G. & Conings, B. Gas Quenching for Perovskite Thin Film Deposition. *Joule* **2**, 1205-1209, doi:10.1016/j.joule.2018.06.009 (2018).
- 67 Sept, D. & Tuszynski, J. A. Inhomogeneous nucleation in first-order phase transitions. *Phys Rev E Stat Phys Plasmas Fluids Relat Interdiscip Topics* **50**, 4906-4910, doi:10.1103/physreve.50.4906 (1994).
- 68 Dudarev, S. L. Inhomogeneous nucleation and growth of cavities in irradiated materials. *PHYSICAL REVIEW B*.
- 69 Cao, J. *et al.* Identifying the Molecular Structures of Intermediates for Optimizing the Fabrication of High-Quality Perovskite Films. *J Am Chem Soc* **138**, 9919-9926, doi:10.1021/jacs.6b04924 (2016).
- 70 Hu, Q. *et al.* In situ dynamic observations of perovskite crystallisation and microstructure evolution intermediated from [PbI(6)](4-) cage nanoparticles. *Nat Commun* **8**, 15688, doi:10.1038/ncomms15688 (2017).
- 71 Zhang, K. *et al.* A prenucleation strategy for ambient fabrication of perovskite solar cells with high device performance uniformity. *Nat Commun* **11**, 1006, doi:10.1038/s41467-020-14715-0 (2020).

- 72 Qin, M. *et al.* Manipulating the Mixed-Perovskite Crystallization Pathway Unveiled by In Situ GIWAXS. *Adv Mater* **31**, e1901284, doi:10.1002/adma.201901284 (2019).
- 73 Ahn, N. *et al.* Highly Reproducible Perovskite Solar Cells with Average Efficiency of 18.3% and Best Efficiency of 19.7% Fabricated via Lewis Base Adduct of Lead(II) Iodide. *J Am Chem Soc* **137**, 8696-8699, doi:10.1021/jacs.5b04930 (2015).
- 74 Liu, C., Cheng, Y.-B. & Ge, Z. Understanding of perovskite crystal growth and film formation in scalable deposition processes. *Chemical Society Reviews* **49**, 1653-1687, doi:10.1039/C9CS00711C (2020).
- 75 Lu, J. *et al.* Diammonium and Monoammonium Mixed-Organic-Cation Perovskites for High Performance Solar Cells with Improved Stability. *Advanced Energy Materials* **7**, doi:10.1002/aenm.201700444 (2017).
- 76 Hoffman, J. M. *et al.* In Situ Grazing-Incidence Wide-Angle Scattering Reveals Mechanisms for Phase Distribution and Disorientation in 2D Halide Perovskite Films. *Adv Mater* **32**, e2002812, doi:10.1002/adma.202002812 (2020).
- 77 Wang, R. *et al.* Caffeine Improves the Performance and Thermal Stability of Perovskite Solar Cells. *Joule* **3**, 1464-1477, doi:10.1016/j.joule.2019.04.005 (2019).
- 78 Chateigner, D. Thin film analysis by X-ray scattering. By Mario Birkholz, with contributions by P. F. Fewster and C. Genzel. Pp. xxii+356. Weinheim: Wiley-VCH Verlag GmbH Co., 2005. Price (hardcover) EUR 119, SFR 188. ISBN-10: 3-527-31052-5; ISBN-13: 978-3-527-31052-4. *Journal of Applied Crystallography* **39**, 925-926, doi:10.1107/s0021889806034698 (2006).
- 79 Dong, J. *et al.* Mechanism of Crystal Formation in Ruddlesden–Popper Sn-Based Perovskites. *Advanced Functional Materials* **30**, doi:10.1002/adfm.202001294 (2020).
- 80 Yang, J. *et al.* Acoustic-optical phonon up-conversion and hot-phonon bottleneck in lead-halide perovskites. *Nat Commun* **8**, 14120, doi:10.1038/ncomms14120 (2017).
- 81 Song, T.-B. *et al.* Perovskite solar cells: film formation and properties. *Journal of Materials Chemistry A* **3**, 9032-9050, doi:10.1039/c4ta05246c (2015).
- 82 Wu, B. *et al.* Discerning the Surface and Bulk Recombination Kinetics of Organic–Inorganic Halide Perovskite Single Crystals. *Advanced Energy Materials* **6**, doi:10.1002/aenm.201600551 (2016).
- 83 Bi, D. *et al.* Polymer-templated nucleation and crystal growth of perovskite films for solar cells with efficiency greater than 21%. *Nature Energy* **1**, doi:10.1038/nenergy.2016.142 (2016).
- 84 Zhou, W. *et al.* Zwitterion Coordination Induced Highly Orientational Order of CH₃NH₃PbI₃ Perovskite Film Delivers a High Open Circuit Voltage Exceeding 1.2 V. *Advanced Functional Materials* **29**, doi:10.1002/adfm.201901026 (2019).
- 85 Tai, Q. *et al.* Antioxidant Grain Passivation for Air-Stable Tin-Based Perovskite Solar Cells. *Angew Chem Int Ed Engl* **58**, 806-810, doi:10.1002/anie.201811539 (2019).

- 86 Samiee, M. *et al.* Defect density and dielectric constant in perovskite solar cells. *Applied Physics Letters* **105**, doi:10.1063/1.4897329 (2014).
- 87 Peng, J., Chen, Y., Zheng, K., Pullerits, T. & Liang, Z. Insights into charge carrier dynamics in organo-metal halide perovskites: from neat films to solar cells. *Chem Soc Rev* **46**, 5714-5729, doi:10.1039/c6cs00942e (2017).
- 88 Jiang, Q. *et al.* Surface passivation of perovskite film for efficient solar cells. *Nature Photonics* **13**, 460-466, doi:10.1038/s41566-019-0398-2 (2019).
- 89 Tress, W. *et al.* Predicting the Open-Circuit Voltage of CH₃NH₃PbI₃ Perovskite Solar Cells Using Electroluminescence and Photovoltaic Quantum Efficiency Spectra: the Role of Radiative and Non-Radiative Recombination. *Advanced Energy Materials* **5**, doi:10.1002/aenm.201400812 (2014).
- 90 Rau, U. Reciprocity relation between photovoltaic quantum efficiency and electroluminescent emission of solar cells. *Physical Review B* **76**, doi:10.1103/PhysRevB.76.085303 (2007).
- 91 Yao, J. *et al.* Quantifying Losses in Open-Circuit Voltage in Solution-Processable Solar Cells. *Physical Review Applied* **4**, doi:10.1103/PhysRevApplied.4.014020 (2015).
- 92 Luo, D., Su, R., Zhang, W., Gong, Q. & Zhu, R. Minimizing non-radiative recombination losses in perovskite solar cells. *Nature Reviews Materials* **5**, 44-60, doi:10.1038/s41578-019-0151-y (2019).
- 93 Duan, C. *et al.* Precursor Engineering for Ambient-Compatible Antisolvent-Free Fabrication of High-Efficiency CsPbI₂Br Perovskite Solar Cells. *Advanced Energy Materials* **10**, doi:10.1002/aenm.202000691 (2020).
- 94 Zhang, M. *et al.* Reconfiguration of interfacial energy band structure for high-performance inverted structure perovskite solar cells. *Nat Commun* **10**, 4593, doi:10.1038/s41467-019-12613-8 (2019).
- 95 Heo, J. H. *et al.* Planar CH₃NH₃PbI₃ Perovskite Solar Cells with Constant 17.2% Average Power Conversion Efficiency Irrespective of the Scan Rate. *Adv Mater* **27**, 3424-3430, doi:10.1002/adma.201500048 (2015).
- 96 Li, N. *et al.* Cation and anion immobilization through chemical bonding enhancement with fluorides for stable halide perovskite solar cells. *Nature Energy* **4**, 408-415, doi:10.1038/s41560-019-0382-6 (2019).
- 97 Meng, X. *et al.* Molecular design enabled reduction of interface trap density affords highly efficient and stable perovskite solar cells with over 83% fill factor. *Nano Energy* **52**, 300-306, doi:10.1016/j.nanoen.2018.07.063 (2018).
- 98 Lee, D.-K., Jeong, D.-N., Ahn, T. K. & Park, N.-G. Precursor Engineering for a Large-Area Perovskite Solar Cell with >19% Efficiency. *ACS Energy Letters* **4**, 2393-2401, doi:10.1021/acsenenergylett.9b01735 (2019).
- 99 Dou, B. *et al.* Roll-to-Roll Printing of Perovskite Solar Cells. *ACS Energy Letters* **3**, 2558-2565, doi:10.1021/acsenenergylett.8b01556 (2018).
- 100 Li, P. *et al.* Inkjet manipulated homogeneous large size perovskite grains for efficient and large-area perovskite solar cells. *Nano Energy* **46**, 203-211, doi:10.1016/j.nanoen.2018.01.049 (2018).

- 101 Zuo, C., Vak, D., Angmo, D., Ding, L., and Gao, M. One-step roll-to-roll air processed high efficiency perovskite solar cells. *Nano Energy* **46**, 185-192 (2018).
- 102 Huang, H. *et al.* Two-step ultrasonic spray deposition of CH₃NH₃PbI₃ for efficient and large-area perovskite solar cell. *Nano Energy* **27**, 352-358, doi:10.1016/j.nanoen.2016.07.026 (2016).
- 103 Ye, F. *et al.* Soft-cover deposition of scaling-up uniform perovskite thin films for high cost-performance solar cells. *Energy & Environmental Science* **9**, 2295-2301, doi:10.1039/c6ee01411a (2016).
- 104 Tang, S. *et al.* Composition Engineering in Doctor-Blading of Perovskite Solar Cells. *Advanced Energy Materials* **7**, doi:10.1002/aenm.201700302 (2017).
- 105 Wu, J. *et al.* A Simple Way to Simultaneously Release the Interface Stress and Realize the Inner Encapsulation for Highly Efficient and Stable Perovskite Solar Cells. *Advanced Functional Materials* **29**, doi:10.1002/adfm.201905336 (2019).
- 106 Christians, J. A., Miranda Herrera, P. A. & Kamat, P. V. Transformation of the excited state and photovoltaic efficiency of CH₃NH₃PbI₃ perovskite upon controlled exposure to humidified air. *J Am Chem Soc* **137**, 1530-1538, doi:10.1021/ja511132a (2015).
- 107 Gao, P., Grätzel, M. & Nazeeruddin, M. K. Organohalide lead perovskites for photovoltaic applications. *Energy Environ. Sci.* **7**, 2448-2463, doi:10.1039/c4ee00942h (2014).
- 108 Cai, B., Xing, Y., Yang, Z., Zhang, W.-H. & Qiu, J. High performance hybrid solar cells sensitized by organolead halide perovskites. *Energy & Environmental Science* **6**, doi:10.1039/c3ee40343b (2013).
- 109 Yang, G. *et al.* Stable and low-photovoltage-loss perovskite solar cells by multifunctional passivation. *Nature Photonics* **15**, 681-689, doi:10.1038/s41566-021-00829-4 (2021).
- 110 *National Renewable Energy Laboratory (NREL) (2020).*
<https://www.nrel.gov/pv/assets/pdfs/best-research-cell-efficiencies.20200104.pdf>.
- 111 Min, H. *et al.* Perovskite solar cells with atomically coherent interlayers on SnO(2) electrodes. *Nature* **598**, 444-450, doi:10.1038/s41586-021-03964-8 (2021).
- 112 Yuan, R. *et al.* Boosted charge extraction of NbO_x-enveloped SnO₂ nanocrystals enables 24% efficient planar perovskite solar cells. *Energy & Environmental Science* **14**, 5074-5083, doi:10.1039/d1ee01519b (2021).
- 113 Kim, M. *et al.* Conformal quantum dot-SnO₂ layers as electron transporters for efficient perovskite solar cells. *Science* **375**, 302-306, doi:10.1126/science.abh1885 (2022).
- 114 Rui Wang, J. X., Kai-Li Wang, Zhao-Kui Wang, Yanqi Luo, David Fenning, Guangwei Xu, Selbi Nuryyeva, Tianyi Huang, Yepin Zhao, Jonathan Lee Yang, Jiahui Zhu, Minhuan Wang, Shaun Tan, Ilhan Yavuz, Kendall N. Houk, Yang Yang. Constructive molecular configurations for surface-defect passivation of perovskite photovoltaics. **366**, doi:10.1126/science.aay9698.

- 115 Zhang, H. *et al.* Bottom-Up Quasi-Epitaxial Growth of Hybrid Perovskite from Solution Process-Achieving High-Efficiency Solar Cells via Template-Guided Crystallization. *Adv Mater* **33**, e2100009, doi:10.1002/adma.202100009 (2021).
- 116 Abbel, R., Galagan, Y. & Groen, P. Roll-to-Roll Fabrication of Solution Processed Electronics. *Advanced Engineering Materials* **20**, doi:10.1002/adem.201701190 (2018).
- 117 Kim, Y. Y. *et al.* Roll-to-roll gravure-printed flexible perovskite solar cells using eco-friendly antisolvent bathing with wide processing window. *Nat Commun* **11**, 5146, doi:10.1038/s41467-020-18940-5 (2020).
- 118 Bu, T. *et al.* Lead halide-templated crystallization of methylamine-free perovskite for efficient photovoltaic modules. *Science* **372**, 1327, doi:10.1126/science.abh1035 (2021).
- 119 Liu, K. *et al.* Zwitterionic-Surfactant-Assisted Room-Temperature Coating of Efficient Perovskite Solar Cells. *Joule* **4**, 2404-2425, doi:10.1016/j.joule.2020.09.011 (2020).
- 120 Deng, Y. *et al.* Defect compensation in formamidinium-caesium perovskites for highly efficient solar mini-modules with improved photostability. *Nature Energy* **6**, 633-641, doi:10.1038/s41560-021-00831-8 (2021).
- 121 Shangshang Chen, X. D., Shuang Xu, Haoyang Jiao, Liang Zhao, Jinsong Huang. Stabilizing perovskite-substrate interfaces for high-performance perovskite modules. *Science* **373**, 902-907, doi:10.1126/science.abi6323 (2021).
- 122 Deng, Y., Wang, Q., Yuan, Y. & Huang, J. Vividly colorful hybrid perovskite solar cells by doctor-blade coating with perovskite photonic nanostructures. *Materials Horizons* **2**, 578-583, doi:10.1039/c5mh00126a (2015).
- 123 Chao, L. *et al.* Solvent Engineering of the Precursor Solution toward Large-Area Production of Perovskite Solar Cells. *Adv Mater* **33**, e2005410, doi:10.1002/adma.202005410 (2021).
- 124 Vidal, R. *et al.* Assessing health and environmental impacts of solvents for producing perovskite solar cells. *Nature Sustainability* **4**, 277-285, doi:10.1038/s41893-020-00645-8 (2020).
- 125 Lee, J. W., Kim, H. S. & Park, N. G. Lewis Acid-Base Adduct Approach for High Efficiency Perovskite Solar Cells. *Acc Chem Res* **49**, 311-319, doi:10.1021/acs.accounts.5b00440 (2016).
- 126 Wang, P. *et al.* Solvent-controlled growth of inorganic perovskite films in dry environment for efficient and stable solar cells. *Nat Commun* **9**, 2225, doi:10.1038/s41467-018-04636-4 (2018).
- 127 Liu, T. *et al.* High-Performance Formamidinium-Based Perovskite Solar Cells via Microstructure-Mediated δ -to- α Phase Transformation. *Chemistry of Materials* **29**, 3246-3250, doi:10.1021/acs.chemmater.7b00523 (2017).
- 128 Zeng, L. *et al.* Controlling the crystallization dynamics of photovoltaic perovskite layers on larger-area coatings. *Energy & Environmental Science* **13**, 4666-4690, doi:10.1039/d0ee02575e (2020).

- 129 Maleki, M., Reyssat, M., Restagno, F., Quere, D. & Clanet, C. Landau-Levich menisci. *J Colloid Interface Sci* **354**, 359-363, doi:10.1016/j.jcis.2010.07.069 (2011).
- 130 Mayer, H. C. & Krechetnikov, R. Landau-Levich flow visualization: Revealing the flow topology responsible for the film thickening phenomena. *Physics of Fluids* **24**, doi:10.1063/1.4703924 (2012).
- 131 E. A. Guggenheim, M. A. The theoretical basis of Raoult's law. *Transactions of the Faraday Society* **33**, 151-156, doi:DOI <https://doi.org/10.1039/TF9373300151> (1937).
- 132 Pratap, S. *et al.* Out-of-equilibrium processes in crystallization of organic-inorganic perovskites during spin coating. *Nat Commun* **12**, 5624, doi:10.1038/s41467-021-25898-5 (2021).
- 133 Petrov, A. A. *et al.* Formamidinium Haloplumbate Intermediates: The Missing Link in a Chain of Hybrid Perovskites Crystallization. *Chemistry of Materials* **32**, 7739-7745, doi:10.1021/acs.chemmater.0c02156 (2020).
- 134 Hamill, J. C., Schwartz, J. & Loo, Y.-L. Influence of Solvent Coordination on Hybrid Organic–Inorganic Perovskite Formation. *ACS Energy Letters* **3**, 92-97, doi:10.1021/acsenerylett.7b01057 (2017).
- 135 Kim, J. *et al.* Efficient planar-heterojunction perovskite solar cells achieved via interfacial modification of a sol–gel ZnO electron collection layer. *J. Mater. Chem. A* **2**, 17291-17296, doi:10.1039/c4ta03954h (2014).
- 136 Wetzelaer, G. J. *et al.* Trap-assisted non-radiative recombination in organic-inorganic perovskite solar cells. *Adv Mater* **27**, 1837-1841, doi:10.1002/adma.201405372 (2015).
- 137 GREEN, M. A. Accuracy of analytical expressions for solar cell fill factors. *Solar Cells* **7 (1982 - 1983)** 337 - 340 (1982).
- 138 Kim, H. S. *et al.* High efficiency solid-state sensitized solar cell-based on submicrometer rutile TiO₂ nanorod and CH₃NH₃PbI₃ perovskite sensitizer. *Nano Lett* **13**, 2412-2417, doi:10.1021/nl400286w (2013).
- 139 Liu, K. *et al.* Fullerene derivative anchored SnO₂ for high-performance perovskite solar cells. *Energy & Environmental Science* **11**, 3463-3471, doi:10.1039/c8ee02172d (2018).
- 140 Lee, S. W., Bae, S., Kim, D. & Lee, H. S. Historical Analysis of High-Efficiency, Large-Area Solar Cells: Toward Upscaling of Perovskite Solar Cells. *Adv Mater* **32**, e2002202, doi:10.1002/adma.202002202 (2020).
- 141 Li, D. *et al.* A Review on Scaling Up Perovskite Solar Cells. *Advanced Functional Materials* **31**, doi:10.1002/adfm.202008621 (2020).
- 142 Jiang, Y. *et al.* Combination of Hybrid CVD and Cation Exchange for Upscaling Cs-Substituted Mixed Cation Perovskite Solar Cells with High Efficiency and Stability. *Advanced Functional Materials* **28**, doi:10.1002/adfm.201703835 (2017).
- 143 Tang, M.-C. *et al.* Ambient blade coating of mixed cation, mixed halide perovskites without dripping: in situ investigation and highly efficient solar cells.

- Journal of Materials Chemistry A* **8**, 1095-1104, doi:10.1039/c9ta12890e (2020).
- 144 Shangshang Chen, X. X., Hangyu Gu, Jinsong Huang. Iodine reduction for reproducible and high-performance perovskite solar cells and modules. *SCIENCE ADVANCES* **7**, doi:10.1126/sciadv.abe8130.
- 145 Fong, P. W. *et al.* Printing High-Efficiency Perovskite Solar Cells in High-Humidity Ambient Environment-An In Situ Guided Investigation. *Adv Sci (Weinh)* **8**, 2003359, doi:10.1002/advs.202003359 (2021).
- 146 Lim, K.-S., Lee, D.-K., Lee, J.-W. & Park, N.-G. 17% efficient perovskite solar mini-module via hexamethylphosphoramide (HMPA)-adduct-based large-area D-bar coating. *Journal of Materials Chemistry A* **8**, 9345-9354, doi:10.1039/d0ta02017f (2020).
- 147 Tan, S. *et al.* Shallow Iodine Defects Accelerate the Degradation of α -Phase Formamidinium Perovskite. *Joule* **4**, 2426-2442, doi:10.1016/j.joule.2020.08.016 (2020).
- 148 Luo, C., Zhao, Y., Wang, X., Gao, F. & Zhao, Q. Self-Induced Type-I Band Alignment at Surface Grain Boundaries for Highly Efficient and Stable Perovskite Solar Cells. *Adv. Mater.* **33**, e2103231, doi:10.1002/adma.202103231 (2021).
- 149 Zhou, Q. *et al.* Dually-Passivated Perovskite Solar Cells with Reduced Voltage Loss and Increased Super Oxide Resistance. *Angew. Chem. Int. Ed. Engl.* **60**, 8303-8312, doi:10.1002/anie.202017148 (2021).
- 150 Zhang, Y. *et al.* Mechanochemistry Advances High-Performance Perovskite Solar Cells. *Adv. Mater.*, e2107420, doi:10.1002/adma.202107420 (2021).
- 151 Jiang, Q. *et al.* Surface passivation of perovskite film for efficient solar cells. *Nat. Photonics* **13**, 460-466, doi:10.1038/s41566-019-0398-2 (2019).
- 152 Zhu, J. *et al.* Formamidine disulfide oxidant as a localised electron scavenger for >20% perovskite solar cell modules. *Energy Environ. Sci.* **14**, 4903-4914, doi:10.1039/d1ee01440d (2021).
- 153 Yoo, J. J. *et al.* Efficient perovskite solar cells via improved carrier management. *Nature* **590**, 587-593, doi:10.1038/s41586-021-03285-w (2021).
- 154 Wu, W. Q., Rudd, P. N., Wang, Q., Yang, Z. & Huang, J. Blading phase-pure formamidinium-alloyed perovskites for high-efficiency solar cells with low photovoltage deficit and improved stability. *Adv. Mater.* **32**, 2000995, doi:10.1002/adma.202000995 (2020).
- 155 Yang, G. *et al.* Stable and low-photovoltage-loss perovskite solar cells by multifunctional passivation. *Nat. Photonics* **15**, 681-689, doi:10.1038/s41566-021-00829-4 (2021).
- 156 Jeong, J. *et al.* Pseudo-halide anion engineering for alpha-FAPbI₃ perovskite solar cells. *Nature* **592**, 381-385, doi:10.1038/s41586-021-03406-5 (2021).
- 157 Gratzel, M. The light and shade of perovskite solar cells. *Nat. Mater.* **13**, 838-842, doi:10.1038/nmat4065 (2014).
- 158 Green, M. A., Ho-Baillie, A. & Snaith, H. J. The emergence of perovskite solar cells. *Nat. Photonics* **8**, 506-514, doi:10.1038/nphoton.2014.134 (2014).

- 159 Chao, L. *et al.* Solvent Engineering of the Precursor Solution toward Large-Area Production of Perovskite Solar Cells. *Adv. Mater.* **33**, 2005410, doi:10.1002/adma.202005410 (2021).
- 160 Han, B. *et al.* Green Perovskite Light-Emitting Diodes with 200 Hours Stability and 16% Efficiency: Cross-Linking Strategy and Mechanism. *Advanced Functional Materials* **31**, doi:10.1002/adfm.202011003 (2021).
- 161 Liu, K., Fong, P. W. K., Liang, Q. & Li, G. Upscaling perovskite solar cells via the ambient deposition of perovskite thin films. *Trends in Chemistry* **3**, 747-764, doi:10.1016/j.trechm.2021.06.003 (2021).
- 162 Azmi, R. *et al.* Moisture-Resilient Perovskite Solar Cells for Enhanced Stability. *Adv. Mater.*, e2211317, doi:10.1002/adma.202211317 (2023).
- 163 Boyd, C. C., Cheacharoen, R., Leijtens, T. & McGehee, M. D. Understanding Degradation Mechanisms and Improving Stability of Perovskite Photovoltaics. *Chem. Rev.* **119**, 3418-3451, doi:10.1021/acs.chemrev.8b00336 (2019).
- 164 Chen, B., Rudd, P. N., Yang, S., Yuan, Y. & Huang, J. Imperfections and their passivation in halide perovskite solar cells. *Chem. Soc. Rev.* **48**, 3842-3867, doi:10.1039/c8cs00853a (2019).
- 165 Liu, C., Cheng, Y. B. & Ge, Z. Understanding of perovskite crystal growth and film formation in scalable deposition processes. *Chem. Soc. Rev.* **49**, 1653-1687, doi:10.1039/c9cs00711c (2020).
- 166 Xiang, W. *et al.* Intermediate phase engineering of halide perovskites for photovoltaics. *Joule*, doi:10.1016/j.joule.2021.11.013 (2021).
- 167 Li, X. *et al.* In-situ cross-linking strategy for efficient and operationally stable methylammonium lead iodide solar cells. *Nat Commun* **9**, 3806, doi:10.1038/s41467-018-06204-2 (2018).
- 168 Luo, L. *et al.* Stabilization of 3D/2D perovskite heterostructures via inhibition of ion diffusion by cross-linked polymers for solar cells with improved performance. *Nat. Energy* **8**, 294-303, doi:10.1038/s41560-023-01205-y (2023).
- 169 Yang, M. *et al.* Reducing lead toxicity of perovskite solar cells with a built-in supramolecular complex. *Nature Sustainability*, DOI: 10.1038/s41893-41023-01181-x, doi:10.1038/s41893-023-01181-x (2023).
- 170 Han, T. H. *et al.* Spontaneous Hybrid Cross-Linked Network Induced by Multifunctional Copolymer toward Mechanically Resilient Perovskite Solar Cells. *Adv. Funct. Mater.* **32**, 2207142, doi:10.1002/adfm.202207142 (2022).
- 171 Zheng, Z. *et al.* Pre-Buried Additive for Cross-Layer Modification in Flexible Perovskite Solar Cells with Efficiency Exceeding 22. *Adv. Mater.* **34**, e2109879, doi:10.1002/adma.202109879 (2022).
- 172 Yin, X. *et al.* Cross-Linking Polymerization Boosts the Performance of Perovskite Solar Cells: From Material Design to Performance Regulation. *Energy Environ. Sci.*, DOI: 10.1039/D1033EE01546G, doi:10.1039/d3ee01546g (2023).
- 173 Zhang, H. *et al.* Multifunctional Crosslinking-Enabled Strain-Regulating Crystallization for Stable, Efficient alpha-FAPbI₃ -Based Perovskite Solar Cells. *Adv. Mater.* **33**, e2008487, doi:10.1002/adma.202008487 (2021).

- 174 Hamill, J. C., Schwartz, J. & Loo, Y.-L. Influence of solvent coordination on hybrid organic–inorganic perovskite formation. *ACS Energy Lett.* **3**, 92-97, doi:10.1021/acsenerylett.7b01057 (2017).
- 175 Liang, Q. *et al.* Manipulating Crystallization Kinetics in High-Performance Blade-Coated Perovskite Solar Cells via Cosolvent-Assisted Phase Transition. *Adv. Mater.* **34**, 2200276, doi:10.1002/adma.202200276 (2022).
- 176 Ahuja, S. K. *et al.* Fourier Transform Infrared (FTIR) Study of Thermal Stability in Vinylidene Fluoride Copolymers. *SPIE Fourier and Computerized Infrared Spectroscopy* **553**, 112-113 (1985).
- 177 Ellzy, M. W., Jensen, J. O. & Kay, J. G. Vibrational frequencies and structural determinations of di-vinyl sulfone. *Spectrochim Acta A Mol Biomol Spectrosc* **59**, 867-881, doi:10.1016/s1386-1425(02)00239-1 (2003).
- 178 del Agua, I. *et al.* DVS-Crosslinked PEDOT:PSS Free-Standing and Textile Electrodes toward Wearable Health Monitoring. *Advanced Materials Technologies* **3**, doi:10.1002/admt.201700322 (2018).
- 179 Zhu, C. *et al.* Strain engineering in perovskite solar cells and its impacts on carrier dynamics. *Nat. Commun.* **10**, 815, doi:10.1038/s41467-019-08507-4 (2019).
- 180 Fei, C. *et al.* Lead-chelating hole-transport layers for efficient and stable perovskite minimodules. *Science* **380**, 823-829, doi:10.1126/science.ade9463 (2023).
- 181 Tongle Bu, J. L., Hengyi Li, Congcong Tian, Jie Su, Guoqing Tong, Luis K. Ono, Chao Wang, Zhipeng Lin, Nianyao Chai, Xiao-Li Zhang, Jingjing Chang, Jianfeng Lu, Jie Zhong, Wenchao Huang, Yabing Qi, Yi-Bing Cheng, Fuzhi Huang. Lead halide-templated crystallization of methylamine-free perovskite for efficient photovoltaic modules. *SCIENCE* **372**, 1327-1332, doi:10.1126/science.abh1035 (2021).
- 182 Zhu, J. *et al.* Formamidine disulfide oxidant as a localised electron scavenger for >20% perovskite solar cell modules. *Energy & Environmental Science* **14**, 4903-4914, doi:10.1039/d1ee01440d (2021).
- 183 Jeong, J. *et al.* Pseudo-halide anion engineering for alpha-FAPbI(3) perovskite solar cells. *Nature* **592**, 381-385, doi:10.1038/s41586-021-03406-5 (2021).
- 184 Minjin Kim, J. J., Haizhou Lu, Tae Kyung Lee, Felix T. Eickemeyer, Yuhang Liu, In Woo Choi, Seung Ju Choi, Yimhyun Jo, Hak-Beom Kim, Sung-In Mo, Young-Ki Kim, Heunjeong Lee, Na Gyeong An, Shinuk Cho, Wolfgang R. Tress, Shaik M. Zakeeruddin, & Anders Hagfeldt, J. Y. K., Michael Grätzel, Dong Suk Kim. Conformal quantum dot-SnO₂ layers as electron transporters for efficient perovskite solar cells. *SCIENCE* **375**, 302-306, doi:10.1126/science.abh18 (2022).
- 185 Yang Zhao, F. M., Zihan Qu, Shiqi Yu, Tao Shen, Hui-Xiong Deng, Xinbo Chu, Xinxin Peng, Yongbo Yuan, Xingwang Zhang, Jingbi You. Inactive (PbI₂)₂RbCl stabilizes perovskite films for efficient solar cells. *SCIENCE* **377**, 531-534, doi:10.1126/science.abp8873 (2022).

- 186 Wei Peng, K. M., Fengchun Cai, Hongguang Meng, Zhengjie Zhu, Tieqiang Li, Shaojie Yuan, Zijian Xu, Xingyu Feng, Jiahang Xu, Michael D. McGehee, Jixian Xu. Reducing nonradiative recombination in perovskite solar cells with a porous insulator contact. *SCIENCE* **379**, 683-690, doi:10.1126/science.ade3126.
- 187 Ni, Z. *et al.* Evolution of defects during the degradation of metal halide perovskite solar cells under reverse bias and illumination. *Nat. Energy* **7**, 65–73, doi:10.1038/s41560-021-00949-9 (2021).
- 188 Ran, C., Xu, J., Gao, W., Huang, C. & Dou, S. Defects in metal triiodide perovskite materials towards high-performance solar cells: origin, impact, characterization, and engineering. *Chem. Soc. Rev.* **47**, 4581-4610, doi:10.1039/c7cs00868f (2018).